NONLINEAR MECHANISMS IN PASSIVE MICROWAVE DEVICES

PhD Thesis Dissertation

by

EDUARD ROCAS

Submitted to the Universitat Politècnica de Catalunya (UPC)
in partial fulfillment of the requirements for the degree of

DOCTOR OF PHILOSOPHY

June 2011

Supervised by Dr. Carlos Collado

PhD program on Signal Theory and Communications

Nonlinear mechanisms in passive microwave devices

ABSTRACT

This work comprises the study, analysis and modeling of the nonlinear mechanisms in a variety of passive microwave devices. Bulk acoustic wave resonators and transmission lines made of high temperature superconductors, ferroelectrics or regular metals and dielectrics are the subject of this work. Both phenomenological and physical approaches are considered and circuit models are proposed and compared with measurements. The nonlinear observables, being harmonics, intermodulation distortion, and saturation or detuning, are properly related to the material properties that originate them. The obtained models can be used in circuit simulators to predict the performance of these microwave devices under complex modulated signals, or even be used to predict their performance when integrated into more complex systems.

Index Terms: Nonlinearities, microwaves, transmission lines, bulk acoustic waves, thermodynamics, self-heating, harmonics, intermodulation distortion, materials.

Aquesta tesi està dedicada als meus pares, Joana i Guillem.

PREFACE

The current tendency in the telecommunication market is a natural push for higher frequency, higher power and smaller devices. In conjunction with that, advanced materials are gradually being incorporated into electronics to achieve better capabilities like fast frequency tuning, ultra-low losses or superior power handling. However, inherent nonlinearities associated with materials' field-dependent properties give rise to undesired effects like harmonics, intermodulation distortion, detuning or saturation, which can potentially degrade the system's performance. In this scenario, with rising stringent requirements for electronics and increasing importance of signal integrity issues, the prediction of devices performance at the design stage is of crucial importance.

I initially started this work with the goal of studying the nonlinear phenomena in bulk acoustic wave devices, ignoring the complexity of the topic and the lack of success of previous researchers on this area. I soon started to also get motivated for other topics like ferroelectrics and high temperature superconductors, and developed my own interests, motivated by the research group I have been working with, which has a wide experience on nonlinear characterization and modeling.

The years at the National Institute of Standards and Technology (NIST) have been of crucial importance and that stage allowed me to deepen my interests for materials science and physics. The success of this thesis is the study of the thermal phenomena in microwave devices and how this impacts the nonlinear behavior. As recognition, two articles were selected as finalists at the Best Paper Competition in the

International Ultrasonics Symposium, Rome, 2009 and the International Microwave Symposium, Anaheim, 2010.

This work wouldn't have been possible without the support of my thesis supervisor at UPC, Carlos Collado, and my advisor at NIST, James C. Booth, who have kept me motivated all the time. Special thanks to Jordi Mateu, Alberto Padilla and Joan O'Callaghan, from UPC, and Nathan D. Orloff, from NIST, for their invaluable help. I also want to thank Robert Aigner, from TriQuint Semiconductor, for his collaborative attitude.

TABLE OF CONTENTS

INTRODUCTION

The telecommunications industry follows a tendency towards smaller devices, higher power and higher frequency, which imply an increase on the complexity of the electronics involved. Moreover, there is a need for extended capabilities like frequency tunable devices, ultra-low losses or high power handling, which make use of advanced materials for these purposes. In addition, increasingly demanding communication standards and regulations push the limits of the acceptable performance degrading indicators. This is the case of nonlinearities, whose effects, like increased Adjacent Channel Power Ratio (ACPR), harmonics, or intermodulation distortion among others, are being included in the performance requirements, as maximum tolerable levels.

In this context, proper modeling of the devices at the design stage is of crucial importance in predicting not only the device performance but also the global system indicators and to make sure that the requirements are fulfilled. In accordance with that, this work proposes the necessary steps for circuit models implementation of different passive microwave devices, from the linear and nonlinear measurements to the simulations to validate them. The objective of this work is to study, analyze and illustrate, in different types of devices, how to implement circuit models to capture the nonlinear behavior. A key step to achieve this goal is an accurate characterization of materials and devices, which is faced by making use of advanced measurement techniques. Therefore, considerations on special measurement setups are being made along this thesis.

Chapter I covers the special case of transmission lines made of High Temperature Superconductors (HTS) and the mechanisms of nonlinear generation that arise from these specific structures. A nonlinear phenomenological model for HTS transmission lines is proposed, which is obtained through the relation between the nonlinear surface impedance and the superfluid current density. Additionally, the HTS nonlinear circuit model is shown to be useful in predicting the performance of a limiting multiplexer filter bank, through simulations. Finally, the analysis of impedance mismatched nonlinear transmission lines is presented and closed-form expressions are obtained.

Chapter II focuses on nonlinearities on Bulk Acoustic Wave (BAW) resonators, which are supposed to be the future filtering solution for mobile applications, and presents phenomenological models that provide a first attempt to reproduce the nonlinear performance. Distributed models, which capture the acoustic propagation through the materials stack, and lumped models, which are a discrete representation of the resonance conditions, are presented and compared with measurements. Additionally, Chapter II includes a detailed study of the second harmonic generation and its proper measurement techniques.

Finally, Chapter III presents the interactions between electro-thermo-mechanical fields in microwave devices and how these can give rise to nonlinearities. Physical and phenomenological models are presented for BAW resonators that take into account the nonlinearities produced by self-heating. Moreover, the impact of

temperature rise and self-heating on transmission lines made of regular metals and dielectrics, and HTS or ferroelectrics is assessed.

This work is presented as a compendium of articles, which all of them discuss the previous work when necessary, and the methodology as well. The following schematic diagram illustrates the relation between the articles and Appendix A and B:

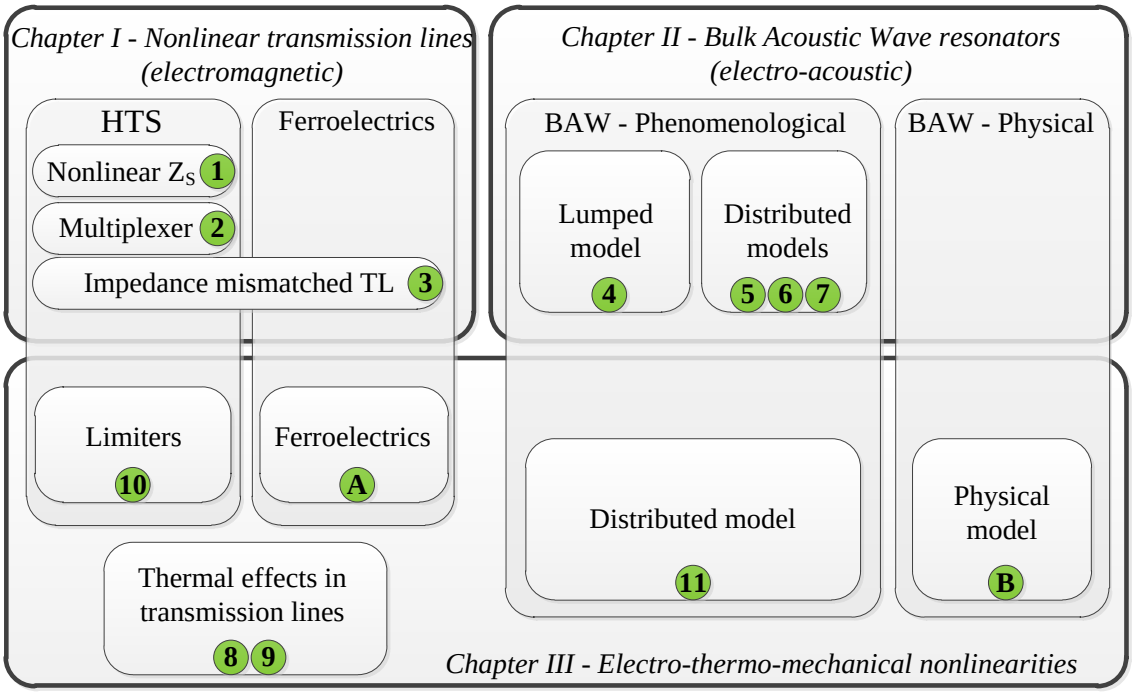

The articles in each chapter, including Appendix A and B, are as follows:

Chapter I – Nonlinear transmission lines

1. E. Rocas, C. Collado, A. Padilla, J. C. Booth, **"On the Relation Between the Nonlinear Surface Impedance and the Superfluid Current Density in High-Temperature Superconductors"**, *IEEE Transactions on Applied Superconductivity*, Accepted for publication and available online at IEEExplore.org as Early Access.

2. E. Rocas, A. Padilla, J. Mateu, N. Orloff, J. M. O'Callaghan, C. Collado, J. C. Booth, **"Superconducting Multiplexer Filter Bank for a Frequency-Selective Power Limiter"**, *IEEE Transactions on Applied Superconductivity*, Accepted for publication and available online at IEEExplore.org as Early Access.
3. J. Mateu, C. Collado, N. Orloff, J. C. Booth, E. Rocas, A. Padilla, J. M. O'Callaghan, **"Third-Order Intermodulation Distortion and Harmonic Generation in Mismatched Weakly Nonlinear Transmission Lines"**, *IEEE Transactions on Microwave Theory and Techniques*, vol. 57, no. 1, pp. 10-18, Jan. 2009

Chapter II – Bulk Acoustic Wave resonators

4. E. Rocas, C. Collado, J. Mateu, H. Campanella, J. M. O'Callaghan, **"Third order intermodulation distortion in Film Bulk Acoustic Resonators at resonance and antiresonance"**, *2008 IEEE MTT-S International Microwave Symposium Digest*, pp. 1259-1262, 15-20 June 2008
5. E. Rocas, C. Collado, A. Padilla, J. Mateu, J. M. O'Callaghan, **"Nonlinear distributed model for IMD prediction in BAW resonators"**, *2008 IEEE International Ultrasonics Symposium*, pp. 1557-1560, 2-5 Nov. 2008
6. C. Collado, E. Rocas, J. Mateu, A. Padilla, J. M. O'Callaghan, **"Nonlinear Distributed Model for Bulk Acoustic Wave Resonators"**, *IEEE Transactions on Microwave Theory and Techniques*, vol. 57, no. 12, pp. 3019-3029, Dec. 2009
7. C. Collado, E. Rocas, A. Padilla, J. Mateu, J. M. O'Callaghan, N. D. Orloff, J. C. Booth, E. Iborra, R. Aigner, **"First-Order Elastic Nonlinearities of Bulk**

Acoustic Wave Resonators", *IEEE Transactions on Microwave Theory and Techniques*, Accepted for publication and available online at IEEExplore.org as Early Access.

Chapter III – Electro-thermo-mechanical nonlinearities

8. E. Rocas, C. Collado, N. Orloff, J. C. Booth, **"Third-order intermodulation distortion due to self-heating in gold coplanar waveguides"**, *2010 IEEE MTT-S International Microwave Symposium Digest*, pp. 425-428, 23-28 May 2010

9. E. Rocas, C. Collado, N. D. Orloff, J. Mateu, A. Padilla, J. M. O'Callaghan, J. C. Booth, **"Passive Intermodulation Due to Self-Heating in Printed Transmission Lines"**, *IEEE Transactions on Microwave Theory and Techniques*, vol. 59, no. 2, pp. 311-322, Feb. 2011

10. E. Rocas, C. Collado, J. Mateu, N. Orloff, J. C. Booth, J. C., **"Modeling of Self-Heating Mechanism in the Design of Superconducting Limiters"**, *IEEE Transactions on Applied Superconductivity*, Accepted for publication and available online at IEEExplore.org as Early Access.

11. E. Rocas, C. Collado, J. C. Booth, E. Iborra, R. Aigner, **"Unified model for Bulk Acoustic Wave resonators' nonlinear effects"**, *2009 IEEE International Ultrasonics Symposium*, pp. 880-884, 20-23 Sept. 2009

A. E. Rocas, C. Collado, J. Mateu, N. Orloff, J. M. O'Callaghan, J. C. Booth, **"A large-signal model of ferroelectric thin-film transmission lines"**, *Submitted to IEEE Transactions on Microwave Theory and Techniques*, March 2011

B. E. Rocas, C. Collado, J. Mateu, N. D. Orloff, R. Aigner, J. C. Booth, **"Electro-thermo-dynamic model for bulk acoustic wave resonators"**, To be *submitted to IEEE Ultrasonics, Ferroelectrics and Frequency Control*, March 2011.

CHAPTER I - NONLINEAR TRANSMISSION LINES

The use of HTS in microwave applications raised a lot of expectations when the technology was discovered. In spite of that, the HTS microwave systems have not succeeded in entering the general market, but remain as an irreplaceable technology for some specific applications. However, the HTS technology has intrinsic nonlinearities that have been a matter of research since its discovery and can potentially degrade the performance of the devices. This chapter analyzes the intrinsic nonlinear phenomena in HTS transmission lines at microwave frequencies.

The first article is a theoretical study of the origins of nonlinearity in HTS, and results into a distributed nonlinear circuit model that captures the HTS nonlinear behavior. The study is based on the two-fluid model for HTS and relates the nonlinear surface impedance to the superfluid current density.

The second article illustrates how the inherent nonlinear behavior of HTS is used to implement a multiplexer filter that can limit the input power in nanoseconds time scale. The presented study allows one to properly design limiting resonators for specific maximum acceptable power levels.

Finally, the third article presents the analysis and study of impedance mismatched nonlinear transmission lines and how this impacts the nonlinear observables, which can be applied to the study of ferroelectric and HTS mismatched transmission lines.

The articles in Chapter 1 are:

- E. Rocas, C. Collado, A. Padilla, J. C. Booth, **"On the Relation Between the Nonlinear Surface Impedance and the Superfluid Current Density in High-Temperature Superconductors"**, *IEEE Transactions on Applied Superconductivity*, Accepted for publication and available online at IEEExplore.org as Early Access.
- E. Rocas, A. Padilla, J. Mateu, N. Orloff, J. M. O'Callaghan, C. Collado, J. C. Booth, **"Superconducting Multiplexer Filter Bank for a Frequency-Selective Power Limiter"**, *IEEE Transactions on Applied Superconductivity*, Accepted for publication and available online at IEEExplore.org as Early Access.
- J. Mateu, C. Collado, N. Orloff, J. C. Booth, E. Rocas, A. Padilla, J. M. O'Callaghan, **"Third-Order Intermodulation Distortion and Harmonic Generation in Mismatched Weakly Nonlinear Transmission Lines"**, *IEEE Transactions on Microwave Theory and Techniques*, vol. 57, no. 1, pp. 10-18, Jan. 2009

On the Relation Between the Nonlinear Surface Impedance and the Superfluid Current Density in High-Temperature Superconductors

Eduard Rocas, *Student Member, IEEE*, Carlos Collado, *Senior Member, IEEE*, Alberto Padilla, and James C. Booth

***Abstract*—The nonlinear surface impedance is related to a local description of the nonlinear superfluid current density that depends on the condensate velocity, by use of the definition of surface impedance as the ratio between the electric field and magnetic field at the conductor surface. To obtain this relation, we follow a rigorous approach based on the time-domain nonlinear London equations and the two-fluid model. The formulation is compared with harmonic balance simulations of an equivalent transmission line circuit that models a plane wave propagating across a vacuum-superconductor boundary, and shows very good agreement for the resulting surface impedance as a function of current density at the surface.**

***Index Terms*—HTS, nonlinear surface impedance, superconductor, superfluid current density, surface reactance, surface resistance.**

I. Introduction

THE surface impedance (Z_S) is one of the most useful and most often applied material parameters used to characterize the properties of a superconductor. It directly describes the electromagnetic properties of the superconductor material, such as the Meissner effect and the square-law scaling of the losses with frequency. Furthermore, the surface impedance can be easily related to measurable figure-of-merit of resonators, such as quality factor and resonance frequency [1]. For these reasons, the surface impedance is the most common parameter used to characterize the linear electromagnetic properties of superconductors. The surface impedance has also been extensively applied to characterize superconductor nonlinear properties.

In a linear regime, a formula for Z_S is found by use of the two-fluid model in phasors, by assuming sinusoidally varying quantities in the steady state. In the nonlinear case experimental characterization is usually directly related to measurements in the linear regime. For example, the resonance frequency and quality factor of a resonator are measured to obtain Z_S, but in the nonlinear case, the measurements are done as a function of the input power. They show measurable detuning and saturation for sufficiently high input power. These measurements give Z_S, as a function of the peak magnetic field; for example, $Z_S(H_{RF})$.

Subsequently, $Z_S(H_{RF})$ can be related to physically-relevant nonlinear parameters, such as the local pair-breaking current density j_c, as described in [2]. Obtaining j_c is extremely useful for different materials comparison and it can contribute to better understand the nature of superconductivity phenomena in high temperature superconductors [3]. Unfortunately it is not straightforward to connect $Z_S(H_{RF})$ with j_c, because of the nonlinear aspect of the problem. This implies, for example, that the expressions for the complex linear Z_s can no longer be simply generalized to the nonlinear regime by simply replacing the London penetration depth with a nonlinear version. This is because the linear expressions were derived in the frequency domain, and nonlinear analysis is better handled in the time domain.

In this work, we obtain new formulas for the nonlinear surface impedance, which is defined as the ratio between tangential electric and magnetic fields at the surface of a conductor sheet [4], as derived from the time-domain nonlinear London equations and the two-fluid model. These formulas relate the experimental observables to the nonlinear device-independent parameters, such as the current density. They differ from the widely used phenomenological formulas, and will be compared with circuit-based simulations of a plane wave propagating through a nonlinear HTS material.

II. Magnetic Field Inside the HTS Nonlinear Penetration Depth

In a superconducting material, the nonlinear problem can be formulated by starting with the definition of current including condensate density nonlinearity [5]

$$j_s = -n_s(v_s) e v_s, \tag{1}$$

where $n_s(v_s)$ is the superfluid current density in the two-fluid model, which depends on the condensate velocity v_s. For intrinsic nonlinearities and $\mathrm{d}_{(\mathrm{x2-y2})}$-wave superconductors, $n_s(v_s)$ can be written as [5], [6]:

$$n_s(v_s) = n_{s,0}\left(1 - a_{T,v} v_s^2\right), \tag{2}$$

Manuscript received August 03, 2010; accepted September 30, 2010. This work was partially supported by the Spanish Ministry of Science and Innovation through Grant TEC-2009-13897-C03-01/TCM, by the AGAUR, Gen. de Catalunya (2008-BE2-00196), and by the Spanish Ministry of Education through Ph.D. fellowships for E. Rocas (BES-2007-16775) and A. Padilla (AP200802235). This work is partially supported by the U.S. Government, which is not subject to U.S. copyright.

E. Rocas is with the Universitat Politècnica de Catalunya (UPC), Barcelona 08034, Spain, and also with the National Institute of Standards and Technology, Boulder, CO 80305 USA.

C. Collado and A. Padilla are with Universitat Politècnica de Catalunya (UPC), Barcelona 08034, Spain (e-mail: collado@tsc.upc.edu).

J. C. Booth is with the National Institute of Standards and Technology, Boulder, CO 80305 USA (e-mail: booth@boulder.nist.gov).

Color versions of one or more of the figures in this paper are available online at http://ieeexplore.ieee.org.

Digital Object Identifier 10.1109/TASC.2010.2085030

where $a_{T,v} >= 0$ is a temperature-dependent coefficient that sets the strength of the nonlinearity and $n_{s,0}$ is the superfluid current density for $v_s = 0$. With (2), (1) can be written as [5]

$$j_s = -n_{s,0}\left(1 - a_{T,v}v_s^2\right)ev_s. \tag{3}$$

This model of nonlinearity is one of the simplest expressions that we can find in the literature. In spite of its simplicity, the model can explain most of the experimental data for intermodulation distortion (IMD) in resonators fabricated from high temperature superconductor (HTS) thin films, as it implies a 3:1 slope for the logarithmic plot of IMD power vs. the input power [7].

If we assume an incident plane wave on a superconductor surface, we can calculate the current and field distributions within the superconductor. In a linear problem, this is usually done by solving the wave equation for the electric and magnetic fields, which leads to an exponential decrease of both quantities within the superconductor. For the nonlinear problem, the wave equation needs to be re-analysed with the appropriate generalization of the relevant quantities.

The condensate velocity is related to the volume current density by use of [5]

$$\frac{m}{\mu e}(-\nabla^2 v_s) = j. \tag{4}$$

Reference [5] proposes to solve a nonlinear version of the London equation that comes from substituting (3) into (4) and assuming that $j_s \sim j$:

$$\nabla^2\vec{v}_s - \frac{1}{\lambda_{L,0}^2}\vec{v}_s\left(1 - a_{T,v}v_s^2\right) = 0, \tag{5}$$

where $\lambda_{\mathrm{L},0}$ is the London penetration depth: $\lambda_{L,0} = \sqrt{m/\mu n_{s,0}e^2}$.

Now the superconductor is considered to occupy the half-space z ≥ 0 and with a uniform incident plane wave propagating towards positive z. The magnetic field is denoted as $h_{0,x}\hat{x}$ and the electric field as $-E_{0,y}\hat{y}$, so the screening current flows parallel to $\hat{y}$; $j_y\hat{y}$ and $-v_{s,y}\hat{y}$. Equation (5) is then simplified to

$$\frac{d^2v_{s,y}}{dz^2} - \frac{1}{\lambda_{L,0}^2}v_{s,y}\left(1 - a_{T,v}v_{s,y}^2\right) = 0. \tag{6}$$

Due to the continuity of tangential fields at z $= 0$, the boundary condition is

$$\left.\frac{m}{\mu e}\frac{dv_{s,y}}{dz}\right|_{z=0} = h_{0,x}, \tag{7}$$

This equation is solved in [5], and the solution assuming $\sqrt{a_{T,v}}v_{s,y} \ll 1$ is

$$v_{s,y}(z) = \frac{v_{s,y0}}{\left(a_{T,v}\frac{v^2{}_{s,y0}}{4} + \left(1 - a_{T,v}\frac{v^2{}_{s,y0}}{4}\right)e^{2z/\lambda_{L,0}}\right)^{1/2}}. \tag{8}$$

The magnetic field inside the superconductor is then

$$h_x(z) = \frac{h_0 e^{2\frac{z}{\lambda_{L,0}}}}{\left(a_{T,v}\frac{v_{s,y0}^2}{4} + \left(1 - a_{T,v}\frac{v_{s,y0}^2}{4}\right)e^{2z/\lambda_{L,0}}\right)^{3/2}}, \tag{9}$$

with $h_0 = \lambda_{L,0}n_{s0}v_{sy0}(1 - (a_{T,v}/4)v_{sy0}^2)$. Equation (9) follows a more complicated relation than the low-signal exponential behavior $h_0e^{-z/\lambda_{L0}}$ of the linear case ($a_{T,v} = 0$), although a plot of both distributions as a function of z shows that they are very similar. However, by use of (9), the initial decay rate $-(1/h_0)(dh/dz)|_{z=0}$ is different from λ_{L0}. The decay rate at the surface depends on the magnitude of v_{sy0} and its inverse is defined as an effective penetration depth $\lambda(v_{sy0})$, resulting in

$$\lambda(v_{sy0}) = \left(-\frac{1}{h_0}\left.\frac{dh}{dz}\right|_{z=0}\right)^{-1} = \lambda_{L,0}\left(1 + \frac{3}{4}a_{T,v}v^2{}_{sy0}\right), \tag{10}$$

if $\sqrt{a_{T,v}}v_{s,y} \ll 1$ is assumed. Note that $\lambda(v_{sy0})$ is also the ratio between the current at the surface $j_0 = (dh/dz)|_{z=0}$ and the magnetic field h_0.

In terms of j_0, we can write

$$\lambda(j_0) = \lambda_{L,0}\left(1 + \frac{3}{4}a_T j^2{}_0\right), \tag{11}$$

with $a_T = (a_{T,v}/n_s^2e^2)$. In a similar way, we could rewrite $n_s(v_s)$ of (2) at the surface as

$$n_{sc}(j_0) = n_{sc0}\left(1 - a_T j^2{}_0\right) \tag{12}$$

and note that $\lambda(j_0)$ is different from the nonlinear London penetration depth $\lambda_L(j_0)$ obtained by replacing n_{s0} for $n_s(j_0)$ in $\lambda_{L,0} = \sqrt{m/\mu n_{s,0}e^2}$, as is usually done:

$$\lambda_L(j_0) = \lambda_{L,0}\left(1 + \frac{1}{2}a_T j^2{}_0\right). \tag{13}$$

As we will see in the next section, the fact that $\lambda(j_0)$ is no longer equal than $\lambda_L(j_0)$ has a significant effect on the calculation of the nonlinear surface reactance.

III. Surface Reactance

We now apply this local model to calculate the surface impedance, which will be obviously nonlinear and dependent on the strength of the magnetic field at the surface. The surface impedance is defined as the ratio between tangential electric and magnetic fields at the surface of a conductor sheet [4]

$$Z_s = \left.\frac{E_t}{H_t}\right|_{surface}. \tag{14}$$

We can calculate the surface impedance by deriving the tangential electric and magnetic fields at the surface and applying (12). By use of the two-fluid model, the electric field inside the superconductor is related to the superfluid current density by $m(d\vec{v}_s/dt) = -e\vec{e}_{\mathrm{int}}$ and with (1), we can write

$$m\frac{d}{dt}\left[\frac{\vec{j}_s}{n_s(v_s)e^2}\right] = \vec{e}_{\mathrm{int}}. \tag{15}$$

Therefore, with (12), the current density and the electric field at z $= 0$ are related by

$$\frac{d}{dt}\left[\mu\lambda^2{}_{L0}\frac{j_0}{(1 - a_T j^2{}_0)}\right] = e_0. \tag{16}$$

Eqn. (16) can be written in powers of j_0 if $a_T \cdot j_0^2 \ll 1$:

$$\frac{d}{dt}\left[\mu{\lambda^2}_{L0}\left(1+a_T{j^2}_0\right)j_0\right]=e_0. \tag{17}$$

Note that j_0 and e_0 are time-dependent quantities. If we assume that the incident wave is sinusoidal ($h = H_0 cos(\omega \cdot t)$) we can approximate j_0 as $j_0 = J_0 cos(\omega \cdot t)$ and obtain the fundamental frequency component of e_0, $E_{0\omega}$, as

$$E_{0\omega}=j\omega\mu{\lambda^2}_{L0}\left(1+\frac{3}{4}a_T{J^2}_0\right)J_0. \tag{18}$$

The nonlinear ratio between electric field and current density can now be calculated by use of equation (18). In a linear problem, $H_0 \sim \lambda_{L0} J_0$ and we can think about extending this equality to the nonlinear problem, and use (18) to calculate the surface impedance. Nevertheless, this would be erroneous because the ratio between J_0 and H_0 is given by the effective penetration depth derived in the previous section. Instead, we maintain the assumption $j_s \sim j$, and by use of (10), we can evaluate (17) at the surface $z = 0$:

$$\frac{d}{dt}\left[\mu{\lambda^2}_L(j_0)\frac{h_0}{\lambda(j_0)}\right]=e_0, \tag{19}$$

and by use of (11) and (13), for $a_T j_0 \ll 1$ we obtain,

$$\frac{d}{dt}\left[\mu\lambda_{L0}\left(1+\frac{1}{4}a_T{j^2}_0\right)h_0\right]=e_0. \tag{20}$$

Hence, as previously done, the fundamental harmonic component is

$$E_{0\omega}=j\omega\mu\lambda_{L0}\left(1+\frac{3}{16}a_T{J^2}_{0\omega}\right)H_{0\omega}. \tag{21}$$

Then we can write the surface reactance directly as

$$X_\omega=\mathrm{Im}\left\{\frac{E_{0\omega}}{H_{0\omega}}\right\}=\omega\mu\lambda_{L0}\left(1+\frac{3}{16}a_T{J^2}_{0\omega}\right). \tag{22}$$

Note that the coefficient $3/16 \cdot a_T$, which quantifies the strength of the nonlinearities, is one fourth as large as the one obtained if the quotient between E_0 and J_0 is used to obtain the surface impedance.

IV. Surface Resistance

The formulation involving the nonlinear surface resistance is more complicated than for the nonlinear surface reactance. We begin by rewriting the ratio between E_0 and J_0 at the surface, but now consider that $j = j_s + j_n$ instead of $j \cdot j_s$. The two-fluid model gives a conductivity that is related with normal condensate fraction n_n by

$$\sigma_1(j)=\frac{e^2 n_n(j)\tau}{m}. \tag{23}$$

Therefore, its corresponding nonlinear dependence on the current density can be written as

$$\sigma_1(j)=\sigma_{10}(1+b_T j^2), \tag{24}$$

with

$$b_T=\left(\left(\frac{\lambda_{L0T}}{\lambda_{L00}}\right)^2-1\right)^{-1}a_T. \tag{25}$$

At the surface $z = 0$, with (15) and $j_n = \sigma_1(j) \cdot e$, we obtain

$$\frac{d}{dt}\left[\mu{\lambda^2}_L(j_0)j_0\right]=\frac{d}{dt}\left[\mu{\lambda^2}_L(j_0)\sigma_1(j_0)e_0\right]+e_0, \tag{26}$$

which can be rewritten as

$$e_0=\frac{d}{dt}\left[\mu{\lambda^2}_L(j_0)j_0-\mu{\lambda^2}_L(j_0)\sigma_1(j_0)\frac{d}{dt}\left(\mu{\lambda^2}_L(j_0)j_0\right)\right] \tag{27}$$

if $\mu^2\lambda_L^4(j_0)\sigma_1^2(j_0)(d^2e_0/dt^2) \ll e_0$, as is usually the case. Now, we replace (13) in (27) to obtain the ratio between the ω-frequency components $E_{0\omega}$ and $J_{0\omega}$:

$$\frac{E_{0\omega}}{J_{0\omega}}=\mu^2\lambda_{L0}^4\sigma_{10}\omega^2\left(1+\left(\frac{1}{4}b_T+a_T\right)J_0^2\right)+j\omega\mu\lambda_{L0}^2\left(1+\frac{3}{4}a_T J_0^2\right). \tag{28}$$

As is shown in the following section, this equation has been verified with nonlinear simulations using a circuit model approach, and show agreement within $\pm 0.5\%$ level.

The surface resistance involves the magnetic field and not just the current density, and we should extend the concept of effective penetration depth of (11) to relate J_0 and H_0, but consider $j = j_s + j_n$ instead of $j \sim j_s$. We should repeat the procedure of Section III but start with

$$\frac{m}{\mu e}(\nabla^2 v_s)+j_{sc}+j_n=0 \tag{29}$$

instead of (6). Then, we need to solve:

$$\nabla^2 v_s-\frac{1}{{\lambda^2}_{L,0}}v_s\left(1-a_{T,v}{v^2}_s\right)-\mu\sigma_{10}\left(1+b{v^2}_{s0}\right)\frac{dv_s}{dt}=0. \tag{30}$$

We have found no solution for this nonlinear equation, but by doing simulations with the equivalent circuit explained in the following section, we have found that, at the surface, the ratio γ between magnetic field and current density phasors follows the relation

$$\gamma=\frac{1}{\lambda_{L0}}\left(1-\frac{9}{16}a_T J_0^2\right)+j\frac{1}{2}\omega\mu\lambda_{L0}\sigma_1\left(1+\frac{6}{16}J_0^2\left(-\frac{1}{4}a_T+b_T\right)\right). \tag{31}$$

The surface impedance $Z_s = (E_0/H_0) = (E_0/J_0)\gamma$ can then be written multiplying (28) and (31) as

$$Z_s=\frac{1}{2}\omega^2\mu^2\lambda_{L0}^3\sigma_1\left(1+\frac{7}{32}a_T+\frac{1}{8}b_T J_0^2\right)+j\omega\mu\lambda_{L0}\left(1+\frac{3}{16}a_T J_0^2\right). \tag{32}$$

This expression agrees well with the simulations described in the next section. Note that the nonlinear term of the surface re-

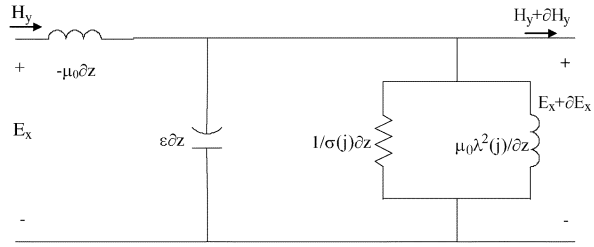

Fig. 1. Two-fluid equivalent circuit for a plane wave that propagates in a superconductor.

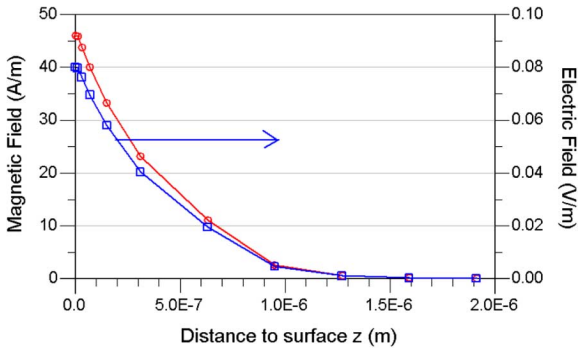

Fig. 2. (Circles, red line) Magnetic and (squares, blue line) electric fields in a superconductor, obtained via a circuit simulation approach.

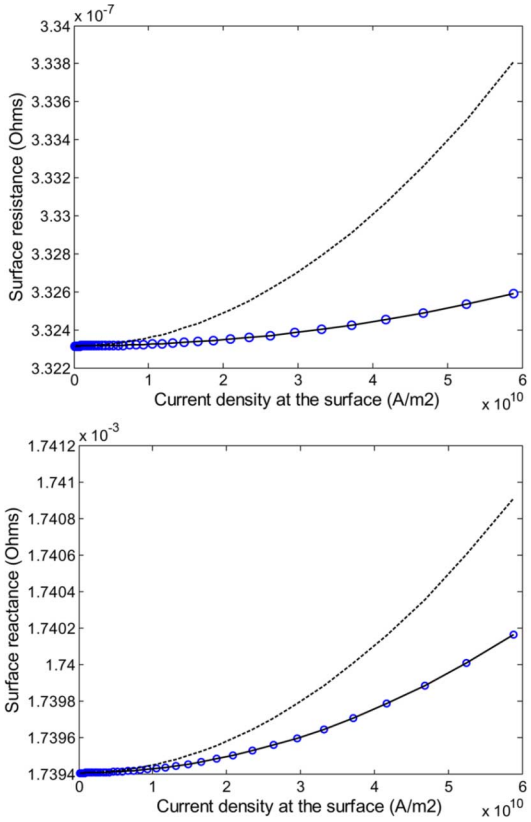

Fig. 3. (Solid line) Surface impedance obtained with (32) and (circles) harmonic balance simulations. Dashed line corresponds to a direct non-linearization of the usual surface impedance.

actance is half that compared to the value obtained directly by use of (13) instead of λ_L in the linear expression of the reactance. In the case of the resistance, the nonlinear terms of (32) are around to be one-fifth as large.

V. Equivalent Circuit Simulations of the Two-Fluid Model

From Maxwell's equations, the electric and magnetic fields inside the semi-infinite superconductor slab are related by

$$\begin{aligned} \partial e_x &= -\mu\partial z\frac{\partial h_y}{\partial t} \\ \partial h_y &= j\partial z + \varepsilon\partial z\frac{\partial e_x}{\partial t}, \end{aligned} \tag{33}$$

where $j = j_s + j_n$ by use of the two-fluid model, and

$$\begin{aligned} \frac{\partial}{\partial t}\left[\frac{\mu\lambda_L^2(j)}{\partial z}j_s\partial z\right] &= e_x \\ j_n\partial z &= \sigma_1(j)\partial z e_x. \end{aligned} \tag{34}$$

Fig. 1 shows an equivalent transmission line circuit that corresponds to (33) and (34) in the TEM approximation. The current density of $\sigma(j)$ and $\lambda(j)$ are calculated by use of $j = (\partial H_y/\partial z)$ at each segment of length dz.

The fields inside the superconductor are calculated by means of numerical techniques to analyse the cascading of several nonlinear circuits such as that described in Fig. 1. We have done this by use of an electromagnetic circuit simulator. Fig. 2 shows the electric and magnetic fields as a function of z.

Fig. 3 shows the surface impedance obtained from simulations and by use of (32). The agreement between the simulated and closed-form expressions is very good. Fig. 3 also shows the surface impedance that would be obtained by use of a direct generalization of the usual linear surface impedance expressions.

VI. Conclusion

We have developed a phenomenological expression for the nonlinear surface impedance consistent with the nonlinear simulations of an incident plane wave on a superconductor surface. We have also shown that the present formulation yields significantly different results than those obtained from a direct extrapolation of the linear formula of the surface impedance derived in the frequency domain.

References

[1] D. Pozar, *Microwave Engineering*. New York: Wiley, 1998, pp. 183–187.

[2] P. P. Nguyen, D. E. Oates, G. Dresselhaus, and M. S. Dresselhaus, "Nonlinear surface impedance for YBa2Cu3O7-x thin films: Measurements and a coupled-grain model," *Physical Review B*, vol. 48, no. 9, pp. 6400–6412, Sept. 1993.

[3] J. C. Booth, B. M. Andersen, and P. J. Hirschfeld, "Disorder effects on the intrinsic nonlinear current density in YBa2Cu3O7– δ," *IEEE Trans. Appl. Supercond.*, vol. 17, no. 2, pp. 906–909, June 2007.

[4] S. Ramo, J. Whinnery, and T. V. Duzer, *Fields and Waves in Communication Electronics*. New York: Wiley, 1994.

[5] D. Xu, S. K. Yip, and J. A. Sauls, "Nonlinear Meissner effect in unconventional superconductors," *Physical Review B*, vol. 51, no. 22, p. 16233–16233, June 1995.

[6] T. Dahm, D. Scalapino, and B. Willemsen, "Phenomenological theory of intermodulation in HTS resonators and filters," *Journal of Superconductivity*, vol. 12, no. 2, p. 339–339, Apr. 1999.

[7] C. Collado, J. Mateu, and J. M. OCallaghan, "Analysis and simulation of the effects of distributed nonlinearities in microwave superconducting devices," *IEEE Trans. Appl. Supercond.*, vol. 15, no. 1, pp. 26–39, Mar. 2005.

Superconducting Multiplexer Filter Bank for a Frequency-Selective Power Limiter

Eduard Rocas, *Student Member, IEEE*, Alberto Padilla, Jordi Mateu, *Senior Member, IEEE*, Nathan Orloff, Juan M. O'Callaghan, *Senior Member, IEEE*, Carlos Collado, *Senior Member, IEEE*, and James C. Booth

***Abstract*—This work proposes a superconducting multiplexer filter bank configuration to be used as a frequency-selective power limiter. The proposed configuration limits narrowband high-power signals within a single frequency band without degrading the signal performance in the rest of the frequency bands. To accomplish this, we need to calculate the limiting power of superconducting filters implemented by means of half-wavelength transmission line resonators. The limiting power is obtained as a function of the resonator geometry, filter bandwidth, and filter order. Practical issues occurring in superconducting filters operating at high power, such as the reduction of the quality factors and de-tuning, are also analyzed and shown to not adversely affect the overall multiplexer power limiter performance.**

***Index Terms*—Critical current, filter, filter bank, limiter, multiplexer.**

I. Introduction

ONE of the fundamental properties of superconducting materials is their ability to switch from a high-loss normal state to a low-loss superconducting state, when cooled below the critical temperature $\mathrm{T_C}$ [1]. But these materials, while in the superconducting state below $\mathrm{T_C}$, can also switch to the high-loss state when a high power signal is injected, because of their nonlinear surface impedance [1]. This property can be used to develop microwave power limiter devices, in which the current flows with high losses when the current density reaches the material-dependent critical current density J_c and consequently the signals are attenuated at the output of the limiter.

The advantages of superconducting materials, for the design of microwave power limiters, over other technologies are mainly their short transition period from the superconducting to the normal state, their very low-loss behavior in the superconducting state, and their ability to reversibly switch between low-loss and high-loss states. Previous work has shown that superconducting transmission line limiters can be used to protect downstream electronics from high-power transients, with nanosecond or less turn-on periods [2], [3]. These result in broadband limiters that provide attenuation over the entire frequency band of interest whenever a high-power signal is present. A more desirable approach is to restrict the limiter response to a narrow frequency band around the high-power signal, without degrading the device performance in the remainder of the frequency band. To accomplish this, we implemented a multiplexed superconducting limiter filter bank.

The limiting power in superconducting transmission line limiters was set by the operating temperature and by the cross-section of the implemented transmission line [2], [3], usually resulting in very narrow line-widths (10 μm to 20 μm). It is expected the use of resonant structures as limiting devices could provide a better control of the limiting power, because additional factors may be used for control, such as quality factor (Q) and coupling between resonators and input and output ports [4]. This approach could also lower the threshold powers significantly compared to those of transmission line limiters.

In this work, we use the measured response of transmission line limiters as the basis for the design of narrowband signal-limiting filters at microwave frequencies. We calculate the current density distribution of the individual resonators that constitute the filter from the incident power, as a function of the filter topology, bandwidth, quality factor, and dimensions, and subsequently determine the filter response as a function of incident power. We also studied the detuning of the filter produced by a high power signal and its effect on the overall multiplexer response.

II. Multiplexing Architecture

Fig. 1 outlines a multiplexing architecture in which the incident signal is split into several frequency bands, and subsequently re-combined. Each frequency band, set by a microwave filter, takes only a portion of the incident signal. When the signal power at one or several frequency bands exceeds the limiting power value, set by the critical current density J_c, the superconducting transmission line resonators switch from the low-loss superconducting state to the high-loss normal state. Therefore, the signal in the high power channel is attenuated and thus the downstream circuitry is protected from the effects of large transient input signals. Because the transition from the superconducting state to the normal state is reversible and occurs on nanosecond timescales, the architecture of Fig. 1 can also be

Manuscript received August 03, 2010; accepted November 08, 2010. This work was supported in part by the Spanish Ministry of Science and Innovation under Grant TEC-2009-13897-C03-01/TCM, by the AGAUR, Generalitat de Catalunya (2008-BE2-00196) and MAT-2008-06761-C03-02; and by Spanish Ministry of Education through PhD fellowships for E. Rocas (BES-2007-16775) and A. Padilla (AP200802235).

E. Rocas, A. Padilla, J. M. O'Callaghan, and C. Collado are with Universitat Politècnica de Catalunya (UPC), Barcelona 08034, Spain.

J. Mateu is with Universitat Politècnica de Catalunya (UPC), Barcelona 08034, Spain. He is also with the Centre Tecnològic de Telecomunicacions de Catalunya (CTTC).

N. Orloff and J. C. Booth are with the National Institute of Standards and Technology, Boulder, CO 80305 USA (e-mail: booth@boulder.nist.gov).

Color versions of one or more of the figures in this paper are available online at http://ieeexplore.ieee.org.

Digital Object Identifier 10.1109/TASC.2010.2093554

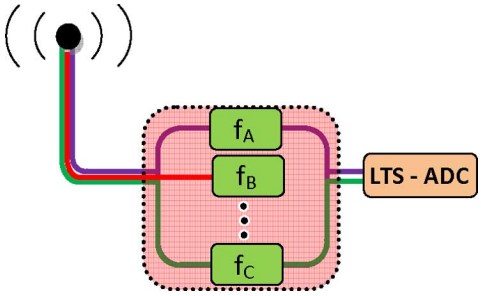

Fig. 1. Outline of the multiplexing architecture, used to protect an analog to digital converter (ADC) from high-power transients.

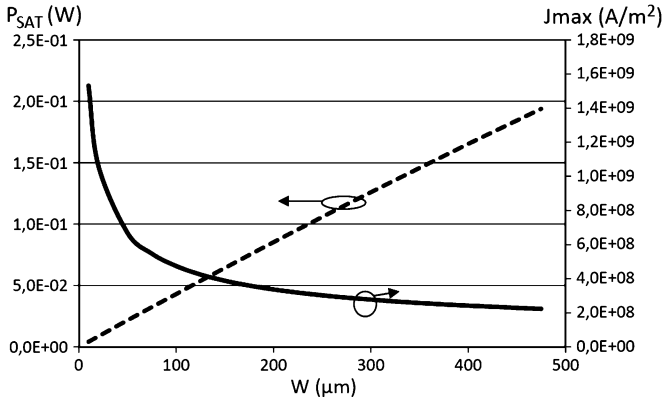

Fig. 2. Dashed line: saturation power as a function of the line width. Solid line: maximum current density as a function of the center conductor width (W), for an input power $\mathrm{P_0} = 5\ \mu\mathrm{W}$.

understood as a high-performance, nanoseconds tunable notch filter.

III. Limiting Power and Geometry in Superconductor Transmission Lines

The superconducting transmission line limiters reported in [2], [3] essentially consist of typical coplanar waveguides (CPW) transmission line, structured to exceed the critical current density for a given input power level. Such devices were fabricated from a 180 nm YBCO thin film deposited on an r-plane sapphire substrate by pulsed-laser deposition, with a thin (20 nm to 50 nm) CeO buffer layer. Sapphire substrates were used for their high thermal conductivity and low microwave loss. The measured surface resistance at 3 GHz and 70 K was approximately in $\mathrm{R_s} \sim 50\ \mu\Omega$. The CPW transmission lines had three different center-conductor line widths (55 μm, 22 μm, and 11 μm) and gap spacings (105 μm, 40 μm, and 20 μm, respectively) between the center conductor and ground planes on either side, to achieve a 50 Ω characteristic impedance. Measurements of the limiting behavior revealed an average critical current density at 70 K of $J_c = 4.4\ \mathrm{MA/cm^2}$.

In this section the material parameters extracted from previous work [2], [3] are used to obtain the saturation power in a different set of CPW transmission lines. Each CPW transmission line has a center conductor that ranges from 10 μm to 450 μm wide, and the gap is set to obtain 50 Ω transmission lines. In a 50 Ω superconducting transmission line, matched both with the source and the load, the total peak current I_0 flowing through a cross-section of the transmission line can be related to the input available power P_0 by

$$P_0 = \frac{I_0^2 Z_0}{2} \tag{1}$$

Note, therefore, that for a given input available power, a whole range of transmission lines of different dimensions would yield the same total currents, as long as the same characteristic impedance is preserved.

The total current is distributed along the cross-section of the transmission line, note that the current density peaks are at the edges of the center conductor and at the inner edges of the ground planes. The current density profile can be calculated by means of numerical techniques such as the Weeks-Sheen method [5], [6]. Fig. 2 displays the maximum current density obtained in the center conductor (in solid line) for an input power of 5 μW, as a function of the center conductor width. As expected, the current density increases for narrower transmission lines. These values are then used, along with (1), to obtain, as a function of center conductor width, the incident power P_0 that gives a current density that exceeds the critical current density of $J_c = 4.4\ \mathrm{MA/cm^2}$. The results in Fig. 2 (dashed line) show an almost linear dependence of saturation power on the conductor width.

This result shows explicitly that the limiting power in a superconducting transmission line can be set by use of the transmission line width. In the following section, we make use of these material properties to obtain the limiting power for frequency-selective resonators.

IV. Superconducting Resonator Limiters

Here we evaluate the saturation power in CPW and microstrip superconducting half-wavelength resonators. Note that, in contrast to the traveling wave transmission line, a resonator need not have a characteristic impedance of 50 Ω. This allows us to use microstrip configurations of several center conductor widths, in addition to CPW configurations. In a half-wavelength transmission line resonator the current distribution along the line follows approximately a sinusoidal profile $I(z) = I_0 \cdot sin(\pi z/l)$, where $l = \lambda/2$ and I_0 is the maximum peak current achieved in the middle of the line. We also know that the I_0 value depends on the Q factor of the resonator. Hence, high-Q resonators reach high-current values, which in turn results in lower saturation powers.

To achieve high Qs in planar technology, designs typically employ relatively wide transmission lines, and concurrently reach high current peaks (I_0). We propose the CPW and microstrip resonator configurations outlined in Figs. 3(a) and 3(b), respectively, which consist of non-uniform transmission lines, where the width of the central region (in grey) is made narrower than the width of the rest of the resonator. Additionally, since the nonlinear behavior in superconductors is a distributed effect [12], this configuration would reduce the nonlinear effects produced in the resonant transmission line.

In non-uniform transmission line resonators the Q factor is

$$Q_0 = \omega_0 \frac{2L_{d1}a_1 + L_{d2}a_2}{2R_{d1}a_1 + R_{d2}a_2}, \tag{2}$$

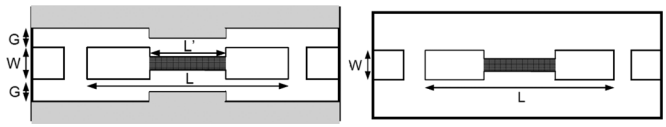

Fig. 3. Outline of the resonators: a) CPW, b) microstrip.

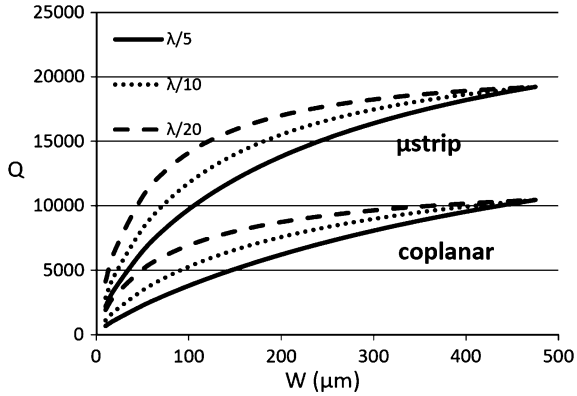

Fig. 4. Q factors as a function of the transmission line width, for microstrip and coplanar resonator configurations and for values of $l_2 - l_1 = \lambda/5, \lambda/10$ and $\lambda/20$.

where L_{d1} and R_{d1} are the inductance and resistance per unit length, corresponding to the wider region, and L_{d2} and R_{d2} are the inductance and resistance per unit length corresponding to the narrower region. The distributed inductance and resistance values can be obtained by means of the Weeks-Sheen method [5], [6], for the widths and thicknesses of each region. The a_1 and a_2 terms are geometrical factors, given as $a_1 = \int_0^{l_1} \sin^2(\pi z/l)dz$ and $a_2 = \int_{l_1}^{l_2} \sin^2(\pi z/l)dz$, respectively, where $2l_1$ is the total length of the wider region of the transmission line resonator of Fig. 3, and $l_2 - l_1$ is the length of the narrower region. Note that when the current distribution differs from a sinusoidal pattern the values of a_1 and a_2 have to be recalculated accordingly. The relation between the driven available power P_0 and the maximum current in the resonator is

$$P_0 = \frac{1}{4} I_0^2 \frac{\omega_0}{Q_L} \frac{(1+2K)}{2K} (2L_{d1}a_1 + L_{d2}a_2), \qquad (3)$$

where Q_L is the loaded Q and K the coupling coefficient between the input (output) port and the resonator.

By use of (2), we extract the Q factor for a set of CPW and microstrip resonators as a function of the line width on the center region of the conductor and for several values of $l_2 - l_1$ ($\lambda/5$, $\lambda/10$ and $\lambda/20$). Note that the wider parts of the transmission lines are set to a fixed value of 450 μm, which results in 50 Ω regions.

The data of Fig. 4 are used, along with (3), to obtain the maximum current I_0 and maximum current density J_{max} for the set of CPW and microstrip resonators. For a critical coupling value $K = 0.5$ and for a fixed drive power $P_0 = 5$ μW, the results for CPW and microstrip resonators are summarized in Figs. 5(a) and 5(b), respectively. The maximum current I_0 increases with the width of the conductor due to the Q dependence, whereas the maximum current density decreases when the center conductor width increases. Additionally, by use of

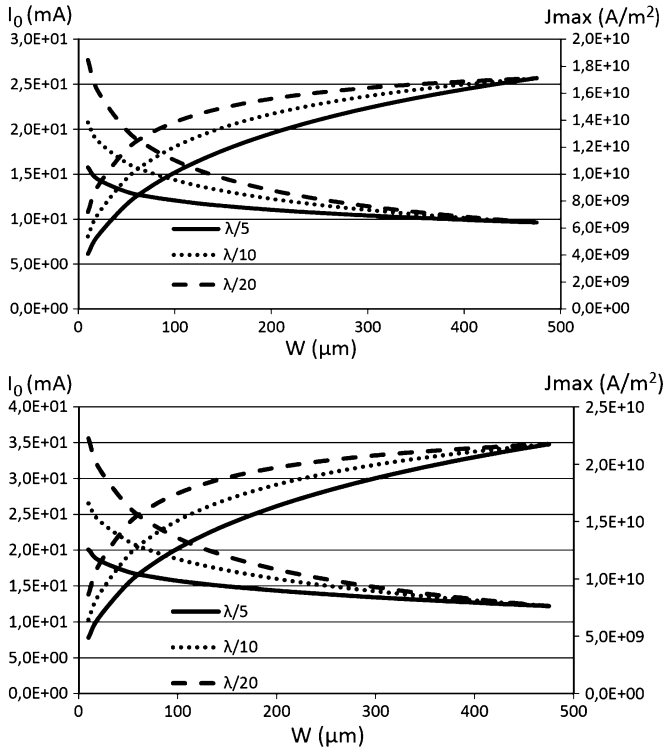

Fig. 5. Maximum current I_0 (left ordinate) and maximum current density J_{max} (right ordinate) as a function of the conductor width and for several values of $l_2 - l_1 = \lambda/5, \lambda/10$ and $\lambda/20$. (a) CPW; (b) microstrip.

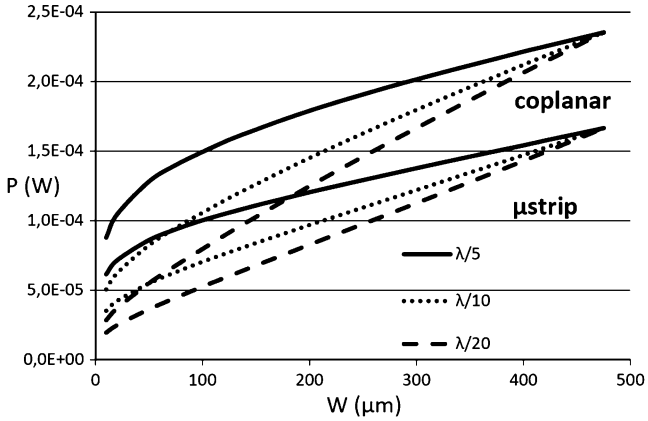

Fig. 6. Saturation power as a function of the conductor width and for $l_2 - l_1 = \lambda/5, \lambda/10$ and $\lambda/20$, for CPW and microstrip.

(3), we also obtain the saturation power for the resonant structures presented above. For the CPW and microstrip resonators, the results are shown in Fig. 6. Note that the saturation power is reduced considerably compared to the case for the transmission line limiters.

V. Power Limiting Superconductor Filter Bank

Next, we need to find the total current flowing through the filter resonators, as was previously done to obtain the saturation power, so that the total current can then be linked to the current density distribution. The resonant structures assumed for this investigation are those presented in the previous section, and their Q factors are summarized in Fig. 4.

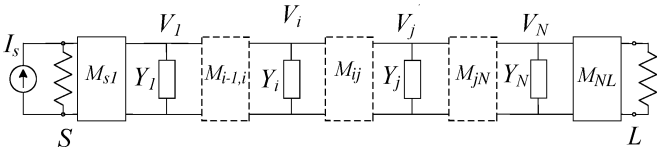

Fig. 7. Outline of the filter circuit model made of in-line coupled resonators.

We start by considering a circuit model of a filter made of N coupled resonators (see Fig. 7), which can be formulated with its general $N \times N$ admittance matrix Y [7]. Note that for clarity Fig. 7 corresponds to an in-line filter configuration. Nevertheless, the formulation below is general for any filter topology. The admittance lumped elements Y_i correspond to the RLC parallel resonator model [8]. The admittance matrix is then used to obtain the voltage V_i at each node of the equivalent-circuit model as a function of the current source I_s, which is related to the driven power $P_0 = I_s^2 Z_0/8$. The resulting dissipated power is

$$P_d = \frac{V_i^2}{2R_i}, \tag{4}$$

where R_i is the lumped resistance that accounts for the resonator losses and can be related to the quality factor as $Q_0 = R_i/\omega L_i$, where L_i is the inductance of the RCL resonator model [8]. The filter configurations assumed in this section use the last resonator in the filter network as the limiting resonator. Note however that the formulation and results could be extended for any other location of the limiting resonator or even when more than a limiting resonator is used. The final position of the limiting resonator would depend on the multiplexing architecture used in the prototype, not yet properly addressed in this work.

The dissipated power at each resonator can also be obtained from the current distribution at each resonator, for half-wavelength resonators, the current distribution at the ith resonator is $I(z) = I_{0\_i} sin(\pi z/l)$. Then, the resulting dissipated power can be obtained as:

$$P_d = I_0^2[2R_{d1}a_1 + R_{d2}a_2], \tag{5}$$

By equating (4) and (5), we can extract the maximum current at each resonator, which is used to obtain the maximum current density and therefore the saturation power. By doing that, we can find the saturation power for several filters, of different order (N) and bandwidth (BW). Fig. 8 shows the saturation power in a fourth order Chebyshev filter with return losses of 20 dB, centered at 3 GHz and for 20 MHz and 200 MHz bandwidths, as a function of the center conductor width.

The results reveal that the required power to saturate the filter decreases when the filter bandwidth decreases and approaches that required in a single resonator for very narrow band filters. This conclusion might be very significant from a practical point of view, since we can set the limiting power by designing filters of different bandwidths. In addition, Fig. 9 shows the saturation power for a Chebyshev filter (with 20 dB return losses) for several orders, N = 3, 4, 6 and 8. In this case, we can be observed that the saturation power is largely independent of the order of the filter.

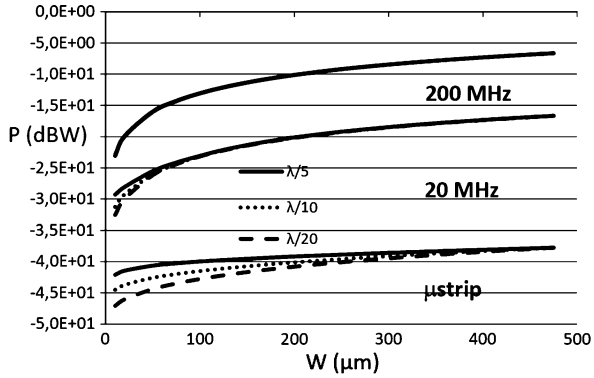

Fig. 8. Saturation power for 4th order Chebyshev filters of 20 MHz and 200 MHz bandwidth. The saturation power for a single microstrip resonator is also depicted for comparison.

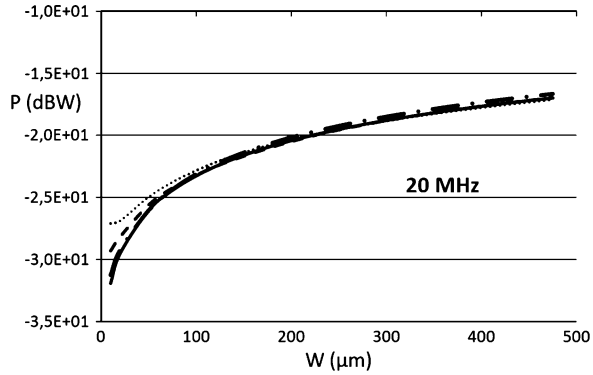

Fig. 9. Saturation power for third-, fourth-, sixth- and eighth-order Chebyshev filters with 20 MHz bandwith. Dotted: eighth, dashed: sixth, dash-dotted: fourth, and solid: third.

VI. Practical Considerations on the Implementation of a Superconducting Power Limiter Multiplexer

The formulation and procedure presented here allow us to extract the limiting power of a superconducting filter by obtaining the total current that flows through the resonators when the maximum current density exceeds the critical current density. However, the inherent nonlinear nature of superconductors [9], which gives rise to the limiting behavior, can also produce effects such as detuning and saturation at high current densities. Therefore, we may expect a variation of the resonant frequency and reduction in Q for the resonators in the filter as the current density increases. The quantification of the detuning and Q reduction can be obtained by means of modeling the nonlinear distributed effects of the superconducting resonators [9]–[13].

Assessment of the detuning effects and Q reduction in a single filter is necessary when the filter is used in a multiplexing architecture, because an out-of band variation of the input reflective coefficient may adversely affect the entire system performance [7]. Fig. 10 shows the above-mentioned effects in a sixth-order Chebyshev filter centered at 3 GHz with a 200 MHz bandwidth, and whose initial Q values are set to 10^4. Figs. 10(a) and 10(b) show the frequency response of the filter when the Q of the last resonator is reduced from 10^4 to 10^3 and 10^2, respectively. The results show that the input reflection coefficient remains fully reflective when out-of-passband,

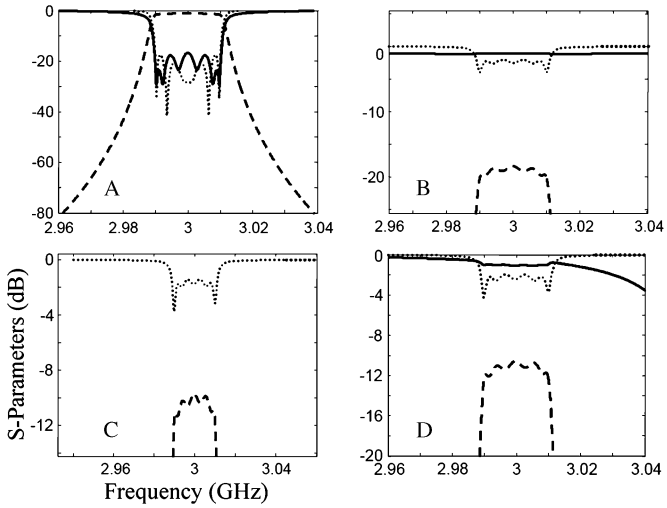

Fig. 10. Filter frequency response. (a) the Q of the last resonator is reduced from 10,000 to 1,000; (b) the Q of the last resonator is reduced from 10,000 to 100; (c) the last resonator is detuned by 2%, maintaining a Q of 10,000; and (d) the last resonator reduces the Q from 10,000 to 100 and detuned 2%. The pink line corresponds to S_{21}, the blue line to S_{11} and the black line to S_{22}.

and the transmission coefficient suffers additional insertion loss. Fig. 10(c) shows the frequency response when the last resonator is detuned by 2%. When the detuning of the last resonator occurs, there is still a fully reflective input coefficient. Finally, in Fig. 10(d) we show the effects of a reduction of Q (from 10^4 to 10^2) and detuning of the last resonator by 2%. From the results of Fig. 10 we may therefore conclude that the nonlinear effects occurring in the superconducting filters do not degrade the overall performance of the multiplexing scheme, and will only produce attenuation of the signal passing through the corresponding filter.

The nonlinear effects also produce spurious signals which may reduce the ADCs dynamic range. Although this is not explicitly addressed in this work, the short narrow limiting section in the middle of the transmission line forecast a low value of intermodulation signals [12].

VII. Conclusion

This work evaluated the use of a superconducting multiplexer filter bank to operate as a frequency-selective power limiter. In order to achieve this functionality, we have formulated the saturation power of the resonators and filters as a function of the superconducting material properties, geometry of the resonators, and the parameters defining the filters, such as the filter bandwidth and filter order. We then used this formulation to calculate the limiting power in several filter configurations. We have used the material parameters extracted from measurements on transmission-line limiters [2]. We conclude that the limiting power in a multiplexing architecture would be much lower than that required in a regular transmission line limiter. The limiting power can be controlled by the dimensions of the resonators that constitute the filters, the operating temperature, and the filter bandwidth. Analysis of the nonlinear effects occurring in a superconducting device shows that the overall performance of the multiplexing structure would not be degraded by the nonlinearities.

References

[1] Z. Y. Shen, *High-Temperature Superconducting Microwave Circuit*. Boston: Artech House, 1994.

[2] J. C. Booth, K. Leong, and S. A. Schima, "A superconducting microwave power limiter for high performance receiver protection," in *IEEE Trans. Microw. Theory and Tech.-Symposium Digest*, 2004, pp. 139–142.

[3] J. C. Booth, D. A. Rudman, and R. H. Ono, "A self-attenuating superconducting transmission line for use as a microwave power limiter," *IEEE Trans. Applied Supercond.*, vol. 13, no. 2, pp. 305–310, June 2003.

[4] C. Collado, J. Mateu, J. C. Booth, and J. M. O'Callaghan, "Detuning and saturation of superconducting devices: Formulation and measurements," in *IEEE Trans. Microw. Theory and Tech.-Symposium Digest*, 2007, pp. 2023–2026.

[5] W. T. Weeks, L. L. Wu, M. F. McAllister, and A. Singh, "Resistive and inductive skin effect in rectangular conductors," *IBM J. Res. Dev.*, vol. 23, pp. 652–660, 1979.

[6] D. M. Sheen, S. M. Ali, D. E. Oates, R. S. Whiters, and J. A. Kong, "Current distribution, resistance, and inductance for superconducting strip transmission lines," *IEEE Trans. Appl. Supercond.*, vol. 1, pp. 108–115, June 1991.

[7] R. J. Cameron, C. M. Kudsia, and R. R. Mansour, *Microwave Filters for Communication systems. Fundamentals, Design, and Applications*. : John Wiley & Sons, 2007.

[8] D. Pozar, *Microwave Engineering*. : John Wiley & Sons, Inc., 1998.

[9] T. Dahm and D. J. Scalapino, "Theory of intermodulation in superconducting microstrip resonator," *J. Appl. Phys.*, vol. 81, no. 4, pp. 2002–2012, 1997.

[10] J. C. Booth, J. Bell, D. Rudman, L. Valle, and R. Ono, "Geometry dependence of nonlinear at microwave frequencies," *J. Appl. Phys.*, vol. 86, no. 2, pp. 1020–1025, 1999.

[11] J. C. Booth, K. Leong, S. A. Schima, C. Collado, J. Mateu, and J. M. O'Callaghan, "Unified description of nonlinear effects in high temperature superconductors," *Journal of Supercond.*, 2006, 10.1007/s10948-006-0126-2, published online.

[12] C. Collado, J. Mateu, and J. M. O'Callaghan, "Analysis and simulation of the effects of distributed nonlinearities in microwave superconducting devices," *IEEE Trans. Appl. Supeconduc.*, vol. 15, no. 1, Mar. 2005.

[13] J. Mateu, J. C. Booth, C. Collado, D. Seron, and J. M. O'Callaghan, "Intermodulation distortion in coupled-resonators filters with nonuniform distributed properties: Use in HTS IMD compensation," *IEEE Trans. Microw. Theory and Tech.*, vol. 54, pp. 1154–1160, Mar. 2006.

Third-Order Intermodulation Distortion and Harmonic Generation in Mismatched Weakly Nonlinear Transmission Lines

Jordi Mateu, *Member, IEEE*, Carlos Collado, *Member, IEEE*, Nathan Orloff, James C. Booth, Eduard Rocas, *Student Member, IEEE*, Alberto Padilla, and Juan M. O'Callaghan, *Senior Member, IEEE*

***Abstract*—This paper describes a procedure to obtain analytical expressions for the spurious signals generated in nonlinear transmission lines with impedance mismatch when they are subject to small-signals. Using these expressions one can rapidly extract the nonlinear parameters describing the nonlinear effects due to the conductor, $L(i)$ and $R(i)$, such as in superconductors, and/or the nonlinear parameters due to the dielectric, $C(v)$ and $G(v)$, such as in ferroelectrics. The resulting closed-form expressions have been validated by equivalent circuit simulations. Spurious signal measurements on several coplanar waveguide superconducting and ferroelectric transmission lines have been explained by the use of the resulting closed-form expressions.**

***Index Terms*—Ferroelectrics, harmonic balance, intermodulation products, nonlinear measurements, nonlinearities, superconductors.**

I. Introduction

BROADBAND response of materials to electromagnetic stimuli provides important information about their electronic and fundamental properties. This information may help to accelerate the development and incorporation of new electronic materials such as high-temperature superconductors (HTSs), ferroelectrics, and magneto-electric and/or multiferroics in general, into devices used for electronic applications [1]–[3]. For such characterization, we have used broadband coplanar waveguide (CPW) structures [2]. We have extracted the electrical parameters for the broadband frequency response of our CPW structures using accurate calibration techniques [4]–[6]; these electrical parameters may then be related to the properties of the constituent materials. Recently, these techniques have been used to characterize fluids embedded in microchannel structures integrated with CPW test structures [7], [8]. While this broadband linear characterization is a necessary step toward the complete understanding of the electromagnetic response of these different materials, it does not always yield sufficient information to distinguish between different theoretical models, and therefore, may not provide a complete understanding of the material properties.

Additional information can be obtained for such materials from the third-order nonlinear response to electromagnetic stimuli [9]–[12] such as intermodulation distortion products or third-order harmonics. These types of spurious signals are often detectable at low signal levels, when there are no measurable effects on the fundamental response of the system (i.e., that occurring at the frequencies of the driving stimuli). For example, third-order intermodulation products are often measureable when no compression effects are seen in a two-port device, or when no de-tuning is observed in a resonator [13].

To obtain the nonlinear response of different materials we have developed a broadband two-tone high-dynamic-range measurement system to capture the spurious signals resulting from the nonlinear transmission lines [11], when they are fed with weak fundamental tones. Accurate circuit models that relate the measured spurious signals to the nonlinear circuit parameters are then essential to characterize the nonlinear properties of the materials using parameters that are independent of the specific test devices used in the measurements. Both commercial and custom simulation software have been used to adjust the relevant parameters in these equivalent circuit models so that their response fits the measured results [11]. In this study, we analyze these circuit models to obtain an analytical closed-form expression of the spurious signals generated in a mismatched nonlinear transmission line (MNLTL) as a function of the nonlinear distributed circuit parameters, which, in turn, may be linked to the nonlinear material properties [9], [11]. Note that these expressions are only valid in a small-signal regime, i.e., when no effects on the fundamental response are observed.

The circuit model for an MNLTL is described in Section II, and the analytical procedure to obtain closed-form expressions is presented in Section III and supported by the formulation of the Appendix. Due to the effect of mismatch, these expressions need to account for the presence of standing waves of the spurious signals on the transmission lines. The complexity of the

Manuscript received June 17, 2008; revised October 14, 2008. First published December 16, 2008; current version published January 08, 2009. This work was supported by the Spanish Ministry of Science and Technology and the Spanish Government (CICYT) under Grant MAT-2005-05656-C03/C04 and Grant TEC-2006-13248-C04-02/TCM and Contract RYC-2005-001125 and Contract BES-2007-16775. This work was supported in part by the U.S. Government.

J. Mateu, C. Collado, E. Rocas, A. Padilla, and J. M. O'Callaghan are with the Department of Signal Theory and Communications, Universitat Politècnica de Catalunya (UPC) and Centre Technologic de Telecomunicacions de Catalunya (CTTC), Barcelona 08034, Spain (e-mail: jmateu@tsc.upc.edu; collado@tsc.upc.edu; eduard.rocas@tsc.upc.edu; alberto.padilla@tsc.upc.edu; joano@tsc.upc.edu).

N. Orloff and J. C. Booth are with the National Institute of Standards and Technology, Boulder, CO 80305 USA (e-mail: orloff@nist.gov; booth@boulder.nist.gov).

Color versions of one or more of the figures in this paper are available online at http://ieeexplore.ieee.org.

Digital Object Identifier 10.1109/TMTT.2008.2009083

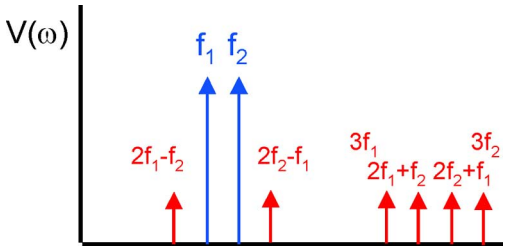

Fig. 1. Third-order nonlinear signals (at frequencies $2f_1 - f_2$, $2f_2 - f_1$, $3f_1$, $2f_1 + f_2$, $2f_2 + f_1$, and $3f_2$) generated by a two-tone incident signal with fundamentals f_1 and f_2.

analysis requires verification of the resulting closed-form expression with simulated results. Section IV compares the spurious signals generated in an MNLTL using both the circuit simulation and the closed-form expressions. Finally, in Section V, we used the obtained closed-form expression to fit the spurious signals measured in an MNLTL [11].

II. Nonlinear Response and Circuit Model for MNLTL

When a broadband nonlinear transmission line is fed with two weak tones, at frequencies f_1 and f_2, spurious signals appear at mixing products and harmonics of the two fundamental driving tones. Typically for third-order nonlinear products, we observe spurious signals at the intermodulation products at frequencies close to fundamental tones $2f_1 - f_2$ and $2f_2 - f_1$, the intermodulation products at high frequencies $2f_1 + f_2$ and $2f_2 + f_1$, as well as the third harmonics at frequencies $3f_1$ and $3f_2$ (see Fig. 1). Understanding the relationships between the different spurious signals generated by the nonlinear effects in the material (conductor or dielectric) is very important in order to find an accurate circuit model to describe their small-signal nonlinear response. Note that due to the distributed nature of the nonlinear effects, additional spurious signals would appear at other mixing frequencies. However, since we operate a small-signal regime, they may be usually neglected.

In the case of a unified description of the different spurious signals resulting from a perfectly matched nonlinear transmission line, one would expect a simple relationship between the spurious signals. In this case, due to the distributed nature of the nonlinear effects, the spurious signals show a characteristic linear dependence on the transmission line length. Closed-form expressions for this case were reported in [9] and [14].

However, when we characterize dielectric materials with high permittivity or *a priori* unknown permittivity, our CPW test structures usually result in mismatched transmission lines. In this case, the relationship between the spurious signals generated is not as straightforward and effects that one expects, such as length dependence due to the distributed origin of the nonlinear properties, might not be directly identified from the measured results.

A. Circuit Simulation

As we have done in our previous studies [9], [11], [14], we used a circuit simulator to extract the circuit parameters characterizing the nonlinear transmission line response. To accomplish this, we modeled the nonlinear transmission line by cascading many nonlinear $RLCG$ elemental cells together, such as the one shown in Fig. 2. The circuit parameters R_0 and L_0 correspond to the resistance and inductance per unit length, respectively, and in a quasi-TEM transmission line may be related to the material properties of the conductor. G_0 and C_0 are the conductance and capacitance per unit length, respectively, and may also be linked to the dielectric properties. The nonlinear properties of the material (conductor or dielectric) may also be accounted for in the equivalent circuit of Fig. 2. To do that, we may use the characteristic $v - i$ curve and the characteristic $\phi - i$ curve (the flux being ϕ) to define the distributed resistance and inductance as a Taylor series expansion

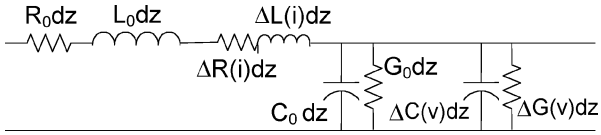

Fig. 2. Equivalent-circuit model of an elemental segment of length dz of a nonlinear transmission line.

$$v = R(i)i = R_0 i + \Delta R_1 i^2 + \Delta R_2 i^3 + \cdots \quad (1)$$
$$\phi = L(i)i = L_0 i + \Delta L_1 i^2 + \Delta L_2 i^3 + \cdots. \quad (2)$$

Similarly we use the characteristic $i - v$ curve and the characteristic $q - v$ curve (q being the charge) to define the distributed conductance and capacitance as a Taylor series expansion as

$$i = G(v)v = G_0 v + \Delta G_1 v^2 + \Delta G_2 v^3 + \cdots \quad (3)$$
$$q = C(v)v = C_0 v + \Delta C_1 v^2 + \Delta C_2 v^3 + \cdots. \quad (4)$$

The general nonlinear telegrapher's equations may be written as

$$\frac{\partial i}{\partial z} = -\frac{\partial q}{\partial t} - G(v)v$$
$$\frac{\partial v}{\partial z} = -\frac{\partial \phi}{\partial t} - R(i)i. \quad (5)$$

Therefore, the nonlinear effects of the conductors are defined by a nonlinear inductance and a nonlinear resistance ($\Delta L(i) = \Delta L_1 \cdot i + \Delta L_2 \cdot i^2 + \cdots$ and $\Delta R(i) = \Delta R_1 \cdot i + \Delta R_2 \cdot i^2 + \cdots$) that depend on the total current i flowing through the line, whereas the nonlinear effects due to the dielectric parts of the circuit are defined by a nonlinear capacitance and a nonlinear conductance ($\Delta C(v) = \Delta C_1 \cdot v + \Delta C_2 \cdot v^2 + \cdots$ and $\Delta G(v) = \Delta G_1 \cdot v + \Delta G_2 \cdot v^2 + \cdots$) that depend on the voltage v on the line. Note that this analogous approach is also used in [15] to obtain the second harmonic generated in a nonlinear transmission line. In [16], a similar small-signal approximation is used to assess the nonlinear effects in left-handed transmission lines.

While the analysis using circuit simulations gives very accurate results, this approach requires significant amounts of computing time. In [9], we state that one requires cascading approximately 200 elemental cells per wavelength to get accurate results. This rapidly ramps up to few thousand cells for long lines, which, in turn, results in the same amount of nonlinear ports to be solved with harmonic balance algorithms. Moreover, this approach gives no insight into how the relevant parameters interact

with each other to generate the measurable quantities. Therefore, iterative steps are required to extract the nonlinear terms from measurements of the spurious signals [11].

III. Formulation

This section uses the equivalent circuit of an elemental segment of a nonlinear transmission line (Fig. 2) to obtain closed-form expressions for the third-order intermodulation products—spurious signals appearing at frequencies $2f_1 - f_2$, $2f_2 - f_1$, $2f_1 + f_2$, and $2f_2 + f_1$—and third harmonics—spurious signals appearing at $3f_1$ and $3f_2$—occurring in an MNLTL. This procedure starts by applying the nonlinear telegraphers' equations, resulting from the set of equations (1)–(5)

$$\frac{\partial i}{\partial z} = -C_0\frac{\partial v}{\partial t} - G_0 v - \frac{\partial i_{nl}}{\partial z} \tag{6}$$

$$\frac{\partial v}{\partial z} = -L_0\frac{\partial i}{\partial t} - R_0 i - \frac{\partial v_{nl}}{\partial z} \tag{7}$$

where the terms $\partial v_{nl}/\partial z$ and $\partial i_{nl}/\partial z$ account for the nonlinear contributions due to the conductive and the dielectric parts, respectively. According to the equivalent circuit of Fig. 2, these terms can be written as

$$\frac{\partial v_{nl}}{\partial z} = \frac{\partial\left(\Delta L(i)i\right)}{\partial t} + \Delta R(i)i \tag{8}$$

$$\frac{\partial i_{nl}}{\partial z} = \frac{\partial\left(\Delta \mathrm{C}(v)v\right)}{\partial t} + \Delta G(v)v. \tag{9}$$

The propagation equation, for a given frequency component ω_i, resulting from the combination of (6) and (7), is

$$\frac{\partial^2 I_i(z)}{\partial z^2} = \gamma_i^2 I_i(z) + \frac{\gamma_i}{Z_{TLi}}\frac{\partial V_{nl,i}}{\partial z} - \frac{\partial^2 I_{nl,i}}{dz^2} \tag{10}$$

where γ_i and $Z_{TL,i}$ are, respectively, the propagation constant and characteristic impedance of the line at ω_i.

The voltage $(\partial v_{nl}/\partial z)$ and current $(\partial i_{nl}/\partial z)$ terms act as nonlinear generators at ω_i, and they may be obtained by using the Fourier transform as

$$\frac{dV_{nl,i}}{dz} = \mathcal{F}\left[\Delta R(i)i, \omega_i\right] + j\omega_i \mathcal{F}\left[\Delta L(i)i, \omega_i\right] \tag{11}$$

$$\frac{dI_{nl,i}}{dz} = \mathcal{F}\left[\Delta G(v)v, \omega_i\right] + j\omega_i \mathcal{F}\left[\Delta C(v)v, \omega_i\right] \tag{12}$$

where i and v are, respectively, the current and voltage at fundamental frequencies f_1 and f_2.

Now using the current and voltage distribution along the line of (32) and (33), derived in the Appendix, and assuming a quadratic nonlinear dependence as

$$\Delta R(i) = \Delta R_2 i^2 \text{ and } \Delta L(i) = \Delta L_2 i^2 \tag{13}$$

$$\Delta G(v) = \Delta G_2 v^2 \text{ and } \Delta C(i) = \Delta C_2 v^2 \tag{14}$$

where ΔR_2, ΔL_2, ΔG_2, and ΔC_2 set the strength of the nonlinear effects, we analytically obtain the nonlinear voltage (11) and current (12) generators at the frequency components where the spurious signals occur. Note also that the assumption of quadratic nonlinear effects is consistent with many experiments reported in the literature [9]–[14].

Assuming that the propagation equation (10) accepts a solution of the form

$$I_{\omega_i}(z) = A_i(z)e^{-\gamma_i z} + B_i(z)e^{\gamma_i z} \tag{15}$$

where $A_i(z)$ and $B_i(z)$ are, respectively, the forward and backward waveform along the transmission line at ω_i, we obtain the following equation:

$$\left(\frac{d^2A_i(z)}{dz^2} - 2\gamma_i\frac{dA_i(z)}{dz}\right)e^{-\gamma_i z} + \left(\frac{d^2B_i(z)}{dz^2} - 2\gamma_i\frac{dB_i(z)}{dz}\right)e^{-\gamma_i z} = \frac{\gamma_i}{Z_{TLi}}\frac{dV_{nL,i}}{\partial z} - \frac{d^2I_{nl,i}}{dz^2} \tag{16}$$

where $dV_{nl,i}/dz$ and $dI_{nl,i}/dz$ are the nonlinear sources at ω_i, detailed in the Appendix. The resulting $A_i(z)$ and $B_i(z)$ should moreover satisfy the boundary conditions at both ends of the transmission line $z = 0$ and $z = l$,

$$\frac{A_i(0)}{B_i(0)} = -\Gamma_{s_i} \tag{17}$$

$$\frac{B_i(l)}{A_i(l)} = -\Gamma_{l_i}e^{-2\gamma_i l} \tag{18}$$

where Γ_{s_i} and Γ_{l_i} are the reflection coefficients at the source $(z = 0)$ and at the load $(z = l)$ at ω_i.

To solve (16), we split the term on the right of (16) into its forward and backward components as

$$\frac{\gamma_i}{Z_{TLi}}\frac{dV_{nl,i}}{\partial z} - \frac{d^2I_{nl,i}}{dz^2} = C_{Fi}e^{-\gamma_i z} + C_{Bi}e^{\gamma_i z} \tag{19}$$

where C_{Fi} and C_{Bi} represent the forward and backward components. Using (19), we can rewrite (16) as

$$\frac{d^2A_i(z)}{dz^2} - 2\gamma_i\frac{dA_i(z)}{dz} - C_{Fi} = 0 \tag{20}$$

$$\frac{d^2B_i(z)}{dz^2} - 2\gamma_i\frac{dB_i(z)}{dz} - C_{Bi} = 0. \tag{21}$$

Now we only need to solve the two ordinary differential equations (20) and (21), use the boundary conditions (17) and (18), and apply (15) to obtain the current distribution along the transmission line $I_i(z)$ at ω_i.

A. Intermodulation Product at $2\omega_1 - \omega_2$

This section uses the analytical procedure described above to obtain the current distribution along the line for the intermodulation product at $2\omega_1 - \omega_2$, $I_{2\omega 1-\omega 2}(z)$. The forward $C_{F2\omega_1-\omega_2}$ and backward $C_{B2\omega_1-\omega_2}$ components are, respectively, detailed in (36) and (37).

The resulting $A_{2\omega_1-\omega_2}(z)$ and $B_{2\omega_1-\omega_2}(z)$ are

$$A_{2\omega_1-\omega_2}(z) = \frac{-K_A}{2\gamma_{12}} + \frac{F_L e^{(\gamma_{12}+\gamma_2^*)z}}{\gamma_2^{2*} - \gamma_{12}^2} + \frac{D_L e^{(\gamma_{12}+\gamma_2^*-2\gamma_1)z}}{\left(\gamma_2^* - 2\gamma_1\right)^2 - \gamma_{12}^2} + \frac{E_L e^{(\gamma_{12}-\gamma_2^*-2\gamma_1)z}}{\left(-\gamma_2^* - 2\gamma_1\right)^2 - \gamma_{12}^2} \tag{22}$$

$$B_{2\omega_1-\omega_2}(z) = \frac{-K_B}{2\gamma_{12}} + \frac{A_L e^{-(\gamma_{12}+\gamma_2^*)z}}{\gamma_2^{*2}-\gamma_{12}^2} + \frac{B_L e^{-(\gamma_{12}+\gamma_2^*-2\gamma_1)z}}{(-\gamma_2^*+2\gamma_1)^2-\gamma_{12}^2} + \frac{C_L e^{-(\gamma_{12}-\gamma_2^*-2\gamma_1)z}}{(\gamma_2^*+2\gamma_1)^2-\gamma_{12}^2} \quad (23)$$

where the constants K_A and K_B are found applying the boundary conditions (17) and (18). The constants A_L, B_L, C_L, D_L, E_L, and F_L are related to the nonlinear terms $\Delta_c = \Delta R_2 + j\omega_{12}\Delta L_2$ and $\Delta_d = \Delta G_2 + j\omega_{12}\Delta C_2$ and are detailed in (38). Note that, throughout this paper, subscripts $12, 1$, and 2 indicate the frequency components at $2\omega_1 - \omega_2$, ω_1, and ω_2, respectively.

The development for the intermodulation product at $2\omega_2 - \omega_1$ would read as (22) and (23) by only replacing the components at ω_1 by the ones at ω_2, and vice versa, and using the components at $2\omega_2 - \omega_1$ instead of at $2\omega_1 - \omega_2$ (this is using the subscript 21 instead of 12).

B. Intermodulation Product at $2\omega_1 + \omega_2$

For the intermodulation product at $2\omega_1 + \omega_2$, we use the forward $C_{F2\omega_1+\omega_2}$ and backward $C_{B2\omega_1+\omega_2}$ components (39) and (40), respectively. The resulting $A_{2\omega_1+\omega_2}(z)$ and $B_{2\omega_1+\omega_2}(z)$ are

$$A_{2\omega_1+\omega_2}(z) = \frac{-K_A}{2\gamma_{12+}} + \frac{D_H e^{(\gamma_{12+}-\gamma_2)z}}{\gamma_2^2-\gamma_{12+}^2} + \frac{E_H e^{(\gamma_{12+}+\gamma_2-2\gamma_1)z}}{(\gamma_2-2\gamma_1)^2-\gamma_{12+}^2} + \frac{F_H e^{(\gamma_{12+}-\gamma_2-2\gamma_1)z}}{(-\gamma_2-2\gamma_1)^2-\gamma_{12+}^2} \quad (24)$$

$$B_{2\omega_1+\omega_2}(z) = \frac{-K_B}{2\gamma_{12+}} + \frac{A_H e^{-(\gamma_{12+}-\gamma_2)z}}{\gamma_2^2-\gamma_{12}^2} + \frac{B_H e^{-(\gamma_{12+}-\gamma_2-2\gamma_1)z}}{(\gamma_2-2\gamma_1)^2-\gamma_{12+}^2} + \frac{C_H e^{-(\gamma_{12+}+\gamma_2-2\gamma_1)z}}{(-\gamma_2+2\gamma_1)^2-\gamma_{12+}^2}. \quad (25)$$

Now the subscript $12+$ refers to the frequency components at $2\omega_1 + \omega_2$. The constants A_H, B_H, C_H, D_H, E_H, and F_H are detailed in (43).

Again the result would be easily expanded for the spurious signals occurring at $2\omega_2 + \omega_1$.

C. Harmonic Generation at $3\omega_1$

The forward and backward components of the current distribution along the line at $3\omega_1$ are found using the forward $C_{F3\omega_1}$ and backward $C_{B3\omega_1}$ components of (46) and (47), respectively. The resulting $A_{3\omega_1}(z)$ and $B_{3\omega_1}(z)$ are

$$A_{3\omega_1}(z) = \frac{-K_A}{2\gamma_3} + \frac{B_3 e^{(\gamma_3-\gamma_1)z}}{\gamma_1^2-\gamma_3^2} + \frac{A_3 e^{(\gamma_3-3\gamma_1)z}}{(3\gamma_1)^2-\gamma_3^2} \quad (26)$$

$$B_{3\omega_1}(z) = \frac{-K_B}{2\gamma_3} + \frac{C_3 e^{(\gamma_1-\gamma_3)z}}{\gamma_1^2-\gamma_3^2} + \frac{D_3 e^{(3\gamma_1-\gamma_3)z}}{(3\gamma_1)^2-\gamma_3^2} \quad (27)$$

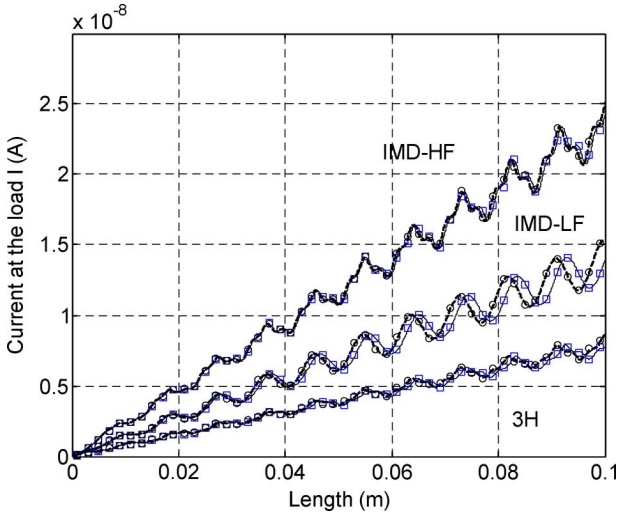

Fig. 3. Current at the end of the line for the spurious frequency components.

where the subscript 3 refers to the frequency components at $3\omega_1$. The constants A_3, B_3, C_3, and D_3 are detailed in (48). Note that these expressions would also be suitable for the third harmonic of ω_2.

In the case of perfectly matched transmission lines, $\Gamma_i = 0$, the above closed-form expression would read as reported in [14].

IV. Verification: Circuit Simulations

This section checks the expressions developed above in (22)–(28) by comparing their results with the ones obtained from a circuit simulation of an MNLTL. The circuit simulation has been performed as outlined in Section II-A, and reported elsewhere [9], [11].

The linear distributed circuit parameters defining the simulated transmission line are $L_0 = 662.8$ nH/m, $C_0 = 490.2$ pF/m, $R_0 = 4\text{e}-3\ \Omega$/m, and $G_0 = 7.4\text{e}-6$ S/m (almost lossless dielectric). This results in a transmission line of 36.7-Ω characteristic impedance, which is then connected to a 50-Ω source and terminated with a 50-Ω load. For this simulation, we consider quadratic nonlinear effects coming from the conductor [see (13)], where $\Delta R_2 = 33.85\ \Omega/hboxmA^2$ and $\Delta L_2 = 1.07\text{e}-9$ H/mA^2. We then feed this line with two tones at $f_1 = 3$ GHz and $f_2 = 3.05$ GHz and evaluate the resulting spurious signals at $2\omega_1 - \omega_2$, $2\omega_2 - \omega_1$, $2\omega_1 + \omega_2$, $2\omega_2 + \omega_1$, $3\omega_1$, and $3\omega_2$ using the corresponding closed-form expressions and the simulated results.

Fig. 3 depicts the current at the end of the line $I(l)$ as a function of its length, l for all spurious signals occurring in the nonlinear transmission line. The labels on the figure IMD-HF, IMD-LF, and 3H refer to the intermodulation distortion at high frequency ($2\omega_1 + \omega_2$ and $2\omega_2 + \omega_1$), the intermodulation distortion at lower frequency ($2\omega_1 - \omega_2$ and $2\omega_2 - \omega_1$) and the third harmonics, respectively. The circles indicate the simulated results at the lower sideband of the spurious signals, i.e., $2\omega_1 - \omega_2$, $2\omega_1 + \omega_2$, and $3\omega_1$, whereas the squares indicate the simulated results at the upper sideband of the spurious signals, i.e., $2\omega_2 - \omega_1$, $2\omega_2 + \omega_1$, and $3\omega_2$. The solid and dashed lines

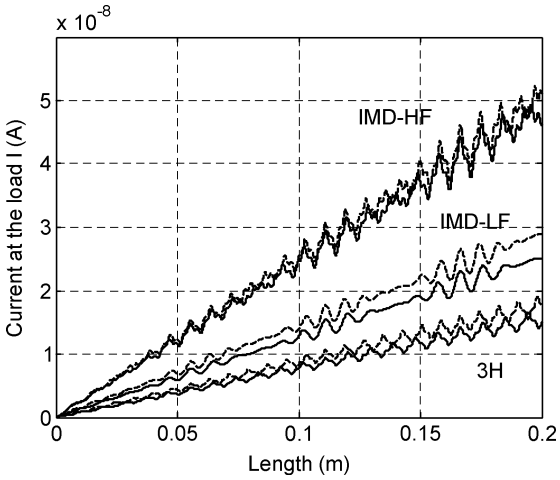

Fig. 4. Current at the end of the line for all spurious frequency components when the fundamental tones f_1 and f_2 are set to 3 and 3.5 GHz, respectively. Solid lines correspond to $2\omega_1 - \omega_2$, $2\omega_2 + \omega_1$, and $3\omega_2$, and dashed lines correspond to $2\omega_2 - \omega_1$, $2\omega_1 + \omega_2$, and $3\omega_1$.

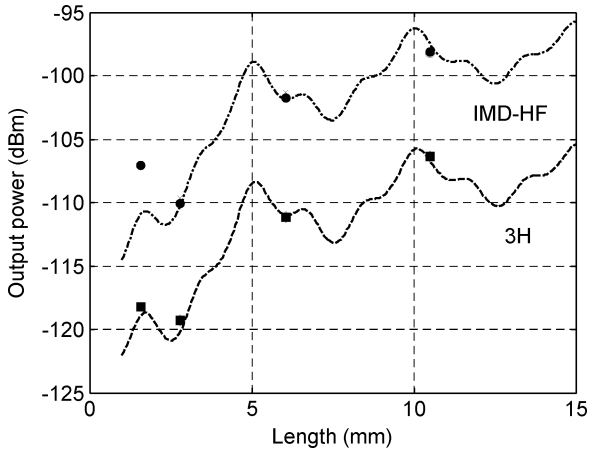

Fig. 5. Measurements and analytical results of the spurious signals occurring in a set of ferroelectric nonlinear transmission lines.

correspond to the values evaluated by the use of the closed-form expressions, all agreeing very well with the simulated results.

The expected linear transmission line length dependence of the spurious signals can be used to confirm the distributed origin of the nonlinear effects and, therefore, rule out contributions from possible external nonlinear sources. Although the results in Fig. 3 show an increment of the spurious signals as a function of the length, they do not follow a linear dependence, as it occurs in a perfectly matched transmission line. The fluctuating length dependence, due to the mismatched effects, may give higher nonlinear effects in shorter lines. This makes it difficult to predict, from the raw data, the distributed origin of the nonlinearities without using simulations or the closed-form expressions developed here. Since the fluctuating behavior comes from the mismatched effects, it depends on the operating frequency and is, therefore, different for each spurious signal. This phenomenon, if not taken into account, may lead to misleading conclusions, such as asymmetries on the IMD (i.e., differences between the signal power at $2\omega_1 - \omega_2$ and $2\omega_2 - \omega_1$) due to memory effects [17].

Although not reported in this section, the closed-form expressions have also been verified when the nonlinear effects come only from the dielectric part and from both conductor and dielectric parts. We have also verified the obtained expressions for a several values of characteristic impedance ranging from 10 to 100 Ω and different frequencies.

As an example, to emphasize the effects of mismatch, this section also evaluates the length dependence of the spurious signals for lines longer than those of Fig. 3 (up to 0.2 m) fed with two input tones whose frequencies (f_1 and f_2) are 3 and 3.5 GHz, respectively, much farther apart than those of Fig. 3. Fig. 4 shows how the asymmetries between the spurious signals are more pronounced. Moreover, unlike in Fig. 3, the IMD-LF traces in Fig. 4 have fluctuations for only limited ranges of length.

From Figs. 3 and 4, we also see that small deviation in the length determination of the line may incur in a few decibel difference of the predicted spurious signal.

V. Verification: Measurements

Simulations using the circuit model of Fig. 2 have been extensively used to analyze the distributed nonlinear effects in superconducting transmission line, confirming the expected length and frequency dependence [18]. Since in superconducting transmission lines the dielectric constants of the substrates are usually well known, one can build transmission lines with characteristic impedances matched to 50 Ω. For this case, we do not expect to observe any fluctuating effect due to the length of the line. The closed-form expressions developed here have also been used to explain such results.

However, this is not the case for substrates with large or nonlinear dielectric constants, such as ferroelectrics [2] or magnetoelectrics [3]. Fabrication of transmission lines incorporating these materials then results in a nonlinear mismatched transmission line.

This section applies the developed closed-form expressions to explain the nonlinear behavior occurring in CPW transmission lines incorporating an $SrTiO_3$ (STO) thin film of 400-nm thickness grown on a $LaAlO_3$ substrate with conductors defined by a 0.3-μm Au layer on top. Here we report the intercept point at 0-dBm input power of the spurious signals occurring in four CPW transmission lines, all with a 50-μm width of center conductor and 20-μm gap between the center conductor and ground planes. The four lines have different length: $L_1 = 1.58$ mm, $L_2 = 2.79$ mm, $L_3 = 6.06$ mm, and $L_4 = 10.52$ mm. Fig. 5 shows the measured intercept point at 0-dBm input power and outlines the length dependence predicted from the closed-form expression developed here. Circles and squares indicate the measured intercept points of the spurious signal at $2\omega_1 + \omega_2$ and $3\omega_1$, respectively. The input tones f_1 and f_2 were set to 6 and 6.1 GHz, respectively. Experiments performed to obtain measurements of the spurious signals are detailed in [11].

We then used the current at the end of the line, obtained from (22)–(28), to extract the power at the output port [19]. The output power generated at spurious frequencies depends on the propagation constant γ and characteristic impedance Z_{TL} of the line—obtained from a multiline thru-reflect line (TRL) calibration [4] as at each frequency point—and the nonlinear terms Δ_c and Δ_d, which are unknown. By equating the resulting output

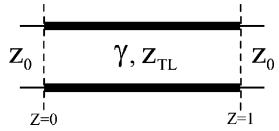

Fig. 6. Outline of a mismatched transmission line.

power expressions with the measured spurious signals, one can extract the nonlinear terms Δ_c and Δ_d. Note that, in this example, where all nonlinear effects are due to the dielectric part, the nonlinear effects from the conductor part are $\Delta_c = 0$. This same procedure has been used in previous studies [9], [11], but the extraction of the nonlinear terms was carried out by iterating circuit simulations to match measured and simulated spurious signals.

Fig. 5 reproduces the fitting of the experimental results reported in [11]. Dashed–dotted and dashed lines show the length dependence obtained from the closed-form expressions. Fig. 5 shows very good agreement between measurements and the length dependence obtained from the closed-form expressions.

VI. Conclusion

This study has developed general closed-form expressions to obtain the spurious signals resulting from a weakly nonlinear mismatched transmission line with quadratic nonlinear effects in both the conductor and dielectric parts of the circuit. The resulting closed-form expressions have been verified with circuit simulations. Assessment of the transmission line length dependence of the spurious signals reveals how the mismatch effect may mask the expected length dependence caused by distributed nonlinear effects. Without an accurate circuit model and extensive simulations, or without the use of the closed-form expressions developed here, nonlinear measurements may give misleading results due to the fluctuating length dependence and the asymmetry between spurious signals. Moreover, since the closed-form expressions show the interaction of the different sources of nonlinear effects, they offer the possibility of evaluating the nonlinear response and identifying the origin of the nonlinear effects in order to discern between different sources.

Appendix

Current and Voltage Distribution at Fundamental Frequencies

In a transmission line for which the characteristic impedance is neither matched to the impedance of the source, nor the load (see Fig. 6), the current and voltage distribution along the line of the fundamental signals is obtained from basic theory of circuit analysis [19].

We start by obtaining the forward current component at the input of the line ($z = 0$), I_{0i}^{+}, at ω_i (i for the fundamental components might by 1 or 2) as

$$I_{0i}^{+} = I_{si}\frac{Z_0}{Z_{in,i}+Z_0}\frac{1}{1-\Gamma_{\rm i}}. \tag{28}$$

I_{si} indicates the current driven by the source and $\Gamma_{\rm i}$ is the reflection coefficient to the source and load both at ω_i. The input impedance $Z_{in,i}$ may be found as

$$Z_{in,i} = Z_{TLi}\frac{Z_0 + Z_{TLi}\tanh(\gamma_i l)}{Z_{TLi} + Z_0\tanh(\gamma_i l)}. \tag{29}$$

The propagation constant γ_i and the characteristic impedance of the transmission line $Z_{TL,i}$, respectively, can be obtained from the linear distributed circuit parameters R_0, L_0, C_0, and G_0 of the line, as

$$\gamma_i = \sqrt{(R_0 + j\omega_i L_0)(G_0 + j\omega_i C_0)} \tag{30}$$

$$Z_{TL,i} = \sqrt{\frac{(R_0 + j\omega_i L_0)}{(G_0 + j\omega_i C_0)}}. \tag{31}$$

From the expressions above, i.e., (28)–(31), the current and voltage distribution along the line at fundamental frequency ω_i, being $i = 1$ or 2, are

$$I_i(z) = I_{01}^{+}[e^{-\gamma_i z} - \Gamma_{\rm i} e^{\gamma_i z}] \tag{32}$$

$$V_i(z) = I_{01}^{+} Z_{TLi}[e^{-\gamma_i z} + \Gamma_{\rm i} e^{\gamma_i z}]. \tag{33}$$

Nonlinear Voltage and Nonlinear Current Generators

Assuming a quadratic nonlinear dependence of the distributed circuit parameters $\Delta R(i)$, $\Delta L(i)$, $\Delta C(v)$, and $\Delta G(v)$, as outlined in (13) and (14), we found the resulting nonlinear sources at the mixing products and harmonics of the fundamental components at ω_1 and ω_2 by applying (13) and (14) into (11) and (12), respectively. Although this Appendix only details the nonlinear voltage and current generators at $2f_1 - f_2$, $2\omega_1 + \omega_2$, and $3\omega_1$, their counterparts at $2\omega_2 - \omega_1$, $2\omega_2 + \omega_1$, and $3\omega_2$, respectively, could be directly derived.

The nonlinear voltage and the nonlinear current generators, respectively, at $2\omega_1 - \omega_2$ are

$$\begin{aligned}\frac{dV_{nl,2\omega_1-\omega_2}}{dz} &= \frac{3}{4} I_{01}^{+2} I_{02}^{+\,*}\Delta_c \\ &\quad\times\Big[-2\Gamma_1 e^{-\gamma_2^* z} + \Gamma_1^2 2e^{(2\gamma_1-\gamma_2^*)z} \\ &\qquad -\Gamma_1^2\Gamma_2^* e^{(2\gamma_1+\gamma_2^*)z} - \Gamma_2^* e^{(-2\gamma_1+\gamma_2^*)z} \\ &\qquad +e^{(-2\gamma_1-\gamma_2^*)z} + 2\Gamma_1\Gamma_2^* e^{\gamma_2^* z}\Big]\end{aligned} \tag{34}$$

$$\begin{aligned}\frac{dI_{nl,2\omega_1-\omega_2}}{dz} &= \frac{3}{4} I_{01}^{+2} I_{02}^{+\,*}\Delta_d Z_{TL,1}^2 Z_{TL,2}^* \\ &\quad\times\Big[2\Gamma_1 e^{-\gamma_2^* z} + \Gamma_1^2 2e^{(2\gamma_1-\gamma_2^*)z} \\ &\qquad +\Gamma_1^2\Gamma_2^* e^{(2\gamma_1+\gamma_2^*)z} + \Gamma_2^* e^{(-2\gamma_1+\gamma_2^*)z} \\ &\qquad +e^{(-2\gamma_1-\gamma_2^*)z} + 2\Gamma_1\Gamma_2^* e^{\gamma_2^* z}\Big]\end{aligned} \tag{35}$$

where $\Delta_c = \Delta R_2 + j(2\omega_1 - \omega_2)\Delta L_2$ and $\Delta_d = \Delta G_2 + j(2\omega_1 - \omega_2)\Delta C_2$. Substituting (34) and (35) into (19), we may isolate the forward and backward components

$$C_{F,2\omega_1-\omega_2} = \left(D_L e^{(-2\gamma_1+\gamma_2^*)z} + E_L e^{(-2\gamma_1+\gamma_2^*)z} + F_L e^{\gamma_2^* z}\right) e^{\gamma_{2\omega_1-\omega_2} z} \quad (36)$$

$$C_{B,2\omega_1-\omega_2} = \left(C_L e^{(2\gamma_1+\gamma_2^*)z} + B_L e^{(2\gamma_1-\gamma_2^*)z} + A_L e^{-\gamma_2^* z}\right) e^{-\gamma_{2\omega_1-\omega_2} z} \quad (37)$$

where

$$\begin{aligned}
A_L &= 2\Gamma_1\left(\frac{-\gamma_{12}}{Z_{TL,12}}k_c + k_d\gamma_2^*\right)\\
B_L &= \Gamma_1^2\left(\frac{\gamma_{12}}{Z_{TL,12}}k_c - k_d\left(2\gamma_1 - \gamma_2^*\right)\right)\\
C_L &= \Gamma_1^2\Gamma_2^*\left(\frac{-\gamma_{12}}{Z_{TL,12}}k_c - k_d\left(2\gamma_1 + \gamma_2^*\right)\right)\\
D_L &= \Gamma_2^*\left(\frac{-\gamma_{12}}{Z_{TL,12}}k_c - k_d\left(-2\gamma_1 + \gamma_2^*\right)\right)\\
E_L &= \left(\frac{\gamma_{12}}{Z_{TL,12}}k_c - k_d\left(-2\gamma_1 - \gamma_2^*\right)\right)\\
F_L &= 2\Gamma_1\Gamma_2^*\left(\frac{\gamma_{12}}{Z_{TL,12}}k_c - k_d\gamma_2^*\right)
\end{aligned} \quad (38)$$

with $k_c = (3/4){I_{01}^+}^2 I_{02}^{+*}\Delta_c$ and $k_d = (3/4){I_{01}^+}^2 I_{02}^{+*} Z_{TL,1}^2 Z_{TL,2}^*\Delta_{\rm d}$.

By the used of analogous expressions to (34)–(38), the intermodulation products at $2\omega_1 + \omega_2$ may be written as

$$\begin{aligned}
\frac{dV_{nl,2\omega_1+\omega_2}}{dz} &= \frac{3}{4}I_{01}^{+2}I_{02}^{+*}\Delta_c \times \left[-2\Gamma_1 e^{-\gamma_2 z} + \Gamma_1^2 2e^{(2\gamma_1-\gamma_2)z} - \Gamma_2\Gamma_1^2 e^{(2\gamma_1+\gamma_2)z} - \Gamma_2 e^{(-2\gamma_1+\gamma_2)z} + e^{(-2\gamma_1-\gamma_2)z} + 2\Gamma_1\Gamma_2 e^{\gamma_2 z}\right] \quad (39)\\
\frac{dI_{nl,2\omega_1+\omega_2}}{dz} &= \frac{3}{4}I_{01}^{+2}I_{02}^{+*}\Delta_d Z_{TL,1}^2 Z_{TL,2} \times \left[2\Gamma_1 e^{-\gamma_2 z} + \Gamma_1^2 2e^{(2\gamma_1-\gamma_2)z} + \Gamma_1^2\Gamma_2 e^{(2\gamma_1+\gamma_2)z} + \Gamma_2 e^{(-2\gamma_1+\gamma_2)z} + e^{(-2\gamma_1-\gamma_2)z} + 2\Gamma_2\Gamma_1 e^{\gamma_2 z}\right] \quad (40)
\end{aligned}$$

where now $\Delta_c = \Delta R_2 + j(2\omega_1 + \omega_2)\Delta L_2$ and $\Delta_d = \Delta G_2 + j(2\omega_1 + \omega_2)\Delta C_2$. The forward and backward components are

$$C_{F,2\omega_1+\omega_2} = \left(E_H e^{(-2\gamma_1+\gamma_2)z} + F_H e^{(-2\gamma_1+\gamma_2)z} + D_H e^{-\gamma_2 z}\right) e^{\gamma_{2\omega_1+\omega_2} z} \quad (41)$$

$$C_{B,2\omega_1+\omega_2} = \left(C_H e^{(2\gamma_1-\gamma_2)z} + B_H e^{(2\gamma_1+\gamma_2)z} + A_H e^{\gamma_2 z}\right) e^{-\gamma_{2\omega_1+\omega_2} z} \quad (42)$$

where

$$\begin{aligned}
A_H &= 2\Gamma_1\Gamma_2\left(\frac{\gamma_{12+}}{Z_{TL,12+}}k_c - k_d\gamma_2\right)\\
B_H &= \Gamma_1^2\Gamma_2\left(\frac{-\gamma_{12+}}{Z_{TL,12+}}k_c - k_d(2\gamma_1 + \gamma_2)\right)\\
C_H &= \Gamma_1^2\left(\frac{\gamma_{12+}}{Z_{TL,12+}}k_c - k_d(2\gamma_1 - \gamma_2)\right)\\
D_H &= 2\Gamma_1\left(\frac{-\gamma_{12+}}{Z_{TL,12+}}k_c + k_d\gamma_2\right)\\
E_H &= \Gamma_2\left(\frac{-\gamma_{12+}}{Z_{TL,12+}}k_c + k_d(-2\gamma_1 + \gamma_2)\right)\\
F_H &= \left(\frac{\gamma_{12+}}{Z_{TL,12+}}k_c + k_d(2\gamma_1 + \gamma_2\right)
\end{aligned} \quad (43)$$

with $k_c = (3/4){I_{01}^+}^2 I_{02}^+\Delta_c$ and $k_d = -(3/4){I_{01}^+}^2/I_{02}^+ Z_{TL,1}^2 Z_{TL,2}\Delta_{\rm d}$.

For the third harmonic at $3\omega_1$, the nonlinear voltage and current generators are

$$\frac{dV_{nl,3\omega_1}}{dz} = \frac{1}{4}I_{01}^{+2}I_{01}^{+*}\Delta_c\left[-3\Gamma_1 e^{-\gamma_1 z} - \Gamma_1^3 e^{3\gamma_1 z} + 3\Gamma_1^2 e^{\gamma_1 z} + e^{-3\gamma_1 z}\right] \quad (44)$$

$$\frac{dV_{nl,3\omega_1}}{dz} = \frac{1}{4}I_{01}^{+2}I_{01}^{+*}\Delta_d Z_{TL,1}^3\left[3\Gamma_1 e^{-\gamma_1 z} + \Gamma_1^3 e^{3\gamma_1 z} + 3\Gamma_1^2 e^{\gamma_1 z} + e^{-3\gamma_1 z}\right] \quad (45)$$

where $\Delta_c = \Delta R_2 + j3\omega_1\Delta L_2$ and $\Delta_d = \Delta G_2 + j3\omega_1\Delta C_2$. The forward and backward components then result as follows:

$$C_{F,3\omega_1} = (A_3 e^{-3\gamma_1 z} + B_3 e^{-\gamma_1 z})e^{\gamma_{3\omega_1} z} \quad (46)$$

$$C_{B,3\omega_1} = (D_3 e^{3\gamma_1 z} + C_3 e^{\gamma_1 z})e^{-\gamma_{3\omega_1} z} \quad (47)$$

where

$$\begin{aligned}
A_3 &= \left(\frac{\gamma_3}{Z_{TL,3}}k_c + 3k_d\gamma_1\right)\\
B_3 &= 3\Gamma_1\left(\frac{\gamma_3}{Z_{TL,3}}k_c + k_d\gamma_1\right)\\
C_3 &= 3\Gamma_1^3\left(\frac{\gamma_3}{Z_{TL,3}}k_c - k_d\gamma_1\right)\\
D_3 &= \Gamma_1^3\left(\frac{\gamma_3}{Z_{TL,3}}k_c - 3k_d\gamma_1^3\right)
\end{aligned} \quad (48)$$

with $k_c = (1/4)I_{01}^{+2}I_{01}^{+*}\Delta_{\rm c}$ and $k_d = (1/4)I_{01}^{+2}I_{01}^{+*}Z_{TL,1}^3\Delta_{\rm d}$.

REFERENCES

[1] D. E. Oates, P. P. Nguyen, G. Dresselhaus, M. S. Dresselhaus, G. Koren, and E. Polturak, "Nonlinear surface impedance of YBCO thin films: Measurements, modelling and effects in devices," *J. Superconduct. Novel Magn.*, vol. 8, no. 6, pp. 725–733, 1995.

[2] M. J. Lancaster, J. Powell, and A. Porch, "Thin-film ferroelectric microwave devices," *Superconduct. Sci. Technol.*, vol. 11, pp. 1323–1334, 1998.

[3] N. Orloff, J. Mateu, M. Murakami, I. Takeuchi, and J. C. Booth, "Broadband characterization of multilayer dielectric thin-films," in *IEEE MTT-S Int. Microw. Symp. Dig.*, 2007, pp. 1177–1180.

[4] R. B. Marks, "A multiline method for network analyzer calibration," *IEEE Trans. Microw. Theory Tech.*, vol. 39, no. 7, pp. 1205–1215, Jul. 1991.
[5] D. F. Williams and R. B. Marks, "Transmission line capacitance measurements," *IEEE Microw. Guided Wave Lett.*, vol. 1, no. 9, pp. 243–245, Sep. 1991.
[6] D. F. Williams and R. B. Marks, "Characteristic impedance determination using propagation constant measurements," *IEEE Microw. Guided Wave Lett.*, vol. 1, no. 6, pp. 141–143, Jun. 1991.
[7] J. C. Booth, J. Mateu, M. Janezic, J. Baker-Jarvis, and J. A. Beall, "Broadband permittivity measurement of liquid and biological samples using microfluidic channels," in *IEEE MTT-S Int. Microw. Symp. Dig.*, 2006 , pp. 1750–1753.
[8] J. Mateu, N. Orloff, M. Renihart, and J. C. Booth, "Broadband permittivity of liquids extracted from transmission line measurements of microfluidic channels," in *IEEE MTT-S Int. Microw. Symp. Dig.*, 2007, pp. 523–526.
[9] C. Collado, J. Mateu, and J. M. O'Callaghan, "Analysis and simulation of the effects of distributed nonlinearities in microwave superconducting devices," *IEEE Trans. Appl. Superconduct.*, vol. 15, no. 1, pp. 26–39, Mar. 2005.
[10] J. R. Ott, P. Lahl, and R. Wördenweber, "Nonlinear microwave properties of ferroelectric thin films," *Appl. Phys. Lett.*, vol. 84, no. 21, pp. 4147–4149, 2004.
[11] J. Mateu, J. C. Booth, and S. A. Schima, "Frequency tuning and spurious signal generation at microwave frequencies in ferroelectric SrTiO thin-film transmission lines," *IEEE Trans. Microw. Theory Tech.*, vol. 55, no. 2, pp. 391–396, Feb. 2007.
[12] R. Hammond, E. Soares, B. Willemsen, T. Dahm, D. Scalapino, and J. Schrieffer, "Intrinsic limits on the Q and intermodulation of low power high temperature superconducting microstrip resonators," *J. Appl. Phys.*, vol. 84, no. 10, pp. 5662–5667, 1998.
[13] D. E. Oates, "Microwave superconductivity," in *Nonlinear Behaviour of Superconducting Devices*, ser. NATO Sci. E: Appl. Sci.. Brussels, Belgium: NATO, vol. 375, ch. 5.
[14] D. Seron, C. Collado, J. Mateu, and J. M. O'Callaghan, "Analysis and simlation of distributed nonlinearities in ferroelectrics and superconductors for microwave applications," *IEEE Trans. Microw. Theory Tech.*, vol. 54, no. 3, pp. 1154–1160, Mar. 2006.
[15] K. S. Champlin and D. R. Singh, "Small-signal second-harmonic generation by a nonlinear transmission line," *IEEE Trans. Microw. Theory Tech.*, vol. MTT-34, no. 3, pp. 351–353, Mar. 1986.
[16] A. B. Kozyrev and D. W. van der Weide, "Nonlinear wave propagation phenomena in left-handed transmission-line media," *IEEE Trans. Microw. Theory Tech.*, vol. 53, no. 1, pp. 238–245, Jan. 2005.
[17] J. C. Pedro and N. B. Carvalho, *Intermodulation Distortion in Microwave and Wireless Circuits*. Norwood, MA: Artech House, 2003.
[18] J. C. Booth, L. R. Vale, and R. H. Ono, "On-wafer measurements of nonlinear effects in high-temperature superconductors," *IEEE Trans. Appl. Superconduct.*, vol. 11, no. 1, pp. 1387–1391, Mar. 2001.
[19] D. Pozar, *Microwave Engineering*. New York: Wiley, 1998.

Jordi Mateu (M'03) received the Telecommunication Engineering and Ph.D. degrees from the Universitat Politècnica de Catalunya (UPC), Barcelona, Spain, in 1999 and 2003, respectively.

Since October 2006, he has been with the Department of Signal Theory and Communications, UPC, and with the Centre Tecnològic de Telecomunicacions de Catalunya (CTTC). From May to August 2001, he was a Visiting Researcher with Superconductor Technologies Inc., Santa Barbara CA. From October 2002 to August 2005, he was Research Associate with CTTC. Since September 2004, he has held several guest researcher appointments with the National Institute of Standards and Technology (NIST), Boulder, CO, where he was a Fulbright Research Fellow from September 2005 to October 2006. In July 2006, he was Visiting Researcher with the Lincoln Laboratory, Massachusetts Institute of Technology (MIT). From September 2003 to August 2005, he was a Part-Time Assistant Professor with the Universitat Autònoma de Barcelona. His primary interest includes microwave devices and system and characterization and modeling of new electronic materials including ferroelectrics, magnetoelectric and superconductors.

Dr. Mateu was the recipient of the 2004 Prize for the best doctoral thesis in fundamental and basic technologies for information and communications presented by the Colegio Oficial de Ingenieros de Telecomunicación (COIT) and the Asociación Española de Ingenieros de Telecomunicación (AEIT). He was also the recipient of a Fulbright Research Fellowship, an Occasional Lecturer Award for visiting MIT and a Ramón y Cajal Contract.

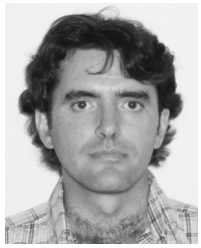

Carlos Collado (A'02–M'03) was born in Barcelona, Spain, in 1969. He received the Telecommunication Engineering degree and Ph.D. degree from the Technical University of Catalonia (UPC), Barcelona, Spain, in 1995 and 2001, respectively. In 1998, he joined the faculty at UPC, where he has been teaching courses on theory of electromagnetism, microwave laboratory, and high-frequency devices and systems. In 2004, he was a Visiting Researcher with the University of California Irvine. Since April 2005, he has been an Associate Professor with UPC. His primary research interests include microwave devices and systems, electrooptics applications, and superconducting devices.

Nathan Orloff was born in Columbia, SC, on August 10, 1981. He received the B.S. degree in physics (with high honors) from the University of Maryland at College Park, in 2004, and is currently working toward the Ph.D. degree in physics at the University of Maryland at College Park. His doctoral thesis concerns the study and extraction of microwave properties of materials including ferroelectrics, magnetoelectrics, superconducting materials, and fluids.

Mr. Orloff was the recipient of the 2004 Martin–Monroe Undergraduate Research Award and the 2006 CMPS Dean's Award for teaching assistants.

James C. Booth received the B.A. degree in physics from the University of Virginia, Blacksburg, in 1989, and the Ph.D. degree in physics from the University of Maryland at College Park, in 1996. His doctoral dissertation concerned novel measurements of the frequency-dependent microwave surface impedance of cuprate thin-film superconductors.

Since 1996, he has been a Physicist with the National Institute of Standards and Technology (NIST), Boulder, CO, originally as a National Research Council (NRC) Post-Doctoral Research Associate (1996–1998) and currently as a Staff Scientist. His research with NIST is focused on exploring the microwave properties of new electronic materials and devices including ferroelectric, magneto-electric, and superconducting thin films, as well as developing experimental platforms integrating microfluidic and microelectronic components for RF and microwave frequency characterization of liquid and biological samples.

Eduard Rocas (S'06) was born in Palafrugell, Catalonia, Spain, in 1982. He received the Telecommunication Engineering degree from the Universitat Politècnica de Catalunya (UPC), Barcelona, Spain, in 2005, and is currently working toward the Ph.D. degree at the UPC.

While working toward the Telecommunication Engineering degree, his final project was associated with the creation of the Intelligent Communications and Avionics for Robust Unmanned Aerial Systems (ICARUS) Research Group. From September 2005 to July 2006, he was involved with the simulation and modeling of advanced SONARs with the Computer Vision and Robotics Group (VICOROB), University of Girona. His research concerns new materials and structures for novel RF/MW devices.

Mr. Rocas was the recipient of an FPU grant and and FPI grant.

Alberto Padilla was born in Barcelona, Spain, in 1984. He received the Telecommunication Engineering degree from the Universitat Politècnica de Catalunya (UPC), Barcelona, Spain, in 2008, and is currently working toward the Ph.D. degree at the UPC.

While working toward the Telecommunication Engineering degree, his final project was associated with the mitigation of nonlinear behavior of high-temperature superconducting planar devices. Since March 2008, he has been with a Microwave Engineer the Department of Signal Theory and Communications, UPC. His research concerns a new class of synthesis for microwave filters for satellite communications.

Juan M. O'Callaghan (SM'01) received the Telecommunication Engineering degree from the Universitat Politècnica de Catalunya (UPC), Barcelona, Spain, in 1987, and the M.S. and Ph.D. degrees from the University of Wisconsin–Madison, in 1989 and 1992, respectively.

He is currently a Full Professor with the UPC. He was an Intern with the Systems Research Center, Honeywell, Bloomington, MN, where he was involved with noise measurement methods for field-effect transistors (FETs) at Ka-band. From 2003 to 2006, he was Manager for MERIT, a consortium of European universities delivering a joint Master's program in information technologies within the Erasmus Mundus Program. He is currently Vice-Dean of academic affaires with Telecom BCN, the telecommunication engineering school of the UPC. He has authored or coauthored over 45 papers in peer-reviewed international magazines. He holds three patents. His research interests include microwave devices and materials and microwave photonics. He has been involved with noise characterization, large-signal properties of GaAs FETs, and advanced microwave materials such as superconductors and ferroelectrics.

CHAPTER II - BULK ACOUSTIC WAVE RESONATORS

Bulk acoustic wave technology is having a great success, as a filtering solution, in the market of mobile applications. Its small footprint, high power handling and high quality factor are key requirements for today's mobile communications, and BAW is substantially better than previous technologies like surface acoustic wave or ceramic filters. However, BAW filters are known to exhibit a high second harmonic and intermodulation distortion, which can potentially limit the potential of this technology by causing undesired effects like receiver desensitization or interference.

This chapter focuses on the intrinsic nonlinearities in BAW resonators from a phenomenological modeling perspective.

The first article describes a lumped model approach of the nonlinear behavior of BAW resonators. The model is based on the modified Butterworth Van Dyke (MBVD) and provides with a model that is simple to set up and can reproduce the intermodulation distortion from a phenomenological perspective.

The second and third articles provide a distributed nonlinear model approach, based on the Krimtholz, Leedom and Matthaei (KLM) model, to reproduce the distributed nature of acoustic propagation through the materials stack.

The fourth article focuses on the second harmonic generation and proposes a methodology to accurately extract the effects of the measurement setup from the results.

The articles in Chapter 2 are:

- E. Rocas, C. Collado, J. Mateu, H. Campanella, J. M. O'Callaghan, **"Third order intermodulation distortion in Film Bulk Acoustic Resonators at resonance and antiresonance"**, *2008 IEEE MTT-S International Microwave Symposium Digest*, pp. 1259-1262, 15-20 June 2008
- E. Rocas, C. Collado, A. Padilla, J. Mateu, J. M. O'Callaghan, **"Nonlinear distributed model for IMD prediction in BAW resonators"**, *2008 IEEE International Ultrasonics Symposium*, pp. 1557-1560, 2-5 Nov. 2008
- C. Collado, E. Rocas, J. Mateu, A. Padilla, J. M. O'Callaghan, **"Nonlinear Distributed Model for Bulk Acoustic Wave Resonators"**, *IEEE Transactions on Microwave Theory and Techniques*, vol. 57, no. 12, pp. 3019-3029, Dec. 2009
- C. Collado, E. Rocas, A. Padilla, J. Mateu, J. M. O'Callaghan, N. D. Orloff, J. C. Booth, E. Iborra, R. Aigner, **"First-Order Elastic Nonlinearities of Bulk Acoustic Wave Resonators"**, *IEEE Transactions on Microwave Theory and Techniques*, Accepted for publication and available online at IEEExplore.org as Early Access.

Third order Intermodulation Distortion in Film Bulk Acoustic Resonators at Resonance and Antiresonance

Eduard Rocas[1], Carlos Collado[1], Jordi Mateu[1,2], Humberto Campanella[3], Juan M. O'Callaghan[1]

[1] Universitat Politècnica de Catalunya (UPC), Campus Nord, Barcelona, Spain
[2] Centre Tecnològic de Telecomunicacions de Catalunya (CTTC), PMT, Castelldefels, Spain
[3] Centro Nacional de Microelectrónica (CNM-CSIC), Campus UAB, Bellaterra, Spain

***Abstract* — This paper presents recent measurements and modeling of the third order intermodulation products of a Film Bulk Acoustic Resonator (FBAR), for a various values of frequency spacing between driving tones. The frequency dependence of voltage and current in the acoustic branch rules out a voltage-dependent nonlinearity. The results show different slopes at resonance and antiresonance, which are correctly adjusted by the model with a current dependent inductor and/or capacitor. The intermodulation distortion is found to be dependent on the frequency spacing between driving tones, indicating memory effects.**

***Index Terms* — Thin-film bulk acoustic wave resonators, intermodulation, nonlinear characterization, resonance, antiresonance.**

I. Introduction

Film bulk acoustic wave resonators (FBARs) allow to achieve very compact high-performance RF and microwave passive components [1]. The ever growing wireless market and a constantly increasing demand for spectrum are steadily pushing for more stringent requirements of such components. This is also the case of FBAR components and their nonlinear performance. In spite of the significance of the nonlinear effects in wireless communication systems [2], and the well-known existence of nonlinearities in piezoelectric based devices such as FBARs [3],[4], there are not many published works focusing on the nonlinear characterization and modeling of the FBAR components and their impact in communication systems. Several physical phenomena occurring in a FBAR (piezoelectricity, elasticity, thermal effects, etc.) have a potential nonlinearity and may give rise to many nonlinear effects such as resonator detuning, saturation, and generation of harmonics and intermodulation distortion (IMD). The ability to predict all these effects with realistic and easy-to-use models would be of great help to designers and would facilitate the use of FBAR devices in future systems.

In contexts other than FBAR devices (superconducting and ferroelectric devices, for example), IMD has shown to be of great value to relate nonlinear phenomena with their measurable effects [5],[6],[7]. Following that guide, in this work we measure the IMD of an FBAR at resonance and antiresonance for a range of input power and for various values of frequency separation between the two tones feeding the resonator. From the measurements we infer the basic features of a nonlinear version of the Butterworth Van Dyke model which we adjust to fit the measured data. The resulting model shows to be useful to predict the IMD at resonance and antiresonance. To our knowledge, there are no previous publications on nonlinear FBAR models able to account for IMD at these two resonant frequencies.

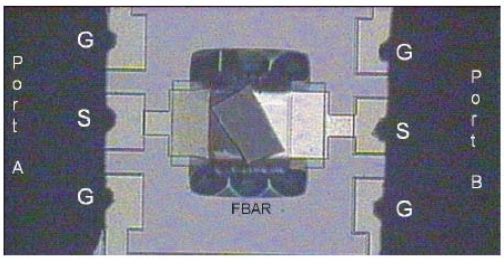

Fig. 1. FBAR tested in this work with coplanar transmission feed lines. The Area of the 1 μm thick AlN membrane is 50x70 μm.

II. Test Device and Linear Modeling

The FBAR tested in this work was implemented following the fabrication process described in [8]. This consists in a piezoelectric aluminium nitride (AIN) membrane (50x70 μm and 1 μm thick) sandwiched between two titanium/platinium layers and deposited on a silicon substrate. The geometry and dimensions of the FBAR tested were set to have resonant frequencies around 2.3 GHz. Embedded input and output coplanar waveguide (CPW) feeding ports were introduced on wafer in the test structure. A picture of the FBAR can be seen in Fig. 1.

A. Frequency Response and Linear Circuit Elements

Since the FBAR nonlinear performance strongly depends on its linear parameters, we first extracted these (or, equivalently, the FBAR equivalent circuit linear elements) from the small-signal frequency response following the procedure described below.

We used an *Agilent 8510* network analyzer to obtain the scattering parameters defining the FBAR frequency response from 1 GHz to 2 GHz. An on-wafer thru-reflect-reflect-match (LRRM) calibration set was previously used to calibrate the

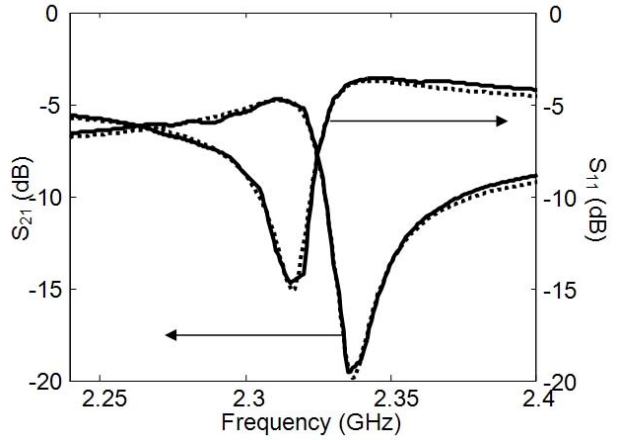

Fig. 2. In solid, measured S_{21} and S_{11} . In dashed, simulated S_{21} and S_{11} modeling the FBAR with the circuit parameter of Fig.3 and Table I.

measurement set-up [9]. These measurements were performed for a power delivered by the network analyzer of -10 dBm, which ensured the linear regime of the measured FBAR response.

Details of the frequency response, S_{21} and S_{11}, are outlined in Fig. 2, in solid lines. Note that the frequency response exhibits a resonance frequency at 2.312 GHz and anti-resonance frequency at 2.337 GHz

B. Circuit Model

The frequency response has been fitted using a modified Butterworth Van Dyke (MBVD) model. As in [8] additional capacitances (C_{ox}) and resistances (R_s and R_{sub}) have been introduced to consider the effects of the CPW feeding ports. The circuit model is outlined in Fig.3. A commercial software, [10], has been used to de-embed the circuit elements. Table I details the resulting parameters defining the circuit model, where the capacitances are in fF, the inductance in nH and the resistances in ohms. Figure 2 also depicts, in dashed lines, S_{21} and S_{11} resulting from the circuit model response, showing very good agreement over the whole frequency range.

III. IMD Measurements in FBAR

We based the nonlinear characterization of the FBAR on performing intermodulation measurements. Due to the strong IMD produced by the FBAR, instead of using sophisticated setups that we used previously [5], we could use a simple one

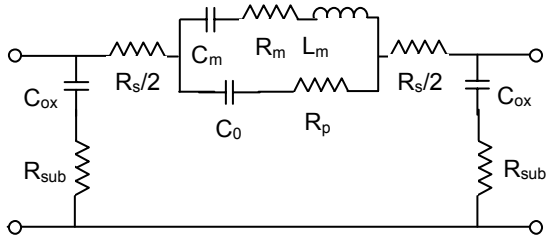

Fig. 3. Equivalent circuit model.

TABLE I
Circuit Parameters

C_m	R_m	L_m	C_o	R_p	R_s	C_{ox}	R_{sub}
10.2	14	464.5	551.1	11	60	438.3	220

in which the two sources synthesized at f_1 and f_2 are then combined to feed the nonlinear device, whose output is then driven to a spectrum analyzer to measure the magnitude of the intermodulation products at $2f_1$-f_2 and $2f_2$-f_1.

We systematically performed a set of IMD measurements at both resonance and antiresonance frequencies. In all these measurements we kept the two input tones balanced, that is P_1=P_2, where P_1 and P_2 are the powers of the tones at f_1 and f_2, respectively. The power driving the device was swept from -10 dBm to 2 dBm and measurements were carried out for Δf (being $\Delta f = f_2$-f_1) of 100 kHz, 50 kHz, 10 kHz, 5 kHz 1 kHz and 100 Hz.

Figure 4 shows the measured fundamental and IMD at resonance and antiresonance, respectively, for a tone spacing of 1 kHz. Circles and triangles represent the power at fundamental frequencies f_1 and f_2, respectively, and diamonds and squares represent the IMD at $2f_1$-f_2 and $2f_2$-f_1, respectively, all as a function of the power driving the FBAR, P_1. No IMD

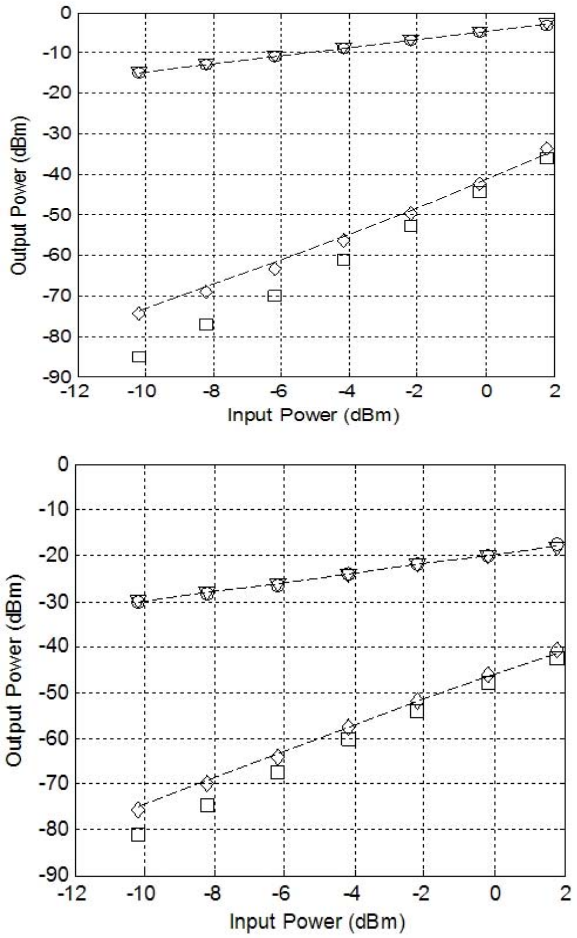

Fig. 4. Measured fundamental and IMD at resonance (top) and antiresonance (bottom)

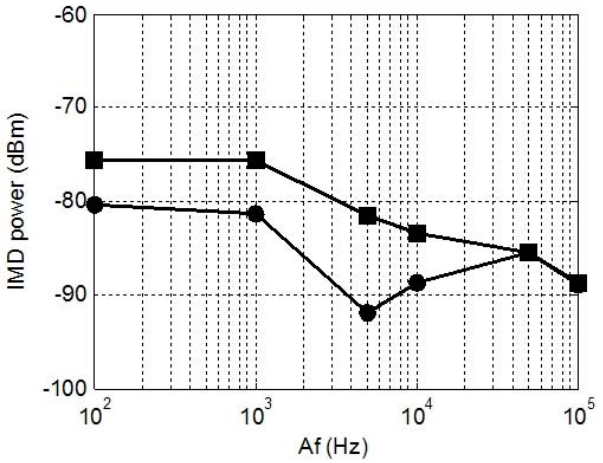

Fig. 5. IMD at $2f_1$-f_2 (squares) and $2f_2$-f_1 (circles) as a function of the frequency spacing Δf, and for a fixed input power of -10 dBm

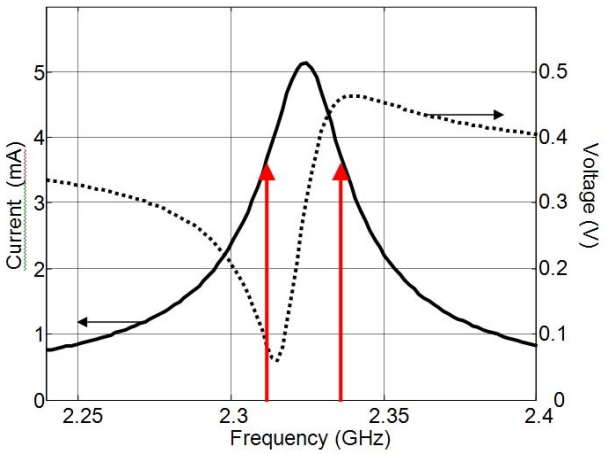

Fig. 6. Current flowing through the acoustic branch (solid line) and applied voltage to it (dotted line), as a function of frequency.

response has been observed when the fundamental tones are set out of the resonant or antiresonant frequencies.

The power of the fundamentals follows a slope 1:1 in log-log scale, over the whole range of measured power, for both cases (resonance and antiresonance), so neither detuning or saturation measurable effects affect the fundamental tones at these power levels (they might however affect IMD, as discussed later). On the other hand the slope of the IMD products is not the same for the resonant case than for the anti-resonant one. Whereas for the resonant case the slope is slightly lower than 3 (in log-log scales), it is slightly higher than 3 for the antiresonant case.

Another important feature observed from the measured IMD is its dependence on the frequency spacing of the input tones Δf and the asymmetries exhibited between the measured IMD at $2f_1$-f_2 and $2f_2$-f_1. Figure 5 shows the IMD at $2f_1$-f_2 and $2f_2$-f_1 for a fixed input power of -10 dBm as a function of the frequency spacing Δf. The increment of the IMD as the tone spacing decreases and the aforementioned asymmetry between the IMD might be due to several origins, but in general they might be attributed to the existence of memory effects with time constants similar to the period of the modulating signal (frequency Δf) in a two tone IMD experiment [11], [12].

IV. Nonlinear Modeling Approach and Discussion

This section presents a model that explains the nonlinear behavior of the IMD occurring at both resonances of the FBAR structure tested.

The nonlinear model proposed uses the linear circuit model presented in section II. B and assumes that the inductance L_m and/or the capacitance C_m, depends on the current in the acoustic branch, as indicated in Fig.3. To analyze the effects of this assumption, Fig. 6 outlines the current in the acoustic branch and the voltage drop between node 1 and 2 of the circuit model of Fig. 3, as a function of frequency. The arrows inserted in Fig. 6 indicate the frequencies of the resonance and anti-resonance. This shows that the current flowing through the acoustic branch of the circuit model is equal at both frequencies, and since the nonlinearities depend on this current, one could expect that the power of the generated IMD was similar in resonance and anti-resonance which is consistent with the measurements at low power levels (Fig. 4). By contrast, Fig. 6 rules out a voltage-dependent nonlinearity, since that would generate vastly different IMD at resonance and anti-resonance, due to the large difference in voltage at these two frequencies.

Having set that the nonlinearities should be current-dependent, the model can also explain the different slopes of the IMD graphs in Fig. 4 by a slight shift in the current response peak (Fig. 6) due to the dependence of C_m or L_m on current. A shift of the current frequency response curve to lower frequencies as the signal power is increased will tend to increase the slope of the IMD at resonance and decrease that of the IMD at antiresonance, while being experimentally unnoticeable to the fundamental signals at f_1 and f_2. This effect may be produced by a nonlinearity that makes C_m increase with increased drive level and/or by a nonlinearity that also makes L_m increase with increased drive level.

A current-dependent C_m was assumed in [13] to fit the large-signal frequency response of quartz resonators. However, the dependence found in [13], set a decrease of C_m with drive level, contrary what we have found in our case, where a dependence of the type $C(i) = C_0(1 + \Delta C_2 * i^2)$ with ΔC_2=80 A^{-2} would fit the IMD curves at resonance and antiresonance throughout the whole range of input power used in the measurement (Fig. 4). Alternatively, one could set the nonlinearity in the inductor L_m by using $L(i) = L_0(1 + \Delta L_2 * i^2)$ with ΔL_2=28 A^{-2} and would obtain equivalent results. The dashed lines in Fig. 4 are obtained by using this equation.

In [14] the nonlinear impedance of several piezoelectric resonators is analyzed considering only the nonlinear elasticity of the piezoelectric material. Contrary to what is found in [13], all the measurements in [14] show an increase in the reactive part of the impedance when *i* increases. This is consistent with an increase of C and/or L with the current that would justify the IMD measurements presented here. (Note that, the increase in C will diminish the absolute value of the reactance, but will produce the reactance increase mentioned previously, since C affects the negative part of the reactance.)

This simple picture of the FBAR nonlinear response might be useful to explain the IMD at both resonance and antiresonance frequencies for a wide range of powers. Additional considerations will have to be made to take into account memory effects and to jointly study IMD with other nonlinear effects such as saturation and detuning.

ACKNOWLEDGMENT

This work was partially supported by the Spanish Government (CICYT) under Grant TEC-2006-13248-C04-02/TCM. E. R and J. M thank the support from BES-2007-16775 and RyC-001125.

REFERENCES

[1] K.M. Lakin; G.R. Kline; K.T. McCarron, "High Q microwave acoustic resonators and filters," Microwave Symposium Digest, 1993., IEEE MTT-S International , vol., no., pp.1517-1520 vol.3, 1993

[2] Pedro and Carvalho, "Intermodulation Distortion in Microwave and Wireless Circuits," Artech House: Norwood, Mass., 2003.

[3] Kaltenbacher, B.; Hofer, M.; Kaltenbacher, M.; Simkovics, R.; Lerch, R., "Identification of material nonlinearities in piezoelectric ceramics," Ultrasonics, 2003 IEEE Symposium on , vol.1, no., pp. 358-361 Vol.1, 5-8 Oct. 2003

[4] S P Joshi, "Non-linear constitutive relations for piezoceramic materials", Smart Materials and Structures. March 1992 Volume: 1 Start Page: 80

[5] J. Mateu, J. C. Booth, S. A. Schima "Frequency Tuning and Spurious Signal Generation in Ferroelectric Thin-film transmission lines" *IEEE Trans. On Microwave Theory and Techniques,* vol. 55, no. 2, February, 2007

[6] C. Collado, J. Mateu, J. M. O'Callaghan, "Analysis and Simulation of the Effects of Distributed nonlinearities in microwave superconducting devices" *IEEE Trans. On Appl. Supercond.* , vo. 15, no.1, pp. 26-39, March 2005

[7] J. Mateu, J. C. Booth, B. H. Moeckly, "Wideband Nonlinear Response of High-Temperature Superconducting Thin Films From transmission line measurements", *IEEE Trans. On Microwave Theory and Techniques,* vol. 55, no. 7, July, 2007

[8] H. Campanella, P. Nouet, P. de Paco, A. Uranga, N. Barniol, and J. Esteve, "Automated on-Wafer Extraction of Equivalent-Circuit Parameters in Thin-Film Bulk Acoustic Wave Resonators and Substrate" *Microwave And Optical Technology Letters* Vol. 50, No. 1, pp. 4-7, 2008

[9] F. Purroy, L. Pradell, "New theoretical analysis of the LRRM calibration technique for vector network analyzers," *IEEE Trans. On Instrumentation and Measurement*, Vol. 50, No.5, pp. 1307-1314, 2001.

[10] *Advanced Design Systems* (ADS)

[11] Ngoya, E.; Le Gallou, N.; Nebus, J.M.; Buret, H.; Reig, P., "Accurate RF and microwave system level modeling of wideband nonlinear circuits," Microwave Symposium Digest., 2000 IEEE MTT-S International , vol.1, no., pp.79-82, 2000

[12] N. Borges de Carvalho, J.C. Pedro, "A Comprehensive Explanation of Distortion Sideband Asymmetries", *IEEE Trans. On Microwave Theory and Techniques*, vol., 50, no. 9, 2002.

[13] J. Nosek, "Drive Level Dependence of the Resonant Frequency in BAW Quartz Resonators and His Modeling", *IEEE Trans. On Ultrasonics, Ferroelectrics and Frequency Control,* Vol. 46, no. 4, July 1999.

[14] R. Perez and A. Albareda "Analysis of nonlinear effects in a piezoelectric resonator", *J. Acoust. Soc. Am*. Vol. 100, no. 6, pp 3561-3569, 1996

Digital Object Identifier: 10.1109/ULTSYM.2008.0379

Nonlinear distributed model for IMD prediction in BAW resonators

Eduard Rocas[1], Carlos Collado[1], Alberto Padilla[1], Jordi Mateu[1,2], J. M. O'Callaghan[1]

[1] Universitat Politècnica de Catalunya (UPC), Campus Nord, Barcelona, Spain
[2] Centre Tecnològic de Telecomunicacions de Catalunya (CTTC), PMT, Castelldefels, Spain

Abstract **— This work presents a distributed nonlinear equivalent circuit to asses the intermodulation distortion (IMD) occurring in a BAW resonator. Closed-form expressions for intermodulation distortion at 2f1-f2 are obtained. Comparisons between analytical and simulated results are in good agreement. Extension of this analysis could be used to predict the nonlinear performance of more complex systems using BAW resonators, such as filters. Finally, measurements are presented and explained using the proposed approach.**

Index Terms **— Bulk acoustic wave resonators, intermodulation, nonlinear distributed model, resonance.**

I. Introduction

Bulk Acoustic Wave resonators and filters are presently used in many communication systems. To fully incorporate them into communication systems, characterization of their nonlinear response is required.

Although there are many works concerned about the nonlinear behavior of piezoelectric based components [1], [2], there are only few studying the intermodulation distortion (IMD) in BAW resonators and filters [3], [4]. These studies are usually based on phenomenological equivalent circuit models that do not consider the distributed nature of the phenomena, such as the Van Dyke model [5], [6].

This work extends the well-known KLM model to account for the nonlinear behavior of BAW components. To do that we analyze the proposed circuit model to obtain closed-form expression of third order IMD. Verification of these expressions has been performed using commercial circuit simulator.

II. KLM linear model

The proposed model can be considered as an extension of the KLM model, outlined in Fig. 1, to take into account the nonlinear behaviour. The KLM circuital model and its parameters are as follows:

$$Z_0 = \rho c A \tag{1}$$

$$C_0 = \varepsilon \frac{A}{d} \tag{2}$$

$$X_1 = \frac{h^2}{\omega^2 Z_0} \sin\left(\frac{\omega d}{c}\right) \tag{3}$$

$$\phi = \frac{\omega Z_0}{2h} \frac{1}{\sin\left(\frac{\omega d}{2c}\right)} \tag{4}$$

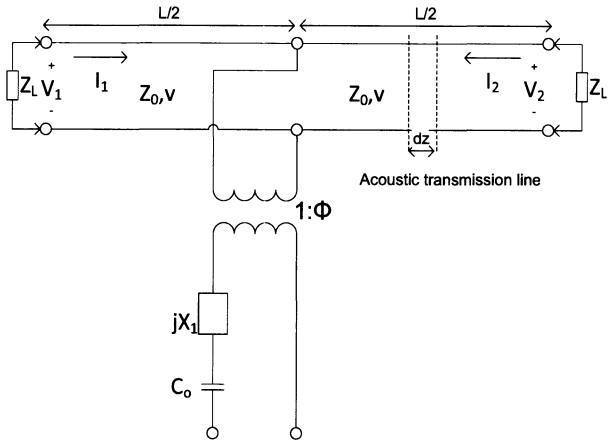

Fig. 1. Original KLM model with its electric (1 and 2) and acoustic ports (3 and 4). The transformer represents the electro-acoustic coupling.

The circuit of Fig.1 models the electric and acoustic phenomena occurring in the BAW device and their coupling. This is especially useful as it makes easy to analyze the propagation of the acoustic signal through the material (current and voltage model particle velocity and acoustic force, respectively). Therefore the piezoelectric material itself, represented as a transmission line in the KLM model, consists of cascading many differential lumped segments that are directly related with the material characteristics. In particular, our approach starts by identifying the nonlinear material constants and its relation with the distributed parameters.

III. Nonlinear acoustic transmission line model

A. Origin of the nonlinear behavior

Although the origin of the nonlinear effects in piezoelectric materials may come from many different sources, such as the piezoelectric constant, permittivity and elasticity, they are unified in the stiffened elastic constant c^D [7]:

$$c^D = c^E + \frac{e^2}{\varepsilon^S} \tag{5}$$

Where c^E accounts for the stiffness, e is the piezoelectric constant and ε^S is the permittivity.

Using the acoustic wave propagation equations:

$$\frac{\partial v}{\partial x} = -\frac{1}{Ac^D}\frac{\partial F}{\partial t}; \quad \frac{\partial F}{\partial x} = -A\rho\frac{\partial v}{\partial t} \tag{6}$$

we may identify the linear distributed inductance $L_d = A\rho$, and nonlinear distributed capacitance as, $C_d = 1/Ac^D$, being C_d the only term that accounts for the nonlinear effects.

B. Nonlinear circuit model

From the previous analysis, and by discarding other possible minor nonlinear sources, such as mass density fluctuations or thermal effects [8], c^D results in a nonlinear distributed capacitance:

$$C_d(v) = C_0 + J_{NL}(v) \tag{7}$$

where C_0 is the low signal capacitance, and $J_{NL}(v)$ is a nonlinear function of voltage. Assuming a quadratic nonlinear dependence on the voltage along the acoustic line, as:

$$J_{NL}(v) = Jv^2 \tag{8}$$

we can write:

$$C_d(v) = C_0 + Jv^2 \tag{9}$$

C. Transmission line current at IMD

A pure half-wavelength pattern on the line exists only for the frequency where there is the maximum current inside the resonator. This frequency is very close to the resonance, so we can assume the following pattern at resonance (z=0 at the center of the line):

$$v_{\omega_i}(z,t) = \mathrm{Re}\left[V_{\omega_i} e^{j\omega_i t}\cos(\frac{\pi z}{l})\right] \tag{10}$$

$$i_{\omega_i}(z,t) = \mathrm{Re}\left[I_{\omega_i} e^{j\omega_i t}\sin(\frac{\pi z}{l})\right] \tag{11}$$

By performing a simple circuit analysis, the nonlinear current is:

$$\frac{\partial I_{NL}}{\partial z} = \frac{\partial}{\partial t}\left(Jv^3\right) \tag{12}$$

That can be rewritten in the frequency domain as:

$$\frac{\partial I_{NL,\omega_i}}{\partial z} = j\omega_i F\left((Jv^3),\omega_i\right) \tag{13}$$

Where $F\left(g(t),\omega_i\right)$ is the ω_i component of the Fourier transform of *g(t)* Using (10) and (13) we get the nonlinear current at the IMD frequency $2\omega_1$-ω_2 (we note ω_{12}):

$$\frac{\partial I_{NL,\omega_{12}}}{\partial z} = \frac{3}{4}V_1^2 V_2^*\left[j\omega_{12}J\right]\cos^3(\frac{\pi z}{l}) \tag{14}$$

IV. Closed-form expression for IMD at resonance

The procedure starts by considering that the generated power on the resonator is equal to the dissipated power on the external loads and on the resonator itself:

$$P_{gen} = P_{res} + P_{ext} + 2j\omega_{12}(W_m - W_e) \tag{15}$$

Since at resonance W_e=W_m, we can write:

$$-\frac{1}{2}\int_{-\frac{l}{2}}^{\frac{l}{2}} V_{12}dI_{NL}^* = \frac{\omega_{12}}{2Q_L}V_{12}V_{12}^* C_d \int_{-\frac{l}{2}}^{\frac{l}{2}}\cos^2(\frac{\pi z}{l})dz \tag{16}$$

where Q_L is the quality factor of the resonator. Replacing (14) into (16) we have:

$$V_{12} = -j\frac{9}{16}Q_L V_1^2 V_2^* \frac{J}{C_d} \tag{17}$$

Where Q_L can be obtained from measurements as follows [9]:

$$Q_L = \frac{1}{2}\omega_0\frac{\partial\phi}{\partial\omega} \tag{18}$$

More details and extension of the previous development can be found in [10].

VI. Measurements

The previous equations were validated with simulations using comercial nonlinear software [ADS]. The verification has been performed for many resonators with unloaded quality

factors ranging from 200 to 2000, and for both distributed and external load losses. The results have shown very good agreement in all cases, with less than 1% error.

A. Test device

The measurements presented in this section correspond to a FBAR consisting of a 1 um thick AlN membrane (50 um x 70 um) between two titanium/platinum electrodes 30 nm and 150 nm thick respectively [11]. The resonator presents a quality factor of 900 at resonance and a coupling coefficient of 2,2%.

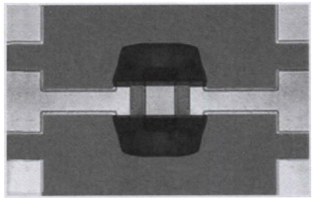

Fig. 2. FBAR tested in this work with coplanar transmission feed lines.

B. Frequency response

Scattering parameters measurements have been performed to fit the model to the frequency response of the measured FBAR. An *Agilent 8510* network analyzer has been used, with a previous on-wafer thru-reflect-reflect-match (LRRM) calibration process [12]. The correct fitting of the linear response, both at frequency close to the resonance and in a wideband frequency range, is the necessary previous step for a proper fitting of the nonlinear response. To this end, two calibrations were performed from 2 GHz to 2.6 GHz and from 2 GHz to 6 GHz to obtain out of resonance scattering parameters, as well as detailed aspects of the resonance and antiresonance. Both measured and simulated S_{11} and S_{21} can be seen in figure 3.

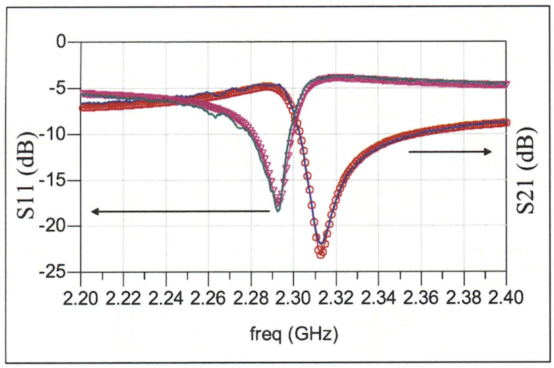

Fig. 3. In solid, measured S_{11} and S_{21}. Circles and triangles represent the simulated frequency response.

C. Nonlinear measurements

A two ports measurement setup consisting of two balanced signal generators is used to feed the FBAR [13]. This allows to measure the third order intermodulation distortion and the second harmonic generation, by using a spectrum analyzer connected to the output port.

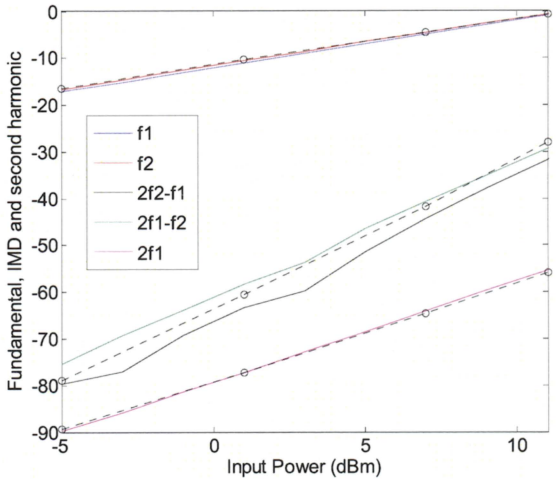

Fig. 4. In solid, measured fundamental, third order IMD and second harmonic in dBm. In dashed, the simulated fundamental and nonlinear products.

An extension of the aforementioned nonlinear distributed capacitance is used to cover also the second harmonic generation effect. The approach considers both first order nonlinear capacitance and quadratic capacitance, as follows:

$$C_d(v) = C_0 + Kv + Jv^2 \tag{19}$$

A complete fitting of the measured FBAR 3rd order IMD and 2nd harmonic can be seen in figure 4 for an input power range of -5 dBm to +10 dBm with K=1,15e-5 and J=1,3e-5, in which saturation is not observed

VII. Conclusion

The analysis outlined in this work can be further used to predict the IMD occurring in BAW based devices and evaluate their impact in communication systems. The nonlinear model can predict the IMD and harmonic generation in a FBAR resonator. By relating the nonlinear response with the material parameters one could design highly linear BAW component.

ACKNOWLEDGMENT

This work was partially supported by the Spanish Government (CICYT) under Grant TEC-2006-13248-C04-02/TCM , MAT2005-05656-C04-03E. R and J. M thank the support from BES-2007-16775 and RyC-001125. Special thank to Humberto Campanella (CNM – Centro Nacional de Microelectrónica) for supplying the sample

REFERENCES

[1] Kaltenbacher, B.; Hofer, M.; Kaltenbacher, M.; Simkovics, R.; Lerch, R., "Identification of material nonlinearities in piezoelectric ceramics," Ultrasonics, 2003 IEEE Symposium on , vol.1, no., pp. 358-361 Vol.1, 5-8 Oct. 2003

[2] S P Joshi, "Non-linear constitutive relations for piezoceramic materials", Smart Materials and Structures. March 1992 Volume: 1 Start Page: 80

[3] J. Nosek, "Drive Level Dependence of the Resonant Frequency in BAW Quartz Resonators and His Modeling", *IEEE Trans. On Ultrasonics, Ferroelectrics and Frequency Control,* Vol. 46, no. 4, July 1999.

[4] R. Perez and A. Albareda "Analysis of nonlinear effects in a piezoelectric resonator", *J. Acoust. Soc. Am.* Vol. 100, no. 6, pp 3561-3569, 1996

[5] Aigner, R.; Ngoc-Hoa Huynh; Handtmann, M.; Marksteiner, S., "Behavior of BAW devices at high power levels," Microwave Symposium Digest, 2005 IEEE MTT-S International , vol., no., pp. 4 pp.-, 12-17 June 2005

[6] E. Rocas, C. Collado, J. Mateu, H. Campanella, J. M. O'Callaghan, "Third order Intermodulation Distortion in Film Bulk Acoustic Resonators at Resonance and Antiresonance". International Microwave Symposium, 2008.

[7] R. Kato and J. Hama, "First-principles calculation of the elastic stiffness tensor of aluminium nitride under high pressure,"

[8] Enlund, J.; Yantchev, V.; Katardjiev, I., "Electric Field Sensitivity of Thin Film Resonators Based on Piezoelectric AlN Thin Films," Ultrasonics Symposium, 2006. IEEE , vol., no., pp.468-471, 2-6 Oct. 2006

[9] Frank Z. Bi and Bradley P. Barber, "Bulk acoustic wave RF technology", IEEE microwave magazine. October 2008.

[10] Collado, C.; Mateu, J.; O'Callaghan, J.M., "Analysis and simulation of the effects of distributed nonlinearities in microwave superconducting devices," Applied Superconductivity, IEEE Transactions on , vol.15, no.1, pp. 26-39, March 2005

[11] H. Campanella, P. Nouet, P. de Paco, A. Uranga, N. Barniol, and J. Esteve, "Automated on-Wafer Extraction of Equivalent-Circuit Parameters in Thin-Film Bulk Acoustic Wave Resonators and Substrate" *Microwave And Optical Technology Letters* Vol. 50, No. 1, pp. 4-7, 2008

[12] F. Purroy, L. Pradell, "New theoretical analysis of the LRRM calibration technique for vector network analyzers," *IEEE Trans. On Instrumentation and Measurement*, Vol. 50, No.5, pp. 1307-1314, 2001.

[13] Ngoya, E.; Le Gallou, N.; Nebus, J.M.; Buret, H.; Reig, P., "Accurate RF and microwave system level modeling of wideband nonlinear circuits," Microwave Symposium Digest., 2000 IEEE MTT-S International , vol.1, no., pp.79-82, 2000

Nonlinear Distributed Model for Bulk Acoustic Wave Resonators

Carlos Collado, *Member, IEEE*, Eduard Rocas, *Student Member, IEEE*, Jordi Mateu, *Member, IEEE*, Alberto Padilla, *Student Member, IEEE*, and Juan M. O'Callaghan, *Senior Member, IEEE*

***Abstract*—This work expands the model proposed by Krimtholz, Leedom, and Matthaei (KLM) model to account for the nonlinear effects occurring in acoustic devices due to the nonlinear stiffened elasticity. We show that a nonlinear distributed capacitance in the acoustic transmission line of the KLM model can account for the distributed nature of the nonlinear effects. Specifically, we use the nonlinear telegrapher's equation to find closed-form equations for intermodulation distortion and harmonic generation. We confirm the validity of these equations by comparing their results with those provided by a KLM equivalent circuit in which the nonlinear transmission line is implemented by cascading many $L-C$ cells having a voltage-dependent capacitance. To further confirm the model, we show measured nonlinear effects in a thin film bulk acoustic resonator in close agreement with the equivalent circuit simulations.**

***Index Terms*—Bulk acoustic wave (BAW), film bulk acoustic resonator, harmonic generation, intermodulation distortion, nonlinear Krimtholz, Leedom, and Matthaei (KLM), nonlinear stiffened elasticity, nonlinearities.**

I. Introduction

BULK ACOUSTIC WAVE (BAW) technology is capable of producing miniature high Q resonators, which are essential elements in compact filters having low-insertion loss and high-frequency selectivity. A widespread use of this technology is expected in the ever-growing wireless market, where handheld devices need to accommodate for requirements such as spectrum crowding, high bandwidth demand, miniaturization, and low cost [1].

However, there are still limitations that may exclude the use of BAW resonators in some microwave applications. In particular, their inherent nonlinear behavior [2] may cause intermodulation distortion (IMD), harmonic generation, and detuning and/or saturation of the filter frequency response.

Manuscript received December 29, 2008; revised August 26, 2009. First published November 13, 2009; current version published December 09, 2009. This work was supported in part by the Spanish Government (CICYT) under Grant TEC-2006-13248-C04-02/TCM.

C. Collado, E. Rocas, A. Padilla, and J. M. O'Callaghan are with the Department of Signal Theory and Communications, Universitat Politècnica de Catalunya (UPC), Barcelona 08034, Spain (e-mail: collado@tsc.upc.edu; eduard.rocas@tsc.upc.edu; alberto.padilla@tsc.upc.edu; joano@tsc.upc.edu).

J. Mateu is with the Department of Signal Theory and Communications, Universitat Politècnica de Catalunya (UPC), Barcelona 08034, Spain and also with the Centre Tecnològic de Telecomunicacions de Catalunya (CTTC), Castelldefels, Barcelona 08860, Spain (e-mail: jmateu@tsc.upc.edu).

Color versions of one or more of the figures in this paper are available online at http://ieeexplore.ieee.org.

Digital Object Identifier 10.1109/TMTT.2009.2034211

Although the nonlinear effects may be due to several causes, most previous publications point to thermal effects and the nonlinearity in stiffness, piezoelectric coefficient, and permittivity as the dominant ones [3]. Quantifying such nonlinear effects with material parameters such as the nonlinear stiffened elasticity is crucial to fully understand the nonlinear behavior of BAW resonators. On the other hand, equivalent circuits of BAW resonators are needed to predict the nonlinear effects occurring in more complex devices, such as filters with several resonators. A definition of the equivalent circuit elements (such as a voltage-dependent capacity) consistent with the material parameters (such as the nonlinear stiffened elasticity) would be very useful to relate material properties with the final system performance.

Tiersten [4] reported on a nonlinear lumped equivalent circuit for rotated Y-cut quartz resonators and its corresponding closed-form expressions to predict the third-order IMD. Thereafter, other works [5]–[9] used lumped approaches based in Tiersten's equations or in nonlinear versions of the Butterworth-van-Dike equivalent circuit (BVD) [10] in which one or several lumped elements of the acoustic branch (series $R-L-C$ circuit) are nonlinear. Some of our previous work [11] also uses a phenomenological approach based on the BVD circuit to model the IMD occurring in a film bulk acoustic resonator (FBAR).

These different approaches based on lumped element equivalent circuits are simple and useful for modeling some limited manifestations of the nonlinear effects. However, the values of the lumped elements in these equivalent circuits are jointly affected by material parameters and device-specific parameters, such as resonator size and geometry. In these conditions, it is hard to consistently relate the values of equivalent circuit elements to material parameters.

A distributed model can be found in [12], in which the authors extend Mason's linear circuit to the nonlinear region. In this paper, we address this problem by extending our preliminary work in [13], which proposes a distributed nonlinear equivalent circuit based on the lineal model proposed by Krimtholz, Leedom, and Matthaei (KLM) [14]. As stated in [14], the roles of the mechanical and electrical parts of the circuit are more clearly distinguished in the KLM equivalent circuit than in the Mason's one, which simplifies the nonlinear extension.

Our version of equivalent circuit is made by replacing the acoustic line in the KLM model with many cascaded elemental $L-C$ cells. These cells have nonlinear elements that are consistent with the stress–strain curve of the piezoelectric layer in the BAW resonator. With this model we are able to relate the nonlinearities in the equivalent circuit (specifically a voltage-depen-

dent distributed capacitance in a transmission line) with nonlinearities in the material (stiffened elasticity).

An additional advantage of the model we are proposing is its validity over wide frequency ranges, which makes the model valid for predicting the generation of second harmonics and out-of-band intermodulation products. This is unlike the simpler version of the BVD model, which is limited to a narrow frequency range if no additional acoustic branches are considered.

As an example, we use the equivalent circuit to fit measured linear and nonlinear data in a thin film bulk acoustic resonator. Furthermore, we use the equivalent circuit to derive closed-form equations for some of the most relevant nonlinear effects: intermodulation distortion and second harmonic generation.

II. Nonlinear Acoustic Transmission Line Model

As mentioned above, the proposed equivalent circuit is based on an extension of the linear KLM model to account for the distributed nonlinear effects in the acoustic wave. This section reviews the basic concepts of the KLM model and details the additional considerations used to include the nonlinear effects in the model.

A. Linear KLM Model

The conventional KLM model [14] (see Fig. 1) includes a transmission line that accounts for the usual equivalences in acoustic wave devices (voltage v is equivalent to force F and current i to velocity). The characteristic impedance Z_0 and phase velocity v_p in this transmission line are given by

$$Z_0 = \rho v_p A \tag{1}$$

$$v_p = \sqrt{\frac{c^D}{\rho}} \tag{2}$$

where A and ρ are, respectively, the area of the electrodes and the density of the piezoelectric material. The term c^D represents the stiffened elasticity and is obtained from the constitutive equations describing the stress–strain curve in a piezoelectric material [15]. Its value is equal to the elasticity under constant electric field c^E plus an additional term that depends on the piezoelectric constant e and the dielectric constant ε^S as

$$c^D = c^E + \frac{e^2}{\varepsilon^S}. \tag{3}$$

The transformation ratio ϕ, electrical capacity C_0, and reactance X_1 shown in Fig. 1 are given by

$$\phi = \frac{\omega Z_0}{2h} \frac{1}{\sin\left(\frac{\omega l}{2v_p}\right)} \tag{4}$$

$$C_0 = \varepsilon^S \frac{A}{l} \tag{5}$$

$$X_1 = \frac{h^2}{\omega^2 Z_0} \sin\left(\frac{\omega l}{v_p}\right) \tag{6}$$

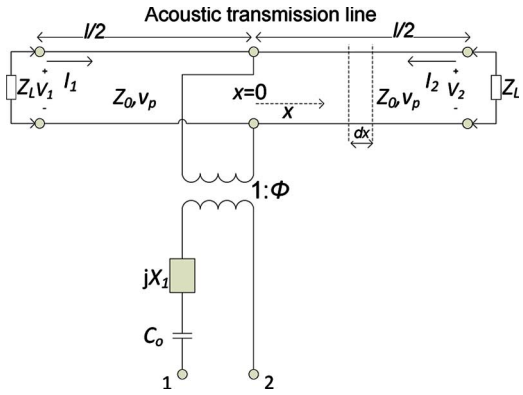

Fig. 1. Equivalent KLM circuit of a BAW resonator [14]. The acoustic transmission line of length l extends along the x-axis and is connected to an electrical network at $x = 0$. Ports 1 and 2 are the input and output ports.

where h is a piezoelectric constant of the crystal ($h = e/\epsilon^S$) and l is its thickness.

The telegrapher's equations of the equivalent transmission line [15] for an acoustic wave propagating along the x-axis can be written as

$$\frac{\partial i}{\partial x} = -\frac{\partial [C_d v]}{\partial t} \tag{7}$$

$$\frac{\partial v}{\partial x} = -\frac{\partial [L_d i]}{\partial t} \tag{8}$$

being $C_d = 1/(A \cdot c^D)$ the distributed capacitance and $L_d = \rho \cdot A$ the distributed inductance.

B. Nonlinear KLM Model

Although it is supposed that the elasticity, which relates the stress with the strain at constant electric field, is the main contribution to the nonlinear response [16], there are also other sources that may be considered, such as the piezoelectric constant or the permittivity [3]. These sources may be drawn together in a unique term c^D in (3) which depends on the stress T as

$$c^D(T) = c_0^D + \Delta c_{NL}^D(T). \tag{9}$$

This function models the piezoelectric stress–strain curve, which for weak nonlinearities can be expanded in a Taylor's series as

$$c^D(T) = c_0^D + \Delta c_1^D \cdot T + \Delta c_2^D \cdot T^2 + \cdots \tag{10}$$

where Δc_1^D, Δc_2^D, ... account for the strength of the nonlinear effects.

In the KLM model, the voltage is equivalent to the force, which is uniform in a cross section of the acoustic transmission line for the propagating mode of interest. Therefore, we can scale the independent variable T in $c^D(T)$ with the area A using $F = -AT$ [15]. We can then denote $c^D(F)$

$$c^D(F) = c_0^D - \frac{\Delta c_1^D}{A} \cdot F + \frac{\Delta c_2^D}{A^2} \cdot F^2 + \cdots \tag{11}$$

Since, in the equivalent circuit, the distributed capacitance in the transmission line (C_d) depends on c^D through $C_d = 1/(A \cdot c^D)$, $c^D(F)$ can be modeled by a nonlinear capacitance

$$C_d(v) = C_{d,0} + \Delta C_{NL}(v) \tag{12}$$

where $C_{d,0}$ represents the linear term of the distributed capacitance. The additional nonlinear term can also be expanded in a Taylor's series as $\Delta C_{NL}(v) = \Delta C_1 v + \Delta C_2 v^2 + \cdots$, where, for example, the first two terms ΔC_1 and ΔC_2 can be written as

$$\Delta C_1 = \frac{1}{Ac_0^D}\frac{\Delta c_1^D}{Ac_0^D} \tag{13}$$

$$\Delta C_2 = \frac{1}{Ac_0^D}\left(-\frac{\Delta c_2^D}{A^2 c_0^D} + \left(\frac{\Delta c_1^D}{Ac_0^D}\right)^2\right). \tag{14}$$

Note that (13) and (14) relate the device-independent nonlinear terms of the piezoelectric constants Δc_1^D and Δc_2^D with the nonlinear terms of the equivalent circuit ΔC_1 and ΔC_2.

Using the nonlinear distributed capacitance (12) into the telegrapher's (7) and (8), we obtain

$$\frac{\partial v}{\partial x} = -L_d \frac{\partial i}{\partial t} \tag{15}$$

$$\frac{\partial i}{\partial x} = -C_{d,0}\frac{\partial v}{\partial t} - \frac{\partial i_{nl}}{\partial x} \tag{16}$$

with

$$\frac{\partial i_{nl}}{\partial x} = \frac{\partial}{\partial t}\left(\Delta C_{NL}(v) v\right). \tag{17}$$

Equations (15)–(17) describe the nonlinear behavior of an acoustic transmission line and will be used in Section III to derive closed-form expressions that relate nonlinear measured IMD and harmonics with the stiffened elasticity of the piezoelectric layer.

Before going into details on the formulation, we summarize the assumptions considered throughout the paper.

1) The equivalent circuit of an elemental section of an acoustic transmission line used in this work is outlined in Fig. 2. For simplicity, we do not consider the series resistance and shunted conductance that would model the losses in an acoustic transmission line [15], however note that those elements could be easily included in the electrical model of Fig. 2.
2) Other sources of nonlinearities beyond those included in the definition of c^D in (3), such as self-heating effects, changes in the density, or nonlinear friction effects are not considered. If necessary, the model could be easily expanded with a nonlinear distributed inductance, series resistance, or shunted conductance.
3) We are not taking into account the nonlinearities arising from C_0 nor those arising from X_1 and ϕ (4)–(6). We assume that the nonlinearity in C_0 due to ε^S and the changes in v_p and h with the stress are negligible compared with those arising inside the resonator due to the nonlinear stiffened elasticity.

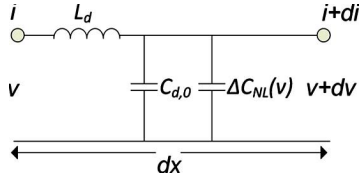

Fig. 2. Lossless transmission line cell modeling and infinitesimal length section of the acoustic transmission line.

III. Closed-Form Expressions for IMD and Second Harmonic

In this section, we derive the equations for power of the intermodulation distortion and second harmonic signals generated in the nonlinear acoustic line having a voltage-dependent distributed capacitance $C_d(v)$ (12). We assume that the line is driven by two tones $v_{g,\omega_i}(t) = \mathrm{Re}\left[V_{g,\omega_i} e^{j\omega_i t}\right]$ at fundamental frequencies ω_i being $i = 1, 2$.

If both driving tones are at resonance, their spatial distribution will be that of a standing wave pattern

$$v_{\omega_i}(x,t) = \mathrm{Re}\left[V_{\omega_i} e^{j\omega_i t}\cos\left(\frac{\pi x}{l}\right)\right] \tag{18}$$

$$i_{\omega_i}(x,t) = \mathrm{Re}\left[I_{\omega_i} e^{j\omega_i t}\sin\left(\frac{\pi x}{l}\right)\right] \tag{19}$$

where the reference $x = 0$ is taken at the center of the resonant line of length l (see Fig. 1).

For simplicity, only the first two nonlinear terms of $C_d(v)$, i.e., first-order nonlinearities (ΔC_1) and second-order nonlinearities (ΔC_2) will be considered. Note however that the procedure could be extended to consider different nonlinear dependences if necessary [17].

The term ΔC_2 causes third-order intermodulation products, occurring at $2\omega_1 - \omega_2$ and $2\omega_2 - \omega_1$, referred here as IMD3, whereas the nonlinear term ΔC_1 produces second-order intermodulation products, at $\omega_1 + \omega_2$ and $\omega_2 + \omega_1$, referred here as IMD2, second harmonic at $2\omega_1$ and $2\omega_2(2H)$, and also additional contribution to IMD3 due to the mixing of the second harmonic with the fundamental signals.

A. Second-Order Nonlinearities

Assuming a quadratic nonlinear dependence of the nonlinear distributed capacitance, (12) becomes

$$\Delta C_{NL}(v) = \Delta C_2 v^2. \tag{20}$$

We obtain the IMD3 occurring in a nonlinear acoustic transmission line following a similar procedure to that in [17]. Using (20) into (17), we may write the nonlinear differential current as

$$\frac{\partial i_{nl}(x,t)}{\partial x} = \frac{\partial}{\partial t}\left(\Delta C_2 v(x,t)^3\right) \tag{21}$$

which can be Fourier transformed to obtain the frequency component at ω_i. This results in $\partial I_{nl}(x)/\partial x = j\omega_i F\left(\Delta C_2 v(x,t)^3, \omega_i\right)$ where $F(.,\omega_i)$ indicates the Fourier transform at ω_i.

For the third-order intermodulation $2\omega_1 - \omega_2$ (denoted as ω_{12}), we can write

$$\frac{\partial I_{nl,\omega_{12}}(x)}{\partial x} = \frac{3}{4} V_{\omega_1}^2 V_{\omega_2}^* \left[j\omega_{12}\Delta C_2\right]\cos^3\left(\frac{\pi x}{l}\right). \tag{22}$$

Note that this term might be seen as a current generator distributed along the acoustic line and following a spatial distribution given by the standing-wave pattern at resonance ($\cos(\pi \cdot x/l)$) affected by the order of the nonlinearities resulting in a term $\cos^3(\pi \cdot x/l)$.

This nonlinear source (22) gives rise to a voltage $V_{\omega_{12}}(x)$, whose spatial distribution should match, except for a multiplicative constant, the one at resonance as in (18). Note that this is true as long as the driving frequencies are both at resonance, i.e., $\omega_1 \approx \omega_2 \approx \omega_{12}$.

The voltage $V_{\omega_{12}}(x)$ can be analytically obtained by equating the power generated at ω_{12} (P_{gen}) to the sum of the power dissipated (P_{dis}) in the resonator and loads, and $2\omega_{12}$ times the net reactive stored energy: $P_{gen} = P_{dis} + 2j\omega_{12}(W_m - W_e)$. Since at resonance $W_m \sim W_e$, we can write [17]

$$\frac{1}{2}\int_{-l/2}^{l/2} V_{\omega_{12}}(x) dI^*_{nl,\omega_{12}}(x) dx = \frac{\omega_{12}}{Q_L}\frac{C_{d,0}}{2}\int_{-l/2}^{l/2} V_{\omega_{12}}(x) V^*_{\omega_{12}}(x) dx \quad (23)$$

where Q_L is the loaded quality factor. The voltage at ω_{12} can be written as $V_{\omega_{12}}(x) = V_{\omega_{12}} g_v(x)$ where $g_v(x)$ describes its spatial dependence normalized to a maximum value, and $V_{\omega_{12}}$ is the magnitude to obtain.

Define the normalized stored energy in the resonator $W_{0,v}$ as a function of the maximum voltage $V_{\omega_{12}}$ as

$$W_{0,v} = \frac{C_d}{2}\int_{-l/2}^{l/2} g_v(x) dx \quad (24)$$

and the spatial coefficient $\Gamma_{\omega_{12}}$ as

$$\Gamma_{\omega_{12}} = \frac{1}{2}\int_{-l/2}^{l/2} \cos^3\left(\frac{\pi x}{l}\right) g_v(x) dx. \quad (25)$$

We may substitute (24) and (25) into (23) to obtain $V_{\omega_{12}}$

$$V_{\omega_{12}} = -j\frac{3}{4}\frac{Q_L}{W_{0,V}}\Gamma_{\omega_{12}} V^2_{\omega_1} V^*_{\omega_2} \Delta C_2. \quad (26)$$

Using the assumption $\omega_1 \approx \omega_2 \approx \omega_{12}$, i.e., $g_v(x) = \cos(\pi x/l)$, the normalized stored energy (24) and the spatial coefficient (25) can be analytically obtained as $W_{0,v} = 1/4 \cdot C_{d,0} \cdot l$ and $\Gamma_{\omega_{12}} = 3/16 \cdot l$, respectively. Then, (26) becomes

$$V_{\omega_{12}} = -j\frac{9}{16} Q_L V^2_{\omega_1} V^*_{\omega_2} \frac{\Delta C_2}{C_{d,0}}. \quad (27)$$

Note that this formulation requires that ω_1 and ω_2 be at resonance. In fact, if we consider the resonance frequency as the frequency where the current (or voltage) is maximum, this frequency is slightly shifted to higher frequencies than the $|S_{21}|$ maximum (usually called series resonance) [18]. This is because the acoustic transmission line is loaded by the external components. However, we can assume that both frequencies are close enough to consider $W_e \sim W_m$ and that $v(x,t)$ follows a standing wave pattern as done in (18).

By using conventional network analysis (Appendix I), we obtain the dissipated power to the load $P_{L,\omega_{12}}$ from the maximum voltage into the acoustic transmission line $V_{\omega_{12}}$ (27). From this analysis, we have derived the power dissipated at the load for the case of a two-port FBAR with 50Ω at the source and load ports

$$P_{L,\omega_{12}} = 36 P^2_{0,\omega_1} P_{0,\omega_2} \left(\frac{Q_L}{\omega_{12} W_0}\frac{\beta}{1+2\beta}\right)^4 (\omega_{12}\Delta C_2)^2 \Gamma^2_{\omega_{12}} \quad (28)$$

where $P_{0,\omega 1}$ and $P_{0,\omega 2}$ are the input power at ω_1 and ω_2, respectively, and β is the external coupling coefficient defined as the ratio between the dissipated power at one of the external loads and the dissipated power inside the resonator. This coupling coefficient can be calculated from the scattering parameters as $\beta = |S_{21}|_m/2(1-|S_{21}|_m)$, being $|S_{21}|_m$ the maximum in the frequency response of $|S_{21}|$.

Equations (27) and (28) have been validated by performing harmonic balance simulations with commercial software [19]. The simulated resonator has $l = 2$ μm of AlN thickness and an area of $A = 3500$ μm^2. The maximum of $|S_{21}|$ occurs at 2.7145 GHz (see Fig. 3), which is slightly shifted down from the frequency that gives maximum current ($f_{\max} = 2.719$ GHz) at the ends of the acoustic transmission line ($x = l/2$ and $x = -l/2$ in Fig. 1). The unloaded quality factor Q_0 is set to 970 by loading the ends of the transmission lines with 0.1-mΩ lumped resistances. The nonlinearities are set to $\Delta C_2 = 10^{-7}$ F/(V^2 · m) which corresponds in order of magnitude to the nonlinear Δc_2 reported in [22]. The 2-μm length of the acoustic transmission line is modeled by 160 nonlinear cells like the one in Fig. 2 (minimum 100 cells per half-wavelength are required to obtained accurate results [17]). The resonator is then fed with two 10-dBm tones spaced 1 kHz and centered at 2.7145 GHz. Table I compares the results of the simulations with those from (27) and (28).

From Table I, we see that the agreement is very good although the predicted phase of the voltage differs slightly from the simulated one. If simulations are done at the frequency that gives

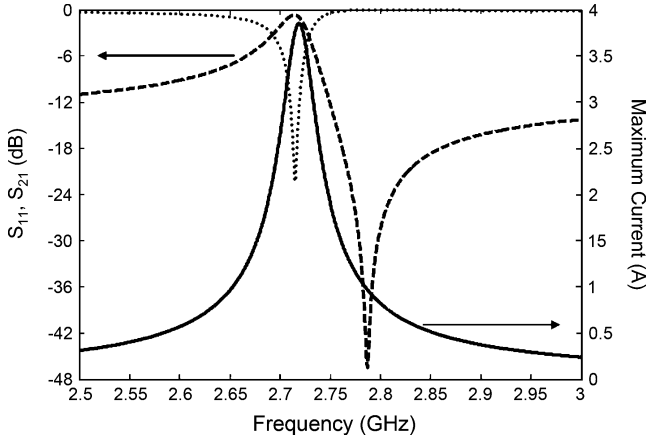

Fig. 3. Left axis: Simulated S_{21} (dashed line) and S_{11} (dotted line) of an AlN-FBAR. Right axis: maximum current reached into the resonator (solid line).

TABLE I
COMPARISON OF (27) AND (28) WITH SIMULATIONS

	Simulation	(27)-(28)	Error
Mag ($V_{\omega 12}$)[V]	6.3 10^{-4}	6.23 10^{-4}	<1.2%
Phase ($V_{\omega 12}$)	13.9°	0.4°	13.5°
$P_{L,\omega 12}$ [dBm]	-48.5	-48.5	<1%

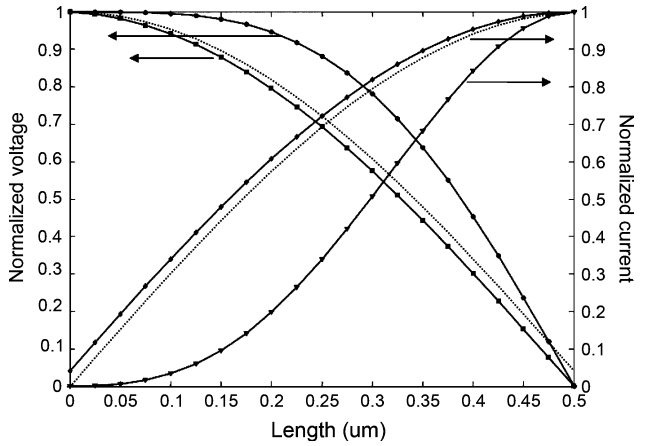

Fig. 4. Voltage (left axis) and current (right axis) distribution in a 1-μm length acoustic transmission line from $x = 0$ to $l/2$ for the fundamental signals (squares) and for the 2H (circles). Dotted line is the distribution corresponding to $\cos(\pi x/l)$ and $\sin(\pi x/l)$.

maximum voltage ($f_{\max} = 2.719$ GHz) the phase error is lower than 0.5°. This small error is due to the assumption $W_e = W_m$ made in our analytical calculations, which does not fully hold in the simulations.

B. First-Order Nonlinearities

For the analysis of the 2H and IMD2 generation, we only consider the first term of Taylor's series expansion of $\Delta C_{NL}(v)$

$$\Delta C_{NL}(v) = \Delta C_1 v. \tag{29}$$

The spurious signals occurring at $2\omega_1$ and $\omega_1 + \omega_2$ by (29) are due to the mixing of the fundamentals at ω_1 and ω_2. On the other hand, the spurious signal at $2\omega_1 - \omega_2$ is due to the mixing of the second harmonic at $2\omega_1$ with the fundamental at ω_2.

1) Second Harmonic and $\omega_1 + \omega_2$ Generation: To obtain the second harmonic, we need to consider the nonlinear current generators at $2\omega_1$ as

$$\frac{\partial I_{nl,2\omega_1}(x)}{\partial x} = \frac{1}{2} V_{\omega_1}^2 \left[j2\omega_1 \Delta C_1\right] \cos^2\left(\frac{\pi x}{l}\right). \tag{30}$$

Unlike in the case described in Section III-A, the nonlinear sources at $2\omega_1$ (30) are weakly coupled to the second resonant mode. This is because the impedance seen at $2\omega_1$ from the center of the acoustic transmission line ($x = 0$ in Fig. 1) to the electrical part of the circuit is very high so the current flowing through the transformer is very small. This high impedance and the symmetrical distribution of the nonlinear sources $\partial I_{nl,2\omega_1}$ along the line, with a maximum at the center of the acoustic line, forces a zero current at $x = 0$ as occurring at the fundamental frequency in the middle of a $\lambda/2$ line with shorts at both ends. Fig. 4 shows the simulated distribution (from $x = 0$ to $x = l/2$) of the voltage and current at ω_1 and $2\omega_1$ in the FBAR assessed in Section III-A with $\Delta C_2 = 0$ and $\Delta C_1 \neq 0$.

The spatial pattern of $V_{2\omega_1}$ results from the combination between the conditions set by the signal generators distributed along the transmission line (30) and the standing wave pattern corresponding to $l = \lambda$. Therefore, since the current at $2\omega_1$ is almost zero at the center of the line, the $\partial I_{nl,2\omega_1}$ generated in a ∂x at $x = 0$ flows directly through the distributed capacitance $C_{d,0}$ (see Fig. 2) generating a voltage drop given by

$$V_{2\omega_1} = -\frac{1}{2} V_{\omega_1}^2 \frac{\Delta C_1}{C_{d,0}}. \tag{31}$$

This is the voltage $V_{2\omega_1}$ that directly couples to the electrical circuit part producing measurable second harmonic at the load.

The same procedure is used for the IMD2 at $\omega_1 + \omega_2$ but replacing the $\partial I_{nl,2\omega_1}$ of (30) by

$$\frac{\partial I_{nl,\omega_1+\omega_2}(x)}{\partial x} = V_{\omega_1} V_{\omega_2} \left[j\left(\omega_1+\omega_2\right)\Delta C_1\right] \cos^2\left(\frac{\pi x}{l}\right) \tag{32}$$

which implies that

$$V_{\omega_1+\omega_2} = -V_{\omega_1} V_{\omega_2} \frac{\Delta C_1}{C_{d,0}} \tag{33}$$

that is, the dissipated power at the load at $\omega_1 + \omega_2$ should be 6 dB greater than that at $2\omega_1$ if the source signals ω_1 and ω_2 are kept balanced ($V_{\omega_1} = V_{\omega_2}$).

The power coupled to the load is obtained by analyzing the linear circuit at $2\omega_1$ (or $\omega_1 + \omega_2$ adding 6 dB) as described in Appendix I, resulting in

$$P_{L,2\omega_1} = 2Z_g \left(\frac{Q_L}{\omega_1 W_{0,v}} \frac{\beta}{1+2\beta}\right)^2 P_{0,\omega_1}^2 \left(\frac{\Delta C_1}{C_{d,0}}\right)^2 \frac{1}{|\phi_{2\omega_1} Z_{2\omega_1}|^2} \tag{34}$$

where Z_g is the source and load impedance, $\phi_{2\omega 1}$ is (4) evaluated at $2\omega_1$, and $Z_{2\omega 1}$ is given by (48). The normalized energy will be $W_{0,v} = 1/4\, C_{d,0} l$.

Expressions (31), (33), and (34) have been validated by performing harmonic balance simulations [19], using the FBAR described in Section III-A, where the nonlinear terms are now $\Delta C_2 = 0$ and $\Delta C_1 = 10^{-5}$ F/(V · m). Comparison between simulated results and closed-form expressions are summarized in Table II, showing very good agreement.

2) Third-Order Intermodulation Product $2\omega 1 - \omega 2$: The results of mixing the spurious signal at $2\omega_1$ (and $2\omega_2$) with the fundamental signal at ω_2 (and ω_1) give rise to IMD3 at $2\omega_1 - \omega_2$ (and $2\omega_2 - \omega_1$), both within the resonance band of the FBAR structure. We have checked that no other components like $\omega_1 - \omega_2$ contribute significantly to the IMD3 since the voltages reached inside the resonator at these low frequencies are very low.

TABLE II
VALIDATION OF (31), (33), AND (34) WITH SIMULATIONS

	Simulation	(31),(33),(34)	Error
Mag ($V_{2\omega l}$)[V]	1.6 10^{-3}	1.6 10^{-3}	<0.1%
Phase ($V_{2\omega l}$)	1.9°	1.7°	0.2°
Mag ($V_{\omega l+\omega 2}$)[V]	3.2 10^{-3}	3.2 10^{-3}	<0.2%
Phase ($V_{\omega l+\omega 2}$)	1.7°	1.7°	<0.1°
$P_{2\omega l}$ [dBm]	-62.8	-63.0	<0.3%
$P_{\omega l+\omega 2}$ [dBm]	-56.8	-57.0	<0.4%

The equation for the third-order intermodulation distortion produced by a first-order nonlinear effect can be derived following steps similar to those used in Section III-A. In this case, the nonlinear sources are

$$\frac{\partial I_{nl,\omega_{12}}(x)}{\partial x} = j\omega_{12}\Delta C_1 V_{2\omega_1}(x)\, V_{\omega_2}^{*} \cos\left(\frac{\pi x}{l}\right) \tag{35}$$

where $V_{2\omega_1}(x)$ is a standing wave pattern described by a function $f_{2\omega_1}(x)$ which resembles a cosine function as shown in Fig. 4. Its maximum value $V_{2\omega_1}$ is given by (31).

As done in Section III-A, we equate the power generated at ω_{12} with the power dissipated using (23). This results in

$$V_{\omega_{12}} = j\frac{1}{2}\frac{Q_L}{W_0}\Gamma'_{\omega_{12}} V_{\omega_1}^2 V_{\omega_2}^{*} \frac{(\Delta C_1)^2}{C_{d,0}} \tag{36}$$

where $\Gamma'_{\omega_{12}} = 1/2\int_{-l/2}^{l/2} f_{2\omega_1}(x)\cos^2(\pi x/l)\,dx$ and $W_0 = 1/4C_{d,0}\cdot l$.

We can also write this equation as

$$V_{\omega_{12}} = j\gamma_{\omega_{12}}\frac{4}{3\pi}Q_L V_1^2 V_2^{*}\left(\frac{\Delta C_1}{C_d}\right)^2 \tag{37}$$

where the factor $\gamma_{\omega_{12}}$ is defined by

$$\gamma_{\omega_{12}} = \frac{\Gamma'_{\omega_{12}}}{\dfrac{1}{2}\displaystyle\int_{-l/2}^{l/2}\cos^3\left(\frac{\pi x}{l}\right)dx}. \tag{38}$$

The term $\gamma_{\omega_{12}}$ quantifies the error assuming that the second harmonic follows the standing-wave pattern at $2\omega_1$, i.e., $f_{2\omega_1}(x) = \cos(\pi x/l)$ (see Fig. 4). We have numerically evaluated (38) for several examples being $\gamma_{\omega_{12}}$ always less than 1.15. Therefore, the error will be within 15% if the approximation $f_{2\omega_1}(x) = \cos(\pi x/l)$ is used to avoid numerical procedures.

Again we are interested in obtaining the dissipated power to the load. In this case, we can write (see Appendix I)

$$P_{L,\omega_{12}} = 64P_{0,\omega_1}^2 P_{0,\omega_2}\left(\frac{Q_L}{\omega_{12}W_{0,v}}\frac{\beta}{1+2\beta}\right)^4 \times (\omega_{12}\Delta C_1)^2\,\Gamma'^2_{\omega_{12}}\left(\frac{\Delta C_1}{2C_{d,0}}\right)^2. \tag{39}$$

It is remarkable to note that the power of the IMD3 generated by a nonlinear model of first-order (39) can be larger than the measured power 2H or IMD2 (34). For example, the ratio between maximum voltages at IMD3 and 2H results in

$$\left|\frac{V_{\omega_{12}}}{V_{2\omega_1}}\right| = \gamma_{\omega_{12}}\frac{8}{3\pi}Q_L\left|V_{\omega 2}\right|\left(\frac{\Delta C_1}{C_d}\right). \tag{40}$$

From (40), we see that the ratio between IMD3 and 2H is proportional to the fundamental signal $V_{2\omega_1}$, the nonlinear coefficient ΔC_1, and the loaded quality factor. This is because, unlike 2H signals, the IMD3 spurious signals are at resonance, so their amplitude is affected by the quality factor of the resonator.

Again we use circuit simulations [19] to validate (37) and (39). Table III summarizes the comparison between simulated values and the values obtained analytically, showing good agreement. In this case, $\gamma_{\omega_{12}}$ (38) has also been numerically solved resulting in $\gamma_{\omega_{12}} = 1.11$, therefore $\Gamma'_{\omega_{12}} = 1.11\cdot 2/3\pi\cdot l$.

TABLE III
VALIDATION OF (37) AND (39) WITH SIMULATIONS

	Simulation	(37),(39)	Error
Mag ($V_{\omega 12}$)[V]	7.48 10^{-4}	7.36 10^{-4}	<1.7%
Phase ($V_{\omega 12}$)	-165.2°	-179.1°	<14°
$P_{L,\ \omega 12}$ [dBm]	-47.1	-47.0	<0.2%

Note than the IMD3 is 10 dB higher than the IMD2 (see Table II) despite the fact that we are only considering nonlinear effects due to first-order nonlinearities.

IV. Experimental Results

The following section uses the circuit model and the closed-form expressions presented in Sections II and III to extract the nonlinear material parameters of a BAW resonator from measurements of the spurious signals at IMD3, IMD2, and 2H.

A. Test Device

The FBAR resonator tested has a 1-μm-thick aluminum nitride (AlN) membrane having an area of 4000 μm^2. The electrodes are made of titanium (30 nm thick) and platinum (150 nm thick). All materials are deposited onto a silicon substrate. Fabrication details are given in [20]. The resulting resonant frequency is around 2.3 GHz.

B. Scattering Parameters and Linear Circuit Model

A preliminary fitting of the linear response (scattering parameters) is required for a proper modeling and characterization of the nonlinear effects occurring in the FBAR presented above. To do that, we measured the scattering parameters from 2 to 6 GHz to include the fundamental resonance and second harmonic frequencies in the analysis. The input power was fixed to -10 dBm to ensure that the FBAR is operating in linear regime, and we performed on-wafer line-reflect-reflect-match calibrations [21]. Fig. 5 depicts the frequency response of the transmission (S_{21}) and reflection coefficient (S_{11}), for a narrow frequency range (from 2.2 to 2.4 GHz).

The effective electromechanical coupling coefficient is $\kappa = 2.2\%$ and the loaded quality factor is $Q_L = 60$ at the resonance (maximum S_{21}), and $Q_L = 350$ at the antiresonance (minimum S_{21}). This low Q_L causes high insertion losses which are incremented by the parasitic effects of the pads [20].

Fig. 6 shows the proposed linear model containing parasitic elements to account for the substrate and pads [20]. The FBAR is modeled using the KLM model (Fig. 1) and the acoustic transmission line is divided into 160 cells containing the distributed linear and nonlinear parameters, like that in Fig. 2. The acoustic line is loaded with two transmission line sections at each side modeling the electrodes. These two transmission lines have a significant impact on the FBARs resonance frequency but we will consider that these electrodes do not contribute to the nonlinearities since the titanium and the platinum have a much more linear strain–stress curve than the AlN [22]. For simplicity, each

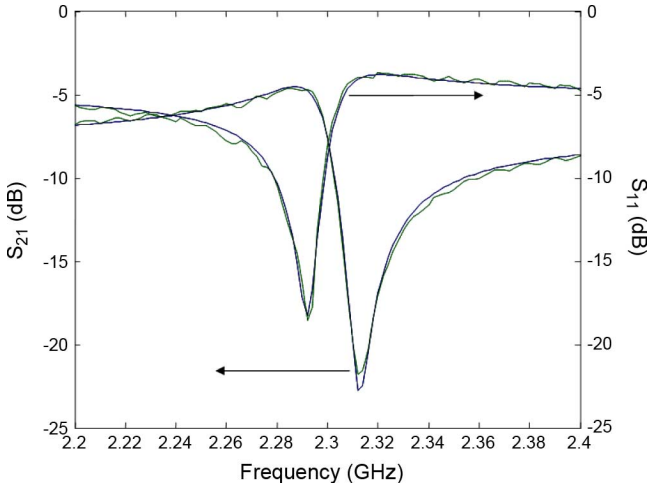

Fig. 5. Simulated (dotted) and measured (solid line) scattering parameters.

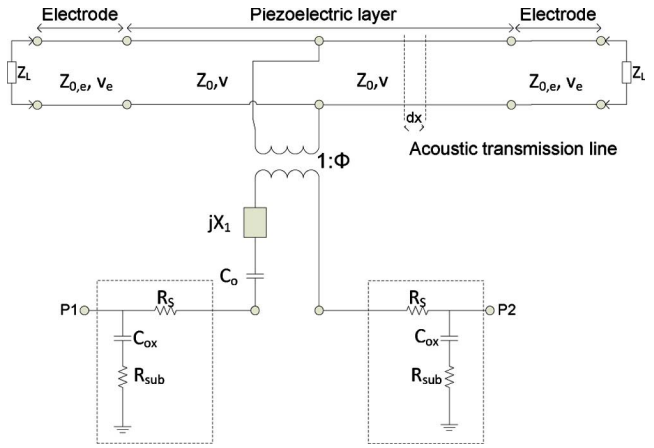

Fig. 6. KLM equivalent circuit including electrodes and parasitic elements (R_s, C_{ox}, and $R_{\rm sub}$).

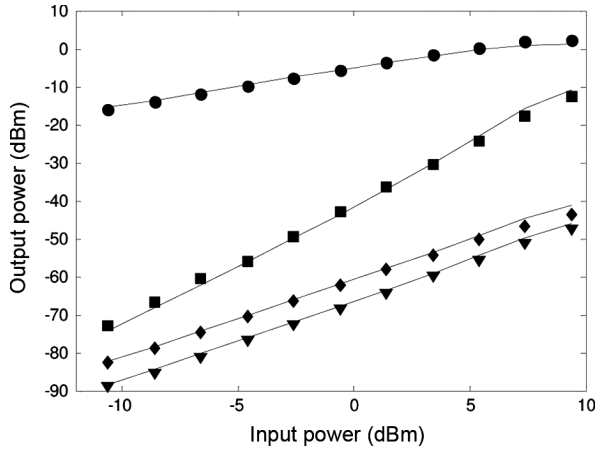

Fig. 7. Measured output power at resonance frequency versus input power for: fundamental power (circles), IMD3 (squares), IMD2 (diamonds), and 2H (triangles). The solid lines represent the simulated results of Section IV-D.

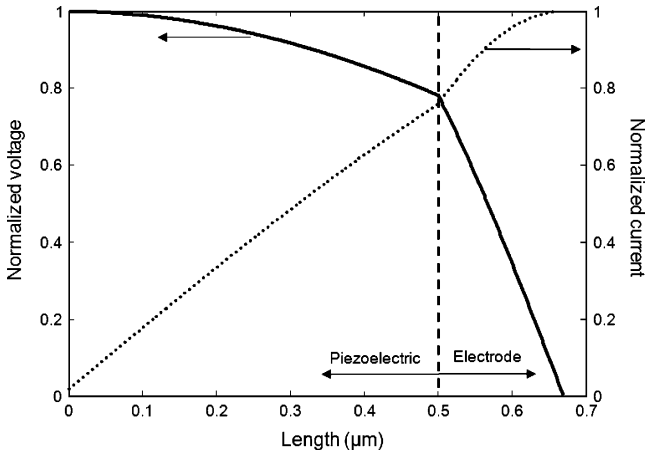

Fig. 8. Normalized current (dotted) and voltage (solid) distribution along the acoustic transmission line: piezoelectric layer and electrode (see Fig. 6).

180-nm Ti/Pt electrode is modeled as a unique linear transmission line with $v_p = 3440$ m/s and $Z_0 = 0.207\ \Omega$, which is additionally loaded by a lumped resistor whose value is higher than that of the air impedance, and accounts for acoustic losses.

The values of the circuital components are adjusted by using optimization routines to fit the measured scattering parameters especially at frequencies close to resonance. Fig. 5 shows the frequency response of the simulated circuit model of Fig. 6 and the measurements.

The acoustic losses are modeled with $Z_L = 4 \cdot 10^{-4}\ \Omega$ at the ends of the electrodes and the values of the parasitic elements are $R_s = 9.8\ \Omega$, $R_{\rm sub} = 282\ \Omega$ and $C_{ox} = 9$ pF. These parasitic elements are consistent with those extracted from other resonators on the same wafer [11].

C. Nonlinear Characterization

To characterize the nonlinear response of our device under test (Fig. 6), we performed intermodulation and second harmonic measurements. For these experiments, we kept both sources balanced in power (i.e., $P_{0,\omega 1} = P_{0,\omega 2}$) and swept their powers from -10 to -10 dBm. Both tones ω_1 and ω_2 are set at resonance with a frequency spacing $\Delta f = f_2 - f_1$ ranging from $\Delta f = 100$ Hz to $\Delta f = 1$ MHz. From these experiments, we obtain the output power of IMD2 $(\omega_1 + \omega_2)$, IMD3 $(2\omega_1 - \omega_2$ and $2\omega_2 - \omega_1)$, and 2H $(2\omega_1$ and $2\omega_2)$ as a function of the input power of the fundamental signal. The dependence of the spurious signals on the fundamental tone frequency spacing (Δf) is also evaluated.

Fig. 7 outlines the measured spurious and fundamental signals, when the two fundamental tones are centered at 2.292 GHz (resonance frequency) and 100 Hz apart. The slope of the fundamental tones is $1:1$ in log–log scale up to $+8$ dBm, indicating that saturation effects do not occur. As one may expect from (28) or (39), and (34), the measured power dependence of IMD3 is $3:1$ (in log–log scale), and $2:1$ (in log–log scale) for 2H and IMD2.

Next, we extract the nonlinear capacitance $\Delta C(v)$ that fits the measurements. We first extract ΔC_1 from the measured 2H and IMD2 experiments using (34); we evaluate if the IMD3 is consistent with this ΔC_1 using (39), and if not, we obtain ΔC_2 using (28).

The parasitic elements will be considered as part of the resonator in order to apply the formulation based on the analysis of

resonators for the third-order intermodulation. See Appendix II for further details.

1) Second Harmonic 2H and IMD2: We use (34) to obtain the value of ΔC_1 that better fits the 2H dissipated power at the external load $Z_g = 50\ \Omega$. To do that, we first obtain: $\phi_{2\omega_1} = 0.59$ and $Z_{2\omega_1} = 123 - j82\ \Omega$ using (4) and (51), respectively, from the fitted parameters, $C_{d,0} = 6.44 \cdot 10^{-4}$ F/m from the properties of the material, $\beta = 0.665$ using $\beta = |S_{21}|/2(1 - |S_{21}|)$ [24], and $Q_L = 58$ using $Q_L = (\omega_0/2) \cdot d\varphi/d\omega_0$ [25], where φ is the phase of S_{21}.

To calculate the normalized energy $W_{0.v}$, we need to know the standing wave pattern in the acoustic transmission line for the fundamental frequencies. Fig. 8 shows this distribution for the voltage and current along the acoustic line and the electrodes. Since the distributions of Fig. 8 do not follow a cosine function, we need evaluate (24) numerically to obtain $W_{0,v}$ (see Appendix II for more details). This results in $W_{0,v} = 1.54 \cdot 1/4 \cdot C_{d,0} \cdot d_T$, that is, a value 54% larger than the value we would obtain if we would consider an acoustic transmission line of total length d_T, where d_T is the thickness of piezoelectric plus electrodes.

Using (34), we find a value of ΔC_1 that fits a measured point of Fig. 7. We obtain $\Delta C_1 = 1.1 \cdot 10^{-5}$ F/(Vm). This value also fits the measured IMD2 since the measured value $P_{L,\omega 1+\omega 2}$ is 6 dB larger than $P_{L,2\omega 1}$.

2) IMD3 From First Order Nonlinearities (ΔC_1): Applying the value of $\Delta C_1 = 1.1 \cdot 10^{-5}$ F/(Vm) obtained above into (39) and using $\Gamma'_{\omega_{12}} \sim 2/3\pi \cdot l$, we obtain an IMD3 output power of $P_{L,\omega_{12}} \sim -120$ dBm, which is much smaller than the measured value. This indicates that the IMD3 cannot be only due to ΔC_1 and there must be an additional contribution due to ΔC_2.

3) IMD3 From Second-Order Nonlinearities (Δc_2): Now we use (28) to extract ΔC_2 from the measured IMD3. In this case, the geometrical factor $\Gamma_{\omega_{12}}$ is calculated using (25) from the voltage shown in Fig. 8. Only nonlinear contributions from the piezoelectric layer are considered, since we assume that the electrodes do not contribute to the nonlinearities. This results in $\Gamma_{\omega_{12}} = 2.01 \cdot 3 \cdot d/16$, where d is the piezoelectric thickness. Doing so we obtain $\Delta C_2 = 2.5 \cdot 10^{-5}$ F/(V^{2}m), and the resulting nonlinear capacitance is $\Delta C_{NL}(v) = 1.1 \cdot 10^{-5} v + 2.5 \cdot 10^{-5} v^2$.

D. CAD-Based Nonlinear Characterization

To validate the data obtained from closed-form expressions, we have found $\Delta C_{NL}(v)$ by fitting the measured data to computer-aided design (CAD) simulations of the equivalent circuit [19]. These simulations are not subject to the simplifying assumptions made in the derivation of (28), (34), and (39). Furthermore, they can easily account for changes in the equivalent circuit due to electrodes and other extraneous elements. For example, the equivalent circuit may be easily modified from that in Fig. 1 to the one in Fig. 6 to include the effect of the electrodes.

Using the same input power than in Section IV-C as a fitting point, we obtain $\Delta C_{NL}(v) = 1.2 \cdot 10^{-5} v + 2.3 \cdot 10^{-5} v^2$, which is within a 8% error in both ΔC_1 and ΔC_2. This agreement indicates that (28) and (34) are quite general as long as the parasitic effects and electrodes are considered when evaluating some terms used in these equation (see details in Appendix II). Fig. 7 shows the measured and simulated results with these extracted nonlinear parameters versus input power.

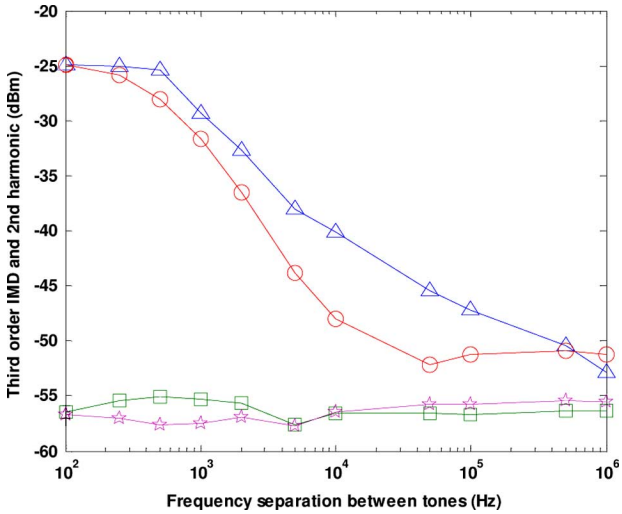

Fig. 9. IMD3 and 2H output power as a function of the tone spacing Δf for an input power of +5.5 dBm. Triangles correspond to $2\omega_1 - \omega_2$, circles to $2\omega_2 - \omega_1$, squares to $2\omega_1$, and stars to $2\omega_2$.

V. Discussion and Further Experiments

The nonlinear coefficients extracted from the measurements ΔC_1 and ΔC_2 can then be related with the material nonlinear parameter $\Delta c_{NL}^D(v)$ through (13) and (14). From (13), we obtain $\Delta C_1 = 1.1 \cdot 10^{-5}$ F/(Vm) and the value of the first-order nonlinear elastic stiffness $\Delta c_1^D = 26.5$. This value is six times greater than that reported in [22], which was obtained from the simulations of mechanical displacements.

Using (14) with $\Delta c_2 = 2.3 \cdot 10^{-5}$ F/(V^{2}m), we obtain the second-order nonlinear elastic stiffness $\Delta c_2^D = -2.1 \cdot 10^{-7}$ N^{-1}m^2. This value is three orders of magnitude greater than the one reported in [22]. In fact the value reported in [22] would not be measurable doing IMD experiments since the IMD3 generated by ΔC_1 would be greater than that generated by such small ΔC_2. The difference between measured and reported results suggests the existence of other causes for the second-order nonlinear effects.

In order to further investigate the nonlinear effects, we performed additional IMD and 2H measurements versus the frequency spacing between the fundamental tones $\Delta f = f_2 - f_1$. The dependence of IMD power level on the frequency spacing between tones is an indication of dependence with the period of the envelope, and may give additional information to discern between different sources of nonlinear effects.

Fig. 9 depicts the IMD3, IMD2, and 2H as a function of the frequency spacing for an input power of +5.5 dBm. While 2H and IMD2 show to be independent of the frequency spacing, that is a constant value of Δc_1^D, IMD3 decreases when the frequency spacing increases, which would result in Δc_2^D depending on the frequency spacing between the input tones. This later effect is not considered in the circuit model presented in this paper.

The observed IMD3 dependence on the frequency spacing between the fundamental tones and the difference in the extracted quadratic nonlinear stiffness Δc_2^D is an added indication that

additional sources may contribute to the second-order nonlinear circuit term $\Delta C_2 v^2$ such as, for example, thermal effects. In addition, Fig. 9 shows asymmetries between the lower and upper ($2\omega_1 - \omega_2$ and $2\omega_2 - \omega_1$) intermodulation products. This behavior is also characteristic of self-heating effect as shown in [23] which is consistent with the low quality factor of the device. Note that as pointed out before, the stiffened elasticity (10) used in this model fails to predict these thermal effects.

VI. Conclusion

In this paper, we present a novel nonlinear distributed equivalent circuit based on the KLM model. Our new model is useful to account for the linear and nonlinear behavior of BAW resonators in a broad frequency band. We have used it to obtain closed-form expressions for the most relevant nonlinear effects: intermodulation distortion and second harmonic generation. We have checked these expressions with equivalent circuit simulations using harmonic balance techniques.

We have shown that the new equivalent circuit can be easily modified to model the effects of the electrodes and other parasitic elements existing in FBAR. With this modified version of the equivalent circuit, we are able to fit the linear and nonlinear measurements in an FBAR (i.e., s-parameters, intermodulation distortion, and second harmonic generation). The measurements can be fitted to the closed-form expressions for intermodulation distortion and second harmonic generation derived in the paper.

Once the model is fitted to the measurements, we can extract the nonlinear material parameters. The value obtained for Δc_1^D is consistent in order of magnitude with the ones reported in the literature, whereas the Δc_2^D gives a larger value than the ones reported. We suggest that this disagreement on Δc_2^D is because there are other nonlinear effects contributing to the IMD3 generation such as self-heating mechanisms.

The work presented in this paper may now be used in the following aspects.

1) The equivalent circuit could also be used as a basic building block to model more complex devices, such as filters containing several resonators.
2) Evaluation of additional nonlinear effects, such as saturation or detuning, which may also be performed by simulating the equivalent circuit proposed.
3) Inclusion of other nonlinear sources in the model. For example, a nonlinear viscosity could be considered adding a shunted nonlinear distributed conductance to the nonlinear transmission line in the model.
4) Extension of the model to consider self-heating mechanisms.

Although the proposed circuit model has been particularly developed for FBARs with longitudinal propagating wave, this can be generally used for modeling the nonlinear performance in other BAW devices using other propagating modes, for example, quartz crystal resonator operating at the shear mode or even surface acoustic wave resonators, being therefore useful in other applications beyond the scope of this paper.

Appendix I
IMD and 2H Power Coupled to the Load

The power coupled to the load connected at port 2 (Fig. 1) at ω_{12}, $P_{L,\omega_{12}}$, can be written as

$$P_{L,\omega_{12}} = \beta P_{res,\omega_{12}} \tag{41}$$

where $\beta = |S_{21}|/2(1-|S_{21}|)$ [24] and P_{res,ω_2} is the dissipated power into the resonator. Then, (41) can be written as a function of the unloaded quality factor Q_0 and the normalized stored energy $W_{0,v}$ as

$$P_{L,\omega_{12}} = \beta \omega_{12} \frac{W_{0,v}}{Q_0} |V_{\omega_{12}}|^2 . \tag{42}$$

The dissipated power into the resonator at the fundamental frequency ω_i is given by

$$P_{res,\omega_i} = 4P_{0,\omega_i} \frac{\beta}{(1+2\beta)^2} \tag{43}$$

where P_{0,ω_i} is the incident power to the resonator. The maximum voltage at ω_i results in

$$|V_{\omega_i}|^2 = 4P_{0,\omega_i} \frac{Q_L}{\omega_i W_{0,v}} \frac{\beta}{(1+2\beta)}. \tag{44}$$

For second-order nonlinearities (ΔC_2), replacing (44) into (26) and the resulting $V_{\omega_{12}}$ into (42), the IMD3 load power gives

$$P_{L,\omega_{12}} = 36 P_{0,\omega_1}^2 P_{0,\omega_2} \left(\frac{Q_L}{\omega_{12} W_0} \frac{\beta}{1+2\beta} \right)^4 (\omega_{12} \Delta C_2)^2 \Gamma_{\omega_{12}}^2 . \tag{45}$$

The IMD3 coupled to the load for first-order nonlinearities (ΔC_1) is calculated using (44), (42), and (36)

$$P_{L,\omega_{12}} = 64 P_{0,\omega_1}^2 P_{0,\omega_2} \left(\frac{Q_L}{\omega_{12} W_{0,v}} \frac{\beta}{1+2\beta} \right)^4 \times (\omega_{12} \Delta C_2)^2 \Gamma'^2_{\omega_{12}} \left(\frac{\Delta C_1}{2C_d} \right)^2 . \tag{46}$$

Note that this formulation is based on the definition of the quality factor Q_L and the coupling coefficient β and it does not depend on the origin of the losses. Therefore, it can be used to account for losses modeled as lumped resistances at the ends of the acoustic transmission line, or for acoustic distributed losses which could be modeled adding a series distributed resistance and/or a shunted distributed conductance in the elemental segment of Fig. 2.

The maximum voltage $V_{2\omega_1}$ at the center of the acoustic transmission line is coupled to the electrical part of the circuit through the transformer 1: ϕ (see Fig. 1) resulting in a electrical voltage $V_{2\omega_1}/\phi_{2\omega_1}$, thus the current at $2\omega_1$ flowing to the source impedance and load will be

$$I_{L,2\omega_2} = \frac{V_{2\omega_1}}{\phi_{2\omega_1}} \frac{1}{Z_{2\omega_1}} \tag{47}$$

where $\phi_{2\omega_1}$ corresponds to (4) evaluated at $2\omega_1$ and $Z_{2\omega_1}$

$$Z_{2\omega_1} = 2Z_g + jX_{2\omega_1} + \frac{1}{j2\omega_1 C_0} \tag{48}$$

with $X_{2\omega_1}$ obtained from (6) at $2\omega_1$. Therefore, the dissipated power at the load Z_g will be

$$P_{L,2\omega_1} = \frac{1}{2} Z_g \left|V_{2\omega_1}\right|^2 \frac{1}{\left|\phi_{2\omega_1} Z_{2\omega_1}\right|^2} \tag{49}$$

which, by using (49), (44), and (31), can be written as

$$P_{L,2\omega_1} = 2Z_g \left(\frac{Q_L}{\omega_1 W_{0,v}} \frac{\beta}{1+2\beta}\right)^2 P_{0,\omega_1}^2 \left(\frac{\Delta C_1}{C_{d,0}}\right)^2 \frac{1}{\left|\phi_{2\omega_1} Z_{2\omega_1}\right|^2}. \tag{50}$$

Appendix II
Parasitic and Electrode Effects

The parasitic elements may be included as part of the resonator, by using as a quality factor the one obtained from measurements instead of the inherent quality factor of the resonator. The term $Q_L(1+2\beta)/\omega W$ accounts for the acoustic power dissipated in the resonator plus the power dissipated in the parasitic resistances. Note that this does not affect (45) and (46) since the parasitic elements are included in the coupling coefficients and quality factor of the whole device.

However, for the second harmonic power calculation, we need to consider the parasitic elements in the circuit analysis. The electrical voltage $V_{2\omega_1}/\phi_{2\omega_1}$ causes a current $I_{L,2\omega_1}$ flowing to the load impedance following (47), although in this case, the impedance $Z_{2\omega_1}$ does not follow (48) and it is obtained by conventional circuit analysis of the electrical part of the device including the electrodes (see Fig. 6). This results in

$$Z_{2\omega_1} = \frac{Z_g\left(Z_g + Z_p\right)}{Z_g Z_p}\left(2\frac{Z_g Z_p}{Z_g + Z_p} + 2R_s + jX_{2\omega_1} + \frac{1}{j2\omega_1 C_0}\right) \tag{51}$$

where $Z_p = R_{sub} + 1/(j2\omega_l C_{ox})$.

In addition, the electrodes may have a significant impact in the spatial distribution of the voltage and current inside the resonator as shown in Fig. 8, so these spatial current and voltage distributions must be considered for the calculation of the normalized energy $W_{0,v}$.

The electrical energy $W_{0,e}$ corresponding to (25) for an ideal acoustic transmission line will be in this case

$$W_{0,e} = \frac{1}{2}\left(C_{d,p}\int_0^{d_p/2} g_{v,p}(x)dx + C_{d,e}\int_{d_p/2}^{d_p/2+d_e} g_{v,e}(x)dx\right) \tag{52}$$

where C_d, $g_v(x)$ and d are the distributed conductance, normalized voltage distribution and layer thickness, respectively, and the sub index "p" and "e" denote piezoelectric layer and electrode, respectively.

The normalized magnetic energy will be

$$W_{0,m} = \frac{1}{2\left|Z_{0,\text{equiv}}\right|^2} \times \left(L_{d,p}\int_0^{d_p/2} g_{i,p}(x)dx + L_{d,e}\int_{d_p/2}^{d_p/2+d_e} g_{i,e}(x)dx\right) \tag{53}$$

where g_i indicates the normalized spatial current distribution. $Z_{0,\text{equiv}}$ is the ratio of maximum voltage and maximum current in a acoustic line loaded with electrodes. This constant can be calculated using conventional microwave analysis of the loaded transmission lines

$$Z_{0,\text{equiv}} = j\left(Z_{0,e}\sin\varphi_e\cos\varphi_p + Z_{0,p}\cos\varphi_e\sin\varphi_p\right) \tag{54}$$

where Z_0 and φ are the characteristic impedance and electrical length, respectively.

The normalized energy $W_{0,v}$ will be then

$$W_{0,v} = W_{0,e} + W_{0,m}. \tag{55}$$

Acknowledgment

The authors would like to thank H. Campanella from the Centre National de Microelectrónica (CNM-CSIC) for providing the FBAR used in this work.

References

[1] K. M. Lakin, "Thin film resonator technology," *IEEE Trans. Ultrason. Ferroelectr. Freq. Control*, vol. 52, no. 5, pp. 707–716, May 2005.
[2] M. Planat and D. Hauden, "Nonlinear properties of bulk and surface acoustic waves in piezoelectric crystals," *Ferroelectrics*, vol. 42, pp. 117–136, 1982.
[3] D. A. Hall, "Nonlinearity in piezoelectric ceramics," *J. Mater. Sci.*, vol. 36, pp. 4575–4601, 2001.
[4] H. F. Tiersten, "Analysis of intermodulation in rotated Y-cut quartz thickness-shear resonators," in *Proc. 28th Annu. Symp. Freq. Control*, 1974, pp. 1–4.
[5] J. Nosek and L. Burianova, "About nonlinear effects in the quartz homeotypes single crystals," in *Proc. IEEE Freq. Control Symp.*, May 2008, pp. 586–591.
[6] J. Nosek, "A precise measurement of some nonlinear effects and its application to the evaluation of nonlinear elastic constants of quartz and GaPO4," *Rev. Sci. Instrum.*, vol. 68, no. 8, pp. 3143–3149, Aug. 1997.
[7] L. Dworsky and R. G. Kinsman, "A simple single model for quartz crystal resonator low level drive sensitivity and monolithic filter intermodulation," *IEEE Trans. Ultrason. Ferroelectr. Freq. Control*, vol. 41, no. 2, pp. 261–268, Mar. 1994.
[8] R. Aigner, N.-H. Huynh, M. Handtmann, and S. Marksteiner, "Behavior of BAW devices at high power levels," in *IEEE MTT-S Int. Microw. Symp. Dig.*, Jun. 2005, pp. 12–17.
[9] M. Ueda, M. Iwaki, T. Nishihara, Y. Satoh, and K.-Y. Hashimoto, "A circuit model for nonlinear simulation of radio-frequency filters using bulk acoustic wave resonators," *IEEE Trans. Ultrason. Ferroelectr. Freq. Control*, vol. 55, no. 4, pp. 849–856, Apr. 2008.
[10] K. S. Van Dyke, "The piezo-electric resonator and its equivalent network," *Proc. IRE*, vol. 16, no. 6, pp. 742–764, Jun. 1928.
[11] E. Rocas, C. Collado, J. Mateu, H. Campanella, and J. M. O'Callaghan, "Third order intermodulation distortion in film bulk acoustic resonators at resonance and antiresonance," in *IEEE MTT-S Int. Microw. Symp. Dig.*, Jun. 2008, pp. 1259–1262.
[12] Y. Cho and J. Wakita, "Nonlinear equivalent circuits of acoustic devices," in *Proc. IEEE Ultrason. Symp.*, Nov. 1993, vol. 2, pp. 867–872.
[13] E. Rocas, C. Collado, A. Padilla, J. Mateu, and J. M. O'Callaghan, "Nonlinear distributed model for IMD prediction in BAW resonators," in *Proc. IEEE Int. Ultrason. Symp.*, Nov. 2008, pp. 1557–1560.
[14] R. Krimholtz, D. A. Leedom, and G. L. Matthaei, "New equivalent circuits for elementary piezoelectric transducers," *Electron. Lett.*, vol. 6, no. 13, pp. 398–399, Jun. 1970.
[15] B. A. Auld, *Acoustic Fields and Waves in Solids*. Malabar, FL: Krieger, 1990, vol. I.
[16] J. Enlund, V. Yantchev, and I. Katardjiev, "4E-6 electric field sensitivity of thin film resonators based on piezoelectric AlN thin films," in *Proc. IEEE Int. Ultrason. Symp.*, Oct. 2006, pp. 468–471.
[17] C. Collado, J. Mateu, and J. M. O'Callaghan, "Analysis and simulation of the effects of distributed nonlinearities in microwave superconducting devices," *IEEE Trans. Appl. Supercond.*, vol. 15, no. 1, pp. 26–39, Mar. 2005.
[18] T. F. Hueter and R. H. Bolt, *Sonics: Techniques for the Use of Sound and Ultrasound in Engineering and Science*. New York: Wiley, 1955.

[19] Agilent Technologies, Advanced Design System, 2006 [Online]. Available: www.agilent.com
[20] H. Campanella, P. Nouet, A. Uranga, P. de Paco, N. Barniol, and J. Esteve, "Automated on-wafer extraction of equivalent-circuit parameters in thin-film bulk acoustic wave resonators and substrate," *Microw. Opt. Technol. Lett.*, vol. 50, no. 1, pp. 4–7, 2008.
[21] F. Purroy and L. Pradell, "New theoretical analysis of the LRRM calibration technique for vector network analyzers," *IEEE Trans. Instrum. Meas.*, vol. 50, no. 5, pp. 1307–1314, Oct. 2001.
[22] S. P. Lepkowski and G. Jurczak, "Nonlinear elasticity in III–N compounds: Ab initio calculations," *Phys. Rev. B, Condens. Matter*, vol. 72, 2005, 245201.
[23] J. R. Wilkerson, K. G. Gard, A. G. Schuchinsky, and M. B. Steer, "Electro-thermal theory of intermodulation distortion in lossy microwave components," *IEEE Trans. Microw. Theory Tech.*, vol. 56, no. 12, pp. 2717–2725, Dec. 2008.
[24] M. J. Lancaster, *Passive Microwave Devices Applications of High Temperature Superconductors*. Cambridge, U.K.: Cambridge Univ. Press, 1997.
[25] K. M. Lakin, "Equivalent circuit modeling of stacked crystal filters," in *Proc. 35th Annu. Freq. Control Symp.*, 1981, pp. 257–262.

Carlos Collado (M'03) received the Telecommunication Engineering and Ph.D. degrees from Universitat Politècnica de Catalunya (UPC), Barcelona, Spain, in 1995 and 2001, respectively, and the M.S. degree in biomedical engineering from UPC in 2002.

In 2001, he was awarded a prize for the best doctoral thesis in electronics and telecommunications area from UPC. He joined the faculty at UPC in 1998 and became an Associate Professor in 2005. From November 2005 to January 2008, he was a Vice Dean of the Technical School of Castelldefels (EPSC-UPC), responsible for the telecommunication and aeronautic engineering degrees. He was a visiting researcher at the University of California Irvine in 2004. His primary research interests include microwave devices and systems.

Eduard Rocas (S'07) was born in Palafrugell, Catalonia, Spain, in 1982. He received the Telecommunication Engineering degree from the Universitat Politècnica de Catalunya (UPC), Barcelona, Spain, in 2005, where his final project was associated with the creation of the intelligent communications and avionics for robust unmanned aerial systems (ICARUS) research group. Currently, he is working towards the Ph.D. degree at UPC focusing his research on new materials and structures for novel RF/MW devices.

From September 2005 to July 2006, he was involved in the simulation and modeling of advanced SONARs at the Computer Vision and Robotics Group (VICOROB), University of Girona, as a FPU Grant Holder.

Jordi Mateu (M'03) received the Telecommunication Engineering and Ph.D. degrees from the Universitat Politècnica de Catalunya (UPC), Barcelona, Spain, in 1999 and 2003, respectively.

In 2007, he joined the Department of Signal Theory and Communications, UPC, initially as a Ramon y Cajal Research Fellow and Associate Professor since 2009. He is also a Research Associate with the Centre Tecnològic de Telecomunicacions de Catalunya (CTTC). From May to August 2001, he was a Visiting Researcher with Superconductor Technologies, Inc., Santa Barbara, CA. From October 2002 to August 2005, he was a Research Associate and Coordinator of the communication subsystem area at CTTC, Spain. Since September 2004, he has held several guest researcher appointments at the National Institute of Standards and Technology (NIST), Boulder, CO, where he was a Fulbright Research Fellow from September 2005 to October 2006. From September 2003 to August 2005, he was a part-time Assistant Professor at Universitat Autònoma de Barcelona. He coauthored over 35 papers in international journals, 45 contributions in international conferences, and two book chapters, and holds two patents.

Dr. Mateu was the recipient of the 2004 Prize for the best doctoral thesis in technologies for information and communications by COIT and AEIT. He was also the recipient of a Fulbright Research Fellowship, an Occasional Lecturer Award for visiting MIT, and a Ramón y Cajal Contract.

Alberto Padilla (S'09) was born in Barcelona, Spain, in 1984. He received the Telecommunication Engineering degree from the Universitat Politècnica de Catalunya (UPC), Barcelona, Spain, in 2008, where his final project was associated with the mitigation of the nonlinear behavior of high-temperature superconducting planar devices. Currently, he is working towards the Ph.D. degree at UPC, focusing his research on new class of synthesis for microwave filters for satellite communications.

Since March 2008, he has been with the Department of Signal Theory and Communications, UPC, as a Microwave Engineer.

Juan M. O'Callaghan (SM'01) received the Telecommunication Engineering degree from the Universitat Politècnica de Catalunya (UPC), Barcelona, Spain, in 1987, and the M.S. and Ph.D. degrees from the University of Wisconsin, Madison, in 1989 and 1993, respectively.

Currently, he is a Full Professor at UPC. He was an intern at Honeywell's Systems Research Center, Bloomington, MN, working on noise measurement methods for FETs, a Ka band. His research interests include microwave devices and materials and microwave photonics. He has worked on noise characterization, large signal properties of GaAs FETs, and advanced microwave materials such as superconductors and ferroelectrics. He has published over 45 articles in peer-reviewed international magazines and holds three patents. From 2003 to 2006, he served as manager for MERIT, a consortium of European universities delivering a joint Master's program in information technologies within the Erasmus Mundus program. He is currently Vice Dean of Academic Affairs at Telecom BCN, the telecommunication engineering school at UPC.

First-Order Elastic Nonlinearities of Bulk Acoustic Wave Resonators

Carlos Collado, *Senior Member, IEEE*, Eduard Rocas, *Student Member, IEEE*, Alberto Padilla, Jordi Mateu, *Senior Member, IEEE*, Juan M. O'Callaghan, *Senior Member, IEEE*, Nathan D. Orloff, James C. Booth, Enrique Iborra, and Robert Aigner

***Abstract*—We propose a procedure to characterize the intrinsic nonlinearities of bulk acoustic wave resonators by performing one-port measurements of the second harmonic and second-order intermodulation spurious signals. Closed-form expressions have been derived that relate the nonlinear stiffened elasticity with experimental observables. These formulas are valid in a wide range of frequencies around the resonance and have been verified with nonlinear circuit simulations. The measurement setup and its effects are also discussed in our approach. Measurements of a set of aluminum nitride-based devices from several manufacturers yield consistent model parameters and allow us to obtain a coefficient of the nonlinear stiffened elasticity intrinsic to this piezoelectric material.**

***Index Terms*—Bulk acoustic wave (BAW), film bulk acoustic resonator, harmonic generation, intermodulation distortion, nonlinear elastic constant, nonlinear Krimholtz, Leedom, Matthaei (KLM), nonlinear stiffened elasticity, nonlinearities.**

I. Introduction

BULK ACOUSTIC wave (BAW) technology is growing rapidly due to the telecommunication industry demands [1]. In parallel with this growth, a better understanding and modeling of the behavior of BAW devices is increasingly important for industrial applications where we need to consider nonlinear effects and minimize their presence. There are several dominant nonlinear effects that can limit the performance and potential of BAW resonators, such as detuning, saturation, higher order harmonics, intermodulation generation, and adjacent channel leakage power.

The interaction between acoustic and electromagnetic fields and complex multilayer composite materials, used for manufacturing BAW devices, makes the nonlinear modeling and characterization of BAW devices challenging. Many of the material properties (piezoelectricity, dielectric constant, elasticity, etc.) convolve the constitutive equations with thermodynamics to properly describe the fields in electro-acoustic devices.

These equations are highly nonlinear, as are many of the material properties on which they depend [2]. In addition to the piezoelectric layer, self-heating mechanisms arising from power dissipated in the piezoelectric layer can contribute to the nonlinear behavior [3]. Besides the possible multiple origins of nonlinear effects, the acoustic-electromagnetic interactions make it difficult to determine which independent variable (stress, strain, electric field, temperature, etc.) is the dominant source of nonlinearities [4].

In a previous paper [5], we described how a first-order stress-dependent nonlinearity in the stiffened elasticity of the piezoelectric layer (corresponding to the first stress-dependent term in a Taylor's-series expansion of the stiffness) might account for the second-order harmonics (H2) and second-order intermodulation products (IMD2) generated in a BAW resonator. We described in [5] the nonlinear circuit model we also use in this work, and showed some preliminary measurements of a two-port BAW device at the mechanical resonance frequency. Those measurements were consistent with the model, but were not conclusive since only one device had been measured.

In this paper, we demonstrate the dependence of H2 and IMD2 on the nonlinearity in the stiffened elasticity of the piezoelectric layer by making measurements on a variety of one-port BAW resonators with the same piezoelectric material [(aluminum nitride (AlN)], but having different geometries, sizes, configurations, and made by different manufacturers. We define and use a well-characterized measurement setup to isolate the nonlinear properties of the piezoelectric material from other parameters that affect IMD2 and H2. In these conditions, we seek to find the same nonlinear properties of the piezoelectric material, regardless of the device being tested.

In addition to the main goal of this paper stated above, the following improvements over previous publications have been realized:

- modification of the existing two ports formulation [5] to account for one-port BAW devices (usual testing configuration) and its extension for a wide range of frequencies around their resonances;

Manuscript received November 18, 2010; accepted November 23, 2010. This work was supported in part by the Spanish Government (MCIN) under Grant TEC-2009-13897-C03-01 and Grant MAT-2008-06761-C03-02, by the Catalonia Government under Grant 2008 BE2 00196, and by the U.S. Government. The work of E. Rocas was supported by the Spanish Ministry of Education under Ph.D. Fellowship BES-2007-16775. The work of A. Padilla was supported by the Spanish Ministry of Education under Ph.D. Fellowship AP200802235.

C. Collado and E. Rocas are with the Department of Signal Theory and Communications, Universitat Politècnica de Catalunya (UPC), Barcelona 08034, Spain, and also with the National Institute of Standards and Technology, Boulder, CO 80305 USA (e-mail: collado@tsc.upc.edu).

A. Padilla, J. Mateu, and J. M. O'Callaghan are with the Department of Signal Theory and Communications, Universitat Politècnica de Catalunya (UPC), Barcelona 08034, Spain.

N. D. Orloff and James C. Booth are with the National Institute of Standards and Technology, Boulder, CO 80305 USA.

E. Iborra is with the Department of Electronic Engineering, Universidad Politècnica de Madrid, Madrid 28040, Spain.

R. Aigner is with Triquint Semiconductors, Apopka, FL 32703 USA.

Color versions of one or more of the figures in this paper are available online at http://ieeexplore.ieee.org.

Digital Object Identifier 10.1109/TMTT.2010.2098042

- development and analysis of a measurement setup to measure intermodulation and harmonics on very reflective one-port devices;
- de-embedding the effect of the imperfections of the measurement setup on the second-harmonic measurements;
- definition of a systematic step-by-step broadband approach for the characterization of the first-order nonlinearities.
- measurements of state-of-the-art devices with the same piezoelectric material but having different geometries, sizes and made by different manufacturers, therefore with different stack configurations.

II. Intrinsic Nonlinearities and Transmission Line Model

A. Nonlinear Stiffened Elasticity

The equations for an acoustic field propagating along the x-direction for the 1-D longitudinal mode are [6], [7]

$$\frac{\partial T}{\partial x} = \frac{\partial(\rho\,\dot{u})}{\partial t}; \quad \frac{\partial \dot{u}}{\partial x} = \frac{\partial}{\partial t}\left(\frac{1}{c^D}T\right) \tag{1}$$

where T is the stress, $\dot{u}$ is the velocity of the particles, ρ is the density, S is the strain, and c^D is the stiffened elastic constant (c^D_{33} in a tensor notation), which is related to the elastic constant c^E, piezoelectric constant e, and dielectric constant ε^S as follows:

$$c^D = c^E + \frac{e^2}{\varepsilon^S}. \tag{2}$$

From (1) and (2), we see that if c^E, e, ε^S are dependent on physical magnitudes (T, S, electric field E, etc.), those dependences may be included in a nonlinear parameter c^D. According to our hypothesis, whose validity will be discussed in Section IV, the stiffened elasticity depends on stress [2], [5] as

$$c^D(T) = c^D_0 + \Delta c^D_{\mathrm{NL}}(T) \tag{3}$$

which can be expanded in a Taylor's series as

$$c^D(T) = c^D_0 + \sum_{n\geq 1} \Delta c^D_n \cdot T^n. \tag{4}$$

In (4), we have used the subscript n to denote the order of the nonlinearity, and c^D_0 is the linear term.

B. Nonlinear Krimholtz, Leedom, Matthaei (KLM) Model

Equation (1) describes the propagation of the acoustic wave in the piezoelectric layer, which is coupled to the electromagnetic source by means of electrodes. This coupling sets the boundary conditions to solve (1) and is often modeled with an equivalent circuit to analyze the response of the device to a given electromagnetic stimulus.

For an electromagnetic or acoustic wave propagating in a nonlinear passive medium, we may use distributed equivalent circuits in which the nonlinear relations between physical magnitudes (e.g., voltage and current) are described independently

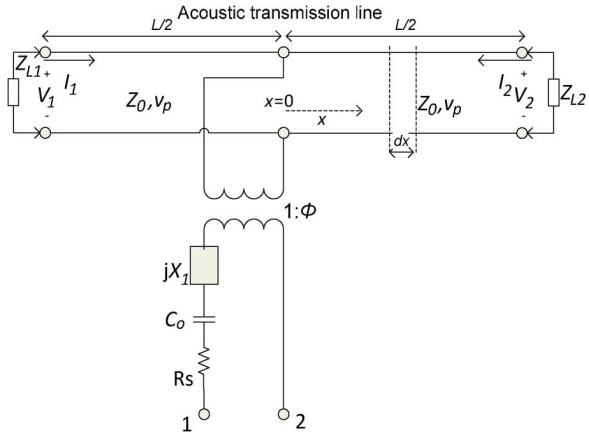

Fig. 1. KLM distributed model of a BAW resonator. The acoustic line, whose length is L, is modeled by cascading several segments of lumped elements. Each segment accounts for a short length dx, as described in [5].

of the physical dimensions of the device [8]. This model allows to parameterize the nonlinear relations between magnitudes by means of device-independent parameters, such as the stiffened elasticity (4). For this reason, we use an equivalent circuit, where the acoustic propagation is kept independent of the electrical part of the electro-acoustic device. The KLM model [9] treats the acoustic and electromagnetic domains as separable, and thus is a good candidate to accurately describe the electro-acoustic propagation and coupling for our devices. Specific details about the nonlinear KLM model can be found in [5].

Fig. 1 shows the variables of the KLM model used through this paper. The mathematical definition of the parameters X_1 and ϕ can be found in [9]. The remaining components of the electric domain, R_S and C_0, model the electrode losses and the electrostatic capacitance, respectively. Z_{L1} and Z_{L2} model the acoustic impedance of the electrodes, which can be different depending on the stack configuration, L is the thickness of the piezoelectric layer, and Z_0 and v_p are, respectively, its acoustic characteristic impedance and velocity.

The acoustic propagation is modeled in terms of voltage (v) and current (i) that account for force (F) and velocity $(\dot{u})$, respectively [6]. For a resonator with an area A, the propagation can be described in terms of distributed capacitance $C_d = 1/(A \cdot c^D)$ and inductance $L_d = \rho$, which give the equivalent electrical distributed circuit for acoustic waves [6]. Note that the KLM model uses force instead of stress. Hence, we use the relation $F = -AT$ for longitudinal modes in BAW devices. Reference [5] shows how to include the nonlinear stiffened elasticity in the KLM model. For completeness, we briefly write down the most important equations referring to the first-order nonlinear term in (4). For $n = 1$, the stiffened elasticity in (4) can be rewritten in terms of force as

$$c^D(F) = c^D_0 - \frac{\Delta c^D_1}{A} \cdot F. \tag{5}$$

Since $C_d = 1/(A \cdot c^D)$, (5) implies a nonlinear capacitance in the equivalent electrical circuit, whose first-order Taylor's series approximation is

$$C_d(v) = C_{d,0} + \Delta C_{d,1} v \tag{6}$$

where $C_{d,0} == 1/(A \cdot c_0^D)$ and $\Delta C_{d,1}$ is as follows:

$$\Delta C_{d,1} = \frac{1}{A c_0^D}\left(\frac{\Delta c_1^D}{A c_0^D}\right). \tag{7}$$

The nonlinear Telegrapher's equations for the acoustic transmission line are then

$$\frac{\partial v}{\partial x} = -L_d \frac{\partial i}{\partial t} \quad \frac{\partial i}{\partial x} = -G_{d,0} v - C_{d,0} - \frac{\partial}{\partial t}(\Delta C_{d,1} v^2) \tag{8}$$

where we have included the term $G_{d,0}$ to account for the acoustic losses, and

$$\frac{\partial i_{nl}}{\partial x} = \frac{\partial}{\partial t}(\Delta C_{d,1} v^2). \tag{9}$$

The formulation above (1)–(9) sets the basis for obtaining the closed-form equations derived in Section III. For circuit simulations, we use the distributed model of the acoustic line described in [5], where the line is modeled by cascading several segments of lumped elements $L_d \cdot \partial x$, $C_d \cdot \partial x$, and $G_d \cdot \partial x$ such that each segment accounts for an elemental length ∂x of the acoustic transmission line.

III. Second-Harmonic and Second-Order IMD

Let us assume that a BAW resonator is driven with two tones at frequencies ω_1 and ω_2. As shown in [5], first-order nonlinearities can generate not only H2 $2\omega_1$ and $2\omega_2$ and IMD2 $\omega_1 + \omega_2$, but also third-order intermodulation products $2\omega_1 - \omega_2$ and $2\omega_2 - \omega_1$ when the H2 remix with the fundamental signals. The formulas given in [5] are valid only for two-port resonators at the frequency at which the circulating power into the resonator is maximal (i.e., "mechanical" resonance). In this section, we modify the formulation to be used for one-port devices (port 2 in Fig. 1 is grounded), and extend it over a range of frequencies around the characteristic resonance frequencies, typically named "series" and "shunt." We will also detail the measurement setup and its effect on the experimental observables.

A. Experimental Setup

In our experiments, we drive the one-port device-under-test (DUT) with two tones at frequencies ω_1 and ω_2. The fundamental tones (ω_1 and ω_2) are then amplified and low-pass filtered to eliminate their second harmonics (see Fig. 2) coming from the sources and the amplifier. Isolators are used to avoid intermodulation effects generated at the amplifiers, and to maintain the voltage standing-wave ratio (VSWR) at port 3, where the DUT is connected, within reasonable values at frequencies beyond the cutoff frequency of the low-pass filters. Note that at higher frequencies, the power flowing from the hybrid to the filter would be reflected if isolators were not placed between the filters and hybrid. The two tones are then combined and driven to a broadband 90° coupler, which enables us to separate the signals incident on the device from those reflected or generated within it (such as H2 and IMD2)

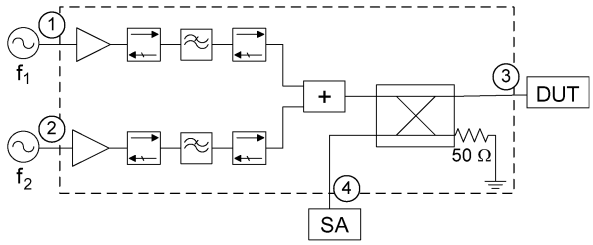

Fig. 2. Four-port setup for intermodulation and second harmonic measurements of one-port devices.

B. Maximum Stress in the Acoustic Transmission Line

Since the nonlinearities are weak when the BAW resonator is driven by external signals at ω_1 and ω_2 , the resulting standing wave at these frequencies is almost identical to that of a perfectly linear material. The generation of spurious signals at $2\omega_1$, $2\omega_2$, and $\omega_1 + \omega_2$ (H2 and IMD2) is governed by (9), which can be interpreted as a set of current sources placed at each transmission line segment of length ∂x and having a dependence on the time derivative of the square of the voltage at that segment. This distributed generation produces standing-wave patterns at $2\omega_1$, $2\omega_2$, and $\omega_1 + \omega_2$ whose amplitude can be related to that of the patterns at ω_1 and ω_2. As discussed in [5], the symmetric distribution of the standing-wave pattern at ω_1 and ω_2 forces a simple relation between the maximum voltages (force) of the spurious signals $V_{2\omega i}(i = 1, 2)$ and $V_{\omega 1+\omega 2}$, and those of the fundamental frequencies $V_{\omega 1}$ and $V_{\omega 2}$

$$V_{2\omega 1} = -\frac{1}{2} V_{\omega 1}^2 \frac{\Delta C_{d,1}}{C_{d,0}} \tag{10}$$

$$V_{\omega 1+\omega 2} = -V_{\omega 1} V_{\omega 2} \frac{\Delta C_{d,1}}{C_{d,0}}. \tag{11}$$

Equations (10) and (11) are valid for one- and two-port resonators and were successfully checked at the mechanical resonance frequency [5] by means of nonlinear circuit simulations using [10]. Here, we extend the comparison to a range of frequencies covering the mechanical ($f_{\max}$), the series (f_r), and the shunt resonance (f_a). The simulated resonator has 2.62 μm of AlN and ideal short-circuits as electrodes, and a value of $\Delta C_{d,1} = 10^{-5}$ F/(V · m) was arbitrarily chosen to check the formulation. Fig. 3 shows the excellent agreement between (10) and simulations using [10]. Equation (11) was also tested with similar results

C. Power Dissipated at the Load

Although (10) and (11) are important equations that relate the maximum voltage in the acoustic line of the H2 and IMD2 signals with the fundamental ones, a practical relation between experimental observables (dissipated power at the load) and available power from the sources is needed.

Fig. 4 shows the definitions that we will be using throughout this section and Section IV. The DUT, modeled as in Fig. 1, is connected by means of a transmission line to port 3 of the measurement setup and the output power is measured by a spectrum

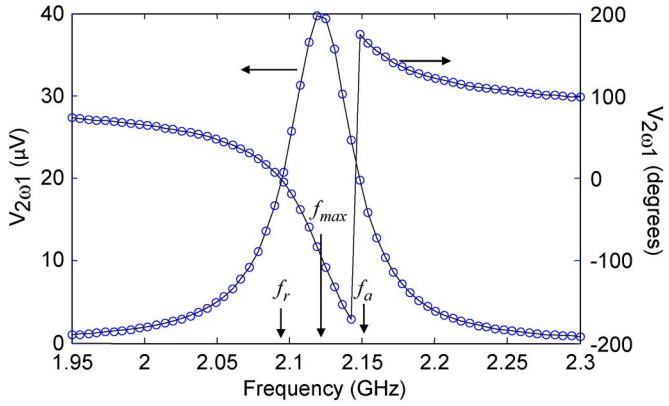

Fig. 3. Magnitude (left-vertical axis) and phase (right-vertical axis) of the second-harmonic voltage at the center of the line calculated with (12) (black continuous line) and simulations (blue circles in online version). Arrows indicate the frequencies: $f_{\max} = 2.120$ GHz, $f_r = 2.096$ GHz, and $f_a = 2.148$ GHz.

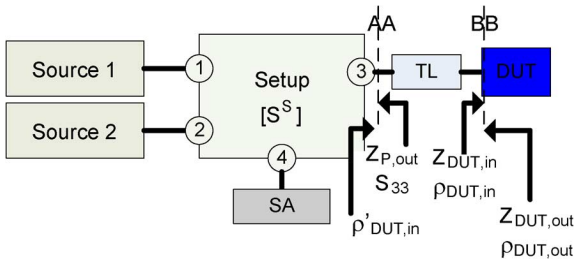

Fig. 4. Schematic of the nonlinear setup and useful definitions.

analyzer connected at port 4. As we will see in Section IV, in a practical experiment, the S_{33} of the four-port setup is measured in the AA plane, and the reflection coefficient of the DUT ($\rho_{\mathrm{DUT,in}}$) in the BB plane. If the VSWR at port 3 is not good enough, there will be a standing-wave pattern between both planes. This standing wave will have a perceptible effect on the measurements at the spectrum analyzer ("SA" in Fig. 4) so we need to include a small transmission line ("TL" in Fig. 4), which accounts for the transitions and probes between both reference planes, in the model shown in Fig. 4.

For simplicity, we will write down the analysis only for the second harmonic $2\omega_1$ because extending the formulation to $2\omega_2$ and $\omega_1+\omega_2$ is straightforward. From the analysis of the circuit, we can demonstrate that the H2 voltage $V_{P,2\omega1}$ at port 3 will be

$$V_{P,2\omega1} = \frac{e^{-j\beta\, l}(1+S_{33,2\omega1})}{(1+\rho_{\mathrm{DUTout},2\omega1})} \times \frac{Z_{\mathrm{DUTout},2\omega1}}{Z_{\mathrm{DUTout},2\omega1}+Z_{s,2\omega1}} \frac{1}{\phi_2\omega1} V_{2\omega1} \quad (12)$$

where $V_{2\omega1}$ is the voltage at the center of the acoustic line ($x=0$ in Fig. 1) that appears in (10), $\beta\cdot l$ is the electrical length of the transmission line TL, the scattering parameters and impedances are defined in Fig. 4, $\phi_{2\omega1}$ is the transformer coupling evaluated at $2\omega_1$, and Z_S is the series impedance of the components of the electrical part in Fig. 1, where

$$Z_S = Rs + jX_{2\omega1} + 1/j2\omega_1 C_0. \quad (13)$$

Hence, the incoming power to the spectrum analyzer ($P_{L,2\omega1}$) with input reference impedance $Z_{\mathrm{ref}} = 50\ \Omega$ will be

$$P_{L,2\omega1} = \frac{1}{2Z_{\mathrm{ref}}}|V_{P,2\omega1}|^2 \frac{|S_{43,2\omega1}|^2}{|1+S_{33,2\omega1}|^2}. \quad (14)$$

In a similar manner, the fundamental voltage $V_{\omega1}$ in (10) can be related with the available source power $P_{\mathrm{av},1}$, resulting in

$$|V_{\omega1}| = \sqrt{8Z_{\mathrm{ref}}P_{\mathrm{av},1}} \times \left|\phi_{\omega1}\frac{Z_{\mathrm{DUT\ in},\omega1}-Z_{s,\omega_1}}{Z_{\mathrm{DUT\ in},\omega1}+Z_{\mathrm{ref}}}\frac{S_{31,\omega1}}{1-S_{33,\omega1}\,\rho'_{\mathrm{DUT\ in},\omega1}}\right|. \quad (15)$$

Equations (10) and (12)–(15) allow us to relate the H2 power with the available source power and, therefore, to determine the value of ΔC_1 that fits the experimental data.

To check these expressions, we will consider an ideal setup and compare them with harmonic balance simulations. If the setup is ideal (only a hybrid), and the DUT is connected directly to port 3 of Fig. 4, then $|S_{31}|^2 = |S_{21}|^2 = |S_{41}|^2 = 0.5$, $S_{33} = 0$, $Z_{\mathrm{DUTout}} = Z_{\mathrm{ref}}$, and $\rho_{\mathrm{out}} = 0$, thus, combining (10), (12), and (14), we obtain

$$P_{L,2\omega1} = \frac{Z_{\mathrm{ref}}^3 P_{\mathrm{av1}}^2}{|(Z_{\mathrm{ref}}+Z_{s,2\omega1})\phi_{2\omega1}|^2} \times \left|\frac{(Z_{\mathrm{DUT\ in},\omega_1}-Z_{s,\omega1})\,\phi_{\omega1}}{(Z_{\mathrm{DUT\ in},\omega_1}+Z_{\mathrm{ref}})}\right|^4 \left|\frac{\Delta C_{d,1}}{C_{d,0}}\right|^2 \quad (16)$$

which directly relates the measured H2 power with the available source power as a function of the nonlinear parameter $\Delta C_{d,1}$.

Fig. 5 shows a comparison between (16) and harmonic balance simulations using the test resonator described in Section III-B. The agreement between simulated data and (16) is excellent in the frequency range of interest (the characteristic resonances are marked with arrows). The maximum H2 power occurs at the mechanical resonance ($f_{\max}$), as expected. Note that, despite the large magnitude of the maximum voltage in the acoustic line $V_{2\omega1}$ (see Fig. 3) at the shunt resonance f_a, there is no spurious signal power flowing out of the resonator because the term Z_s of (13) tends to infinity at that frequency. This occurs when ideal resonators (no losses and ideal electrodes) are considered, as in this case.

IV. Second Harmonic and IMD2 Experiments

We performed measurements on eight devices obtained from an industrial manufacturer (A) and from a research center (B), all of them with different areas. The devices made by A are square and trapezoidal shaped, with 1.25 μm of AlN thickness and areas ranging from 1.2×10^{-8} m^2 to 6.4×10^{-8} m^2. The devices from B are pentagonal shaped with 1.27 μm of AlN thickness, and their areas range from 1.2×10^{-8} m^2 to 5.1×10^{-8} m^2. Samples from A and B use different materials and stack configurations for the electrodes and the Bragg mirror.

In order to characterize the first-order nonlinear stiffened elasticity, we have followed the procedure described below, which is divided into the following five steps.

Step 1) Characterization of the measurement setup.

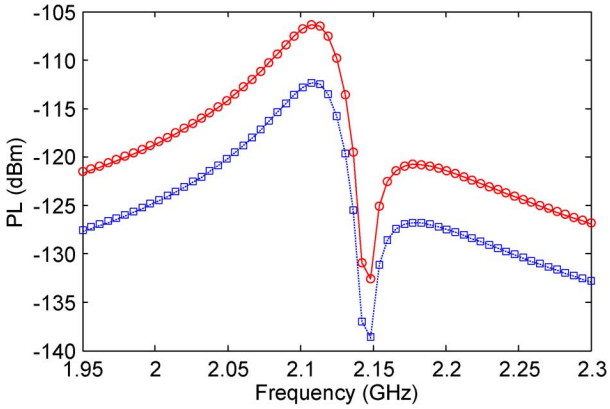

Fig. 5. Power P_L delivered to port 4 (Fig. 4) by use of (18) (continuous line) at $2\omega_1$ (blue line in online version) and $\omega_1+\omega_2$ (red line in online version) and nonlinear simulations (squares and circles, respectively).

Step 2) Determination of a linear circuital model of the DUT by measuring its reflection coefficient.

Step 3) Measurement of H2 and IMD2 over a broad frequency, keeping a constant difference between the two driving frequencies.

Step 4) De-embedding the stray effects produced by the measurement setup.

Step 5) Determination of the value of $\Delta C_{d,1}$ that best better fits the measurement and its corresponding value of the geometry-independent parameter Δc_1^D.

Step 1. Characterization of the Measurement Setup: The measurement setup, with a 90° broadband coupler (2–8 GHz), is shown in Fig. 2. The measurement of the 4 × 4 scattering matrix of the whole setup is the first step in our characterization process. Fig. 6 shows the scattering parameters of the setup. The insertion loss (S_{43}) from the DUT to the spectrum analyzer ranges between 4–5 dB, and the return loss at the port, where the device is connected (S_{33}), is around 10 dB at frequencies around the second harmonic of the fundamental frequencies. This poor VSWR is due to reflections at the output of the low-pass filters in spite of having an isolator between the filter and the power combiner.

Step 2. Linear Measurements of the DUT: The linear parameters of a DUT were measured with on-wafer thru-reflect-line calibrations [11]. The measured reflection coefficient was fit with a linear model (Fig. 1) by means of information, supplied by the manufacturers, on the electrodes and Bragg mirror. For example, we show the measured imaginary part of the reflection coefficient and circuit simulations of device A1 around the operation frequencies in Fig. 7. The inset in Fig. 7 shows its broadband response and simulations.

As shown in Fig. 7, where we only show the imaginary part of the reflection coefficient for simplicity, the KLM model agrees very well with the response of the resonator. Note that a better fit of the linear model implies a more accurate prediction of the voltage inside the acoustic transmission line model at the fundamental frequencies, which is responsible for the harmonic generation.

Step 3. H2 and IMD2 Measurements: The DUT is driven by two frequency tones $f_1 = f_0 - \Delta f/2$ and $f_2 = f_0 + \Delta f/2$,

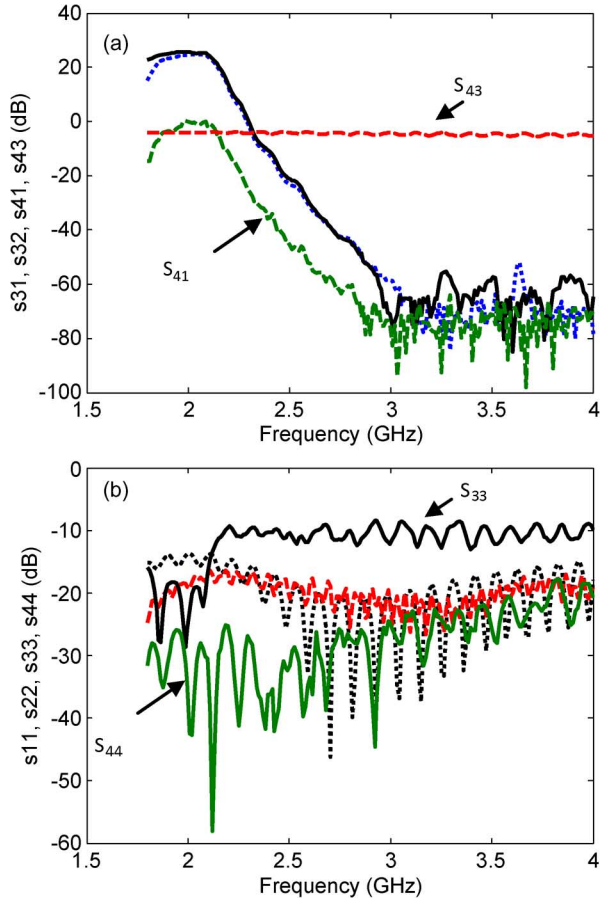

Fig. 6. S-parameters of the setup for numbering in Fig. 4. (a) S_{31} (continuous black line), S_{32} (dotted blue line in online version), S_{41} (dashed green line in online version), and S_{43} (dashed red line in online version). (b) S_{11} (dotted black line), S_{22} (dashed red line in online version), S_{33} (black line), and S_{44} (green line in online version).

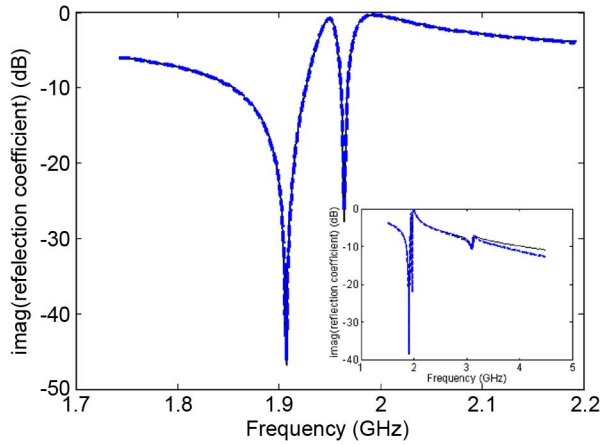

Fig. 7. Imaginary part of the reflection coefficient from device A1 measured (black continuous line) and simulated (blue dashed line in online version). The minimums correspond to the characteristic resonance frequencies (series and shunt). The inset shows the broadband response.

where $\Delta f = 1$ kHz and the frequency f_0 is swept from 1.88 to 1.98 GHz while keeping Δf constant. The input power to the device [Port 3 in Fig. 4] is 20 dBm at each fundamental frequency. The reflected signal and spurious signals generated inside the resonator are directed by the 90° coupler to the spectrum

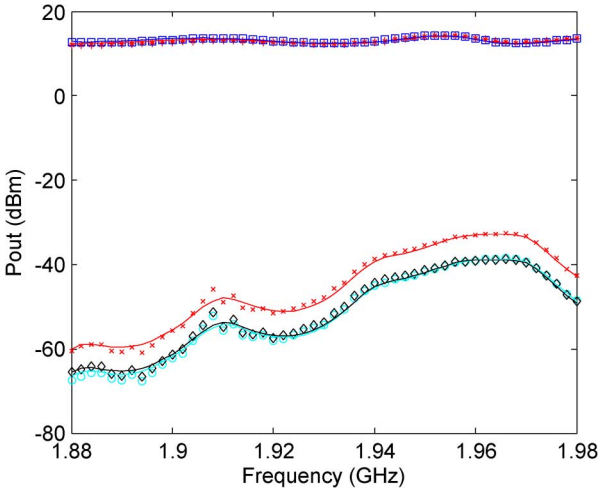

Fig. 8. Output power at the fundamental tones (blue and red line in online version), H2 (cyan line in online version and black line), and IMD2 (red line in online version). Horizontal axis shows the f_0 values at each measurement point.

analyzer. Before connecting the DUT, we measure an on-wafer open stub in order to set the levels of intermodulation and harmonics generated by the measurement setup and we make sure these are negligible throughout the whole measurement process.

Fig. 8 shows the measured second harmonics and IMD2 for device A1. Continuous lines show nonlinear circuit simulations, such as those explained in Section III-C, but including the measured S-parameters of the setup from Step 1 and the linear circuit model from Step 2. With a unitless value of $\Delta c_1^D = 10.5$, measurements and nonlinear simulations overlap. The output power at the fundamental tones shows a small ripple due to the imperfections of the measurement setup. This ripple is more significant at higher frequencies (H2 and IMD2) due to the poor mismatch at port 3, as previously discussed.

Fig. 8 reveals the advantage of performing broadband measurements instead of single-frequency point measurements. For instance, if single-frequency measurements (as done in our previous work [12]) were performed at a frequency close to the series resonance (first dip in Fig. 7), erroneous results could be obtained because the nonlinear behavior is affected by spurious resonances. Therefore, broadband measurements enable us to avoid the issue of anomalous nonlinear responses arising from spurious modes.

To this point, we have made use of nonlinear circuit simulations to consider the influence of the measurement setup on the experimental observables. In the next steps, we show how the nonlinear stiffened elasticity can be obtained from the measurements without having to use a nonlinear circuit simulator.

Step 4. De-Embed the Effect of the Setup: As shown above, the effect of the imperfections of the measurement setup on the second-harmonic measurements is significant. We can, however, de-embed this effect by means of conventional microwave circuit theory. To completely remove this effect, we need to determine the output power that the device would deliver to a perfectly matched 90° coupler ($P_{L,id,2\omega1}$) versus the input power to the device $P_{\text{in},\omega1}$. We can then define the normalized magnitude $P_{L,id,2\omega1}/P_{\text{in},\omega1}^2$ that is independent of the measurement setup.

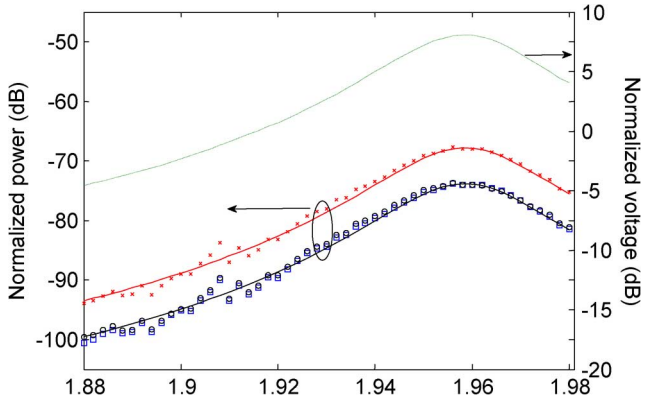

Fig. 9. Left vertical axis: normalized measured H2 (squares for $2\omega_1$ and circles for $2\omega_2$), measured IMD2 (stars), simulated H2 (black continuous line) and simulated IMD2 (red continuous line in online version). Right vertical axis: Maximum voltage at the fundamental frequencies (green line in online version).

The input power to the device, at each fundamental frequency $P_{\text{in},\omega1}$ (and $P_{\text{in},\omega2}$), is calculated with

$$P_{\text{in},\omega1} = \frac{|S_{31,\omega1}|^2}{\left|\left(1 - S_{33,\omega1}\rho'_{\text{DUT,in},\omega1}\right)\right|^2} P_{\text{av},i} \qquad (17)$$

where we follow the definitions in Fig. 4.

The power $P_{L,id,2\omega1}$, as a function of the measured power $P_{L,2\omega1}$, at port 4 of Fig. 4 can be calculated by use of the transducer power gain [13] from port 3 to port 4 of Fig. 4. We then obtain

$$P_{L,id,2\omega1} = \frac{1}{2}\frac{\left|1 - S_{33,2\omega1}\rho'_{\text{DUT in},2\omega1}\right|^2}{|S_{43,2\omega1}|^2} P_{L,2\omega1}. \qquad (18)$$

By use of (16)–(18), we can normalize $P_{L,id,2\omega1}$ versus $P_{\text{in},\omega1}$, which has again been checked with simulations. Fig. 9 plots the simulated (continuous line) and measured (circles) normalized power $10\cdot\log_{10}(P_{L,id,2\omega1}/P_{\text{in},\omega1}^2)$ for the device A1. Fig. 9 also plots the square voltage at the center of the line normalized to the input power for the fundamental signal obtained in the simulations. As expected, the maximum is reached at the mechanical resonance frequency of the resonator at which the stored energy is higher.

From Fig. 9, we see that the measurements of the H2 and IMD2 data follow the same frequency pattern as $V_{\omega1}$. The data are therefore consistent with the initial hypothesis, which proposes a nonlinear stress-dependent parameter that is the origin of the second-harmonic generation.

Step 5 Find Δc_1 That Better Fits the Measurement: In this section, we determine the best fit nonlinear parameters $\Delta C_{d,1}$ from the normalized measured data for each device with (10)–(18), and then, with these values, we extract the intrinsic parameter Δc_1^D with (7). Fig. 10(a) and (b) shows the results for resonators A and B, respectively, and Table I shows the best fit values of Δc_1^D.

As shown in Table I, a value of the nonlinear first-order stiffened elasticity around 10.5 is in reasonable agreement for all the A resonators despite having different areas and shape (furthermore, unlike other samples, A3 has a border ring to eliminate

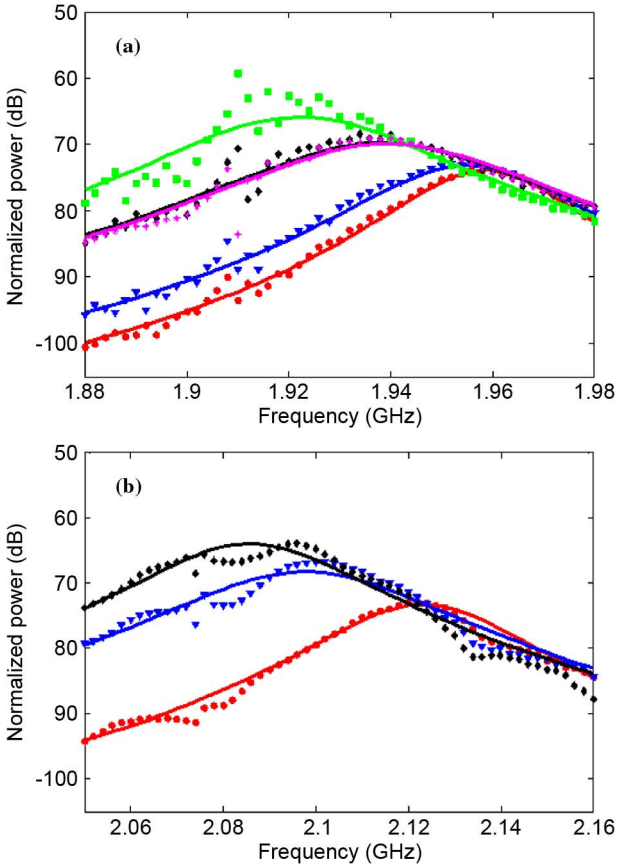

Fig. 10. Normalized H2 power. (a) A-devices: A1 (blue triangles in online version), A2 (green squares in online version), A3 (black diamonds), A4 (red circles in online version), A5 (magenta stars in online version). (b) B-devices: B1 (red circles in online version), B2 (blue triangles in online version), B3 (black diamonds).

TABLE I
EXTRACTED ΔC_1

	Shape	Area (m^2)	Using (12)-(19)	Using simulations
A1	rectangle	4.88e-8	12.1	10.5
A2	rectangle	1.25e-8	12.0	10.5
A3	rectangle	2.33e-8	12.2	10.6
A4	rectangle	6.41e-8	12.1	10.5
A5	trapezoid	2.41e-8	12.7	11.0
B1	pentagon	5.05e-8	14.3	13.0
B2	pentagon	2.04e-8	14.4	13.3
B3	Pentagon	1.21e-8	14.2	12.8

spurious modes), and 13.0 is in reasonable agreement for all the B resonators.

A systematic error is found between the values obtained with the formulation and the values obtained by harmonic balance simulations. The derivation of (10) and (11) assumes that the acoustic transmission line is symmetrical with respect to $x = 0$ (see Fig. 1) or, in other words, the electrodes connected at both ends of the transmission line are electrically equal [5]. This does not usually happen in BAW resonators with a Bragg mirror so the applicability of (10) and (11) is questionable in this type of device. Nevertheless, we have performed several simulations, sweeping the frequencies around the mechanical resonance frequency, with different electrodes, and the maximum error we have found is around 20%. For example, we have checked by means of simulations that (10) overestimates $V_{2\omega 1}$ by a maximum 16% over the measured frequency range for the A devices and by 14% for the B devices, as shown in Fig. 11.

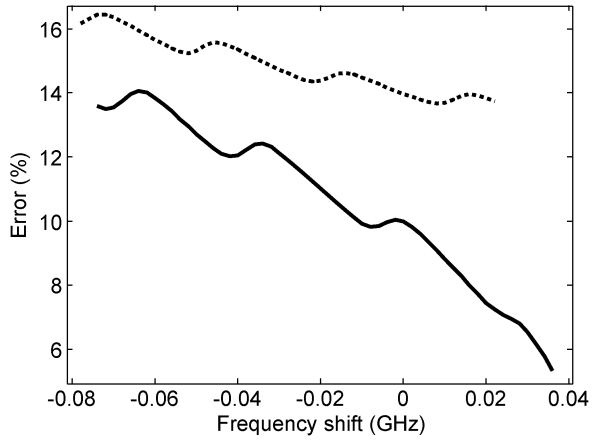

Fig. 11. Comparison between (10) and simulations for the B2-device (continuous line) and the A4-device (dotted line). Horizontal axis represents the frequency variation with respect to the mechanical resonance frequency (2.124 GHz for B2 and 1.958 GHz for A4).

These differences cause a mismatch smaller than 1.5 dB on the load power and agree well with the differences in the values of Table I. If the asymmetry of the transmission line were considered, the formulation and the simulations would be in an excellent agreement. This process would, however, require prior knowledge of the standing-wave pattern for the fundamentals and H2 signals, which implies nonlinear simulations, to achieve accuracy better than 20%.

V. DISCUSSION AND CONCLUSIONS

We have presented a systematic step-by-step broadband approach for the characterization of the first-order nonlinearities in BAW resonators. We have shown that broadband measurements are advantageous for avoiding the anomalous nonlinear behavior due to spurious resonances, instead of single-point frequency measurements especially close to the series resonance frequency.

We have found consistent values of stress-dependent nonlinearity in the stiffened elasticity of the piezoelectric material (AlN) of a set of resonators having widely different geometries, configurations, and delivered by two different manufacturers. We have determined values of Δc_1^D within a range 10.7 ± 0.3 for the five samples of one manufacturer and 13.1 ± 0.3 for the three samples of the other manufacturer. This consistency in the values of Δc_1^D proves that the first-order stress-dependent nonlinearity in the stiffened elasticity of the AlN piezoelectric is the origin of second harmonics and IMD2 products in BAW resonators. Moreover, both values are quite close, despite the AlN layers having been fabricated following different processes. Purely mechanical hydrostatic pressure measurements of AlN, reported in [14], give a value of the first-order nonlinear elasticity $\Delta c_{e1} = 4$, which is of the same order of magnitude as the values of Δc_1^D obtained in this study. This shows that c_e could be a significant contributor to the nonlinear term c_D.

We have used two alternative approaches to arrive at these conclusions, one based on simulation, and another based on closed-form equations that take into account the model of the BAW resonators and the effects of the measurement setup. We have checked for consistency between both approaches and have found that they diverge by at most 16% due to the simplifying assumptions taken in the closed-form approach. Despite these differences, the formulation gives a reasonable value of the nonlinear stiffened elasticity that is close to the uncertainties, around ± 0.5 dB, of the harmonic and intermodulation measurements.

This first-order nonlinearity is known to partially contribute to other spurious signals, such as third-order intermodulation products, and thus it sets the baseline level of spurious signals generated within the BAW resonator.

REFERENCES

[1] F. Z. Bi and B. O. Barber, "Bulk acoustic wave RF technology," *IEEE Microw. Mag.*, vol. 9, no. 5, pp. 65–80, Oct. 2008.

[2] D. A. Hall, "Nonlinearity in piezoelectric ceramics," *J. Mater. Sci.*, vol. 36, no. 19, pp. 4575–4601, 2001.

[3] E. Rocas, C. Collado, J. C. Booth, E. Iborra, and R. Aigner, "Unified model for bulk acoustic wave resonators' nonlinear effects," in *Proc. IEEE Int. Ultrason. Symp.*, Nov. 2009, pp. 880–884.

[4] J. Blackburn and M. Cain, "Nonlinear piezoelectric resonance: A theoretically rigorous approach to constant *I/V* measurements," *J. Appl. Phys.*, vol. 100, no. 11, pp. 1–10, Dec. 2006, 114101.

[5] C. Collado, E. Rocas, J. Mateu, A. Padilla, and J. M. O'Callaghan, "Nonlinear distributed model for bulk acoustic wave resonators," *IEEE Trans. Microw. Theory Tech.*, vol. 57, no. 12, pp. 3019–3029, Dec. 2009.

[6] B. A. Auld, *Acoustic Fields and Waves in Solids*. Malabar, FL: Krieger, 1990, vol. I.

[7] K. M. Lakin, G. R. Kline, and K. T. McCarron, "High-Q microwave acoustic resonators and filters," *IEEE Trans. Microw. Theory Tech.*, vol. 41, no. 12, pp. 2139–2146, Dec. 1993.

[8] C. Collado, J. Mateu, and J. M. O'Callaghan, "Analysis and simulation of the effects of distributed nonlinearities in microwave superconducting devices," *IEEE Trans. Appl. Supercond.*, vol. 15, no. 1, pp. 26–39, Mar. 2005.

[9] R. Krimholtz, D. A. Leedom, and G. L. Matthaei, "New equivalent circuits for elementary piezoelectric transducers," *Electron. Lett.*, vol. 6, no. 13, pp. 398–399, Jun. 1970.

[10] Advanced Design System (ADS). Agilent Technol., Santa Clara, CA, 2007.

[11] G. F. Engen and C. A. Hoer, "Thru-reflect-line: An improved technique for calibrating the dual six-port automatic network analyzer," *IEEE Trans. Microw. Theory Tech.*, vol. MTT-27, no. 12, pp. 987–993, Dec. 1979.

[12] E. Rocas, C. Collado, A. Padilla, J. Mateu, and J. M. O'Callaghan, "Nonlinear distributed model for IMD prediction in BAW resonators," in *IEEE Ultrason. Symp.*, Nov. 2008, pp. 1557–1560.

[13] D. Pozar, *Microwave Engineering*. New York: Wiley, 1998.

[14] S. P. Łepkowski and G. Jurczak, "Nonlinear elasticity in III-N compounds: *Ab initio* calculations," *Phys. Rev. B, Condens. Matter*, vol. 72, no. 24, pp. 1–12, Dec. 2005, Art. ID 245201.

Carlos Collado (A'02–M'03–SM'10), photograph and biography not available at time of publication.

Eduard Rocas (S'06), photograph and biography not available at time of publication.

Albert Padilla, photograph and biography not available at time of publication.

Jordi Mateu (A'02–M'04–SM'10), photograph and biography not available at time of publication.

Juan M. O'Callaghan (SM'01), photograph and biography not available at time of publication.

Nathan D. Orloff, photograph and biography not available at time of publication.

James C. Booth, photograph and biography not available at time of publication.

Enrique Iborra, photograph and biography not available at time of publication.

Robert Aigner, photograph and biography not available at time of publication.

CHAPTER III - ELECTRO-THERMO-MECHANICAL NONLINEARITIES

Thermal considerations are becoming more and more important in today's microwave components due to increasing requirements for higher power handling. With high temperatures and high dynamic thermal oscillations, temperature-dependent material properties originate nonlinearities that can limit the devices performance. This chapter covers the interaction of the electromagnetic, mechanical and thermal fields and how this impacts the nonlinear behavior of transmission lines and BAW resonators. Both physical and phenomenological models are proposed, which can be used to predict the nonlinear indicators at the design stage.

The first and second articles study the mechanism by which third-order intermodulation distortion is generated even in transmission lines made of materials whose properties do not depend on the electromagnetic fields. The third article assesses the impact of self-heating on the performance of limiters made of HTS transmission lines.

Appendix A covers the nonlinearities in ferroelectric ($Ba_{0.3}Sr_{0.7}TiO_3$) thin films, where the measurable observables are used to obtain a large-signal model of the transmission lines.

The fifth article and Appendix B propose models to explain the electro-thermo-mechanical nonlinearities in BAW resonators from a phenomenological approach and a physically rigorous approach respectively.

The articles, including Appendix A and B, in Chapter 3 are:

- E. Rocas, C. Collado, N. Orloff, J. C. Booth, **"Third-order intermodulation distortion due to self-heating in gold coplanar waveguides"**, *2010 IEEE MTT-S International Microwave Symposium Digest*, pp. 425-428, 23-28 May 2010
- E. Rocas, C. Collado, N. D. Orloff, J. Mateu, A. Padilla, J. M. O'Callaghan, J. C. Booth, **"Passive Intermodulation Due to Self-Heating in Printed Transmission Lines"**, *IEEE Transactions on Microwave Theory and Techniques*, vol. 59, no. 2, pp. 311-322, Feb. 2011
- E. Rocas, C. Collado, J. Mateu, N. Orloff, J. C. Booth, J. C., **"Modeling of Self-Heating Mechanism in the Design of Superconducting Limiters"**, *IEEE Transactions on Applied Superconductivity*, Accepted for publication and available online at IEEExplore.org as Early Access.
- E. Rocas, C. Collado, J. C. Booth, E. Iborra, R. Aigner, **"Unified model for Bulk Acoustic Wave resonators' nonlinear effects"**, *2009 IEEE International Ultrasonics Symposium*, pp. 880-884, 20-23 Sept. 2009

A. E. Rocas, C. Collado, J. Mateu, N. Orloff, J. M. O'Callaghan, J. C. Booth, **"A large-signal model of ferroelectric thin-film transmission lines"**, *Submitted to IEEE Transactions on Microwave Theory and Techniques*, March 2011

B. E. Rocas, C. Collado, J. Mateu, N. D. Orloff, R. Aigner, J. C. Booth, **"Electro-thermo-dynamic model for bulk acoustic wave resonators"**, To be *submitted to IEEE Ultrasonics, Ferroelectrics and Frequency Control*, March 2011.

Third-Order Intermodulation Distortion due to Self-heating in Gold Coplanar Waveguides

Eduard Rocas[1,2], Carlos Collado[1,2], Nathan Orloff[2], James C. Booth[2]

[1]Universitat Politècnica de Catalunya, Barcelona, CAT, 08034, Spain
[2]National Institute of Standards and Technology, Boulder, CO, 80305, USA

***Abstract* — We present measurements and modeling of a self-heating mechanism responsible for third-order intermodulation distortion in coplanar waveguide transmission lines. Temperature variations, at the envelope frequency of the input signal, induce dynamic changes in the distributed resistance that, when mixed with the fundamental tones, give rise to intermodulation.**

***Index Terms* —Coplanar waveguides, nonlinearities, electro-thermal effects, intermodulation distortion.**

I. Introduction

The existence of a self-heating mechanism that induces third-order intermodulation distortion (IMD3) is a well-known process in power amplifiers, on which successful efforts have been done on its modeling [1]-[4]. In contrast, passive microwave devices have received little attention, where few lumped models exist for discrete components such as connectors, attenuators and terminations [5]. For purposes of characterization and prediction, a nonlinear distributed model of the transmission lines with self-heating mechanism involved is required, in which the experimental observables can be related with the material properties and their temperature derivatives.

In this work, we present a distributed model to account for these nonlinearities induced by self-heating in transmission lines. The model introduces a thermal domain that simulates the heat flow along the transmission line and through the substrate, and is coupled to the electromagnetic domain.

The model was tested by use of coplanar waveguides (CPW) made of gold on sapphire, and showed good agreement with measured results on transmission lines of different lengths.

II. Unified Model

Despite temperature-induced changes in the material properties, models usually, for simplicity, make use of only the steady-state ambient temperature to predict the device's performance, without taking into account the dynamic temperature fluctuations [6][7]. In fact, as presented in this work, time-dependent temperature fluctuations can lead to undesired nonlinear effects that must be consistently modeled by an electro-thermal model.

A. Generation Mechanism

A scheme showing the generation process of IMD3 due to self-heating is shown in Fig. 1, in which the two-tones test represents a useful method in nonlinear analysis. A two-tone signal (f_1 and f_2) can be interpreted as a sinusoidal modulated signal at a frequency $\Delta f=f_2-f_1$ centered at $f_0=f_1+\Delta f/2= f_2-\Delta f/2$.

In the CPWs under study, dissipation is largely due to conductor losses for a substrate with negligible loss, such as sapphire. In such a case, the quadratic relation between instantaneous dissipated power and current implies that heat fluctuations are generated at frequencies Δf, $2f_1$, f_1+f_2 and $2f_2$. However, the relation between dissipation ($P_d(f)$) and temperature ($T(f)$) [8],

$$T(f) = Z_{th}(f)P_d(f), \qquad (1)$$

states that only variations at the envelope frequency Δf will produce substantial temperature changes due to the low-pass filter behavior of the thermal impedance $Z_{th}(f)$ that is related to the slow nature of thermal dynamics [8].

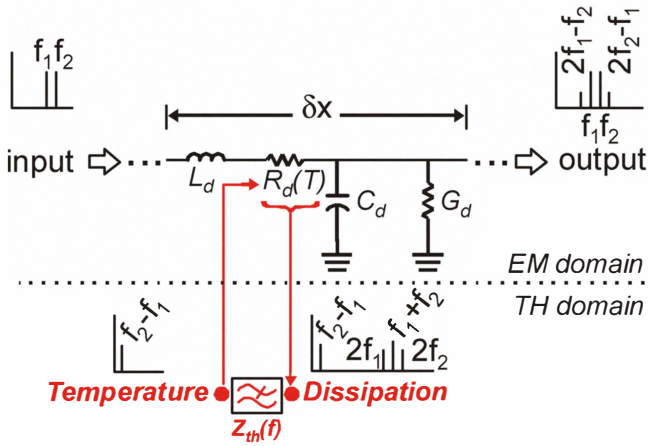

Fig. 1. Process by which IMD3 is generated in a transmission line. Resistive losses are responsible for temperature fluctuations that in turn change the metal resistivity, giving rise to a dynamically generated nonlinearity.

As seen in Fig. 1, temperature fluctuations change the metal resistivity $\rho(T)$ and, therefore, the distributed resistance $R_d(T)$ of the line. In fact, the temperature-induced changes can also be treated as an amplitude modulation of the input signals f_1 and f_2 by a modulating signal at frequency Δf, which gives rise

to IMD3 at $2f_1$-f_2 and $2f_2$-f_1. So, in such a situation, measurements of IMD3 while sweeping the tones spacing will lead to a low-pass filter shape [5] that could be used to de-embed the thermal impedance if an accurate model is used:

$$P_{IMD3} \propto \left|Z_{th}(\Delta f)\right|^2. \qquad (2)$$

B. Model Implementation

A consistent model to account for the aforementioned process needs the interaction of an electromagnetic and a thermal domain. Then, we build the electromagnetic domain as a cascade of sections of a certain length Δx, of lumped elements $R_{d,\Delta x}(T) = R_d(T)\cdot\Delta x$, $L_{d,\Delta x} = L_d\cdot\Delta x$, $G_{d,\Delta x} = G_d\cdot\Delta x$, $C_{d,\Delta x} = C_d\cdot\Delta x$, where $R_d(T)$, L_d, G_d, and C_d are the distributed parameters of the coplanar waveguide. For very thin conductor strips as used in our experiments, the distributed resistance changes with temperature as follows: $R_d(T) = R_{d,0}(1+\alpha T)$, where α is the temperature coefficient of resistivity.

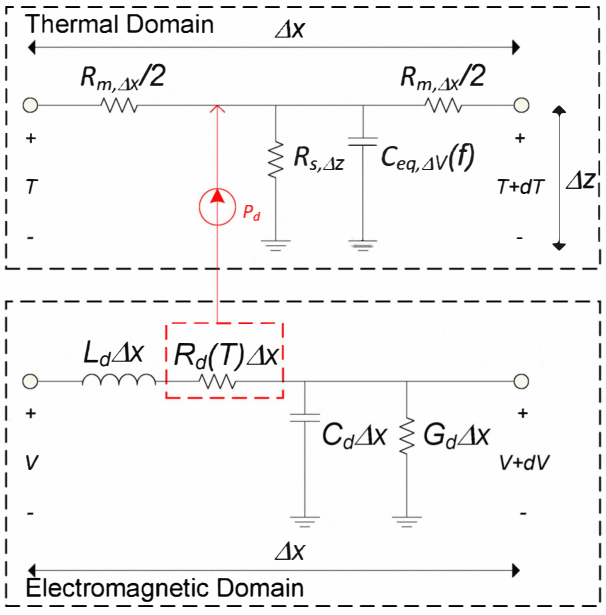

Fig. 2. Implementation of a section of transmission line in both electromagnetic and thermal domains.

On the other hand, thermal modeling of the heat flow along the transmission line and through the substrate is implemented by means of the thermal resistance $R_{th} = \Delta_u / k_{th}$ and the volumetric heat capacity $C_{th} = \varsigma C_p$, that can be separately defined for the metal and the substrate [8] (in the previous expressions, k_{th}, ς and C_p are the thermal conductivity, density, and heat capacity of the material, respectively, and Δ_u is a length increment in the direction of the heat propagation that can either be Δx along the line or Δz through the substrate (see Fig. 2)). So, with the above-mentioned thermal distributed parameters, each section of transmission line can be thermally modeled along the metal and through the substrate with a series resistance and shunt capacitance in the respective directions. In fact, the shunt capacitances can be combined in parallel with $C_{eq,\Delta V}(f)$ to represent an equivalent overall heat capacity of the metal and substrate ΔV in volume (Fig. 2).

In Fig. 2, the horizontal axis corresponds to the direction along the line, while the vertical axis is perpendicular to the wafer. So the thermal domain model presented is distributed along the horizontal axis but concentrated on the vertical axis. This means that Δx represents a section of the line and Δz is the total substrate thickness. The latter means that the 3D heat dissipation process has to be consistently modeled by use of a 2D model, even when the heat diffusion area on the XY plane changes as a function of frequency [8]. Such a frequency-dependent lateral diffusion area can be taken into account by use of a frequency-dependent equivalent heat capacity $C_{eq,\Delta V}(f)$, similar to that used in [5]. Moreover, the fact that a CPW consists of a center conductor between two ground planes implies that an equivalent width W_{eq} in terms of dissipation (usually related to the physical width by a geometrical factor [8]), has to be considered if a 2D model is used.

In Figure 2, $R_{m,\Delta x} = R_{m,th}/(W_{eq}t_m)$ and $R_{s,\Delta z} = R_{s,th}/(W_{eq}\Delta x)$ are the thermal resistances for a section of metal and substrate respectively, where t_m is the metal thickness. Heat radiation and convection are considered negligible, as well as heat flow through the probes, which are modeled using high value resistances at the terminations of the thermal domain.

Finally, dissipation in the electromagnetic domain is coupled to the thermal domain as a current source (see Fig. 2). This makes use of the fact that, in such a thermal transmission line, current and voltage are analogous to heat and temperature, respectively [8].

III. Measurements and Results

Linear and nonlinear characterization of two coplanar waveguides was carried out at room temperature for purposes of model validation.

A. Test Wafer and Linear Measurements

Two 480 nm-thick gold CPWs, with the same geometry except for different length l_A=4.200 mm and l_B=9.933 mm, were fabricated using photolithographic techniques on a 430 μm-thick sapphire substrate. A 20 nm-thick titanium intermediate layer was used for better adhesion between gold and substrate. The center conductor, ground planes and gap widths are 30 μm, 200 μm and 15 μm, respectively.

A procedure of multi-line TRL calibrations and impedance comparison was applied to extract the distributed parameters of the CPWs. Details on these extraction technique can be found in [9]. Extracted resistance and inductance per unit length from measurements is shown in Fig. 3. The extracted capacitance per unit length is C_d=162 pF/m, and G_d is negligible.

978-1-4244-7732-6/10/$26.00 ©2010 IEEE

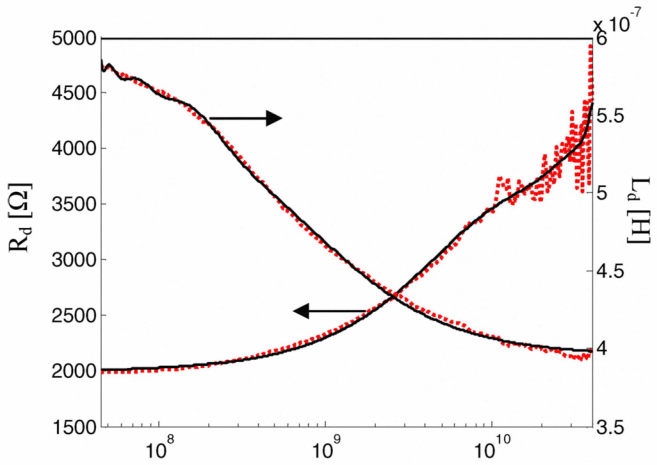

Fig. 3. Resistance and inductance per unit length as extracted from measurements (dashed lines) and a polynomial fit (solid lines).

Figure 3 also shows the polynomial fit for R_d and L_d, which smoothes the data from measurements and is used in the circuit model.

B. Nonlinear Measurements

As previously noted, the dependence of the intermodulation distortion level on the envelope frequency of the input signal is probably the convincing evidence for self-heating induced nonlinearities. To evaluate this and to validate the model with measurements, IMD3 has been measured on both CPWs for a wide range of tone spacings. The upper tone was set at f_2=6 GHz, while the lower tone $f_1=f_2-\Delta f$ varied so that Δf ranges Δf=2 Hz to Δf=1 GHz at an input power of 20 dBm per tone.

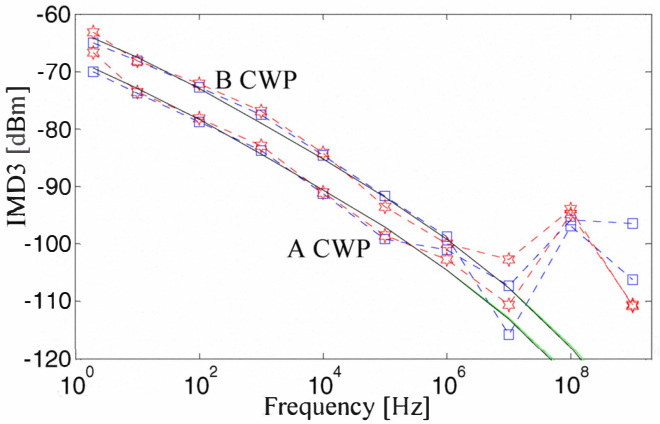

Fig. 4. Measurements ($2f_1$-f_2 and $2f_2$-f_1 are squares and circles respectively) and simulations (solid lines overlapped) of the generated IMD3 of the two CPWs presented in this work. The higher IMD3 level corresponds to the longer B CPW (l_B=9.933 mm), and the lower corresponds to A CPW (l_A=4.2 mm).

A special measurement setup intended to increase the measurement dynamic range at the spectrum analyzer by means of cancellation of the fundamental tones was used. Further details on this measurement setup can be found in [9]. The measurement results can be seen in Fig. 4 in dashed lines for both CPWs A and B.

As observed from the measurements, the baseline IMD3 level of the system itself is around -100 dBm for the specified input power, while the measurement noise floor is at -140 dBm. This makes the system nonlinearities predominant over the device for modulation frequencies of 1 MHz and above.

Theoretical thermal conductivity values used in this work are $k_{s,th}$ = 42 $W\cdot m^{-1}\cdot K^{-1}$ and $k_{m,th}$ = 318 $W\cdot m^{-1}\cdot K^{-1}$ for sapphire and gold, respectively [8]. A temperature coefficient of resistivity for gold of α = 0.0037 K^{-1} is also used for both lines [8].

Equation (2) states that the measured intermodulation level is proportional to the square of the thermal impedance, and this is used next to extract the equivalent heat capacity $C_{eq,\Delta V}(f)$ as a function of frequency, implemented as $C_{eq,V}(f)=C_{d,th}(f)\cdot W_{eq}\cdot z$.

The procedure to extract $C_{eq,\Delta V}(f)$ from the measured results by means of (2) starts by obtaining the magnitude of the un-scaled thermal impedance $Z_{th,u}(f)$. Then, $|Z_{th,u}(f)|$ is extrapolated to obtain the theoretical DC value of the thermal resistance, given by $R_{s,\Delta z}$. Finally, $C_{eq,\Delta V}(f)$ is obtained from the following relation:

$$C_{eq,\Delta V}(f)=\sqrt{\frac{\frac{1}{|Z_{th,u}(f)|}-\frac{1}{R_{s,\Delta z}^2}}{f^2}}. \qquad (3)$$

By means of the procedure above, an equivalent heat capacity can be described using a polynomial in log-log scale:

$$C_{d,th}(f)=10^{C_{th,0}+C_{th,1}\log(f)+C_{th,2}\log(f)^2}, \qquad (4)$$

in which $C_{th,0}$=3.94, $C_{th,1}$=-0.784 and $C_{th,2}$=0.0186 are used in the model to simulate the results shown in Fig. 4. A low-order polynomial is used to keep the tendency of the thermal impedance at frequencies above those used for the fitting.

As can be seen in Fig. 4, the agreement between measurements and modeling is very good for both lines using W_{eq}=700 µm. Only a small deviation is observed at the modulation frequency of 2 Hz, which could be an indication of the probes effect.

978-1-4244-7732-6/10/$26.00 ©2010 IEEE

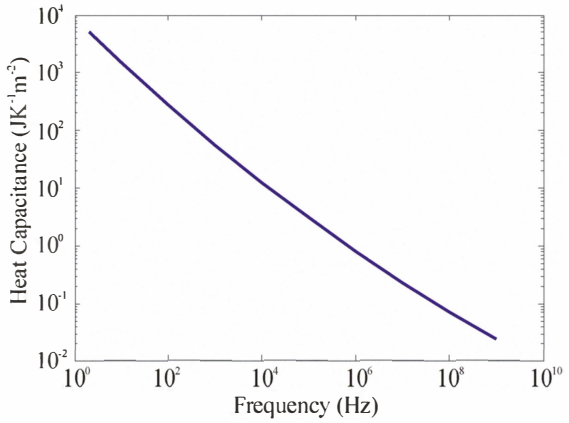

Fig. 5. Extracted heat capacitance $C_{d,th}(f)$.

IV. Discussion

Further research could be performed to relate the extracted frequency-dependent equivalent heat capacity to the heat diffusion area. This may result in a better description of the 3D dissipation process.

The model presented in this work is useful not only for use in nonlinear prediction but also also for simulating the steady-state temperature distribution along the transmission lines. Figure 6 shows the current and temperature distribution for CPW B (l_B = 9.933 mm) with a clear cause-effect relation between them. In fact, the nonlinear generation mechanism presented has some similarities with the 3ω technique [10], in which the generated third harmonic is used to extract the thermal properties of the substrate at low frequencies.

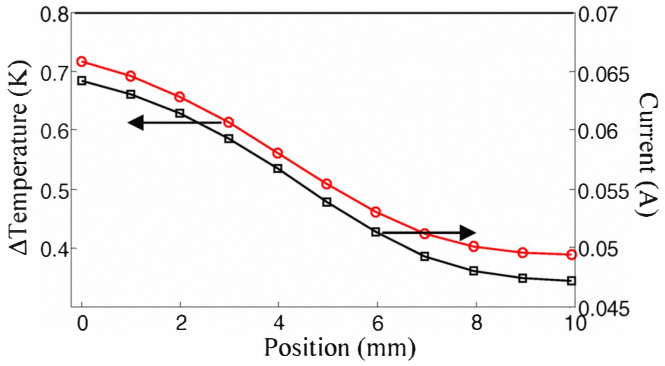

Fig. 6. Simulation of the steady state temperature increment distribution (circles) and current distribution (squares) along CPW B (l_B = 9.933 mm).

Future research will consider metals other than gold, with higher and lower temperature coefficients of resistivity. A thicker metal layer should also be evaluated to check the validity of the model. Substrates with better and poorer thermal conductivities could also be addressed for a better understanding of how the self-heating impacts the IMD3 level.

Acknowledgement

This work was partially supported by the Spanish Government (CICYT) under Grant TEC-2006-13248-C04-02/TCM. E.R. thanks the support from BES-2007-16775. C.C thanks the support from Generalitat de Catalunya, grant 2008-BE2-00196. The authors thank David Novotny for his help in performing this work.

References

[1] A. E. Parker and J. G. Rathmell, "Self-heating process in microwave transistors", in *URSI Commission C Appl. Radio Sci. Workshop, P. Wilkinson, Ed.,* Hobart, Australia, 2004, pp. 1-8

[2] J. Vuolevi, T. Rahkonen, "Analysis of third-order intermodulation distortion in common-emitter BJT and HBT amplifiers," *IEEE Trans. on Circuits and Systems II: Analog and Digital Signal Processing*, vol.50, no.12, pp. 994-1001, Dec. 2003

[3] V. Camarchia, F. Cappelluti, M. Pirola, S. D. Guerrieri, G. Ghione, "Self-consistent electrothermal modeling of class A, AB, and B power GaN HEMTs under modulated RF excitation", *IEEE Trans. on Microwave Theory and Techniques*, vol. 55, pp. 1824-1831, 2007.

[4] J. Vuolevi, T. Rahkonen, J. Manninen, "Measurement technique for characterizing memory effects in RF power amplifiers", *IEEE Trans. on Microwave Theory and Techniques*, vol. 49, no 8, August 2001, pp. 1383-1389

[5] J. R. Wilkerson, K. G. Gard, A. G. Schuchinsky, M. B. Steer, "Electro-thermal theory of intermodulation distortion in lossy microwave components", *IEEE Trans. on Microwave Theory and Techniques*, vol. 56, no. 12, Part 1, pp. 2717-2725, Dec. 2008.

[6] N. B. Hassine, D. Mercier, P. Renaux, D. Bloch, G. Parat, B. Ivira, P. Waltz, C. Chappaz, R. Fillit, S. Basrour, "Self heating under RF power in BAW SMR and its predictive 1D thermal model", *Frequency Control Symposium, 2009 Joint with the 22nd European Frequency and Time forum. IEEE International*, vol., no., April 2009, pp.237-240.

[7] B. Ivira, P. Benech, R. Fillit, F. Ndagijimana, P. Ancey, G. Parat, "Modeling for temperature compensation and temperature characterizations of BAW resonators at GHz frequencies", *IEEE Trans. on Ultrasonics, Ferroelectrics, and Frequency Control,* vol. 55, no. 2, pp. 421-430, Feb. 2008

[8] F. P. Incropera and D. P. de Witt, *Fundamentals of Heat and Mass Transfer*, 5th ed., J. Wiley & Sons N.Y., 2002.

[9] J. Mateu, J. C. Booth, S. A. Schima, "Frequency tuning and spurious signal generation at microwave frequencies in ferroelectric $SrTiO_3$ thin-film transmission lines", *IEEE Trans. on Microwave Theory and Techniques*, vol. 55, no. 2, pp. 392-396, Feb. 2007.

[10] D. G. Cahill, "Thermal conductivity measurement from 30 to 750 K: The 3ω method", *Review of Scientific Instruments*, vol. 61, pp. 802–808, 1990.

978-1-4244-7732-6/10/$26.00 ©2010 IEEE

Passive Intermodulation Due to Self-Heating in Printed Transmission Lines

Eduard Rocas, *Student Member, IEEE*, Carlos Collado, *Senior Member, IEEE*, Nathan D. Orloff, Jordi Mateu, *Senior Member, IEEE*, Alberto Padilla, Juan M. O'Callaghan, *Senior Member, IEEE*, and James C. Booth

***Abstract*—This paper proposes a mechanism by which third-order intermodulation distortion, due to self-heating, is generated in transmission lines. This work shows how transmission lines made of several materials, whose properties are independent of the electric and magnetic fields, can generate important levels of intermodulation distortion. A circuit model supported by finite-element simulations is presented to account for the temperature generation and also for its impact on the nonlinear performance. Closed-form expressions are used to calculate the generated intermodulation products and are derived from the circuit model and compared with simulations. Finally, measurements and simulations of different transmission lines are presented, showing very good agreement.**

***Index Terms*—Intermodulation distortion, nonlinearities, printed lines, self-heating, temperature, thermal effects, transmission lines.**

I. Introduction

INTERMODULATION distortion and harmonic generation in passive transmission lines are usually associated with the dependence of the material properties on the electromagnetic fields. Such is the case for transmission lines made of superconductors [1] or ferroelectric materials [2]. However, several papers have shown the existence of third-order intermodulation distortion, even in transmission lines made of inherently linear materials, such as copper on commercial substrates [3], [4]. In this case, and depending on the speed of the signal modulation, self-heating mechanisms can be the cause of third-order intermodulation distortion, which can generate serious problems in communication systems [5]. This occurs because temperature oscillations cause variations of the material properties without generating harmonics.

The dependence of device performance on temperature has always been a source of concern in the process of designing microwave devices exposed to temperature variations [6], [7], and the correct choice of materials plays a vital role. Attention has usually focused on minimizing the temperature dependence of material properties, as well as on minimizing the loss that is responsible for the temperature rise. Significant temperature dependence of material properties can cause the performance of the device to change considerably over a given temperature range and can also generate nonlinear distortion.

While thermally generated intermodulation distortion is a well-known nonlinear process in power amplifiers where thermal effects have always been a matter of concern [8]–[10], only few papers have been published on this topic. This has happened despite the impact that temperature variations can have on the linear and nonlinear performance of passive microwave devices. The effect of resistive heating on intermodulation distortion generation in electrical contacts is analyzed in detail in [11]. More recently, [12] has shed light by modeling this effect in lumped devices such as attenuators, microwave chip terminations, and coaxial terminations.

Fewer papers have focused on the self-heating process due to the lossy nature of distributed structures, such as transmission lines [13], [14]. The approach found in the 3ω-method [15] is a rigorous procedure to extract thermal material properties by measuring the third-harmonic generated by self-heating in metallic strips at audio frequencies. The existing nonlinear transmission line models [16] do not address these underlying mechanisms of passive intermodulation generation in printed transmission lines and are based strictly on phenomenological approaches. Only [17] and [18] analyze the thermal heating contribution to intermodulation in coaxial waveguides and transmission lines, respectively.

This work presents a circuit model to account for the temperature rise due to self-heating in transmission lines and describes in detail how these temperature variations generate third-order intermodulation distortion. The distributed electromagnetic circuit model of a transmission line is coupled to a thermal domain that models the heat generation and propagation, yielding the temperature at each point of the line. The temperature rise is then used to change the material properties on the electromagnetic domain circuit model. We extend the results in [19] by presenting finite-element thermal simulations to support the model. In addition, we validate the model with measurements

Manuscript received September 15, 2010; accepted October 08, 2010. Date of publication November 29, 2010; date of current version February 16, 2011. This work was supported in part by the U.S. Government and by the Spanish Ministry of Science and Innovation under Grant TEC-2009-13897-C03-01/TCM. The work of E. Rocas was supported by the Spanish Ministry of Education under a Ph.D. Fellowship (BES-2007-16775). The work of C. Collado was supported by the Generalitat de Catalunya under a grant (2008-BE2-00196). The work of A. Padilla was supported under a Ph.D. Fellowship (AP2008-02235). This paper is an expanded paper from the IEEE MTT-S Int. Microwave Symposium, Anaheim, CA, May 23–28, 2010.

E. Rocas and C. Collado are with the Department of Signal Theory and Communications, Universitat Politècnica de Catalunya (UPC), Barcelona 08034, Spain, and are also with the National Institute of Standards and Technology (NIST), Boulder, CO 80305 USA (e-mail: eduard.rocas@tsc.upc.edu).

N. D. Orloff and J. C. Booth are with the National Institute of Standards and Technology (NIST), Boulder, CO 80305 USA.

J. Mateu, A. Padilla, and J. M. O'Callaghan are with the Department of Signal Theory and Communications, Universitat Politècnica de Catalunya (UPC), Barcelona 08034, Spain.

Color versions of one or more of the figures in this paper are available online at http://ieeexplore.ieee.org.

Digital Object Identifier 10.1109/TMTT.2010.2090356

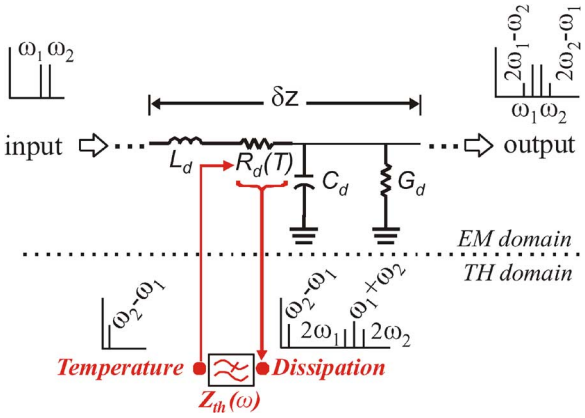

Fig. 1. Passive intermodulation distortion generation process in a transmission line segment of length δz. Resistive losses are responsible for temperature fluctuations that, in turn, change the metal resistivity.

of coplanar waveguides on single crystal sapphire substrates, made with conductors of three different metals in order to give a better understanding of the intermodulation generation mechanism. The assumption of weak distributed nonlinearities is made so that the nonlinearities represent a small perturbation of the linear performance.

Closed-form expressions that allow prediction of intermodulation levels on matched transmission lines are derived from the circuit model implementation and compared with circuit simulations. Finally, the model is tested with intermodulation measurements on lines of several lengths fabricated from different conductor materials with good agreement between modeled and measured results.

II. Mechanism of Passive Intermodulation Generation Due to Self-Heating in Distributed Transmission Lines

The scheme in Fig. 1, in which the two-tone test is reproduced, shows the generation process of third-order intermodulation distortion due to self-heating in a transmission line along the z-axis. The input signals, ω_1 and ω_2, can also be understood as an AM modulated signal with carrier suppression centered at ω_0 with an envelope frequency $\Delta\omega/2$ so that $\omega_1 = \omega_0 - \Delta\omega/2$ and $\omega_2 = \omega_0 + \Delta\omega/2$.

If a low-loss substrate is considered, the loss due to the conductor dominates and the dissipated power $Q_d(z,\omega)$ in each elemental segment ∂z of transmission line is proportional to the square of the current through that segment. This results in dissipated power, with frequency components at dc, $\Delta\omega$, $2\omega_1$, $2\omega_2$, and $\omega_1 + \omega_2$. Each of the frequency components of the dissipated power gives rise to temperature oscillations T, according to the corresponding thermal impedance $Z_{\rm th}(\omega)$ at each specific frequency [9]

$$T(z,\omega) = Z_{\rm th}(\omega) Q_d(z,\omega). \tag{1}$$

As a result, the steady-state temperature rise changes the material properties and, as a result, the linear performance of the device, as well. On the other hand, the oscillating temperature generates third-order intermodulation distortion. The slow dynamics related with the heat propagation in a media translates into a low-pass-filter behavior of the thermal impedance [20], thus making the dissipated signal at $\Delta\omega$ the most relevant oscillating temperature component. As in the steady-state case, temperature variations at $\Delta\omega$ can change materials properties; for example, the metal resistivity, resulting in third-order intermodulation distortion at $2\omega_1 - \omega_2$ and $2\omega_2 - \omega_1$. In this work, a temperature-independent dielectric is considered. A detailed scheme of the generation process in an infinitesimal section of transmission line can be seen in Fig. 1.

As a result of the above-described process, measurements of the third-order intermodulation signals at different separations between tones might be used to unveil the low-pass filter shape of the thermal impedance [10] since

$$P_{\rm 3IMD} \propto |Z_{\rm th}(\Delta\omega)|^2 \tag{2}$$

where $P_{\rm 3IMD}$ is the third-order intermodulation distortion power.

III. Self-Heating Mechanism Model

A circuit model of a transmission line, based on the previously described mechanism, could be used for the analysis and simulation of nonlinear effects under any type of input signal. Further, it could also be used, for example, to predict nonlinearities in more complex devices that make use of these transmission lines, such as filters [21]. The challenge of such a model, however, is based on the interaction of two physical domains, the electromagnetic and thermal domains, both of which must be properly modeled.

A. Electromagnetic Domain

A distributed implementation of the electromagnetic domain of a transmission line allows for relating the measured observables with the material properties [1]. The transmission line is constructed as a cascade of cells. Each cell contains the distributed parameters modeling a segment of a transmission line $R_d(T)$, L_d, C_d, and G_d. These stand for the temperature-dependent distributed resistance and the distributed inductance, capacitance, and conductance, respectively [22]. The resulting nonlinear telegrapher equations are

$$\frac{\partial v(z,t)}{\partial z} = -R_d(T) i(z,t) - L_d \frac{\partial i(z,t)}{\partial t} \tag{3}$$

$$\frac{\partial i(z,t)}{\partial z} = -G_d v(z,t) - C_d \frac{\partial v(z,t)}{\partial t}. \tag{4}$$

The distributed resistance $R_d(T)$ has contributions from each of the conductors in the transmission line, which act as heat generators. This allows us to simulate the temperature rise at each conductor independently and also to simulate the contribution to the intermodulation arising from each conductor. In a coplanar waveguide, the center conductor resistance $R_{d,N}(T)$ and the ground planes resistance $R_{d,M}(T)$ can be considered separately, as shown in Fig. 2

If a low-loss nondispersive substrate is used, G_d is negligible and C_d is constant over frequency. On the other hand, $R_{d,X}(T)$ and L_d are frequency-dependent and need to be properly described at each frequency point.

Each contribution to the distributed resistance $R_{d,N}(T)$ and $R_{d,M}(T)$ can be expanded by use of a first-order Taylor's series,

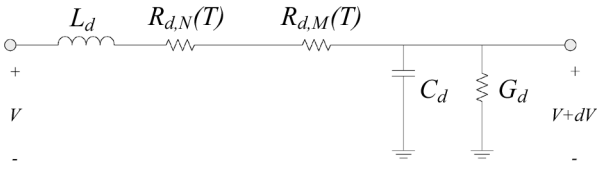

Fig. 2. Electromagnetic-domain model of an infinitesimal section of a transmission line.

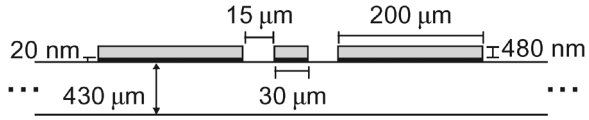

Fig. 3. Dimensions of the coplanar waveguides used in this work.

and casting it into a temperature-invariant term and a temperature-dependent term

$$R_{d,X}(T) = R_{d,X,T_R} + \Delta R_{d,X} T \tag{5}$$

where $X = N$ or M stand for the center conductor and ground planes, respectively, and R_{d,X,T_R} set the distributed resistance at room temperature T_R. The relation between the parameter $\Delta R_{d,X}$ and the temperature-dependent resistivity of the conductors is detailed in Appendix I.

B. Thermal Domain

A thermal model implementation of a transmission line should be able to predict the steady-state temperature rise and temperature oscillations that lead to intermodulation generation. Moreover, a physical relation with the material thermal properties and device geometry is necessary to allow the model to predict the nonlinear distortion of a device in the design stage.

1) Heat Generation in a Transmission Line: The geometry of a regular coplanar waveguide consists of two ground planes on each side of a center conductor. The metal layer varies, generally, from tens to thousands of nanometers thick and is deposited on a low-loss substrate. In such a structure, the generated heat in the metal strip is mostly dissipated by conduction through the substrate. This is because of its low thermal resistance to heat flow when compared to radiation and convection effects [20]. Fig. 3 shows the dimensions of the coplanar waveguides used in this work.

The first step toward the construction of a thermal model of a coplanar waveguide is to identify the heat sources. As previously mentioned, this work considers negligible dielectric losses in the substrate so that metal resistivity is the only source of dissipation. Fig. 4 illustrates the simulated current distribution at the beginning of the line $z = 0$ of a coplanar waveguide, of the same dimensions as in Fig. 3, and made of gold on a sapphire substrate with a thin titanium adhesion layer. The transmission line is designed, considering dispersion, to be roughly matched at 6 GHz by use of an electric resistivity of $\rho_e = 27.67\ \mathrm{n\Omega \cdot m}$. The line is driven by two tones of 20 dBm each, where the upper tone is set at 6 GHz and the lower is 1 kHz apart.

In the simulations of Fig. 4, the current density peaks are at the edges of the center conductor and at the inner edges of the ground planes. This has a direct translation in the location of

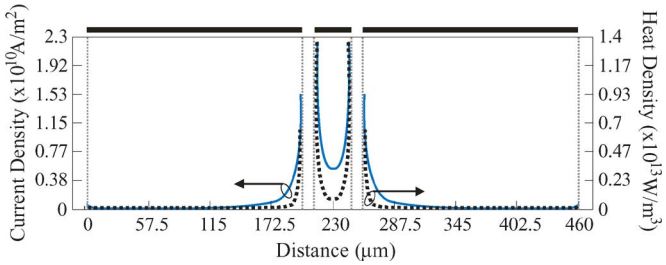

Fig. 4. Current distribution and joule heat at the beginning of a coplanar waveguide, driven by two tones at 20 dBm.

heat sources since the heat generated per unit volume can be expressed as [12]

$$Q = J^2 \rho_e \tag{6}$$

where J is the current density in $\mathrm{A \cdot m^{-2}}$ and ρ_e is the electric resistivity in $\Omega \cdot \mathrm{m}$. Fig. 4 also illustrates the heat density, obtained by use of finite-element simulations [23], due to (6).

The heat density surface integral on the center conductor results in an average dissipated power of 9.26 $\mathrm{W \cdot m^{-1}}$ versus 3.54 $\mathrm{W \cdot m^{-1}}$ for the ground planes, which clearly illustrates the fact that the center conductor contributes more to the overall dissipation. This gives an idea of the correspondent contribution of each metal strip to the distributed resistance, which follows the relation

$$R_{d,X,T_R} = \frac{P_{d,X}}{I_{\mathrm{rms}}^2} \tag{7}$$

where $P_{d,X}$ and I_{rms} are the average dissipated power per unit length and the root mean square (rms) current, respectively.

For the coplanar waveguide under study, we used finite-element software [23] to get the distributed resistance contributions arising from the center conductor $R_{d,N,T_R} = 2281\ \Omega/\mathrm{m}$ and the ground planes $R_{d,M,T_R} = 882\ \Omega/\mathrm{m}$ at 6 GHz and at room temperature. Therefore, the center conductor is expected to generate a higher temperature contribution, given its higher losses.

2) Steady-State Temperature Rise: Temperature rise, as a result of heat generation, follows a low-pass filter behavior, and thus is frequency dependent. Therefore, a clear idea of the temperature profile on the cross section of the coplanar waveguide is necessary to propose a thermal model implementation. Fig. 5 shows the steady-state temperature on the cross section of the previously presented coplanar waveguide, obtained with finite-element simulation [23]. Radiation and convection effects were shown to be negligible through simulations. Table I contains the material properties used for the finite-element simulations utilized in this work.

The electric resistivity values are obtained by measurements of the transmission lines, explained in Section V. Other properties for Au, Pt, and Ti can be found in [24]. Sapphire properties are found in [25] and PdAu density and thermal conductivity is found in [26]. The specific heat value of PdAu is inferred from the Pd and Au specific heat since specific heat values for these metals are similar.

As shown in Fig. 5, the temperature distribution across the center conductor can be considered uniform, as it changes by less than 3% from the edge to the center of the strip. The ground

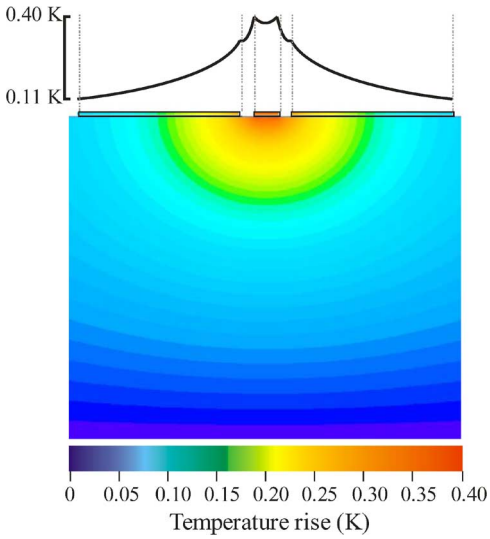

Fig. 5. Steady-state temperature rise profile on the cross section of the coplanar waveguide.

TABLE I
MATERIAL PROPERTIES USED IN THE FINITE-ELEMENT SIMULATIONS

	Au	Pt	PdAu	Ti	Sapphire
Resistivity, ρ_e (nΩ·m)	27.67	238.9	444.18	450	-
Thermal conductivity, k (W·m^{-1}·K^{-1})	301	69.1	26.1	17	42
Specific heat, c_p (J·kg^{-1}·K^{-1})	128	134	190	528	750
Density, η (kg·m^{-3})	19320	21450	12023	4500	3970

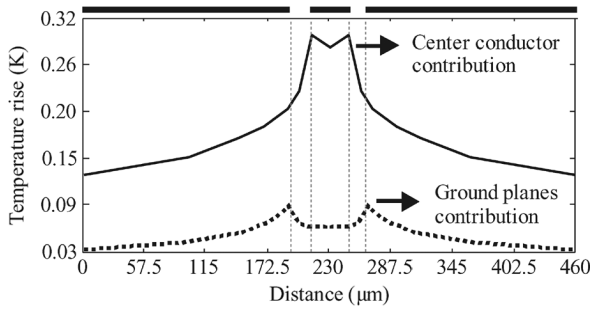

Fig. 6. Steady-state temperature contributions arising from the dissipation in the center conductor and the ground planes, independently.

planes, though, show a clear temperature gradient. Thus, additional finite-element simulations, by use of specifically implemented software,[1] have unveiled the temperature-rise contributions arising from the center conductor and the ground planes independently. Fig. 6 shows the results of the simulation, where the ground planes contribute less to the overall temperature rise than the center conductor. A reasonable approximation of the temperature rise in the center conductor can, therefore, be obtained by considering only its dissipation.

3) Oscillating Temperature: The thermal penetration depth is defined as $\delta_p = 4\sqrt{k/c_p\eta\omega}$, which illustrates the fact that the resistance to heat propagation through materials depends not only on the material properties, but also the frequency [20]. In the previous equation, k is the thermal conductivity, η is the density, c_p is the specific heat, and ω is the frequency of the temperature oscillations $\omega = \Delta\omega$. This translates into locally accentuated temperature distributions at higher frequencies with smaller maximum values. Fig. 7 shows the oscillating temperature profile at the surface of the cross section of the coplanar waveguide for different envelope frequencies, obtained by means of simulations.

Simulations reveal that the temperature rise at the center conductor can be considered totally independent from the dissipation in the ground planes, for this specific geometry, when the envelope frequency increases. This allows the simplification of the model by considering only the center conductor in the thermal domain. With the equations in Section VI, a comparison between the contributions levels to the third-order intermodulation distortion, confirm the negligible contribution from the ground planes.

Fig. 7 also reveals that above a certain envelope frequency, a uniform temperature distribution in the center conductor, which is the main contribution to self-heating nonlinearities, can no longer be considered. The impact that the frequency-dependent temperature profile has on the distributed resistance is embedded in the frequency-dependent thermal impedance $Z_{\rm th}(\omega)$. Therefore, the model will provide an effective temperature rise at each frequency. In other words, the change produced in the distributed resistance by the existing temperature profile is the same as the change produced by a uniform effective temperature.

4) Thermal Impedance: A complete thermal-domain circuit implementation should be 3-D to consider heat flow along the z-axis, laterally and vertically through the substrate. The thermal domain implementation in Fig. 8 makes use of a series impedance $Z_{\Delta z,{\rm th},S}(\omega)$, which models heat flow along the center conductor in the z axis direction. It also includes a parallel impedance $Z_{\Delta z,{\rm th},P}(\omega)$ that models heat flow both laterally and vertically from the center conductor to the substrate.

The steady-state series and parallel thermal impedances are de-embedded by performing finite-element simulations with specifically implemented 3-D electrothermal finite-element software for different line lengths and for all different metals. The results are shown in Fig. 9, where we can observe that the parallel thermal impedance is roughly the same for all three metals. This indicates that the substrate has a dominating effect and is inversely proportional to length. On the other hand, the series impedance is different for all metals and is higher for poorer thermal conductors.

C. Electro-Thermal Coupling

Once the circuit implementations of both electromagnetic and thermal domains have been explained, the next step is to set the interaction between them. This interaction is a bidirectional process in the sense that the generated heat from the electromagnetic domain changes the temperature. This, in turn, changes the distributed resistance in the electromagnetic domain and, therefore, the generated heat.

The transmission line is implemented in Δz-long electrothermal cell segments. Heat generation by the Joule effect in

[1]Specifically implemented 3-D electro-thermal finite-element software.

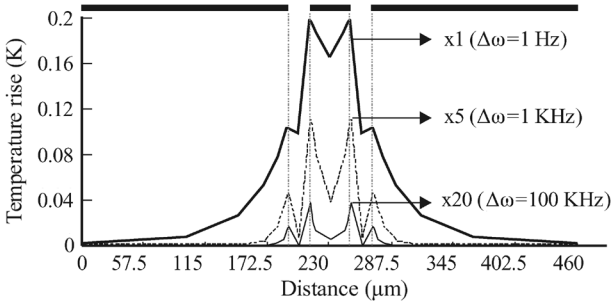

Fig. 7. Temperature distributions at different envelope frequencies. The plots have been scaled for better visualization purposes.

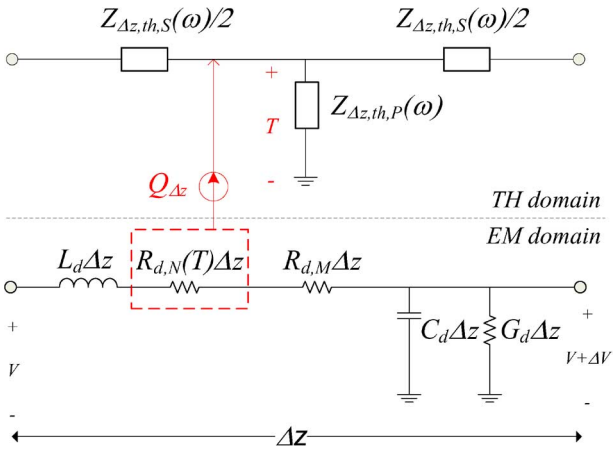

Fig. 8. Complete electrothermal circuit model of a Δz segment of a transmission line.

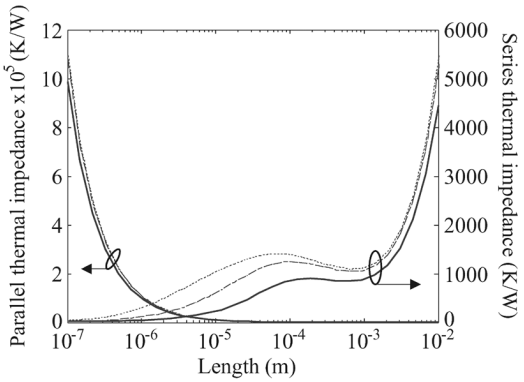

Fig. 9. Steady-state series and parallel thermal impedances as a function of length. The solid line represents Au, whereas the dashed line represents PdAu, and the dotted line represents Pt.

the center conductor at a certain position z of the transmission line can be expressed as

$$Q_{\Delta z}(z,t) = Q_d(z,t)\Delta z. \tag{8}$$

Due to the analogy between heat and electric current in the heat equation, a current source is used to inject the generated heat $Q_{\Delta z}(z,t)$ in its correspondent thermal domain. Temperature rise, which is the analog of voltage in the thermal circuit domain, is then used to change the distributed resistance value $R_{d,N}(T)$.

The series thermal impedance has been checked to play a negligible role in the heat flow process by comparing the steady-state temperature rise along a transmission line with the model with $Z_{\Delta z,\mathrm{th},S}(0)$ and with an open circuit instead of $Z_{\Delta z,\mathrm{th},S}(0)$ to finite-element simulations with specifically implemented 3-D electrothermal finite-element software, as shown in Section V.C-1. Therefore, a simplified model that makes use of only the parallel impedance will be used throughout this work.

The parallel impedance has a linear relation with length so that $Z_{\Delta z,\mathrm{th},P}(\omega) = Z_{d,\mathrm{th},P}(\omega)/\Delta z$, where $Z_{d,\mathrm{th},P}(\omega)$ is the thermal impedance per unit length in the z axis direction. The proposed circuit implementation of $Z_{\Delta z,\mathrm{th},P}(\omega)$ is a resistance $R_{\Delta z,\mathrm{th}}$ in parallel with a frequency-dependent capacitance $C_{\Delta z,\mathrm{th}}(\omega)$ with $R_{\Delta z,\mathrm{th}} = R_{d,\mathrm{th}}/\Delta z$ and $C_{\Delta z,\mathrm{th}}(\omega) = C_{d,\mathrm{th}}(\omega)\cdot\Delta z$. The term $R_{d,\mathrm{th}}$ in K · m/W represents the steady-state distributed thermal resistance to heat flow. $C_{d,\mathrm{th}}(\omega)$ is the distributed volumetric heat capacity that embeds the frequency dispersive effects.

IV. Closed-Form Expressions

Given the model presented in this work, closed-form expressions of the circuit implementation can be derived. In the present derivation, a matched transmission line is assumed despite extended expressions for mismatched transmission lines could be obtained by use of the procedure explained in [27].

A. Heat Generation

We consider a matched transmission line fed with two tones, ω_1 and ω_2, in close frequency. The current at each of the fundamental frequencies could be described as

$$i_n(z,t) = |I_n|e^{-\alpha_n z}\cos(\omega_n t + \phi_n - \beta_n z) \tag{9}$$

with $n = 1, 2$. In (9), $I_n = |I_n|e^{j\phi_n}$ and α_n, β_n, and ϕ_n are the attenuation constant, phase constant, and phase, respectively. Therefore, the instantaneous dissipated power per unit length $Q_d(z,t)$, due to resistive losses in the center conductor, is

$$Q_d(z,t) = \frac{\partial P_d(z,t)}{\partial z} = R_{d,N,T_R}\left(\sum_{n=1,2} i_n(z,t)\right)^2 \tag{10}$$

where $P_d(z,t)$ is the instantaneous propagating power, and as expected for a two-tone test, the quadratic nature of power dissipation leads to several spectral components

$$\begin{aligned} Q_d(z,t) = {} & R_{d,N,T_R} \\ & \cdot \mathrm{Re}\left(\frac{1}{2}|I_1|^2 e^{-2\alpha_1 z} + \frac{1}{2}|I_2|^2 e^{-2\alpha_2 z}\right. \\ & + I_1^* I_2 e^{j\Delta\omega t - \gamma_v z} + \frac{1}{2} I_1^2 e^{j2\omega_1 t - 2\gamma_1 z} \\ & + \frac{1}{2} I_2^2 e^{j2\omega_2 t - 2\gamma_2 z} \\ & \left. + I_1 I_2 e^{j(\omega_1+\omega_2)t - (\gamma_1+\gamma_2)z}\right) \end{aligned} \tag{11}$$

with $\gamma_v = (\alpha_1 + \alpha_2) + j(-\beta_1 + \beta_2)$, where $\gamma_n = \alpha_n + j\beta_n$ is the propagation constant of I_n.

As in the 3ω-technique [15], we assume that heat flows mostly perpendicular to the substrate with a negligible heat flow along the z axis of the line so only $Z_{d,\mathrm{th},P}(\omega)$ is considered.

Equation (1), in which $Q_d(z,\omega)$ is the Fourier transform of $Q_d(z,t)$ at frequency ω, states the physical relation between heat dissipation and temperature through the thermal impedance. Therefore, by use of the dissipated power at the envelope frequency $Q_d(z,\omega) = R_{d,N,T_R} I_1^* I_2 e^{-\gamma_v z}$, the temperature distribution at the envelope frequency $\Delta\omega$ is

$$T(z,\Delta\omega) = Z_{d,\mathrm{th},P}(\Delta\omega) R_{d,N,T_R} I_1^* I_2 e^{-\gamma_v z}. \quad (12)$$

We can provide the steady-state temperature along the line because of its impact on the linear performance of the device, where $Z_{d,\mathrm{th},P}(0) = R_{d,\mathrm{th}}$

$$T(z,0) = R_{d,\mathrm{th}} R_{d,N,T_R} \left(\frac{1}{2}|I_1|^2 e^{-2\alpha_1 z} + \frac{1}{2}|I_2|^2 e^{-2\alpha_2 z} \right). \quad (13)$$

B. Temperature-Induced Intermodulation Distortion

As previously stated, a temperature-independent dielectric is considered so that only the $\Delta R_{d,N}$ term that appears in (5) is responsible for the nonlinear behavior so long as it quantifies the temperature dependence of the distributed resistance. Therefore, for a matched transmission line with negligible heat propagation along z, the nonlinear voltage per unit length can be obtained by introducing (5) in (3) and separating the resulting equation in a linear term and a nonlinear term, where the nonlinear term is

$$\frac{\partial v_{nl}(z,t)}{\partial z} = \Delta R_{d,N} T(z,t) i(z,t) \quad (14)$$

Considering the case of a two-tone test in which the line is driven by two different tones (9) at frequencies ω_1 and ω_2, the frequency component $\omega_{12} = 2\omega_1 - \omega_2$ of (14) would be

$$\frac{\partial V_{nl,\omega_{12}}(z)}{\partial z} = \frac{1}{2}\Delta R_{d,N} T^*(z,\Delta\omega) I_1 e^{-\gamma_1 z} \quad (15)$$

where $T(z,\Delta\omega)$ is the temperature oscillations at the envelope frequency $\Delta\omega$. By substituting (12) into (15), we obtain

$$\frac{\partial V_{nl,\omega_{12}}}{\partial z} = \frac{1}{2}\Delta R_{d,N} I_1^2 I_2^* Z_{d,\mathrm{th},P}^*(\Delta\omega) R_{d,N,T_R} e^{-\gamma_c z} \quad (16)$$

with $\gamma_c = (2\alpha_1 + \alpha_2) + j(2\beta_1 - \beta_2)$. If we combine the telegrapher equations

$$\frac{\partial^2 i}{\partial z^2} = L_d C_d \frac{\partial^2 i}{\partial t^2} + (R_d C_d + L_d G_d)\frac{\partial i}{\partial t} + R_d G_d i + C_d \frac{\partial^2 v_{nl}}{\partial z \partial t} + G_d \frac{\partial v_{nl}}{\partial z} \quad (17)$$

which can be rewritten as

$$\frac{\partial^2 I_i(z)}{\partial z^2} = \gamma_i^2 I_i(z) + \frac{\gamma_i}{Z_i}\frac{\partial V_{nl,i}}{\partial z} \quad (18)$$

where $i = 1, 2$ refers to frequencies ω_1 and ω_2 with

$$\gamma_i = \sqrt{(R_{d,i} + j\omega_i L_d)(G_d + j\omega_i C_d)} \quad (19)$$

and

$$Z_i = \sqrt{\frac{R_{d,i} + j\omega_i L_d}{G_i + j\omega_i C_d}}. \quad (20)$$

We now substitute (16) in (18) to get

$$\frac{\partial^2 I_{12}(z)}{\partial z^2} = \gamma_{12}^2 I_{12}(z) + \frac{\gamma_{12}}{Z_{12}}\frac{1}{2}\Delta R_{d,N} I_1^2 I_2^* Z_{d,\mathrm{th},P}^* \times(\Delta\omega) R_{d,N,T_R} e^{-\gamma_c z} \quad (21)$$

where the subscript 12 refers to frequency $\omega_{12} = 2\omega_1 - \omega_2$. Equation (21) can be solved for the nonlinear current along the line

$$I_{12}(z) = \frac{1}{2Z_{12}}\Delta R_{d,N} I_1^2 I_2^* R_{d,N,T_R} Z_{d,\mathrm{th},P}^*(\Delta\omega) \times \frac{\gamma_{12}\left(e^{-\gamma' z} - 1\right)}{\gamma'(\gamma' + 2\gamma_{12})} e^{-\gamma_{12} z} \quad (22)$$

with

$$\gamma' = \gamma_c - \gamma_{12} = (2\alpha_1 + \alpha_2 - \alpha_{12}) + j(2\beta_1 - \beta_2 - \beta_{12}). \quad (23)$$

Equation (22) can be approximated to

$$I_{12}(z) = \frac{1}{8Z_{12}}\Delta R_{d,N} I_1^2 I_2^* R_{d,N,T_R} Z_{d,\mathrm{th},P}^*(\Delta\omega) \times \frac{(e^{-2\alpha_1 z} - 1)}{\alpha_1} e^{-\gamma_{12} z}. \quad (24)$$

Thus, if we assume $|I_1| = |I_2|$, the power delivered to a matched load is

$$P_{L,12} = k_{12} \left|\Delta R_{d,N} Z_{d,\mathrm{th},P}(\Delta\omega) R_{d,N,T_R}\right|^2 |I_1|^6 \quad (25)$$

with

$$k_{12} = \frac{(e^{-2\alpha_0 l} - 1)^2 \mathrm{Re}(Z_{12})}{128|Z_{12}|^2 \alpha_0^2} e^{-2\alpha_{12} l}. \quad (26)$$

C. Validation of Expressions With Simulations

The above-presented expressions are validated by making use of circuit simulations with the electrothermal model implemented with 100 cells, such as the one shown in Fig. 8. Both the equations and electromagnetic domain of the circuit model use the distributed parameters of the gold line previously used in the thermal analysis.

Though understanding the intermodulation process is the final goal of this work, an important preliminary step consists in checking the temperature rise. Simulations with the model have been performed by using two tones, at 20 dBm each, and at variable frequency spacing between them. The upper tone is fixed at 6 GHz. The same frequency-dependent thermal impedance $Z_{d,\mathrm{th},P}(\omega)$ is used on both equations and simulation.

Equation (13), which gives the steady-state temperature distribution along the z axis, has been checked with a matched transmission line, resulting in perfect agreement. To better il-

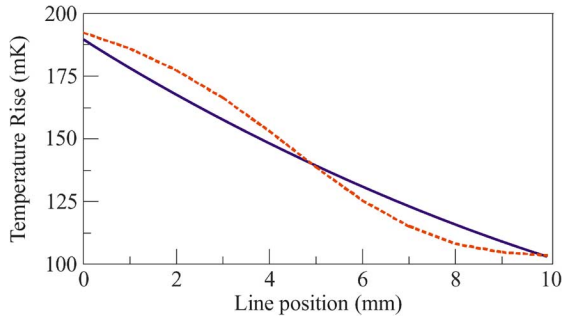

Fig. 10. Steady-state temperature rise along the 9.93-mm gold line. Solid line is using (13) and dashed line represents the results from simulation.

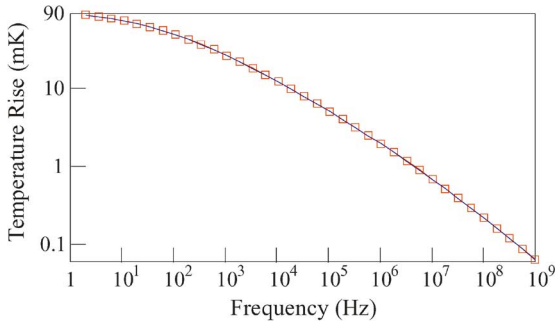

Fig. 11. Temperature rise at $z = 9.93$ mm of a 9.93-mm gold line for a wide range of envelope frequencies. Squares and solid line are simulation and equation, respectively.

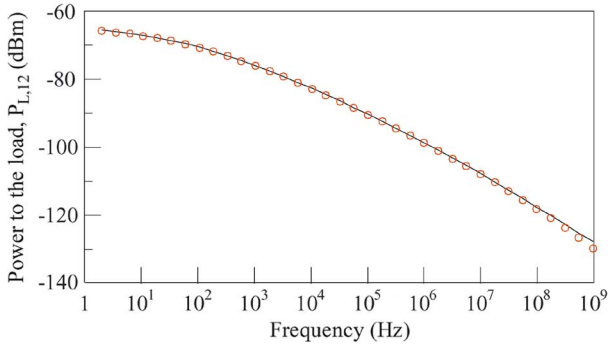

Fig. 12. Power delivered to a matched load at the end of the 9.93-mm gold line. Circles and solid line are simulation and equation respectively.

lustrate this with a real case, Fig. 10 shows the results for (13) and the circuit model implementation of a 9.93-mm gold line, and $\Delta\omega = 100$ Hz, where simulations give a small ripple due to the imaginary part of $Z_0 = 50.35 - j2\ \Omega$. For the real 9.93-mm gold line circuit implementation, distributed parameters extracted from measurements are used to construct the transmission line as a cascade of cells.

Additionally, temperature rise oscillations are validated, by use of (12) and simulations, at different envelope frequencies at $z = 9.93$ mm (Fig. 11).

Once the equations of the temperature rise have been validated, the nonlinear signal, generated as a consequence of temperature oscillations, can be evaluated. Fig. 12 shows the result of (25) and simulations of the intermodulation power delivered to a matched load at $z = 9.93$ mm for a wide range of envelope frequencies.

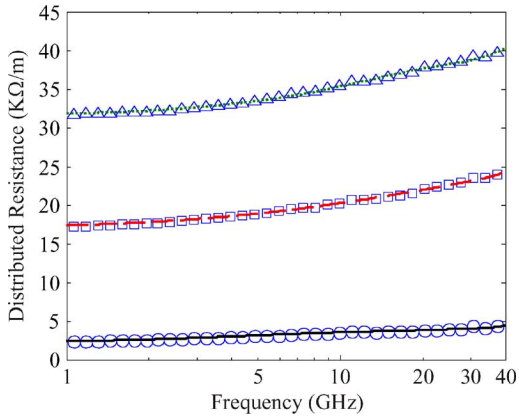

Fig. 13. Extracted distributed resistance (symbols) and polynomial fit (lines) for the different coplanar waveguides. Circles and solid line represent gold, squares and dashed line represent platinum, and triangles and dotted line represent palladium-gold.

V. Measurements and Results

A test wafer has been constructed to validate the model with measurements. Metals with different temperature coefficients of resistivity have been selected to construct coplanar waveguides of different lengths. To check the model, measurements of the resistivity at different temperatures have been performed. Third-order intermodulation distortion measurements for a wide range of envelope frequencies have also been used.

A. Test Wafer

Coplanar waveguides, with the cross-section geometry shown in Fig. 3, have been constructed following standard fabrication techniques on a sapphire substrate, chosen for its low dielectric losses at microwave frequencies. Different metals have been deposited, including gold (Au), platinum (Pt), and palladium-gold (PdAu) with a 55% gold content. The reason for choosing these metals is that they offer different combinations of resistivity values and resistivity change with temperature, which translates into different levels of intermodulation distortion. Three transmission lines, A, B, and C for each type of metal, have been measured. Their lengths are $l_A = 1$ mm, $l_B = 4.2$ mm, and $l_C = 9.93$ mm, to demonstrate the distributed effects.

B. Linear Measurements and Model

The first step in constructing the linear part of the circuit model is to obtain the distributed parameters of the fabricated transmission lines. The procedure used in this work consists in performing a multiline thru-reflect-line (TRL) calibration to obtain the propagation constant. It is then used, along with an impedance comparison method, to obtain the distributed parameters R_{d,T_R}, L_d, C_d, and G_d. Details on this procedure can be found in [28].

The linear measurements have been performed at a low power, -5 dBm, to ensure the linear regime of the devices. Results for the extracted distributed resistance and inductance are shown in Figs. 13 and 14, respectively.

The extracted values of the distributed conductance G_d are below the sensitivity of the measurements; its impact is, there-

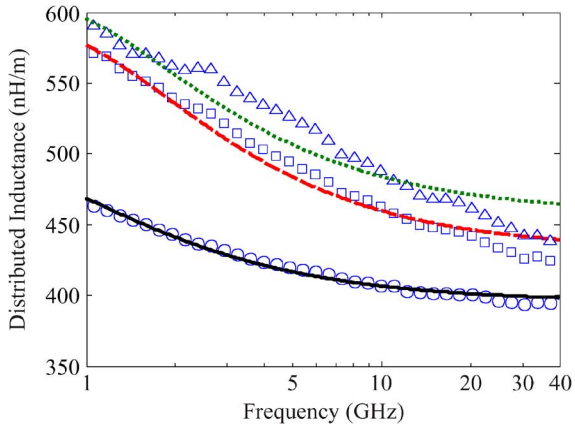

Fig. 14. Extracted distributed inductance (symbols) and polynomial fit (lines) for the different coplanar waveguides. Circles and solid line represent gold, squares and dashed line represent platinum, and triangles and dotted line represent palladium-gold.

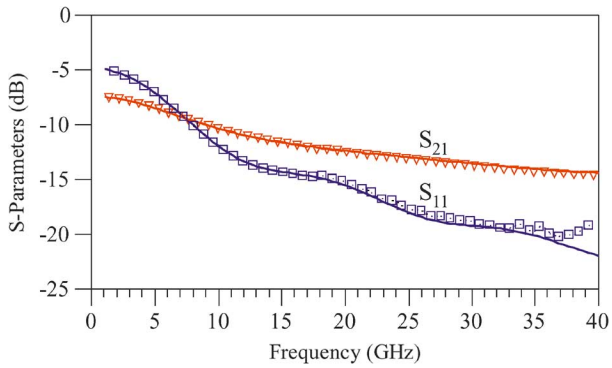

Fig. 15. Measured and simulated S-parameters for line B, made of palladium-gold. The line length is 4.2 mm. Squares and triangles represent measurements. Solid lines represent simulation.

fore, considered negligible. On the other hand, the extracted distributed capacitance, which is constant over frequency due to the nondispersive nature of sapphire, has a value of $C_d = 162$ pF/m.

The presented extracted distributed resistance and inductance are fitted to polynomials so that they can be easily used in the circuit model implementation. Next, the calibrated S-parameters from measurements are compared to the simulated S-parameters of the circuit implementation for each line to check that the extraction procedure is correct.

For example, Fig. 15 illustrates both measured and simulated S-parameters for PdAu line B. Characteristic impedances obtained at 6 GHz are $Z_{0,\mathrm{Au}} = 50.35 - j2\ \Omega$, $Z_{0,\mathrm{Pt}} = 60.16 - j25.64\ \Omega$, and $Z_{0,\mathrm{PdAu}} = 69.53 - j40.29\ \Omega$.

C. Nonlinear Measurements and Model

Once the linear measurements and modeling are complete, the thermal impedance that correctly predicts the temperature along the line is obtained. An accurate temperature simulation is crucial to properly simulate its effect on the metal resistivity and also to predict the third-order intermodulation generation. In the model presented, the thermal resistance $R_{d,\mathrm{th}}$ and the thermal capacitance per unit length $C_{d,\mathrm{th}}(\omega)$ represent the resistance to heat flow at steady state and its frequency dependence, respectively. These can, therefore, be solved separately. As stated in (2), the third-order intermodulation measurements unveil the frequency dependence of the thermal impedance, which is used in this work to obtain $C_{d,\mathrm{th}}(\omega)$. On the other hand, finite-element thermal simulations are used to obtain $R_{d,\mathrm{th}}$.

TABLE II
ELECTRIC AND THERMAL PARAMETERS OF THE CENTER CONDUCTOR AT $z = 0$ USING TWO TONES AT 20 dBm EACH

	Au	Pt	PdAu
I_{Total} (A)	$6.4{\cdot}10^{-2}$	$5.6{\cdot}10^{-2}$	$5.1{\cdot}10^{-2}$
Q_d (W·m^{-1})	9.26	50.3	80.5
T_{Av} (K)	0.29	1.6	2.65
$R_{d,\mathrm{th}}$ (K·m/W)	$3.13{\cdot}10^{-2}$	$3.18{\cdot}10^{-2}$	$3.29{\cdot}10^{-2}$

1) Finite-Element Thermal Simulations: The thermal resistance $R_{d,\mathrm{th}}$ sets the steady-state temperature, given a certain heat dissipation in the center conductor. It depends not only on the material properties of the metal and substrate, but also the geometry of the strip. Finite-element simulations can be used to obtain the thermal resistance $R_{d,\mathrm{th}}$ with (1) as the division of temperature over heat.

We look at the heat density through the line, shown in Fig. 4, and perform the surface integral at the center conductor. A steady-state thermal simulation is done with [23] to obtain the temperature profile on the cross section of the line. Table II summarizes the current I_{Total} and heat flux Q_d at $z = 0$ for all types of metal transmission lines, the average temperature rise on the center conductor T_{AV}, and the thermal resistance $R_{d,\mathrm{th}}$ obtained.

As can be seen from Table II, the change in the thermal resistance $R_{d,\mathrm{th}}$ is around 5% for the three metals. This implies that the upper metal layer plays a negligible role in how the heat flows to the substrate. Approximate values for $R_{d,\mathrm{th}}$ might be obtained with closed-form expressions such as those found in [13] and [14] to get $R_{d,\mathrm{th}} = 0.026$ K · m/W and $R_{d,\mathrm{th}} = 0.028$ K · m/W, respectively, neglecting the titanium adhesion layer.

The circuit model can also be used to simulate the temperature distribution along the line. To check this, we performed 3-D steady-state thermal finite-element simulations with specifically implemented 3-D electrothermal finite-elelent software. This is done by use of the current distribution previously obtained with the circuit model, as shown in Fig. 16.

Results in Fig. 16 show the contribution to temperature rise due to dissipation in the center conductor for the circuit model and finite-element simulations. There is total agreement between them. Moreover, Fig. 16 also shows the total temperature rise in the center conductor as a consequence of dissipation in the center conductor and the ground planes obtained with finite-element simulations. The simulations for the circuit model have been performed with and without the series thermal impedance $Z_{\Delta z,\mathrm{th},S}(\omega)$, which totally overlap.

These results confirm that, for the given geometry, the heat propagation along the z axis is negligible and the circuit model can be used to estimate the total temperature rise in the center conductor.

2) Third-Order Intermodulation Distortion: Forward third-order intermodulation distortion measurements, of $2\omega_1 - \omega_2$ and $2\omega_2 - \omega_1$, have been performed on all lines by means of the

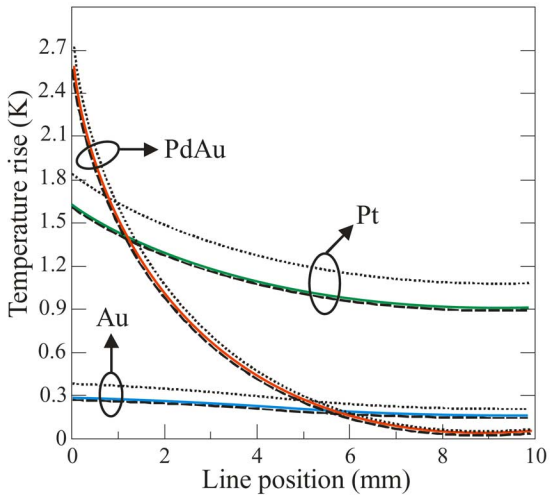

Fig. 16. Steady-state temperature rise profiles along the C lines for the different metals. Solid and dashed lines represent the contribution to temperature rise in the center conductor, as a consequence of its dissipation, from using the circuit model and finite elements, respectively. The dotted lines represent the total temperature rise in the center conductor, as a consequence of dissipation in both the center conductor and the ground planes, obtained with finite-element simulations. Simulations using the circuit model, with $Z_{\Delta z,\mathrm{th},S}(\omega)$ and with an open circuit instead of $Z_{\Delta z,\mathrm{th},S}(\omega)$, overlap.

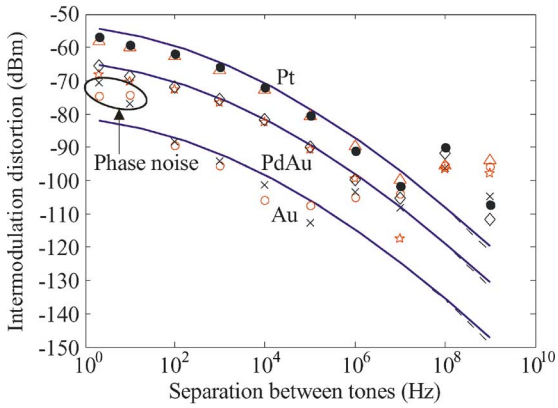

Fig. 17. Measured and simulated third-order intermodulation in A line, $l_{\mathrm{A}} = 1$ mm. $2f_1 - f_2$ (dashed line) and $2f_2 - f_1$ (solid line) overlap for all the simulations. Unfilled circles and crosses represent $2f_1 - f_2$ and $2f_2 - f_1$ for Au. Triangles and filled circles represent $2f_1 - f_2$ and $2f_2 - f_1$ for Pt. Stars and diamonds represent $2f_1 - f_2$ and $2f_2 - f_1$ for PdAu.

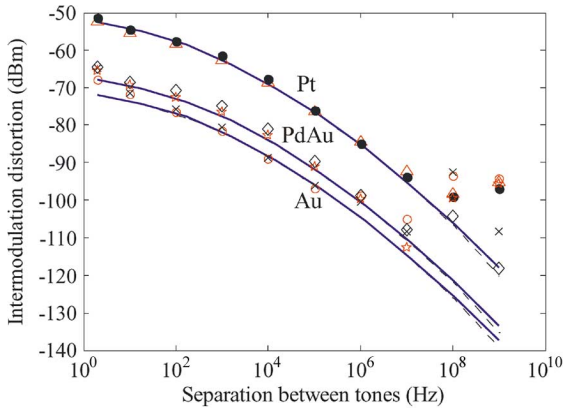

Fig. 18. Measured and simulated third-order intermodulation in B line, $l_{\mathrm{B}} = 4.2$ mm. $2f_1 - f_2$ (dashed line) and $2f_2 - f_1$ (solid line) overlap for all the simulations. Unfilled circles and crosses represent $2f_1 - f_2$ and $2f_2 - f_1$ for Au. Triangles and filled circles represent $2f_1 - f_2$ and $2f_2 - f_1$ for Pt. Stars and diamonds represent $2f_1 - f_2$ and $2f_2 - f_1$ for PdAu.

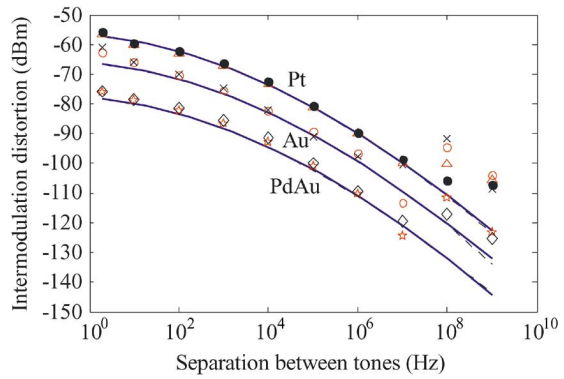

Fig. 19. Measured and simulated third-order intermodulation in C line, $l_{\mathrm{C}} = 9.93$ mm. $2f_1 - f_2$ (dashed line) and $2f_2 - f_1$ (solid line) overlap for all the simulations. Unfilled circles and crosses represent $2f_1 - f_2$ and $2f_2 - f_1$ for Au. Triangles and filled circles represent $2f_1 - f_2$ and $2f_2 - f_1$ for Pt. Stars and diamonds represent $2f_1 - f_2$ and $2f_2 - f_1$ for PdAu.

two-tone test [10]. A special measurement setup [28] consisting of a configuration that cancels the fundamental signals ω_1 and ω_2 after the device-under-test is used to achieve a high-dynamic range at the spectrum analyzer. For such measurements, the input power has been fixed at 20 dBm, while the tones spacing has been taken from 2 Hz up to 1 GHz. Results can be seen in Figs. 17–19.

High separation between tones measurements are limited by the baseline intermodulation level of the measurement setup. On the other hand, small separations between tones measurements can be limited by the phase noise of the sources. The shortest Au line represents the worst scenario for this type of measurements because it shows a low intermodulation level. System nonlinearities easily dominate at intermediate and high separation between tones ($\Delta f > 10^5$ Hz) and phase noise dominates for small separation between tones ($\Delta f < 10^2$ Hz). The results in Figs. 17–19 unveil the low-pass filter behavior of the thermal impedance, showing similar results as those found in [12], which can be used to extract the frequency-dependent thermal capacitance $C_{d,\mathrm{th}}(\omega)$. Measurements of any of the metals could be used to extract $C_{d,\mathrm{th}}(\omega)$, as long as the thermal impedance is dominated by the substrate. The platinum B line is preferable, though, because it shows the highest dynamic range above the baseline intermodulation level of the measurement setup, which is around -100 dBm. The extracted phenomenological $C_{d,\mathrm{th}}(\omega)$, for the procedure explained in Appendix II, can be seen in Fig. 20, where its frequency-dependence embeds the 3-D dissipation effect.

Once the thermal model is completely implemented, the last step consists of determining the nonlinear variable $R_{d,N}(T)$. This sets how the distributed resistance of the center conductor changes with temperature. To do that, we use the relation between $R_{d,N}(T)$ and temperature, presented in Appendix I, so that the temperature coefficient of resistivity of the metal is used. Since the material properties are process dependent, we performed resistance measurements at dc of the fabricated coplanar waveguides at several temperatures.

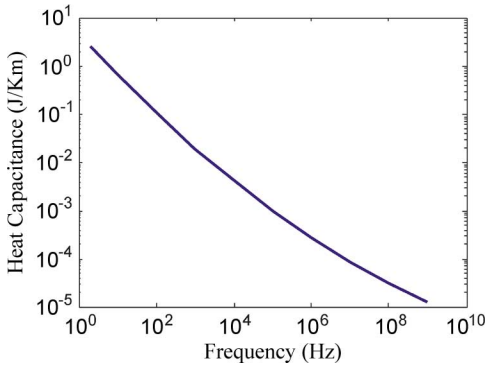

Fig. 20. Extracted $C_{d,\mathrm{th}}(\omega)$ from measurements on the platinum B line.

The measured values for the temperature coefficients of resistivity are $\delta_{\mathrm{Au}} = 0.0039987\ \mathrm{K}^{-1}$, $\delta_{\mathrm{Pt}} = 0.002824\ \mathrm{K}^{-1}$, and $\delta_{\mathrm{PdAu}} = 0.000372\ \mathrm{K}^{-1}$. The resistivity values at room temperature are shown in Table I.

The complete electrothermal model can now be constructed, making use of the measured δ values and the extracted thermal resistance and capacitance. Simulations of the third-order intermodulation distortion with the model are presented, along with the measurements in Figs. 17–19. These show good agreement and the predicted dependence on the line length.

VI. Discussion

The good agreement obtained between measurements and modeling indicates that scaling with the line length is correctly predicted. From the results above, the high difference between nonlinear levels on lines made of different metals can also be observed. The results show that there is not a simple relation between length and intermodulation level, and this is because the distributed nonlinearity increases with length, but also gets attenuated by it. Therefore, depending on the length, a high attenuation transmission line can show more or less nonlinearity than a lower loss transmission line. In addition, the fact that the platinum and the palladium-gold lines are highly mismatched translates into a variable relation between length and intermodulation level [27].

However, several considerations to minimize the intermodulation can be made from (25), in particular that referred to the correct choice of materials. In this sense, metals and dielectrics with low losses and weakly temperature-dependent properties are preferable. Additionally, high thermal conductivity dielectrics provide the right path for heat, minimizing temperature rise.

To check that the ground planes have a negligible contribution to the intermodulation distortion generation, we use (25). We consider that each ground metal strip has the same thermal impedance of the center conductor, which is a reasonable approximation. With this assumption, we get a much lower contribution coming from the ground planes of $\Delta 3\mathrm{IMD}_{\mathrm{Au}} = 10\log(|P_{L,12,M}/P_{L,12,N}|_{\mathrm{Au}}) = -27.1$ dB when compared with that coming from the center conductor in the gold lines. For the platinum and palladium-gold lines, we get $\Delta 3\mathrm{IMD}_{\mathrm{Pt}} = -42$ dB and $\Delta 3\mathrm{IMD}_{\mathrm{PdAu}} = -48.4$ dB. These results confirm the validity of the simplified model.

From the closed-form expressions obtained, we observe that the third-order intermodulation distortion generation process might also be described, for a specific separation between tones, by a phenomenological model of a quadratic current-dependent distributed resistance of the form

$$R_d(I) = R_{d,0} + R_{d,2}I^2. \tag{27}$$

Several authors have suggested the use of (27) to explain the relation between losses and intermodulation [16]. However, this phenomenological model is incorrect, and predicts a nonexistent third harmonic.

VII. Conclusions

We have presented the mechanism by which third-order intermodulation distortion is generated in transmission lines and its circuit model. Additionally, closed-form expressions have been obtained and validated along with the model. The model has been properly checked with measurements of lines of different lengths and made composed of different metals.

This work also reveals the negligible impact of the ground planes when compared to that of the center conductor and in terms of nonlinear behavior due to self-heating. Additionally, the envelope frequency-dependent intermodulation cannot be described by a constant slope of a certain decibel/decade.

The advantage of having such a distributed circuit model for a nonlinear transmission line is that it can be used for prediction purposes of any device in which transmission lines are used such as filters or directional couplers. Moreover, its usefulness is not restricted to a specific kind of input signal and can predict the nonlinear effects on complex modulated signals like global system for mobile communication (GSM) or code division multiple access (CDMA) for example.

Appendix I
Distributed Resistance Temperature Dependence

The distributed resistance at a specific frequency can be described as a function of the resistivity increment as follows:

$$R_d = R_{d,T_R}\left(1 + \gamma\Delta\rho(T)\right) \tag{28}$$

where R_{d,T_R} is the distributed resistance at ambient temperature. The resistivity increment due to temperature rise $\Delta\rho(T)$ can be identified in the following relation:

$$\rho(T) = \rho_{T_R} + \Delta\rho(T) = \rho_{T_R}(1 + \delta \cdot T). \tag{29}$$

γ is the local derivative, at the room temperature resistivity value, of the function that relates the distributed resistance with the metal resistivity. Therefore, γ is a factor that relates the increment in the distributed resistance, as a consequence of an increment in the resistivity, for a specific geometry and metal

$$\gamma = \frac{1}{R_{d,T_R}}\frac{\partial R_d(\rho)}{\partial\rho}\bigg|_{\rho_{T_R}}. \tag{30}$$

By using the Weeks method [29], we obtain the γ factor for the center conductor, for the given geometry at 6 GHz to be

$\gamma_{\mathrm{Au}} = 2.98 \cdot 10^7\ \Omega^{-1} \cdot \mathrm{m}^{-1}$, $\gamma_{\mathrm{Pt}} = 4.12 \cdot 10^6\ \Omega^{-1} \cdot \mathrm{m}^{-1}$, and $\gamma_{\mathrm{PdAu}} = 2.24 \cdot 10^6\ \Omega^{-1} \cdot \mathrm{m}^{-1}$.

APPENDIX II
THERMAL CAPACITANCE EXTRACTION PROCEDURE

The procedure starts by converting the intermodulation measurements to a linear scale to get the unscaled magnitude of the thermal impedance $|Z_{u,\mathrm{th},P}(\omega)|$. $|Z_{u,\mathrm{th},P}(\omega)|$ is then fitted to a polynomial and scaled to a value previously obtained using the circuit model to get $|Z_{d,\mathrm{th},P}(\omega)|$. A frequency-dependent thermal capacitance of the form

$$C_{d,\mathrm{th}}(\omega) = 10^{C_{\mathrm{th},0}+C_{\mathrm{th},1}\log(\omega)+C_{\mathrm{th},2}\log(\omega)^2} \tag{31}$$

is used so that its coefficients can be obtained from the relation that follows from a simple circuit analysis of Fig. 8:

$$C_{d,\mathrm{th}}(\omega) = \frac{1}{\omega}\sqrt{\frac{1}{\delta z^2\left|Z_{d,\mathrm{th},P}(\omega)\right|^2} - \frac{1}{R_{d,\mathrm{th}}^2}}. \tag{32}$$

The extracted phenomenological $C_{d,\mathrm{th}}(\omega)$ has coefficients $C_{\mathrm{th},0} = 5.0868$, $C_{\mathrm{th},1} = -0.14$, and $C_{\mathrm{th},2} = 0.0007$.

ACKNOWLEDGMENT

The authors thank Dr. Y. Wang and Dr. T. M. Wallis, both with the National Institute of Standards and Technology (NIST), Boulder, CO, for their help with this work.

Work partially supported by the U.S. Government not subject to U.S. copyright.

REFERENCES

[1] C. Collado, J. Mateu, and J. M. O'Callaghan, "Analysis and simulation of the effects of distributed nonlinearities in microwave superconducting devices," *IEEE Trans. Appl. Superconduct.*, vol. 15, no. 1, pp. 26–39, Mar. 2005.

[2] J. Mateu, J. C. Booth, S. A. Schima, C. Collado, D. Seron, and J. M. O'Callaghan, "Measurements and analysis of microwave nonlinearities in ferroelectric thin film transmission lines," in *IEEE MTT-S Int. Microw. Symp. Dig.*, Jun. 11–16, 2006, pp. 1622–1625.

[3] A. P. Shitvov, D. E. Zelenchuk, A. G. Schuchinsky, and V. F. Fusco, "Passive intermodulation in printed lines: Effects of trace dimensions and substrate," *IET Microw., Antennas, Propag.*, vol. 3, no. 2, pp. 260–268, Mar. 2009.

[4] D. E. Zelenchuk, A. P. Shitvov, and A. G. Schuchinsky, "Effect of laminate properties on passive intermodulation generation," in *LAPC Antennas Propag. Conf.*, Apr. 2–3, 2007, pp. 169–172.

[5] P. L. Lui, "Passive intermodulation interference in communication systems," *Electron. Commun. Eng. J.*, vol. 2, no. 3, pp. 109–118, Jun. 1990.

[6] P. N. Radha, "Predicting junction temperature and MTTF for MMIC devices," *RF Design*, vol. 28, no. 8, pp. 68–70, 2005.

[7] R. Hopper and C. Oxley, "Thermal measurement a requirement for monolithic microwave integrated circuit design," in *Proc. ARMMS*, Apr. 2008, pp. 385–390.

[8] V. Camarchia, F. Cappelluti, M. Pirola, S. D. Guerrieri, and G. Ghione, "Self-consistent electrothermal modeling of class A, AB, and B power GaN HEMTs under modulated RF excitation," *IEEE Trans. Microw. Theory Tech.*, vol. 55, no. 9, pp. 1824–1831, Sep. 2007.

[9] A. E. Parker and J. G. Rathmell, "Self-heating process in microwave transistors," presented at the Appl. Radio Sci. Workshop, Hobart, TAS, Australia, Feb. 18–20, 2004.

[10] J. H. K. Vuolevi, T. Rahkonen, and J. P. A. Manninen, "Measurement technique for characterizing memory effects in RF power amplifiers," *IEEE Trans. Microw. Theory Tech.*, vol. 49, no. 8, pp. 1383–1389, Aug. 2001.

[11] R. S. Timsit, "High speed electronic connectors: A review of electrical contact properties," *IEICE Trans. Electron.*, vol. ESS-C, no. 8, pp. 1532–1544, 2005.

[12] J. R. Wilkerson, K. G. Gard, A. G. Schuchinsky, and M. B. Steer, "Electro-thermal theory of intermodulation distortion in lossy microwave components," *IEEE Trans. Microw. Theory Tech.*, vol. 56, no. 12, pp. 2717–2725, Dec. 2008.

[13] R. Wilcoxon, "The effects of geometry and dielectric material on stripline and microstrip internal temperatures," *IEEE Trans. Compon. Packag. Technol.*, vol. 28, no. 4, pp. 674–679, Dec. 2005.

[14] J. Adam, "New correlations between electrical current and temperature rise in PCB traces," in *20th Annu. IEEE Semiconduct. Thermal Meas. Manag. Symp.*, Mar. 9–11, 2004, pp. 292–299.

[15] D. G. Cahill, "Thermal conductivity measurement from 30–750 K: The 3ω method," *Rev. Sci. Instrum.*, vol. 61, pp. 802–808, 1990.

[16] D. E. Zelenchuk, A. P. Shitvov, A. G. Schuchinsky, and V. F. Fusco, "Passive intermodulation in finite lengths of printed microstrip lines," *IEEE Trans. Microw. Theory Tech.*, vol. 56, no. 11, pp. 2426–2434, Nov. 2008.

[17] J. Z. Wilcox and P. Molmud, "Thermal heating contribution to intermodulation fields in coaxial waveguides," *IEEE Trans. Commun.*, vol. COM-24, no. 2, pp. 238–243, 1976.

[18] G. H. Strauss, "Intrinsic sources of IM generation," Naval Res. Lab., CITY, STATE, Memo. Rep. 4233, 1980, ch. 5.

[19] E. Rocas, C. Collado, N. D. Orloff, and J. C. Booth, "Third order intermodulation distortion due to self-heating in gold coplanar waveguides," in *IEEE MTT-S Int. Microw. Symp. Dig.*, May 2010, pp. 425–428.

[20] F. P. Incropera, D. P. DeWitt, T. L. Berqman, and A. S. Lavine, *Fundamentals of Heat and Mass Transfer*. New York: Wiley, 2002.

[21] C. Collado, J. Mateu, O. Menendez, and J. M. O'Callaghan, "Nonlinear distortion in a 8-pole quasi-elliptic bandpass HTS filter for CDMA system," *IEEE Trans. Appl. Superconduct.*, vol. 15, no. 2, pp. 992–995, Jun. 2005.

[22] D. Pozar, *Microwave Engineering*. New York: Wiley, 1998.

[23] QuickField. Tera Software, Svendborg, Denmark, 2010.

[24] "Material property data," MatWeb, Blacksburg, VA, 2010. [Online]. Available: http://www.matweb.com

[25] "Characteristics of single crystal sapphire," KYOCERA, Kyoto, Japan, 2010. [Online]. Available: http://global.kyocera.com/prdct/fc/product/pdf/s_c_sapphire.pdf

[26] C. Y. Ho, "Thermal conductivity of ten selected binary alloy systems," *J. Phys. Chem. Ref. Data*, vol. 7, no. 3, pp. 959–1177, 1978.

[27] J. Mateu, C. Collado, N. D. Orloff, J. C. Booth, E. Rocas, A. Padilla, and J. M. O'Callaghan, "Third-order intermodulation distortion and harmonic generation in mismatched weakly nonlinear transmission lines," *IEEE Trans. Microw. Theory Tech.*, vol. 57, no. 1, pp. 10–18, Jan. 2009.

[28] J. Mateu, J. C. Booth, and S. A. Schima, "Frequency tuning and spurious signal generation at microwave frequencies in ferroelectric SrTiO3 thin-film transmission lines," *IEEE Trans. Microw. Theory Tech.*, vol. 55, no. 2, pp. 391–396, Feb. 2007.

[29] W. T. Weeks, L. L. Wu, M. F. McAllister, and A. Singh, "Resistive and inductive skin effect in rectangular conductors," *IBM J. Res. Develop.*, vol. 23, no. 6, pp. 652–660, Nov. 1979.

Eduard Rocas (S'07) received the Telecommunication Engineering degree from the Universitat Politècnica de Catalunya (UPC), Barcelona, Spain, in 2005, where his final project was associated with the creation of the Intelligent Communications and Avionics for Robust Unmanned Aerial Systems (ICARUS) Research Group, and is currently working toward the Ph.D. dgree at UPC.

From September 2005 to July 2006, he was involved in the simulation and modeling of advanced SONARs with the Computer Vision and Robotics Group (VICOROB), University of Girona, as an Formación del Profesorado Universitario (FPU) Grant Holder. Since November 2006, he has been with UPC as a doctoral student (Formación de Personal Investigador (FPI) Grant Holder), where his research is focused on new materials and structures for novel RF/microwave (MW) devices. Since January 2009, he has been a Guest Researcher with the National Institute of Standards and Technology (NIST), Boulder, CO.

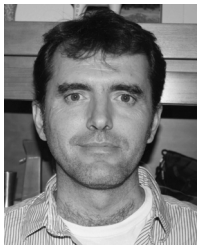

Carlos Collado (A'02–M'03–SM'10) received the Telecommunication Engineering degree, Ph.D. degree, and M.S. degree in biomedical engineering degree from the Universitat Politècnica de Catalunya (UPC), Barcelona, Spain, in 1995, 2001, and 2002, respectively.

In 1998, he joined the faculty of UPC, and became an Associate Professor in 2005. From November 2005 to January 2008, he was Vice-Dean of the Technical School of Castelldefels (EPSC), UPC, where he was responsible of the telecommunication and aeronautic engineering degrees. In 2004, he was a Visiting Researcher with the University of California at Irvine. From 2009 to 2010, he was a Guest Researcher with the National Institute of Standards and Technology (NIST), Boulder, CO. His primary research interests include microwave devices and systems with focus on nonlinearities of passive devices.

Dr. Collado was the recipient of a 2001 prize for the best doctoral thesis in electronics and telecommunications from UPC.

Nathan D. Orloff was born in Columbia, SC, on August 10, 1981. He received the B.S. degree in physics (with high honors) and Ph.D. degree from the University of Maryland at College Park, in 2004 and 2010, respectively. His doctoral research focused on the development of a broadband on-wafer calibration and characterization approach that has been applied to number of novel material systems.

He is interested in novel dielectric characterization techniques, complex-nonlinear device modeling, on-wafer measurement, and the integration of microelectronics and microfluidics.

Dr. Orloff was the recipient of the 2004 Martin Monroe Undergraduate Research Award, the 2006 CMPS Award for Excellence for Teaching Assistants, the 2010 Michael J. Pelczar Award for Excellence in Graduate Study, and an honorable mention for the 2010 Block Award for Best Poster Presentation from the Aspen Center for Physics.

Jordi Mateu (M'03–SM'10) received the Telecommunication Engineering and Ph.D. degrees from the Universitat Politècnica de Catalunya (UPC), Barcelona, Spain, in 1999 and 2003, respectively.

In October 2006, he joined the Signal Theory and Communications Department, UPC, initially as a Ramon-y-Cajal Research Fellow, where since March 2009, he has been an Associate Professor. Since 2007 he has also been an Associate Researcher with the Centre Tecnològic de Telecomunicacions de Catalunya (CTTC), Castelldefels, Spain. From May to August 2001, he was a Visiting Researcher with Superconductor Technologies Inc., Santa Barbara CA. From October 2002 to August 2005, he was a Research Associate with CTTC. Since September 2004, he has held several guest researcher appointments with the National Institute of Standards and Technology (NIST), Boulder, CO, where he was a Fulbright Research Fellow from September 2005 to October 2006. In July 2006, he was a Visiting Researcher with the Lincoln Laboratory, Massachusetts Institute of Technology (MIT). From September 2003 to August 2005, he was a Part-Time Assistant Professor with the Universitat Autònoma de Barcelona. In Summer 1999, following graduation, he was a Trainee Engineer with the Investment Technology Department, Gillette, Isleworth, U.K. He has authored or co-authored over 40 papers in international journal, over 55 contributions in international conferences, and three book chapters. He holds two patents. He has collaborated and led several research projects for national and international public and private organizations and companies. He is reviewer of several journals and international conferences. His primary interests include microwave devices and system and characterization and modeling of new electronic materials including ferroelectrics, magnetoelectric, superconductors, and acoustic devices. His recent research interests also include the synthesis, design, and development of novel microwave filtering structures.

Dr. Mateu was the recipient of the 2004 Prize for the best doctoral thesis in Fundamental and Basic Technologies for Information and Communications by the Colegio Oficial de Ingenieros de Telecomunicación (COIT) and Asociación Española de Ingenieros de Telecomunicación (AEIT). He was also the recipient of a Fulbright Research Fellowship, an Occasional Lecturer Award for visiting MIT, and a Ramón y Cajal Contract.

Alberto Padilla was born in Barcelona, Spain, in 1984. He received the Telecommunication Engineering degree from the Technical University of Catalonia (UPC), Barcelona, Spain, in 2008. His final project concerned the mitigation of the nonlinear behavior of high-temperature superconducting planar devices.

Since March 2008, he has been with the Department of Signal Theory and Communications, UPC. He is currently a Trainee—Stagiaire Researcher with the European Space Agency (ESA)–European Space Research and Technology Centre (ESTEC), where his focus is focused on the synthesis and design of a new class of receiver filters for satellite communications.

Mr. Padilla was the recipient of a Ph.D. grant (FPU) from the Spanish Ministry of Education in January 2009.

Juan M. O'Callaghan (SM'01) received the Telecommunication Engineering degree from the Universitat Politècnica de Catalunya (UPC), Barcelona, Spain, in 1987, and the Ph.D. degree from the University of Wisconsin–Madison, in 1993.

In 2003, he became a Full Professor with UPC. In 1989, he was with the Systems Research Center, Honeywell, Bloomington, MN, where he was involved with noise measurement methods for field-effect transistors (FETs) at Ka-band. In 1993, he became a tenure-track faculty member with UPC. From 2003 to 2006, he was a Manager for MERIT, a consortium of European universities delivering a joint Master's program in Information Technologies within the Erasmus Mundus Program (see www.meritmaster.org). From 2006 to 2009, he was Vice-Dean of academic affairs with Telecom BCN, the telecommunication engineering school of UPC (see www.telecombcn.upc.edu). He has coauthored over 55 papers in peer-reviewed international journals and 90 contributions to conference proceedings. He holds four patents. His research interests include microwave devices and materials and microwave photonics. He has been involved with noise characterization, large-signal properties of GaAs FETs, and advanced microwave materials such as superconductors and ferroelectrics.

Dr. O'Callaghan was the recipient of the 2001 prize to the most outstanding research project from the Catalan Association of Telecommunication Engineers (ACET). In 2004, one of the theses he supervised received the prize for the best doctoral thesis in fundamental and basic technologies for information and communications by the Colegio Oficial de Ingenieros de Telecomunicación (COIT) and Asociación Española de Ingenieros de Telecomunicación (AEIT).

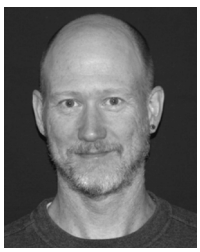

James C. Booth received the B.A. degree in physics from the University of Virginia, Charlottesville, in 1989, and the Ph.D. degree in physics from the University of Maryland at College Park, in 1996. His doctoral dissertation concerned novel measurements of the frequency dependent microwave surface impedance of cuprate thin film superconductors.

Since 1996, he has been a Physicist with the National Institute of Standards and Technology (NIST), Boulder, CO, initially as aNational Research Council (NRC) Postdoctoral Research Associate (1996–1998) and currently as the leader of the High Frequency Devices and Characteristics Project. His research with NIST is focused on exploring the microwave properties of new electronic materials and devices, including ferroelectric, magneto-electric, and superconducting thin films, as well as the development of experimental platforms integrating microfluidic and microelectronic components for RF and microwave frequency characterization of liquid and biological samples.

Modeling of Self-Heating Mechanism in the Design of Superconducting Limiters

Eduard Rocas, *Student Member, IEEE*, Carlos Collado, *Senior Member, IEEE*, Jordi Mateu, *Senior Member, IEEE*, Nathan Orloff, and James C. Booth

***Abstract*—We propose a modeling method to simulate how the local temperature rises, due to power dissipation, and how this affects the performance of a high temperature superconductor (HTS) limiter. For given material properties, power, and frequency we determined, by use of both electromagnetic and thermal modeling, the spatial distribution of the temperature rise across an HTS transmission line. This temperature rise in turn affects the local description of the superconductor nonlinearities. To model this effect, we use an iterative technique that combines the Weeks-Sheen method to calculate the current-density distribution with a finite-element method to calculate temperature rise at each point of the transmission line. Simulations of coplanar waveguide HTS limiters on sapphire and quartz are presented.**

***Index Terms*—HTS, limiter, self-heating, superconductor.**

I. Introduction

HIGH temperature superconductor (HTS) materials can undergo a transition from the superconducting state to the non-superconducting state when the current density exceeds a critical level. At this point, pair-breaking begins to occur, and the material gradually loses its superconducting properties. This implies higher losses, and therefore higher dissipation, which produce a temperature rise, which in turn increases the fraction of carriers in the normal state. These transient effects end when electrothermal equilibrium is reached.

The above-mentioned current-density dependence of superconductor material properties has been exploited to develop power limiters based on HTS materials, which is an emerging microwave application for high temperature superconductors [1]. The short switching times, one nanosecond or less, ensure that very little energy is transmitted through the limiter prior to switching, and so guarantees a high degree of protection to the downstream electronics from high-power transient signals. This characteristic makes HTS technology a viable candidate compared to conventional limiting technologies, such as diodes.

Manuscript received August 03, 2010; accepted October 07, 2010. This work was partially supported by the Spanish Ministry of Science and Innovation under Grant TEC-2009-13897-C03-01/TCM and Grant MAT-2008-06761-C03-02; by the AGAUR, Generalitat de Catalunya (2008-BE2-00196), and by Spanish Ministry of Education through PhD fellowship for E. Rocas (BES-2007-16775).

E. Rocas is with Universitat Politècnica de Catalunya (UPC), Barcelona 08034, Spain. He is also with the National Institute of Standards and Technology, Boulder, CO 80305 USA.

C. Collado and J. Mateu are with Universitat Politècnica de Catalunya (UPC), Barcelona 08034, Spain (e-mail: collado@tsc.upc.edu).

N. Orloff and J. C. Booth are with the National Institute of Standards and Technology, Boulder, CO 80305 USA (e-mail: booth@boulder.nist.gov).

Color versions of one or more of the figures in this paper are available online at http://ieeexplore.ieee.org.

Digital Object Identifier 10.1109/TASC.2010.2090449

The origin of this switching behavior is a nonlinear process driven by the current-density-dependent surface impedance, where the strength of the nonlinearity is described by a temperature-dependent material parameter related to the critical current density $j_c(T)$. In this situation, and taking into account that the local temperature can increase substantially when the device switches to the non-superconducting state, it is necessary to consider electro-thermal effects when designing HTS limiters.

For this purpose, we implement an electro-thermal simulation method that combines the Weeks-Sheen technique [2], [3] to determine the current density distribution with a two-dimensional thermal domain equivalent circuit to obtain the local temperature increase. Both electromagnetic and thermal simulations are coupled and solved concurrently by an iterative convergence algorithm, where the dissipated power is used as the input to the thermal-domain simulation, and the obtained temperature rise is used to change the material properties in the electromagnetic domain simulation.

Based on this approach, we present simulations comparing the limiting performance of coplanar waveguides on substrates with different thermal properties: sapphire and quartz. The results confirm the importance of the thermal material properties, and consequently the temperature rise, on the performance of the superconducting limiters.

II. Electromagnetic Model

We use the method described in [2]–[4] to calculate the current density in the cross-section of a planar transmission line. The method described in [2] involves meshing the cross-section in small unit cells that effectively act as transmission lines, so that a uniform current density is considered at each cell. The mutual inductances between the small transmission lines are then calculated and used to obtain the current density at each point of the waveguide cross-section, and also to obtain the distributed resistance R_d, and the distributed inductance L_d. Reference [3] extended this method to calculate the distributed parameters of superconductor transmission lines by use of a complex conductivity, and [4] completed the analysis with an iterative algorithm that takes into account the fact that the superfluid current density depends on the ratio between the current density at each point $j(x, y)$, and the critical current density j_c. In this work, we apply an improved convergence algorithm that allows for simulations at higher power levels, compared to the algorithm used previously for the analysis of weak nonlinearities in a low-power regime [5].

We begin with the nonlinear London penetration depth [4], with a temperature dependence based on the two-fluid model

$$\frac{1}{\lambda_L^2(t_N, j_N)} = \frac{1}{\lambda_{L,0}^2}\left(1 - t_N^4\right)\left(1 - f_{NL}(j_N)\right), \qquad (1)$$

where t_N and j_N represent the normalized temperature T and current density j values relative to their critical values T_c and j_c respectively: $t_N = T/T_c$, and $j_N = j/j_c$. The parameter $\lambda_{L,0}$ is the penetration depth at $t_N = 0$ and, at low values of j, and $f_{NL}(j_N)$ is given by

$$f_{NL}(j) = b_T \left(\frac{j}{j_c}\right)^2, \qquad (2)$$

where b_T is a temperature-dependent parameter that provides useful information about the d-wave or s-wave nature of a superconducting material [4]. In this work, we will use the b_T values extracted from measurements of YBCO in [6]. As seen in (1), an increase in both the temperature and the current density modify the London penetration depth, implying a decrease in the superconducting carrier density for $j \sim j_c$. When the current density increases, the losses increase with a resulting temperature increase, which in turn further increases the losses, etc.

The electromagnetic model makes use of a complex conductivity that includes the above-defined nonlinear London penetration depth, which is defined as

$$\sigma(t_N, j_N) = \sigma_1(t_N, j_N) - j\sigma_2(t_N, j_N), \qquad (3)$$

where the real part of the complex conductivity is

$$\sigma_1(t_N, j) = \sigma_{1,0}\left(1 - \left(1 - t_N^4\right)\left(1 - f_{NL}(j)\right)\right), \qquad (4)$$

where $\sigma_{1,0}$ is the normal state conductivity at $\mathrm{T_c}$. The imaginary part of the conductivity is

$$\sigma_2(t_N, j) = \frac{1}{\omega\mu_0\lambda_{L,0}^2}\left(1 - t_N^4\right)\left(1 - f_{NL}(j)\right). \qquad (5)$$

The electromagnetic domain simulation calculates the current density $j(x, y)$ at each point of the transmission line cross section and then updates the complex conductivity, locally at each point, by use of (3)–(5). A convergence algorithm is used to recalculate the current density, which is compared to the previously obtained value. The iterative procedure ends when convergence is achieved.

As an example, Fig. 1 shows the current density distribution obtained for the cross section of a coplanar waveguide with a 10 μm wide center strip and a 5 μm gap. The HTS film is 150 nm thick and the ground planes are 100 μm wide. The simulation method for the electromagnetic domain described in this section does not consider temperature changes due to self-heating mechanisms. At low powers, the temperature rise due to self-heating is negligible because the losses are very small. But at higher powers, when the current density is comparable to the critical current density, the self-heating can have an important impact that is strongly dependent on the thermal properties of the substrate.

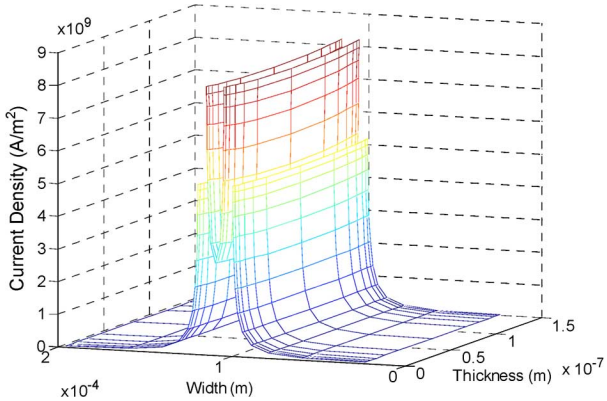

Fig. 1. Current density in a coplanar waveguide with width 10 μm and gap 5 μm. The HTS thickness is 150 nm and the input power is 0 dBm.

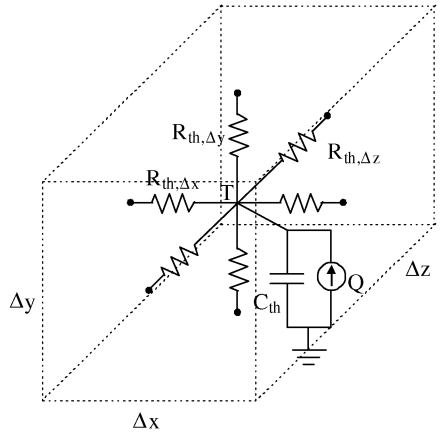

Fig. 2. Equivalent circuit implementation of an elemental cell to model heat propagation in a body.

III. Thermal Model

The heat propagation in a body, with internal heat generation, follows the heat equation defined as [7]

$$\frac{\partial T}{\partial t} = \frac{k}{c_p\rho}\left(\frac{\partial^2 T}{\partial x^2} + \frac{\partial^2 T}{\partial y^2} + \frac{\partial^2 T}{\partial z^2}\right) + q, \qquad (6)$$

where k is the thermal conductivity, ρ is the mass density, c_p is the heat capacity, and q is the internally generated heat per unit volume. Eq. (6) is fundamental in determining the temperature distribution in a body and is consistent with a three-dimensional matrix of thermal resistances, in which a thermal capacitance is connected to ground at each node [7]. In such an analog circuit representation of the heat equation, heat is represented by current, and temperature is represented by voltage. Therefore, a current source of value equal to $Q = \int_{\Delta V} q$ is connected at each node, which models the internally generated heat in a volume ΔV; that is, the power dissipation by the Joule effect calculated in the electromagnetic domain. Fig. 2. shows an elemental three-dimensional cell of the circuit model.

The thermal resistance $R_{th,\Delta u}$ for any direction Δu, where $\Delta u = \Delta x$, Δy, or Δz and heat capacitance $\mathrm{C}_{th,i}$ of the cell i can be defined as

$$R_{th,\Delta u} = \Delta u / 2kA_{\Delta u}, \qquad (7)$$

$$C_{th} = c_p \rho D V_i, \qquad (8)$$

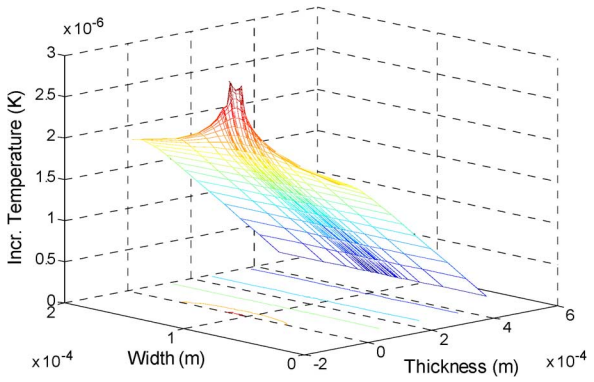

Fig. 3. Temperature rise distribution in the cross-section of a coplanar waveguide of YBCO on a 0.5 mm-thick sapphire substrate.

where $A_{\Delta u}$ is the area perpendicular to Δu. The circuit model can be understood as a three-dimensional matrix representing the thermal impedance $\mathbf{Z_{th}}$. Use of the thermal impedance, in K/W units, implies that the temperature rise T produced at each node by an amount of heat $\mathbf{Z_{th}} \cdot Q$ can be calculated by means of conventional circuit analysis, stored, and used to obtain the temperature at each point for a given heat source distribution, with:

$$[T] = [Z_{th}][Q]. \tag{9}$$

The three-dimensional model can be reduced to a two-dimensional problem if only the cross-section of the transmission line is analyzed.

IV. Electro-Thermal Model

Electro-thermal simulations to reproduce the interactions between electromagnetic and thermal domains can be performed by combining the numerical techniques described in the last two sections. To couple both domains we employ the following procedure. First, the current density distribution is calculated. The dissipated power (heat) is also obtained at each point. Then the dissipated heat is used as the input for the thermal domain model and the temperature rise at each point is calculated by use of (9). The resultant temperature rise is used to recalculate the complex conductivity in the electromagnetic domain, by use of (3)–(5). Steps 1–3 are then repeated until acceptable convergence is achieved.

The identical meshing is used in both techniques to ensure proper coupling. An adaptive meshing is used in the HTS thin film to accurately compute the higher current density at the edges of the strips. In addition, the substrate is also adaptively meshed to reproduce the temperature rise in detail near the HTS thin film. The reference temperature is set as the boundary condition at the bottom of the substrate. This is a reasonable consideration in real experiments, where the sample is usually in very good thermal contact with a copper chuck to keep the sample thermally stable at a desired temperature.

Fig. 3 shows the temperature rise, obtained by electro-thermal simulations, at the cross-section of a YBCO thin-film transmission line on a 0.5 mm-thick sapphire substrate of thermal conductivity $k = 42\ \mathrm{W/(K \cdot m)}$. The geometry of the transmission line is the same as that presented in Section II. We used the YBCO material parameters described in [6]. The reference temperature is fixed at 77 K and the input power is 0 dBm. As can be seen in Fig. 3, the temperature change is very small at that input power.

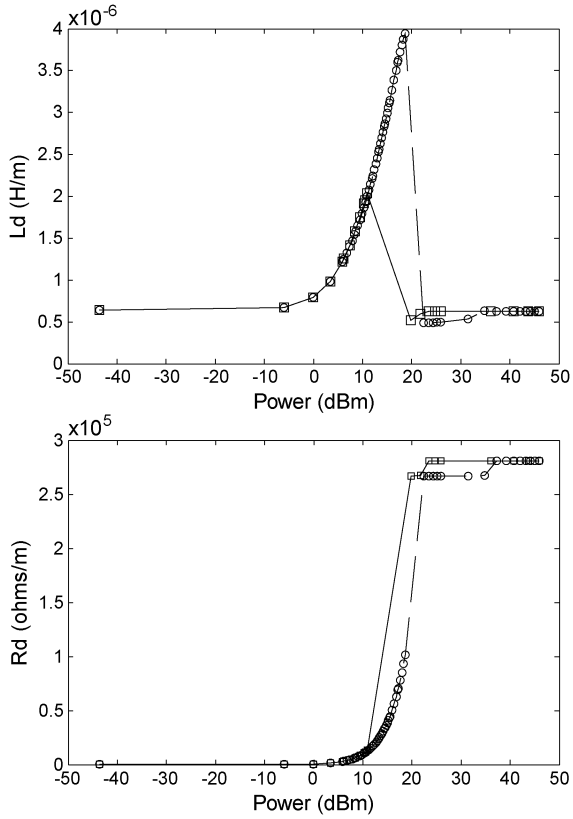

Fig. 4. Distributed inductance and resistance versus input power for two different samples, one having a sapphire substrate (circles, dashed line) and the other having a quartz substrate (squares, continuous line).

V. Limiter Comparison for Different Substrates

We used the electro-thermal model developed above to compare the performance of a coplanar waveguide power limiter on two different substrates, sapphire and quartz, to demonstrate the impact of the thermal properties on the limiter performance. A thermal conductivity of $k = 2\ \mathrm{W/(K \cdot m)}$ is used for quartz, compared to $42\ \mathrm{W/(K \cdot m)}$ for sapphire.

We obtain the distributed inductance and resistance as a function of the input power as described previously for identical coplanar waveguide devices. Fig. 4 shows the distributed inductance and resistance, for devices on a sapphire and a quartz substrate, for different input powers. A reference temperature of 83 K is considered along with a critical temperature of $\mathrm{T_c} = 90\ \mathrm{K}$ and a critical current density of $j_c = 5 \times 10^{10}\ \mathrm{A/m^2}$.

As seen in Fig. 4, the distributed inductance increases abruptly when the input power approaches a certain threshold. At that point, the HTS material in the center conductor switches to the normal state and the inductance drops. After that, a second transition occurs when the ground planes switch to the normal state. The distributed resistance follows a similar behavior and the transition of the ground planes can be more easily observed. Note that, for both substrate materials quartz

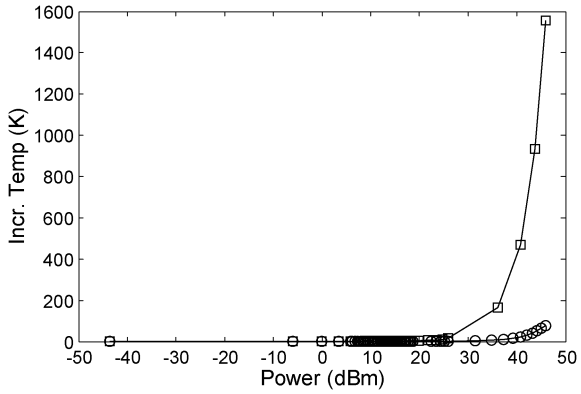

Fig. 5. Temperature rise at the center conductor of two different samples made of a sapphire substrate (circles) and a quartz substrate (squares), for different input powers.

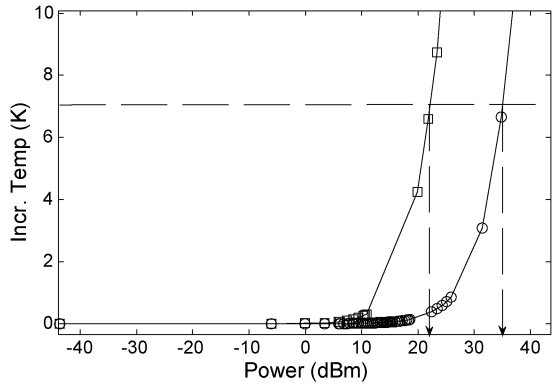

Fig. 6. Temperature rise and upper power threshold in two different samples made of a sapphire substrate (circles) and a quartz substrate (squares).

and sapphire, the threshold is approximately the same, although the quartz sample shows a more abrupt transition.

The impact that the thermal properties of the substrate have on the limiter performance is more noticeable if we examine the temperature rise. Fig. 5 shows the temperature increase at the center conductor for the two different substrates. The temperature increases much more abruptly if a quartz substrate is used, as it fails to propagate the dissipated heat effectively due to its lower thermal conductivity. This sudden temperature rise, over 1000 K as shown in Fig. 5, would destroy the device.

This analysis also determines the upper power threshold at which the limiter can still recover its superconducting state instantaneously. For high-power continuous-wave signals, in which the temperature rise can be higher than the critical temperature, the thermal inertia of the system requires some time to cool back down to its nominal temperature.

Fig. 6 shows the power threshold at which the transition is still reversible. If the reference temperature is fixed at 83 K, a temperature increment of 7 K implies reaching the critical temperature of 90 K. Therefore, the 7 K temperature increment sets the upper power threshold for fast-switching behavior between the limiting and the superconducting state. As shown in Fig. 6, the upper threshold is around 35 dBm for the sapphire sample and 22 dBm for the quartz sample.

VI. Conclusion

This work presents a method for simulating the interaction between the electromagnetic and the thermal domains in predicting the performance of HTS microwave circuits. We showed that, for a continuous wave on a HTS transmission line, the temperature rise due to self-heating enhances the switching from the superconducting state to the lossy normal state. Moreover, the correct choice of substrate, in terms of its thermal properties, plays a fundamental role in spreading the heat and consequently in setting the limiting power. Otherwise, device destruction due to overheating can occur. Additionally, the numerical method presented allows for prediction of the upper threshold power, above which the device exceeds the critical temperature T_c.

References

[1] J. C. Booth, D. A. Rudman, and R. H. Ono, "A self-attenuating superconducting transmission line for use as a microwave power limiter," *IEEE Trans. Appl. Supercond.*, vol. 13, no. 2, pp. 305–310, Jun. 2003.

[2] W. T. Weeks, L. L. Wu, M. F. McAllister, and A. Singh, "Resistive and inductive skin effect in rectangular conductors," *IBM J. Res. Dev.*, vol. 23, pp. 652–660, Nov. 1979.

[3] D. M. Sheen, S. M. Ali, D. E. Oates, R. S. Withers, and J. A. Kong, "Current distribution, resistance, and inductance for superconducting strip transmission lines," *IEEE Trans. Appl. Supercond.*, vol. 1, pp. 108–115, Jun. 1991.

[4] T. Dahm and D. J. Scalapino, "Theory of intermodulation in superconducting microstrip resonator," *J. Appl. Phys.*, vol. 81, no. 4, pp. 2002–2012, Feb. 1997.

[5] C. Collado, J. Mateu, and J. M. O'Callaghan, "Analysis and simulation of the effects of distributed nonlinearities in microwave superconducting devices," *IEEE Trans. Appl. Supercond.*, vol. 15, no. 1, pp. 26–39, Mar. 2005.

[6] K. T. Leong, J. C. Booth, and S. A. Schima, "A current-density scale for characterizing nonlinearity in high-Tc superconductors," *IEEE Trans. Appl. Supercond.*, vol. 15, no. 2, pp. 3608–3611, Jun. 2005.

[7] F. P. Incropera, D. P. DeWitt, T. L. Berqman, and A. S. Lavine, *Fundamentals of Heat and Mass Transfer*. Hoboken: Wiley, 2002.

10.1109/ULTSYM.2009.0215

Unified Model for Bulk Acoustic Wave Resonators' Nonlinear Effects

Eduard Rocas[1,2], Carlos Collado[1], James C. Booth[2], Enrique Iborra[3], Robert Aigner[4]

[1]Universitat Politècnica de Catalunya (UPC), Barcelona, Spain
[2]National Institute of Standards and Technology, Boulder, CO, USA
[3]Grupo de Microsistemas y Materiales Electrónicos, Universidad Politécnica de Madrid, Spain
[4]Triquint Semiconductor, FL, USA

***Abstract* — We present a nonlinear model for Bulk Acoustic Wave resonators that combines different sources of nonlinearity by use of device-independent material-specific parameters to predict intermodulation and harmonic generation. The model accounts for intrinsic nonlinearities due to the stiffened elasticity and thermal effects that arise from temperature changes in a sample driven by an amplitude-modulated signal. Nonlinear parameters of the aluminum nitride piezoelectric layer have been extracted that are in agreement with previously published results.**

***Index Terms* — Intermodulation, thermal effects, second harmonic, Bulk Acoustic Wave resonators.**

I. Introduction

The demand for accurate modeling of the nonlinearities in bulk acoustic wave (BAW) resonators has recently increased because of the need to fulfill expected requirements in microwave filters [1]. Despite increased demand, accurate modeling is challenging because of the numerous sources of nonlinearity, which may or may not be negligible [2]. Existing models usually make use of nonlinear lumped circuit elements, which are specific to the geometry of the measured device and are difficult to relate to the material properties. Such approaches usually lead to narrow-band, phenomenological descriptions that fail to predict nonlinear effects for different geometries and materials [3], [4].

This work presents a device-independent physical model to account for nonlinear effects in BAW resonators that is valid for a broad range of frequencies. Intrinsic nonlinearities arising from the dependence of the stiffened elasticity on the stress give rise to second harmonics, whereas its variation with the dynamic changes of temperature accounts for the measurable intermodulation distortion.

II. Unified Nonlinear Model

The dependence of the elasticity of the piezoelectric layer (generally aluminum nitride (A1N) in BAW devices) on the stress has been shown to be an important contribution to second-harmonic generation [5]. This sets the intrinsic nonlinear properties of the material that can be modeled by using a nonlinear distributed capacitor in a distributed implementation of the acoustic transmission line in the Krimtholz, Leedom and Matthaei (KLM) model [6].

The process by which intermodulation distortion is generated, follows a totally different mechanism. Dissipation, arising mostly from viscous damping, is related to the square of the input signal, which in turn leads to several spectral components of the dissipated power. One of these components is the envelope in "two-balanced tones" test, whose frequency is half the difference Δf between two signals f_1 and f_2. Because a temperature rise follows a low-pass filter-like behavior, or the speed of temperature variations in a material is determined by its diffusivity, the frequency $\Delta f / 2$ of the envelope becomes the dominant spectral component in terms of temperature variations. This leads to a dependence on temperature-dependent material properties at the envelope's frequency. This dependence then gives rise to intermodulation distortion ($2f_1 - f_2$ and $2f_2 - f_1$) when low frequency changes are up-converted by mixing with the fundamental frequencies f_1 and f_2 [7]. The mechanism of generation for intrinsic and thermal effects is shown in Fig. 1, where the nonlinear capacitor is defined as

$$C_d(S,T) = C_{d,0} + \Delta C_1 S + \Delta C_2 S^2 + \Delta C_T T, \quad (1)$$

which is related with the stiffened elasticity of the material:

$$c^D(S,T) = c_0^D + \Delta c_1^D S + \Delta c_2^D S^2 + \Delta c_T^D T, \quad (2)$$

where S and T are the stress and temperature, respectively, at each infinitesimal section of the piezoelectric layer. The device-independent parameters Δc^D_1, Δc^D_2 in (2) account for the intrinsic nonlinearities and can be linked to ΔC_1, ΔC_2 in (1) as shown in [5]. Similarly, the parameter Δc^D_T accounts for thermal effects and is linked with ΔC_T by

$$\Delta C_T = -\frac{1}{c_0^D}\frac{\Delta c_T^D}{A c_0^D}, \quad (3)$$

where A is the area of the device.

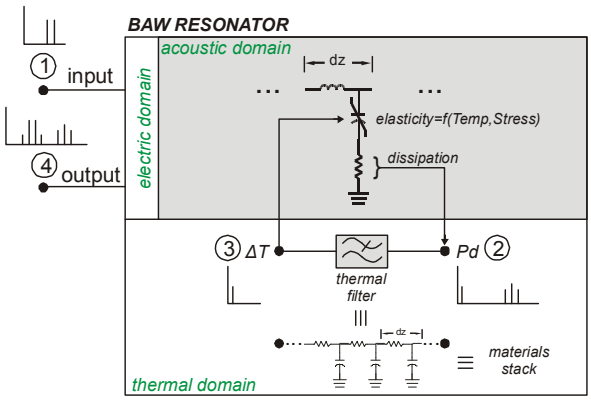

Fig. 1. Nonlinear generation mechanisms in BAW resonators.

978-1-4244-4390-1/09/$25.00 ©2009 IEEE

A. KLM linear model

The model presented can be considered to be an extension of the KLM model that accounts for nonlinear effects. Specific details of the KLM model implementation can be found in [6]. The piezoelectric layer is implemented as a cascade of infinitesimal cells that enable the circuit parameters to be related to the nonlinear material properties, as shown in Fig. 2. The different material layers of the stack are cascaded as a transmission line in the acoustic domain of the circuit model. Two types of losses are introduced to correctly fit the model to the measured S-parameters. A series resistance models the electric loss due to the electrodes, while a parallel conductance in each cell assesses the acoustic viscous damping of the distributed piezoelectric layer.

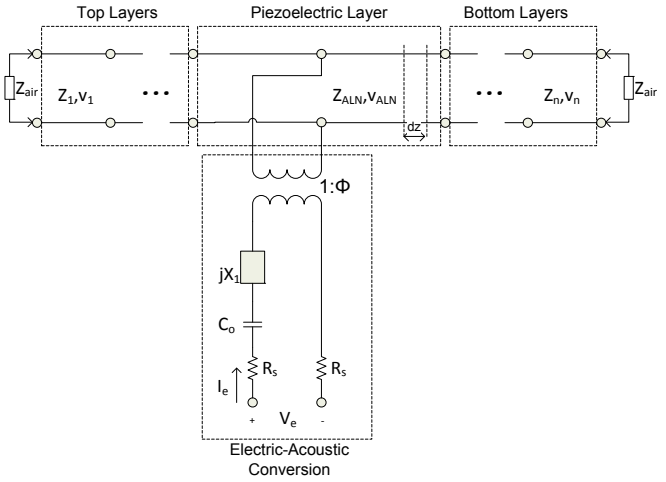

Fig. 2. Nonlinear KLM model: The piezoelectric layer is divided into sections whose lengths are *dz*. The upper and lower layers are modeled cascading acoustic transmission lines.

B. Nonlinear model implementation

i. Intrinsic nonlinearities

As previously stated, the piezoelectric layer is divided into smaller cells and can be directly constructed with the distributed parameters of the equivalent acoustic transmission line. We only discretize the piezoelectric layer, and treat the other layers with equivalent transmission lines, because it is the main source of acoustic losses and it is where most of the acoustic energy is stored. The nonlinear distributed capacitance depends on the mechanical stress at the position of each cell, which accounts for the intrinsic nonlinearities that lead to harmonic and intermodulation generation [5].

ii. Heat flow

Besides intrinsic nonlinearities, the dependence on the temperature is also introduced in order to model the thermal effects occurring in the device. This is achieved with a dynamic thermal model of the BAW resonator that is coupled to the acoustic transmission line to model self-heating mechanisms, as seen in Fig. 3. The heat flowing through the layers is modeled, according to the heat equation, as a cascade of series resistances and shunt capacitances that accounts for thermal conductivity and heat capacity, respectively, of each material layer [8]. The terminations of the thermal lines model the silicon substrate at the bottom layer, as well as the convection and radiation resistances at the top layer, which are both followed by a DC voltage source used to model the ambient temperature [9].

iii. Self heating mechanisms

As seen in Fig. 4, the dissipated heat due to acoustic viscous damping at each infinitesimal length *dz* of the acoustic line is coupled to the thermal domain as a current source. The sensed temperature, or the voltage in the thermal transmission line, is used to change the elasticity according to (2).

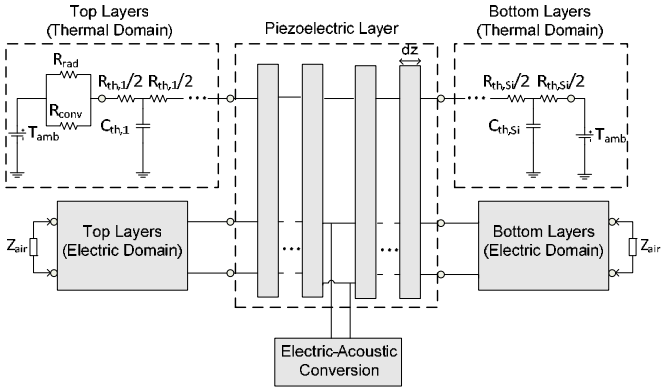

Fig. 3. Nonlinear model including the dynamic thermal domain. Detail of grey blocks is shown in Fig 2 and Fig. 4.

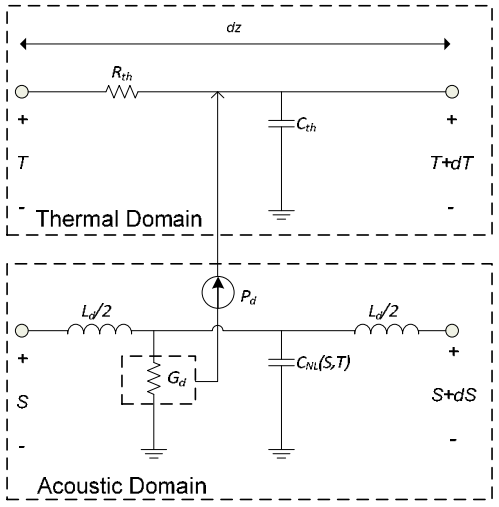

Fig. 4. Implementation of a section *dz* of the piezoelectric layer. The distributed parameters of the acoustic domain are L_d, C_{NL} [5]; G_d models the viscosity, and the dissipated power P_d acts as a heat source.

III. Measurements and Results

Harmonics and intermodulation products of two tones (f_1 and f_2) have been measured over a broad range of frequencies, 1.88 GHz to 1.98 GHz at 0.01 GHz intervals, in order to obtain the nonlinear parameters Δc^D_1, Δc^D_2, and Δc^D_T of the piezoelectric layer AlN. Several rectangular and trapezoidal shaped state-of-the-art one-port BAW resonators from two different suppliers, with different stack configurations and areas ranging from 12,500 μm^2 to 64, 100 μm^2, were measured. For clarity we show the measured data of only two of the rectangular-shaped resonators, which correspond to one of the suppliers. The areas of these resonators are 23,300 um^2 and 64,100 um^2, which will be noted as A2 3 and A64, respectively.

A. Second harmonic and IMD2

Figures 5 shows measurements and simulations of the second harmonic $2f_1$ and $2f_2$ (2H) and the second order intermodulation products $f_1 + f_2$ (IMD2) for resonators A64 (Fig. 5(a)) and A23 (Fig. 5(b)). In Fig. 5, the central frequency $f_0 = (f_1 + f_2) / 2$ is shown as the horizontal axis, which is linearly swept from 1.88 GHz to 1.98 GHz. The difference between f_1 and f_2 is kept constant at Δf = 220 Hz. The output power of both tones is approximately 19 dBm.

The circles and stars in Fig. 5 show the measured second harmonics $2f_1$ and $2f_2$ (points collapse) , and triangles correspond to the measured IMD2. The left vertical axis shows the output power flowing from the device. The right vertical axis shows the output power of the 2H and IMD2 signals normalized with the output power of the fundamental tones after de-embedding the effects of the measurement setup. The ripple in the output power originates from the measurement IMD one-port setup that includes amplifiers, filters, isolators, a combiner and one 90º broadband hybrid. The continuous lines fit the measurements using the unitless Δc^D_1 = 11 for both resonators. The proposed model and response of both resonators agree very well over the measured frequency range, except around 1.91 GHz, where a small spurious resonance appears. The frequency pattern of the de-embedded normalized power corresponds to the frequency dependence of the stress inside the piezoelectric layer at the fundamental frequencies (f_1 and f_2), which elucidates stress-dependent parameters that are responsible for these intrinsic nonlinearities.

Measurements performed on all resonators from the other supplier were fitted with a value of Δc^D_1 = 12, which is comparable to the previous value obtained from A23 and A64 and previous reports [10]. Moreover, these findings support the hypothesis that the stiffened elasticity of Al N is responsible for the 2H and IMD2 generation.

B. Third-order intermodulation measurements

Figures 6 show measurements and simulations (resonators A64: Fig 6(a) and A23: Fig. 6(b)) of the third order intermodulation products $2f_1 - f_2$ and $2f_2 - f_1$ (IMD3). The spacing between tones was also set to Δf = 220 Hz. Limitations in the measurement setup, specifically the phase noise of sources, lead to a lower bound on the dynamic range and resulted in a noise floor at approximately -60 dBm. By performing simulations, we were able to show that the IMD3 due to the intrinsic value Δc^D_1 is smaller than the measured values. In order to account for the measured IMD3, we introduced the additional terms Δc^D_2 and/or Δc^D_T.

The data given in Fig.6 have been fitted using Δc^D_1 = 11, Δc^D_2 = -1e-10 N^{-1}·m^2 and Δc^D_T = -5.8e6 Pa/K, where the temperature derivative term can also be read as $\Delta c^D_T / c^D_0$ = -15 ppm/K, which agrees in order of magnitude with the values reported in [9] and [11]. We have included Δc^D_2 to fit the dependence of the intermodulation distortion level on Δf / 2, which will be described later. This value of Δc^D_2 also has the same order of magnitude previously measured by means of mechanical measurements [10].

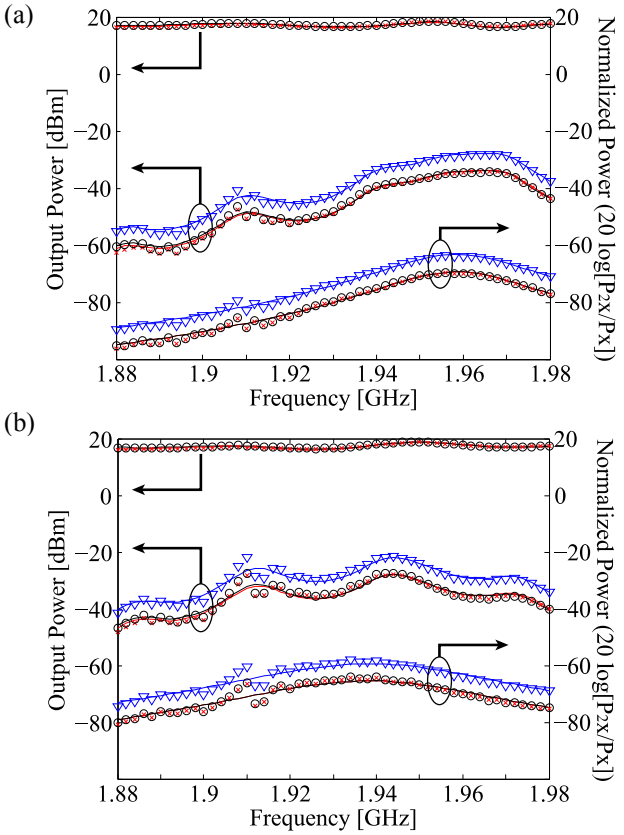

Fig. 5. 2H (circles) and IMD2 (triangles) for A64 (a) and A23 (b) resonators. Left vertical axis indicates the output power and right vertical axis shows normalized values.

For the largest resonator (A64), Fig. 6(a) shows good agreement between the proposed model and the measured IMD3 data, over the measured frequency range above the noise floor. In contrast, the smaller resonator (A23) in Fig. 6(b) shows good agreement at the maximum level of the IMD3, but the model fails to predict the IMD3 when the spurious resonances play an important role. This could be due to the inherent one-dimensional nature of the implemented

model, and further development is underway. In addition, a small bump around 1.97 GHz can be seen in Fig. 6(b), which is also not predicted by our model. We believe that other dissipation sources could play a role in the third-order intermodulation distortion, which may also be dependent on the resonator area.

i. Third-order intermodulation vs. frequency envelope

Perhaps, the most indicative measure of the role of thermal effects is the dependence of the intermodulation distortion level on Δf [7]. Measurements with the two test tones at the frequency where intermodulation output power is a maximum have been performed as a function of the tone spacing. Figure 7 shows the characteristic low-pass filter shape of the thermal impedance where the horizontal axis represents Δf. Squares and circles represent the measured IMD3 and solid lines show the simulations using the reported $\Delta c^D_1 = 11$, $\Delta c^D_2 = -1e-10$ N$^{-1}\cdot$m^2, $\Delta c^D_T = -5.8e6$ Pa/K.

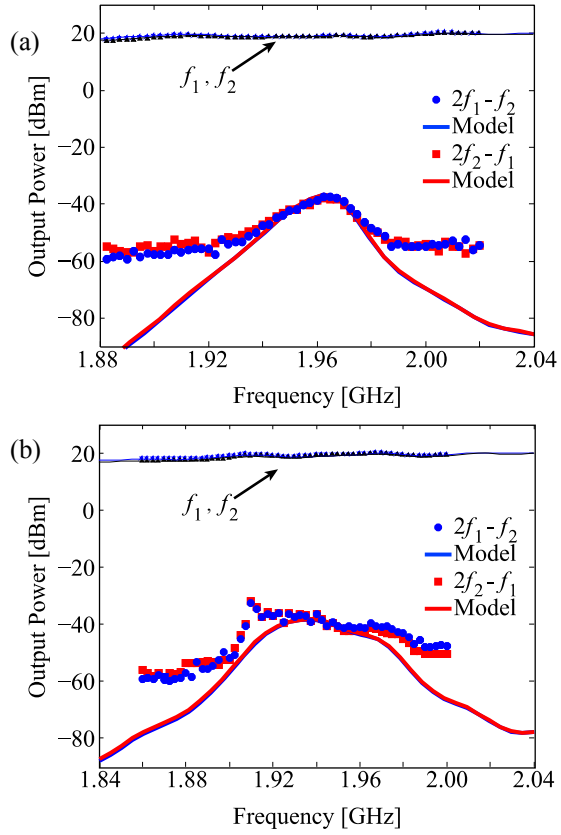

Fig. 6. Stars, triangles, squares and circles represent the measured f_1, f_2, $2f_1 - f_2$ and $2f_2 - f_1$ for the A64 (a) and A 23 (b) resonator. The solid lines are simulations using an input power of 19 dBm.

This shows over this broad parameter space that the third-order intermodulation is due to the contribution of different sources of IMD3: Δc^D_1, Δc^D_2 and Δc^D_T. Figure 7 shows the contribution of each constant, independent of the others. The dashed line with circles shows the IMD3 level generated by Δc^D_1 as a result of mixing between the second harmonic with the fundamental. The dashed line with triangles shows the IMD3 level generated by the existence of Δc^D_2, which directly generates third-order components. Intermodulation due to thermal effects is represented by the dashed line with squares. From Fig. 7, IMD3 for slow envelope variations of the driving signal is due, almost entirely, to thermal effects. When the envelope frequency increases, self-heating effects lose importance and intrinsic (thermally independent) values of Δc^D_1 and Δc^D_2 become more significant, which produces a smoothing of the IMD3 vs. Δf slope.

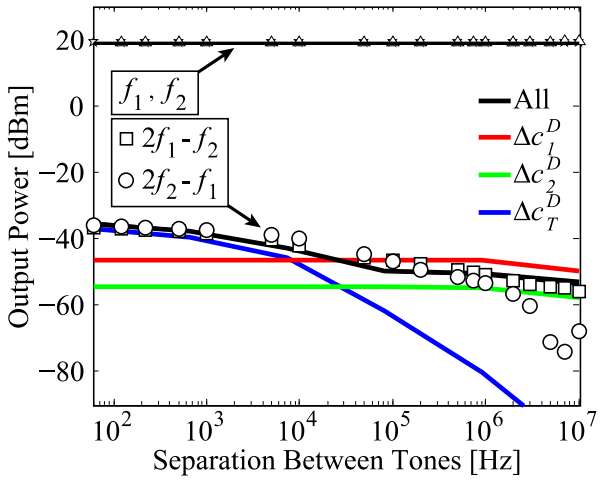

Fig. 7. IMD3 level for different separations between tones for the A64 resonator. Stars, triangles, squares and circles are f_1, f_2, $2f_1$-f_2 and $2f_2$-f_1, respectively. Contributions to the IMD3 level of each source by itself are also plotted with dashed lines: circles, triangles and squares represent Δc^D_1, Δc^D_2 and Δc^D_T contributions, respectively.

A small disagreement between measurements and simulation can be seen in Fig. 7 for values of Δf between 10 kHz to 100 kHz. Further improvements of the thermal model may account for this discrepancy by introducing additional terms to account for frequency-dependent heat diffusion. This may produce the desired slower decay and improve the agreement between the model and measurements. Furthermore, such developments may reproduce the measured asymmetries of $2f_1 - f_2$ and $2f_2 - f_1$ from 1 MHz up to 10 MHz.

VII. Summary and Conclusions

We have presented a nonlinear BAW model that allows us to obtain geometry-independent material parameters that account for second-harmonic and intermodulation generation with bulk material properties. The model is able to predict the harmonic generation and second-order intermodulation due to the stiffened elasticity as a function of stress. We have obtained a value of $\Delta c^D_1 = 11$ for the samples provided by one manufacturer (rectangular-shaped with several different areas), and $\Delta c^D_1 = 12$ for a set of samples from another manufacturer (trapezoidal-shaped with several different areas). These results show that the nonlinear-stiffened elasticity is predominantly responsible for second-harmonic generation at

these broad measurement frequencies and array of devices areas and shapes.

Thermal effects were also modeled from third-order intermodulation measurements, and a value of Δc^{D}_{T} = -5.8e6 Pa/K was obtained for all the square-shaped resonators. This value is consistent with the value reported in [9] and [11]. Further research should accurately model heat diffusion through the material's stack. Additional investigation is underway to assess the role of other heat sources, such as the electrical resistance of the electrodes, effects of nonlinear permittivity, etc.

ACKNOWLEDGMENT

This work was partially supported by the Spanish Government (CICYT) under Grant TEC-2006-13248-C04-02/TCM. E.R. thanks the support from BES-2007-16775. The authors thank A. Padilla, N. D. Orloff, J. Mateu and J. O'Callaghan for their fruitful discussions and critical review of this manuscript.

REFERENCES

[1] C.W. Liu and M. Damgaard. "IP2 and IP 3 Nonlinearity Specifications for 3G/WCDMA Receivers". *Microwave Journal*, May 2009.

[2] D.A. Hall, "Nonlinearity in Piezoelectric Ceramics", *J. Mat. Sci.* 36, pp. 4575-4601, 2001.

[3] M. Ueda, M. Iwaki, T Nishihara, Y. Satoh, K. Hashimoto, "A Circuit Model for Nonlinear Simulation of Radio-Frequency Filters Using Bulk Acoustic Wave Resonators," *IEEE Trans. Ultrason. Ferroelec. Freq. Control*, , vol. 55, no. 4, pp. 849-856, April 2008.

[4] E. Rocas, C. Collado, J. Mateu, H. Campanella and J.M O'Callaghan, "Third order Intermodulation Distortion in Film Bulk Acoustic Resonators at Resonance and Antiresonance". *IEEE MTT-S International Microwave Symposium Digest*, pp. 1259-1262, June 2008.

[5] C. Collado, E. Rocas, J. Mateu, A. Padilla, J. M. O'Callaghan," Nonlinear Distributed Model for BAW Resonators", *IEEE Trans. on Microwave Theory and Techniques*. Accepted for publication, 2009.

[6] R. Krimholtz, D.A. Leedom and G.L. Matthaei, "New equivalent circuits for elementary piezoelectric transducers," *Electronics Letters* , vol. 6, no. 13, pp. 398-399, June 1970.

[7] J. Vuolevi, T. Rahkonen and J.P.A. Manninen, "Measurement technique for characterizing memory effects in RF power amplifiers," *IEEE Trans. on Microwave Theory and Techniques*, vol. 49, no. 8, pp. 1383-1389, 2001.

[8] F.P. Incropera and D. P. de Witt, "Fundamentals of Heat and Mass Transfer", 5th ed., J. Wiley & Sons N.Y., 2002.

[9] J.D. Larson and Y. III Oshrn yansky , "Measurement of Effective k_t^2, Q, R_p, R_s, vs. Temperature for Mo/AlN FBAR Resonators," *Proc. 2002 IEEE Ultrasonics Symposium*, pp. 939-943, 2002.

[10] S.P. Łepkowski and G. Jurczak , "Nonlinear elasticity in III-N compounds: Ab initio calculations", *Physical Review B,* vol. 72, 245201, pp. 1-12. 2005.

[11] D.K. Pandey, R.R. Yadav, "Temperature dependent ultrasonic properties of aluminium nitride", *Applied Acoustics*, vol. 70, no. 3, pp. 412-415, March 2009.

APPENDIX A TO CHAPTER III - A Large-Signal Model of Ferroelectric Thin-Film Transmission Lines

Eduard Rocas, *Student IEEE Member*, Carlos Collado, *Senior IEEE Member*, Jordi Mateu, *Senior IEEE Member*, Nathan Orloff, J.M. O'Callaghan, *Senior IEEE Member*, James C. Booth

***Abstract*— This work evaluates the microwave nonlinear properties and tuning at RF frequencies of ferroelectric $Ba_{0.3}Sr_{0.7}TiO_3$ thin-films by on-wafer measurements of the second and third-order harmonics and intermodulation products of several coplanar transmission lines as a function of DC bias. We analyze these data by use of a large-signal circuit model to obtain the nonlinear distributed capacitance as a function of voltage.**

Whereas the model with an electric field-dependent dielectric constant for the ferroelectric material is able to predict the tuning when a DC voltage is applied and also the generated harmonics, it disagrees with the measured third-order intermodulation products at frequencies $2\omega_1-\omega_2$ and $2\omega_2-\omega_1$. Nonlinear effects due to self-heating mechanisms are also considered, along with an additional phenomenological source of nonlinearities, to model all the observables. Interactions between the ferroelectric and self-heating components give rise to a deep null in both the measured and modeled IMD component.

***Index Terms*— Circuit modeling, ferroelectric films, large-signal model, microwave measurements, nonlinear response, thermal effects.**

I. INTRODUCTION

FERROELECTIC thin-film materials are attractive for many microwave applications, such as those requiring frequency agility, phase shifting, harmonic generation or pulse shaping [1], due to the possibility of changing the material's permittivity with an applied electric field. A detailed understanding of this tuning mechanism at DC, as well as at RF frequencies, is crucial to assess critical issues such as maximum tuning speed or spurious signal generation in ferroelectric-based devices.

In our previous work [2], we presented measurements and analysis of the microwave nonlinear response in a $Ba_{0.3}Sr_{0.7}TiO_3$ (BSTO) thin-film on a $LaAlO_3$ (LAO) substrate. Those measurements involved broadband microwave characterization of the thin film up to 40 GHz with an applied 0 to 40 V DC bias voltage. Such measurements yielded the distributed capacitance of the structures and the tuning (change in permittivity with DC bias voltage) properties for a DC bias. In [2], we also reported on measurements of the third harmonic for a fixed fundamental frequency at 2 GHz and zero DC voltage, yielding a small-signal model that was able to model the third-harmonic generation around zero applied DC voltage, demonstrating the tuning capability of the device on a nanosecond time scale. These results gave limited insight into the time response and nonlinear effects of the ferroelectric transmission lines, and as discussed in [2], further experiments were required for a complete characterization of the ferroelectric thin-films. For example, measurements of the IMD products in addition to third harmonic provide information about the dynamics of the system.

This work aims to provide a full characterization and modeling of the nonlinear effects produced in tunable ferroelectric devices. To that end, we measured the complete set of second-order and third-order spurious signals generated in several BSTO transmission lines, in the paraelectric state, at room temperature. A large-signal model has been proposed to explain all observed spurious signals.

The full characterization requires driving the BSTO transmission lines with a two-tone signal at frequencies f_1 and f_2 and measuring, at the output, the second harmonics (2H), third harmonics (3H), second-order intermodulation products (2IMD) at frequencies f_1+f_2 and the third-order intermodulation products (3IMD) at frequencies $2f_1+f_2$, $2f_2+f_1$, $2f_1-f_2$ and $2f_2-f_1$. These measurements have been carried out for several values of applied DC bias voltage, and also the values of f_1 and f_2 have been varied to sweep the frequency difference between the two drive tones ($\Delta f = f_2 - f_1$) between 2 Hz and 1 GHz.

To describe the measured results, we built a large-signal circuit model in incremental steps to include all the experimental results. We started by using a simple nonlinear equivalent circuit, which models a nonlinear transmission line by cascading many resistance, inductance, capacitance and conductance (RLCG) elemental segments, where the distributed capacitance C(v) depends on the voltage dropped at each section. This circuit model, or a variation of it, has been used to explain the nonlinear distributed effects in superconductors [3] and ferroelectrics [4], and has been successfully applied to generate nonlinear models of more sophisticated devices, such as filters [5].

This model is able to predict the second and third harmonic, the second-order intermodulation products, and the third-order intermodulation products at higher frequencies $2f_1+f_2$ and $2f_2+f_1$. However, it fails to predict the in-band third-order intermodulation products $2f_1-f_2$ and $2f_2-f_1$. These spurious signals are significantly higher in amplitude than the low bound given by the large-signal model. This anomalous imbalance, which depends on the tone spacing Δf, reveals the existence of additional sources of nonlinearities due to self-

heating effects [6], [7].

The circuit model is then generalized in the same way as recently done, for metallic transmission lines on dielectric substrates [7], to account for the self-heating-induced nonlinearities. This is accomplished by defining a nonlinear voltage and temperature-dependent distributed capacitance. The resultant circuit models predict, for first time, all the non-linear manifestations occurring in the nonlinear ferroelectric transmission line, including asymmetries between $2f_1$-f_2 and $2f_2$-f_1 due to an interaction of two sources of nonlinearity. Therefore, it can help to provide a better understanding of the nonlinear electro-thermo-dynamics inherent in ferroelectric materials.

In addition, this model, as used with superconductors in [8] may be useful for predicting the nonlinearities of more complex ferroelectric devices under DC voltages or even devices that are driven by complex modulated signals with high peak power levels in their envelopes, like those in Wideband Code Division Multiple Access (WCDMA) systems [5].

II. Large-Signal Model of Ferroelectric Transmission Lines

In this section, we analyze the harmonics and intermodulation distortion occurring in a ferroelectric transmission line due to its inherent tunability, by analyzing the equivalent circuit model of Fig. 1 (self-heating effects will be considered in Section V). The circuit model corresponds to an elemental segment of a whole transmission line, where *L*, *R*, *C* and *G* are the inductance, resistance, capacitance and conductance per unit length [9].

A. Inherent nonlinear response of ferroelectrics

In a transverse electric and magnetic mode (TEM) ferroelectric transmission line, where the dielectric permittivity depends on the applied electric field, $\varepsilon(E)$, the *C* and *G* become voltage-dependent; i.e., $C(v) = C_0+\Delta C(v)$ and $G(v) = G_0+\Delta G(v)$.

Most of the previously reported work [2],[10], based on nonlinear experiments around zero DC voltage, suggest a quadratic voltage-dependent capacitance, which is appropriate for a ferroelectric material in the paraelectric state. This work considers a slightly more complicated function in order to describe the voltage-dependent capacitance for a wide range of applied DC voltage as

$$\begin{aligned} C(v) &= C_0 - \Delta C_2 v^2 \qquad \text{if } v \le v_0 \\ C(v) &= C_0 - \Delta C_a v - \Delta C_b v^2 \quad \text{if } v > v_0 \end{aligned} \quad , \tag{1}$$

where C_0 is the linear part of the distributed parameters, ΔC_2 is a scaling constant that sets the strength of the quadratic dependence at zero DC bias and

$$\Delta C_b = \Delta C_2 - \frac{\Delta C_a}{v_0} \tag{2}$$

is set to keep the continuity of $C(v)$ at voltage v_0. The proposed function represents a smooth transition, captured by v_0, from a square dependence at low voltages to first-order and second-order dependence at higher voltages.

Although the voltage dependence of the distributed conductance would also produce spurious signals, previous work demonstrates that the predominant contribution for the nonlinear response is due to the voltage-dependent capacitance [11]. Therefore, the value ΔC_2 may be related to the harmonics generated at zero DC voltage, and the parameters ΔC_a and v_0 must fit the second harmonic and third harmonic when a certain DC bias voltage $v > v_0$ is applied.

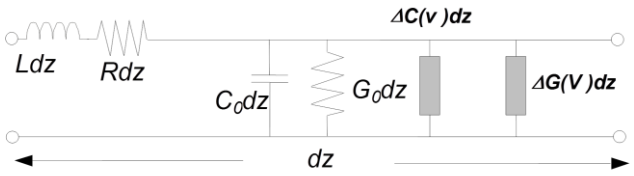

Fig.1. Telegrapher's model of an elemental segment of a ferroelectric transmission line of length *dz*.

B. Harmonics and intermodulation at given DC-bias voltage

Harmonics and intermodulation products can be calculated in passive transmission lines by use of the nonlinear telegrapher's equations [3]. From the equivalent circuit of Fig. 1, in which we show the general case of a ferroelectric material with nonlinear capacitance and conductance, the telegraphers' equations may be written as:

$$\begin{aligned} \frac{di}{dz} &= -\frac{d\big(C(v)v\big)}{dt} - G(v)v, \\ \frac{dv}{dz} &= -\frac{d\big(Li\big)}{dt} - Ri. \end{aligned} \tag{3}$$

The nonlinear contribution due to the voltage-dependent capacitance can be modeled as a nonlinear current as follows:

$$\frac{di_{nl}}{dz} = -\frac{d\big(\Delta C(v(z,t))v(z,t)\big)}{dt} \ , \tag{4}$$

and by use of the procedure detailed in [3], the current generated by the nonlinear effects in the frequency domain for a given frequency f_i can be written as

$$\frac{dI_{nl,f_i}}{dz} = j\omega_i F\big(\Delta C(v(z,t))v(z,t),\, f_i\big) \ , \tag{5}$$

where $v(z,t)$ is the voltage distribution in the transmission line and $F(\,g(t)\,,\, f_i\,)$ is the Fourier transform of function $g(t)$ at f_i.

For intermodulation experiments, where the transmission line is driven with a two-tone signal at frequencies f_1 and f_2, the voltage distribution along the line may be written as $v_{rf}(z,t) = \mathrm{Re}\big\lfloor V_1(z)e^{-j\omega_1 t} + V_2(z)e^{-j\omega_2 t}\big\rfloor$, where $V_1(z)$ and $V_2(z)$ are the voltage distribution along the line at frequencies f_1 and f_2, respectively.

At zero DC bias, $v_{DC}=0$, the first equation in (1) generates only third harmonics and third-order intermodulation products, according to (5):

$$\frac{dI_{nl,f_i}}{dz} = j\omega_i F\big(\Delta C_2 v_{rf}{}^3(z,t),\, f_i\big) \ , \tag{6}$$

which, for third harmonics and third-order IMD, results in

$$F\left(\Delta C_2 {v_{rf}}^3(z,t), 3f_k\right)\big|_{v_{DC}=0} = \frac{1}{4}\Delta C_2 {V_k}^3(z)$$
$$F\left(\Delta C_2 {v_{rf}}^3(z,t), 2f_k - f_j\right)\big|_{v_{DC}=0} = \frac{3}{4}\Delta C_2 {V_k}^2(z) V_j^*(z) \quad (7)$$
$$F\left(\Delta C_2 {v_{rf}}^3(z,t), 2f_k + f_j\right)\big|_{v_{DC}=0} = \frac{3}{4}\Delta C_2 {V_k}^2(z) V_j(z),$$

where $k,j = 1,2$ and $k \neq j$.

By use of the nonlinear current generators (6) at each spurious frequency, the dissipated power at the load can be found as shown in [11]. For example, the power delivered to the load at $2\omega_1+\omega_2$ is:

$$P_{2f_1+f_2}\big|_{v_{DC}=0} = \frac{9}{16}(2\omega_1+\omega_2)^2 |\Delta C_2|^2 P_1^2 P_2 l^2 K_{2f_1+f_2}(f_1, f_2), \quad (8)$$

where P_1 and P_2 are the available power of the incident sources, l is the length of the transmission line and $K_{2f1+f2}(f_1, f_2)$ accounts for the linear effects of the line, including losses, dispersion and impedance mismatch. The $K_{2f1+f2}(f_1, f_2)$ term can be obtained from the linear distributed circuit parameters as shown in [12]. In analogy to (7), we can use (5) and (6) to obtain the output power for other spurious signals at IMD and third-harmonic frequencies.

When a DC voltage v_{DC} is applied, the 3IMD and 3H can be found following the previous procedure by use of $v_{DC}+v_{rf}(z,t)$ in (5). Note as well that for $v_{DC} > v_0$, the second equation in (1) should be used instead of the first.

Additionally, in this case a second harmonic and second-order intermodulation term will appear as well. The resulting nonlinear Fourier transform coefficients at frequencies $2f_k$ and f_1+f_2 for $v_{DC} < v_0$ is

$$F\left(\Delta C_2 \left(V_{DC} + v_{rf}(z,t)\right)^3, 2f_k\right)\big|_{v_{DC}<v_0} = \frac{3}{2}\Delta C_2 V_{DC} {V_k}^2(z)$$
$$F\left(\Delta C_2 \left(V_{DC} + v_{rf}(z,t)\right)^3, f_1 + f_2\right)\big|_{v_{DC}<v_0} = 3\Delta C_2 V_{DC} V_1(z) V_2(z), \quad (9)$$

where $k = 1,2$, whereas for $v_{DC} > v_0$ the previous equation can be read as

$$F\left(\Delta C_a v^2(z,t) + \Delta C_b v^3(z,t), 2f_k\right)\big|_{v_{DC}>v_0} = \frac{1}{2}\left(3\Delta C_b V_{DC} + \Delta C_a\right){V_k}^2(z)$$
$$F\left(\Delta C_a v^2(z,t) + \Delta C_b v^3(z,t), f_1 + f_2\right)\big|_{v_{DC}>v_0} = \left(3\Delta C_b V_{DC} + \Delta C_a\right) V_1(z) V_2(z). \quad (10)$$

The expressions above represent the DC and RF voltage dependence of the spurious signals generated in a ferroelectric transmission lines as a function of the circuit parameters ΔC_2, ΔC_a , ΔC_b and, consequently, as a function also of the electric-field dependence of the permittivity.

III. Samples and Broadband Microwave Measurements

Extraction of the nonlinear terms ΔC_2, ΔC_a , ΔC_b from the measurements of the spurious signals requires characterization of all linear distributed circuit parameters defining the circuit model of Fig. 1, that is, C_0, G_0, L and R. In what follows we present the samples and test structures we have measured, and outline the characterization procedure to obtain C_0, G_0, L and R.

A. Samples and structures

Our measurement structures consist of 300 nm thick Au coplanar waveguide transmission lines patterned on a 400 nm thick BSTO thin-film grown by pulsed-laser deposition on a 16x16 mm^2 LAO substrate. The center conductor line width of the transmission lines is 20 μm, and the gap spacing is 10 μm. Measurements of different-length transmission lines, L_1 = 4.20 mm and L_2 = 9.93 mm, will verify the distributed nature (length dependence) of the nonlinear effects predicted by (8). Identical structures are also patterned on a bare LAO substrate. The BSTO has a curie temperature (T_C) of ~230 K, which for room temperature measurements the material is in the paraelectric state.

B. Linear distributed circuit parameters

We performed an initial multiline thru-reflect-line (TRL) calibration [13] in a reference set of CPW transmission lines fabricated on a non-dispersive and low-loss substrate. This reference calibration set consisted of gold lines on a sapphire substrate, along with embedded on-wafer lumped resistors to obtain the transmission line capacitance per unit length, for the reference calibration set, by use of the procedure detailed in [14]. From the complex propagation constant obtained and the distributed capacitance of the reference calibration set, we determined the characteristic impedance of the transmission lines in the reference sample [15]. Then, we can use the calibration comparison method [16] to estimate the characteristic impedance of transmission lines fabricated on lossy and/or dispersive dielectrics. We used this method to obtain the characteristic impedances of the transmission lines on the bare LAO substrate and on the BSTO thin-film. By combining the characteristic impedance with the propagation constant obtained from the multiline TRL calibration performed on the sample and on the bare substrate, we extracted the linear, frequency-dependent, distributed parameters C_0, G_0, L and R, for the lines on BSTO thin-film and on the bare LAO substrate.

To verify the results we measured the DC resistance of the transmission lines on bare LAO and BSTO thin film and obtained the conductivity of the gold conductors by use of the measured cross-section of the center conductor. The conductivity obtained was used to calculate the frequency-dependent inductance and resistance per unit length for the geometries under consideration, by means of a commercial quasi-static finite element analysis. The simulated $L(f)$ and $R(f)$ showed good agreement with the $L(f)$ and $R(f)$ obtained above over the entire frequency range.

IV. IMD and Harmonics Measurement Set-up

As outlined in the introduction, a full characterization of the ferroelectric nonlinear response requires accurate measurements of all second-order and third-order spurious signals generated when a two-tone signal feeds the test transmission line. The measurement set-up used to achieve this is shown in Fig. 2, and has been previously used to characterize the nonlinear response of superconductors [17], STO ferroelectric films [11] and self-heating effects in copper and gold transmission lines [7].

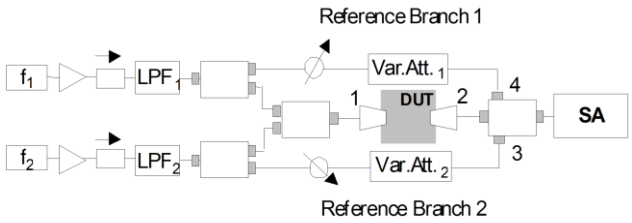

Fig. 2. Diagram of the nonlinear measurement setup.

This measurement setup consists of two sources at f_1 and f_2. Each source feeds a cascaded amplifier, isolator and low-pass filter (LPF) before the signal is split equally into two branches by use of a power divider. The LPF plays an important role in the system performance, and is discussed in detail below. Two of the branches having f_1 and f_2 are combined together through a two-port combiner to feed the device under test (DUT) with the two-tone signal. The two other branches of the measurement system go through a variable attenuator and a phase-shifter. Then the output of the DUT, which contains the fundamental tones as well as the nonlinear products to be measured, is combined with the reference branches through a three-port combiner. Each reference branch is manually adjusted to feed the three-port combiner (indicated by port 3 and port 4 of Fig. 2) with the same amplitude and opposite phase as the fundamental tones coming from the DUT (through port 2, in Fig. 2). By use of this technique, we may attenuate the fundamental tones by up to 60 dB, which dramatically increases the measurement dynamic range at the spectrum analyzer. This measurement configuration also reduces the phase noise of the fundamental tones, which otherwise could mask the spurious signals at $2f_1$-f_2 and $2f_2$-f_1, for small tone spacing.

Since the spurious signal level is usually much below that of the fundamental signal, a very linear measurement system is required to minimize the effects of baseline nonlinearities. Besides the linearity of the spectrum analyzer, which is achieved by cancelling the fundamentals, we need to feed the DUT and the reference branches with low-distortion tones. This is particularly significant in this setup, where the impedance mismatch of the reference branches may produce reflections of the incident and spurious signals. We achieve this low distortion by placing the fundamental tones just below the cut-off frequency of a high-performance LPF to suppress the second and third harmonics generated by the source, amplifier and/or isolator.

The measurement setup described above operates over the frequency range from 2 GHz to 8 GHz for the fundamental signals. We characterize the linear and nonlinear response of the system itself, within the frequency range, by connecting port 1 directly to port 2 (see Fig. 2), omitting the probes and the sample. The system itself shows no spurious signal above noise level, which is around –100 dBm, for incident powers up to +20 dBm. Characterization of the measurement system, including the probes, requires measurements of linear transmission lines or well-characterized nonlinear transmission lines as a reference. Measurements of CPW lines on a bare LAO substrate are detailed in the following section.

V. Measurement Results. Large-Signal Model

This section presents the spurious signal measurements outlined in the introduction. We start by performing measurements on the bare LAO transmission lines. The aim of measuring these transmission lines is twofold: first, it demonstrates the high dynamic range of the measurement set-up of Fig. 2. Second, as the transmission line geometries are the same as the ones on BSTO thin film, measurements of the 3IMD at $2f_1$-f_2 and $2f_2$-f_1 will allow us to explore the existence of heating effects produced due to conductor losses [7]. These measurements will then be used to complement the equivalent circuit model of Fig. 1 to model heating effects. The new circuit model will allow us to explain all the spurious signal manifestations occurring on the BSTO transmission lines.

A. Nonlinear effects in LAO substrate

No measurable harmonic signals have been measured down to the noise floor, around –100 dBm, neither IMD signals at frequencies f_1+f_2 and f_2+f_1, $2f_1$+f_2 and $2f_2$+f_1, when the patterned transmission lines are fed with two tones centered at 6 GHz over a wide range of tone spacing.

Fig. 3, on the other hand, shows the measured IMD at frequencies $2f_1$-f_2 and $2f_2$-f_1 as a function of the tone spacing Δf, which clearly displays self-heating effects due to transmission line conductive losses [7]. This occurs because the dissipated power due to the finite metal conductivity (dielectric losses in the LAO substrate are negligible) causes the temperature of the transmission line to rise according to the thermal impedance of the structure. Therefore, the distributed resistance R changes due to effect of the temperature variations on the temperature-dependent resistivity, which can be modeled as shown in the equivalent circuit of Fig. 4 [7].

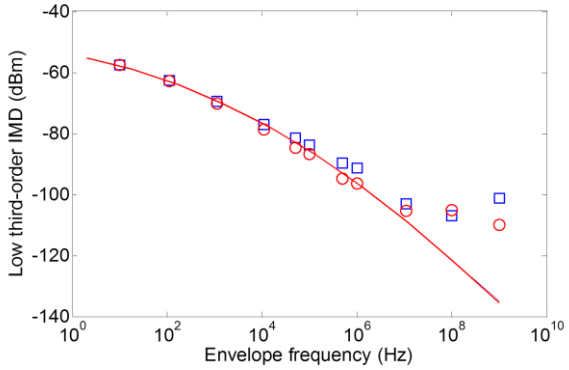

Fig. 3. Simulations (continuous line) and measurements of third-order intermodulation products $2f_1$ - f_2 (circles), $2f_2$ - f_1 (squares) of L_2 = 9.33 mm transmission line on LAO substrate. For Δf >1 MHz simulation and measurements disagree because the baseline intermodulation level of the system is around -100 dBm for this measurement.

This self-heating mechanism generates 3IMD, which is higher as the envelope frequency of the combined input signal decreases, due to the slow dynamics of heat propagation through the substrate. The frequency dependence of the 3IMD

level is due to the thermal impedance of the transmission line. This allows us to obtain the frequency-dependent thermal impedance, and to relate dissipation to temperature rise for the given geometry and substrate. This thermal impedance will then be also used in the model for the BSTO lines, where we will assume that the heat flow through the substrate is not significantly affected by the very thin BSTO layer. Note that for Δf >1 MHz, simulation and measurements disagree because the baseline intermodulation level of the system is around -100 dBm for this measurement.

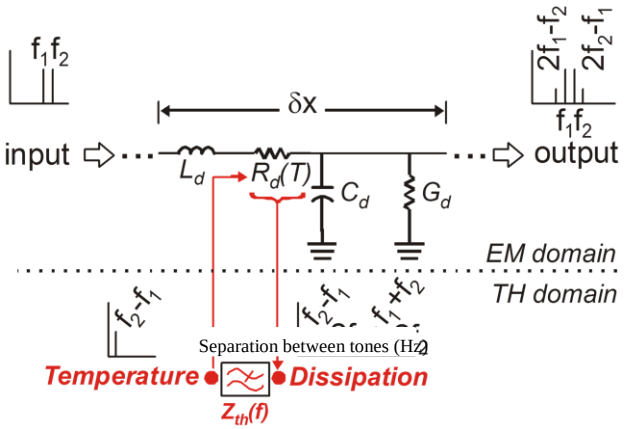

Fig. 4 Equivalent circuit model considering the self-heating effects. The temperature oscillations produce dynamic changes in the metal conductivity, and give rise to third-order intermodulation distortion.

Fig. 3 also shows, as solid lines, the envelope frequency dependence obtained by use of the circuit model of Fig. 4, showing very good agreement between measurements and simulation.

B. Measurement of 2H and 3H as a function of the DC bias voltage on BSTO transmission line

These experiments measure all spurious signals occurring in the L_1 BSTO transmission line at 2H, 3H, 2IMD and 3IMD, when a two-tone signal centered at 6 GHz with a fixed tone spacing of Δf = 14 kHz feeds the transmission line. The input power of the two tones is balanced and swept from -8 dBm to +22 dBm. This experiment has been performed for several DC bias voltages applied: 0.005 V, 10 V, 20 V and 30 V, selected in accordance with previous measurements on ferroelectrics [11] to capture the dependence of the distributed capacitance on voltage.

Figures 5 and 6 show the second-order distortion measurements, at $2f_1$, $2f_2$ and f_1+f_2, and third-order distortion, at $3f_1$, $3f_2$, $2f_1+f_2$ and $2f_2+f_1$ respectively, for the DC bias voltages mentioned above. Fig. 5a shows 2H for 0.005 V and 10 V DC bias and demonstrates that the second harmonic signals dramatically increase as the bias voltage is increased from zero, which is consistent with the circuit model proposed in section II. Also, note however that a very small deviation of the bias voltage from zero (0.005 V) produces measurable second harmonic signals. Note that the baseline nonlinear level of the system, in Figs. 5 and 6, is determined by the input power at the spectrum analyzer, and thus depends on the line loss and length. Moreover, a small tendency to saturation is observed at high powers which is caused by the power amplifiers of the measurement system.

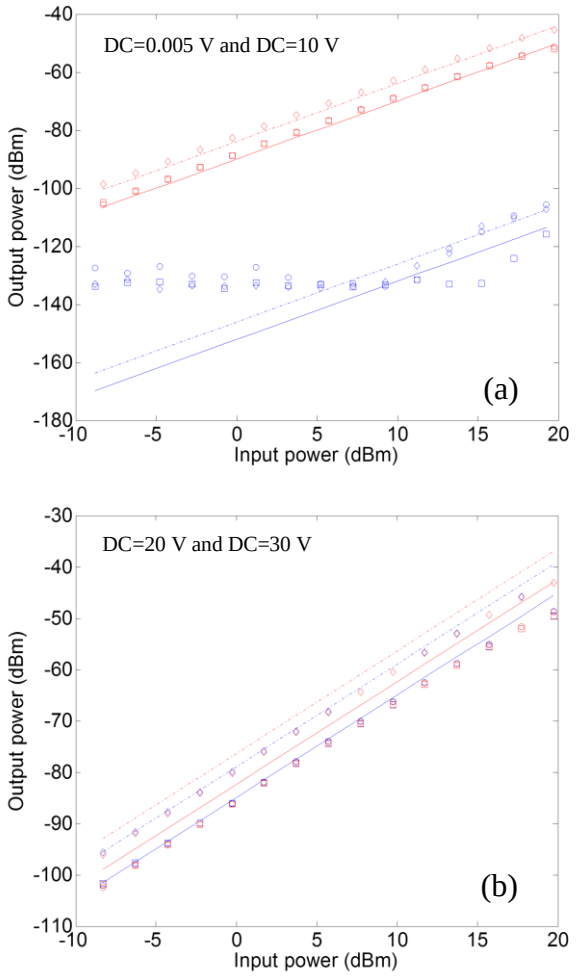

Fig. 5 Output power measured at $2f_1$ (squares), $2f_2$ (circles) and f_1+f_2 (diamonds) and simulations of second harmonics (continuous lines) and f_1+f_2 (dotted line) for several DC voltages; Fig 5a plots 0.005 V (blue) and 10 V (red) and Fig. 5b plots 20 V (blue) and 30 V (red).

We use the measurements above to extract the nonlinear parameters ΔC_2, ΔC_a and v_0 along with the previous obtained linear parameters L, R, C_0 and G_0. These parameters are: $\Delta C_2 = 1.6 \cdot 10^{-14}$ [F/V^2], $\Delta C_a = 4 \cdot 10^{-14}$ [F/V], v_0 = 5 V, which describe a voltage-dependent capacitance. The simulated results for these values are also plotted as solid lines in Figs. 5 and 6, showing good agreement between simulations and measurements for the entire power range. Fig. 7 uses these values to plot the relative capacitance deviation $\Delta C/C_0$ as a function of the voltage, which is consistent with previous results [2], and indicates the degree of tunability in ferroelectrics that can be achieved on nanosecond time scales.

At this point, we should mention that the nonlinear circuit model obtained from Figs. 5 and 6, fails, as expected, to explain the measured 3IMD at $2f_1-f_2$ and $2f_2-f_1$, primarily due to the existence of self-heating effects in the BSTO sample.

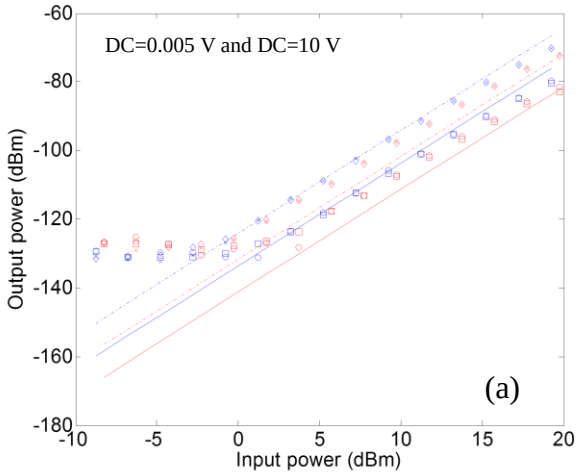

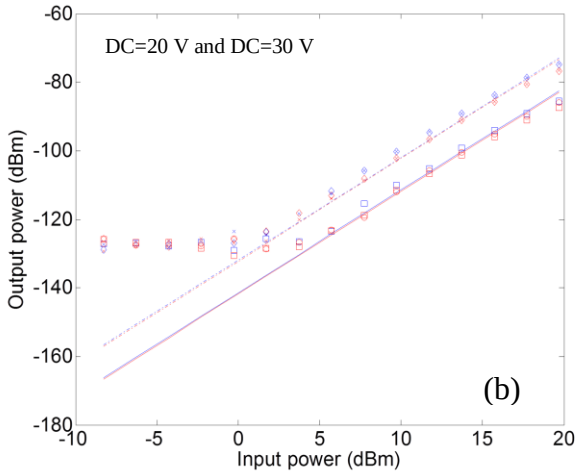

Fig. 6 Output power measured at $3f_1$ (squares), $3f_2$ (circles) , $2f_1+f_2$ (diamonds) and $2f_1+f_2$ (triangles), and simulations of third harmonics (continuous lines) and high frequency third-order products (dotted lines) for several DC voltages; Fig 6a plots 0.005 V (blue) and 10 V (red) and Fig. 6b plots 20 V (blue) and 30 V (red). (diamonds).

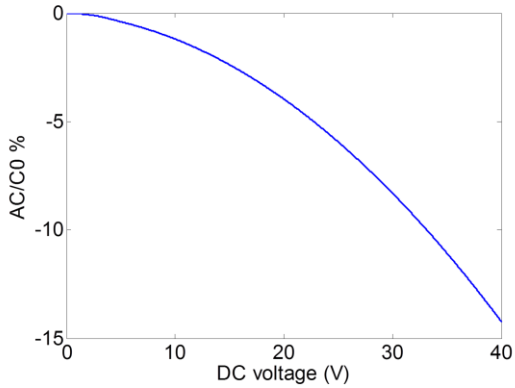

Fig. 7. Relative change in the distributed capacitance obtained by use of (1), from the nonlinear measurements shown in Figs. 5 and 6.

C. 3IMD at $2f_1$-f_2 and $2f_2$-f_1: self-heating effects

In order to complete our circuit model, we include self-heating effects by merging the circuit of Fig.1 with the circuit of Fig. 4. We performed IMD and harmonics measurements in lines L_1 and L_2, keeping the central frequency constant and sweeping the envelope frequency Δf from 2 Hz to 1 GHz for v_{DC} = 0. This broad envelope frequency range gives enough information to discern between memory effect nonlinearities, caused by self-heating [6][7], and non-memory effects caused by inherent, ferroelectric-type, nonlinearities. As done in [11], we have verified that a nonlinear capacitance scales better with frequency, for the inherent nonlinearities, than a nonlinear conductance.

Fig. 8 shows the measured harmonics and intermodulation distortion as a function of the envelope frequency Δf. These measurements reveal that, for high envelope frequencies, $\Delta f > 10^6$, the 3IMD at $2f_1$-f_2 and $2f_2$-f_1 is almost 10 dB higher than the 3IMD at $2f_1+f_2$ and $2f_2+f_1$, and the 3IMD at $2f_1$-f_2 and $2f_2$-f_1 dramatically increases as Δf decreases. In addition, there is a dramatic attenuation of the lower side-band IMD signal for envelope frequencies just below 10^5 Hz.

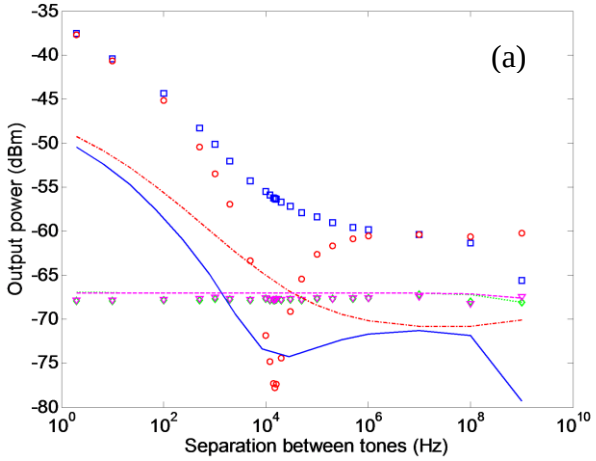

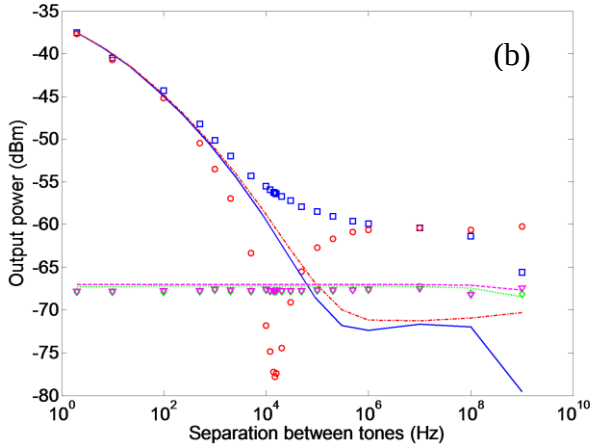

Fig. 8. Measured third-order IMD products at $2f_1$-f_2 (squares), $2f_2$-f_1 (circles), $2f_1+f_2$ (diamonds) and $2f_2+f_1$ (triangles) of the L_1 tranmission line. Simulations are plots with blue continuous line, dashed-dotted red line, dotted green line and dashed magenta line respectively. Fig 8a shows simulations considering only a temperature-dependent distributed resistance. Fig 8b considers a temperature-dependent distributed capacitance along with the temperature-dependent resistance.

As an initial step, we used the temperature-dependent resistance of the metallic electrodes obtained from the measurements on bare LAO substrate transmission lines in our combined model. Note that this assumption makes sense, because the conductors for the BSTO sample are identical to

the LAO transmission lines. However, dielectric losses are included in the model, and they also contribute to the temperature rise due to dissipation. Because of this, the spatial distribution of the generated heat along the LAO-BSTO coplanar waveguide differs from that along the bare LAO coplanar line. In spite of this, we can use the same thermal impedance for the two transmission lines because the BSTO film is very thin with negligible thermal resistance and the thermal properties of the LAO substrate dominate the heat diffusion irrespective of the origin of the dissipation. Therefore, the negligible impact of the BSTO thin-film on the heat path does not affect the obtained temperature derivative for the capacitance.

Fig. 8a shows calculations of the low-frequency 3IMD along with measured data arising from a temperature-dependent gold resistivity. The agreement could not be improved by changing the thermal impedance. By means of simulations, we see that a specific length of transmission line could be fitted, but the resultant model does not scale properly with line length.

The two lines are impedance-mismatched, and the voltage standing-wave ratio is high, which implies different standing-wave patterns for lines of different lengths. We have verified that the measured 3IMD, for the shortest line L_1 in Fig. 8a, can only be explained by means of a temperature-dependent capacitance or conductance.

In order to improve the agreement between the circuit model and data of Fig. 8, we must include in the circuit model a nonlinear term describing the change in the distributed capacitance and/or conductance with temperature. Additional measurements of the scattering parameters at 40 ºC allows us to neglect the temperature-dependent conductance as a source of nonlinearity, so we include in the model an additonal term $\Delta C_T \cdot T$ to the capacitance described in (1), where

$$C_T(v) = C(v) + \Delta C_T \cdot T(v) \quad (11)$$

The complete model, along with an additional phenomenological nonlinearity explained in the following subsection, is shown in Fig. 9.

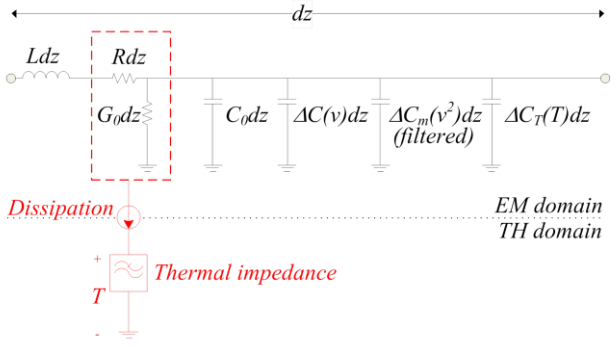

Fig. 9. Complete circuit model implementation of an electro-thermal cell. The electromagnetic domain contains the linear and nonlinear distributed parameters, and the thermal domain contains the thermal impedance.

The transmission line circuit model is implemented, in a distributed manner, as a cascade of cells. Each cell includes the electromagnetic domain, which contains the linear and nonlinear distributed circuit parameters, and the thermal domain, which models the thermal impedance. The dissipation ocurring in the electromagnetic domain as a result of conductive and dielectric losses is coupled to the thermal domain to obtain the temperature rise. By doing this, the temperature-dependent capacitance can be properlly modeled, along wth the temperature-dependent resistance.

The simulated results with this new term set to $\Delta C_T = -4.4 \cdot 10^{-12}$ F/K are shown in Fig. 8b. This temperature-dependent term allows us to describe the 3IMD at $2f_1$-f_2 and $2f_2$-f_1 for Δf < 1 KHz. However it does not explain the cancellation point around Δf = 10 KHz, with a cancellation of more than 40 dB, nor the IMD values for Δf > 10 KHz. This fit therefore suggests the existence of an additional mechanism of nonlinearity.

D. 3IMD at low frequencies: Phenomenological model

This subsection introduces an additional new term for the voltage-dependent capacitance. Although the origin of this mechanism is not yet fully understood, we suggest introducing the frequency-dispersive permittivity phenomena [18]. This new term is required to be low-pass filtered and quadratically dependent on the voltage, as indicated below:

$$C_{T,m}(v) = C(v) + \Delta C_T \cdot T + \Delta C_m \cdot v^2\Big|_{filtered} \quad (12)$$

The complete circuit model of Fig. 9 is then used to fit all spurious signals generated in the BSTO transmission line. Fig. 10 displays the measured and simulated results for the measured IMD in the two transmission lines L_1 and L_2, showing very good agreement for $\Delta C_m = 3 \cdot 10^{-3}$ F/V^2.

These results demonstrate that the self-heating mechanisms and the thermal model reproduce the asymmetry between $2f_1$-f_2 and $2f_2$-f_1. We have also verified that the cancellation does not change when changing the input power, which means that the unknown effects and the thermal effects follow the same power-law dependence. In addition, when no heating effects exist, for instance when Δf is large enough or in cryogenic measurements on STO transmission lines [11], this new term also successfully models both the spurious signals at $2f_1$-f_2 and $2f_2$-f_1 and the spurious signals at $2f_1$+f_2 and $2f_2$+f_1. Table I summarizes the nonlinear coefficients of the obtained model:

TABLE I
NONLINEAR COEFFICIENTS OF THE LARGE-SIGNAL MODEL

Nonlinear term	Value
ΔC_2	$1.6 \cdot 10^{-14}$ F/V^2
ΔC_a	$4 \cdot 10^{-14}$ F/V
v_0	5 V
ΔC_T	$-4.4 \cdot 10^{-12}$ F/K
ΔC_m	$3 \cdot 10^{-3}$ F/V^2

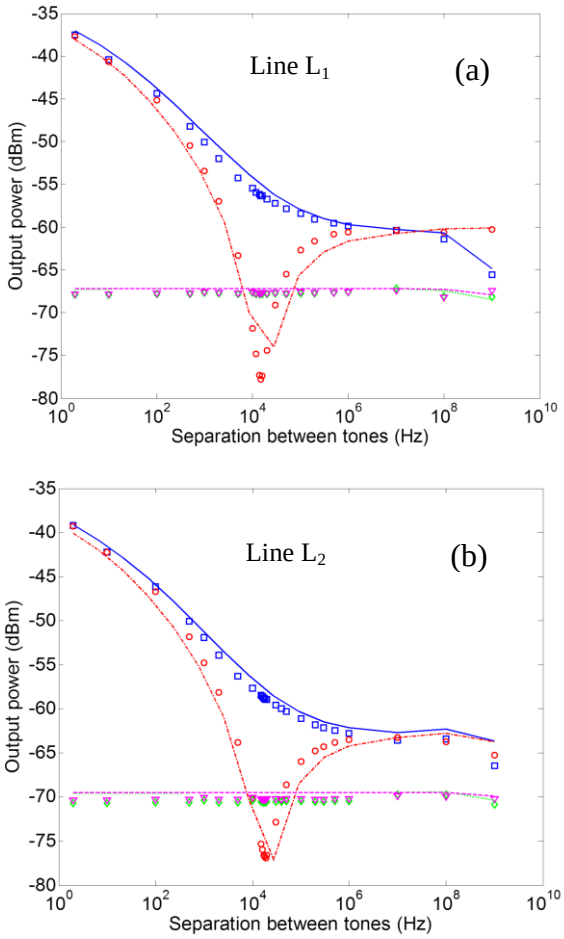

Fig. 10 Measured third-order IMD products at $2f_1$-f_2 (squares), $2f_2$-f_1 (circles), $2f_1$+f_2 (diamonds) and $2f_2$+f_1 (triangles) of the L_1 (a) and L_2 (b) transmission lines. Simulations are plot with blue solid line, dashed-dotted red line, dotted green line and dashed magenta line respectively.

VI. Conclusion

This work has demonstrated a comprehensive procedure for evaluating and modeling the nonlinear response of ferroelectric transmission lines. The procedure includes an accurate characterization of the linear and nonlinear properties of the ferroelectric thin-film material. The nonlinear characterization consists of systematic measurements and analysis of the spurious signals generated in ferroelectric nonlinear transmission lines. The measurement system was shown to be useful for characterizing the origin of these nonlinear effects and for studying their time dependence.

The self-heating effects occurring in any dissipative transmission line have also been included in the circuit model. This allows us to model not only a single set of harmonics and intermodulation products but also to consider the nonlinear effects as a function of the time dependence envelope of the signal. Note that this is crucial for the development of comprehensive models that would eventually be used to evaluate the response of real telecommunication devices which may be subject to a very complex electromagnetic environment, over a wide range of incident waveforms beyond the small-signal assumptions.

References

[1] M. J. Lancaster, J. Powel and A. Porch, "Thin-film ferroelectric microwave devices" *Supercond. Sci. Technol.* No. 11, pp. 1323-1334, November 1998.

[2] J. Mateu, J.C. Booth, S.A. Schima, C. Collado, D. Seron, J. M. O'Callaghan, "Measurements and Analysis of Microwave Nonlinearities in Ferroelectric Thin Films Transmission Lines", in *IEEE MTT-S Int. Microwave Symp. Dig.*, June 2006.

[3] C. Collado, J. Mateu and J. M. O'Callaghan, "Analysis and Simulation of the Effects of Distributed Nonlinearities in Microwave Superconducting Devices", *IEEE Transactions on Applied Superconductivity.* vol. 15, no. 1, pp. 26-39, March 2005.

[4] D. Seron, C. Collado, J. Mateu, J. M. O'Callaghan, "Analysis and Simulation of Distributed Nonlinearities in Ferroelectric and Superconductors for Microwave Applications", *IEEE Trans. Microwave Theory and Tech.* vol. 54, no 3, pp. 1154-1160, March 2006.

[5] C. Collado, J. Mateu, O. Menendez and J.M. O'Callaghan, "Nonlinear distortion in a 8-pole quasi-elliptic bandpass HTS filter for CDMA system", *IEEE Transactions on Applied Superconductivity.* vol. 15, no. 2, pp. 992-995, June 2005

[6] J. R. Wilkerson, K. G. Gard, A. G. Schuchinsky and M. B. Steer, "Electro-Thermal Theory of Intermodulation Distortion in Lossy Microwave Components", *IEEE Transactions on Microwave Theory and Techniques*, vol. 56, no. 12, pp. 2717-2725, Dec. 2008

[7] Rocas, E.; Collado, C.; Orloff, N. D.; Mateu, J.; Padilla, A.; O'Callaghan, J. M.; Booth, J. C., "Passive Intermodulation Due to Self-Heating in Printed Transmission Lines", *IEEE Trans. Microwave Theory and Tech*, accepted 2010

[8] J. Parron, C. Collado, J. Mateu, J.M. Rius, N. Duffo, J.M O'Callaghan, "General electromagnetic simulation tool to predict the microwave nonlinear response of planar, arbitrarily-shaped HTS structures", *IEEE Transactions on Applied Superconductivity.* vol. 11, no. 1, pp. 399-402, Mar 2001

[9] D. M. Pozar, *Microwave Engineering*, John Wiley & Sons, Inc, 1998

[10] J.C. Booth, R. H. Ono, I. Takeuchi, and K.-S. Chang, "Microwave frequency tuning and harmonic generation in ferroelectric thin film transmission lines," *Appl. Phys. Lett.*, vol. 81, no. 4, pp718-720, 2002.

[11] J. Mateu, J.C. Booth and S.A. Schima,"Frequency Tuning and Spurious Signal Generation at Microwave Frequencies in Ferroelectric $SrTiO_3$ Thin-Film Transmission Lines", *IEEE Trans. Microwave Theory and Tech*, Vol. 55, No. 2, pp. 391 – 396, Feb. 2007

[12] J. Mateu, C. Collado, N. Orloff, J.C. Booth, E.Rocas, A. Padilla and J. M. O'Callaghan, "Third order intermodulation distortion and harmonic generation in mismatched weakly nonlinear transmission lines", *IEEE Trans. Microwave Theory and Tech.* Vol. 57, No. 1, pp. 10-18, 2009.

[13] R.B. Marks, "A Multiline method for Network Analyzer calibration", *IEEE Trans. Microwave Theory and Tech.* vol. 39, no 7, pp. 1205-1215, July 1991.

[14] D. F. Williams and R. B. Marks, "Transmission line capacitance measurements", *IEEE Microwave and Guided wave Lett.*, vol., 1. no.9, pp. 243-245, Sept. 1991.

[15] R. B. Marks, D. F. Williams "Characteristic Impedance Determination Using Propagation Constant Measurement", *IEEE Microwave and Guided wave Lett.*, vol., 1. no.6, pp. 141-143, June 1991.

[16] D. F. Williams and R. B. Marks, "Accurate Transmission Line Characterization", *IEEE Microwave and Guided wave Lett.*, vol., 3. no.8, pp. 247-249, Aug. 1993.

[17] J. Mateu, J. C. Booth, B. H. Moeckly, "Frequency Dependence of the Nonlinear Response in YBaCuO transmission lines", *Applied Physics Letters*, Vol. 90, No. 12512, pp 1-3, Jan. 2007.

[18] D. Damjanovic, S. S. N. Bharadwaja, N. Setter, "Toward a unified description of nonlinearity and frequency dispersion of piezoelectric and dielectric responses in Pb(Zr, Ti)O3", Materials Science and Engineering B, Volume 120, Issues 1-3, *The 8th International Symposium on Ferroic Domains (ISFD-8, 2004)*, 15 July 2005, Pages 170-174.

APPENDIX B TO CHAPTER III - Electro-thermo-mechanical Model for Bulk Acoustic Wave Resonators

Eduard Rocas, *Student Member, IEEE*, Carlos Collado, *Senior Member, IEEE*, Jordi Mateu, *Senior Member, IEEE*, Nathan D. Orloff, Robert Aigner, James C. Booth

***Abstract*—In this work we present the electro-thermo-mechanical constitutive relations, expanded up to the third-order, for a BAW resonator. The obtained relations are implemented into a circuit model, which is validated with extensive linear and nonlinear measurements. The mathematical analysis, along with the modeling, allows one to explain, for the first time, all observable effects in a BAW resonator by use of a unified physical description. Moreover, the term that is responsible for the second harmonic and the frequency shift with DC voltage is showed to be the same. Finally, we unveil the impact of an applied DC voltage on the acoustic losses.**

***Index Terms*—Nonlinearities, Self-Heating, Temperature, Thermal Effects, Intermodulation Distortion, Second Harmonic, Bulk Acoustic Wave Resonators.**

I. INTRODUCTION

BULK Acoustic Wave (BAW) technology is accomplishing its market expectations with a promising future in the field of microwave filters for mobile applications. Several advantages, including miniaturization, power handling and frequency operation, make BAW filters preferable among other existent technologies [1][2][3]. But, in spite of the current success of this technology, there is still a lack of a complete understanding of all observable effects in BAW resonators, what could eventually be crucial to push this technology beyond its current limits. In particular, harmonic generation due to intrinsic effects, intermodulation distortion and detuning due to temperature changes are being a matter of active research [4].

The intrinsic nonlinear behavior of the piezoelectric phenomena causes harmonics generation, intermodulation distortion, and frequency detuning with an applied DC voltage. Although recent work has shed light to the possible origin of these nonlinearities [5], none is concluding, neither none successfully models all those undesired effects with a unified nonlinear description.

On the other hand, temperature has always been a matter of special attention with regard to BAW resonators. Temperature induces changes to the material properties and dimensions that should ideally be compensated, generally by use of additional compensation layers, if the frequency drift is to be minimized [6]. An accurate understanding and modeling of the material temperature derivatives is crucial to resize properly the compensation layers. Several authors have faced this problem [6][7], but none of them has considered the clamping conditions that force one to use the Poisson's ratio to properly account for the thickness thermal expansion in Solidly Mounted Resonators (SMR). In addition, temperature concerns not only involve the frequency drift in BAW devices, but also the temperature rise due to self-heating, which can limit the power handling of, for example, Film Bulk Acoustic Resonators (FBAR) [8], and/or contribute to the third-order intermodulation distortion [ref].

Reference [10] was the first distributed nonlinear modeling approach to cover intrinsic effects through the integration of nonlinearities in different sections of the circuit model. A similar approach is followed in [5][11], but with a grouping of the nonlinear sources. On the other hand, our previous work [9] proposed a phenomenological approach to cover intrinsic and thermal effects.

In this article we propose a rigorous electro-thermo-mechanical study, based on the expansion of the Gibbs electrical energy function, capable of explaining most of the observable effects within a BAW resonator with a unified physical description. We derive a circuit model from the obtained constitutive equations and validate it with linear and nonlinear measurements on BAW resonators, what allows identifying the dominant terms that produce the frequency shift in temperature with an applied DC voltage, and the generation of harmonics and intermodulation distortion.

II. CONSTITUTIVE RELATIONS IN A BAW RESONATOR

The working mechanism of a BAW resonator lies on several physical principles that can be explained with the electro-thermo-mechanical constitutive equations and the Newton's second law of motion. The first group of equations describes the energy coupling between fields associated to each physical domain (electrical, mechanical and thermal as shown in the Heckmann's diagram in Fig. 1), whereas Newton's second law states the relation between particle velocity and stress in a medium. A rigorous nonlinear analysis of those constitutive relations allows modeling most of the experimental observables in BAW resonators.

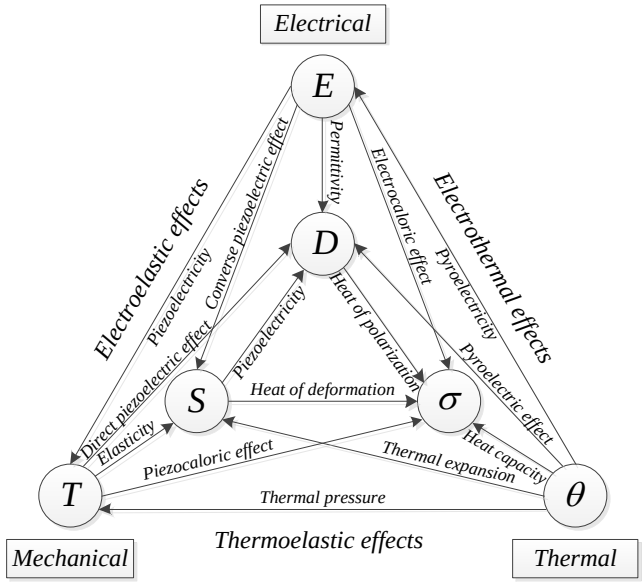

Fig. 1. The Heckmann's diagram shows the electro-thermo-mechanical relations on a crystal.

We start obtaining the nonlinear electro-thermo-mechanical relations for a piezoelectric material, which can be simplified then for non-piezoelectric dielectrics and metals. We make the choice of independent variables to be strain, *S*, electric field, *E*, and temperature, θ, in order to obtain equations describing the stress, *T*, and electric displacement, *D*, which have a direct representation in the Mason model [12]. Moreover, this selection of independent variables allows having the field derivatives of the material properties on magnitudes that can be easily changed when performing measurements, such as the electric field and the temperature.

Appendix I describes the procedure we have followed to obtain the nonlinear constitutive equations by use of a third-order Taylor series expansion of the relations between fields plotted in Fig. 1, in a uni-axial notation. The procedure detailed there does not assume approximations other than the series truncation and results in

$$T = c^{E\theta}S - e^{\theta}E - \tau^{E}\theta + \Delta T_{NL} \quad (1)$$

$$D = e^{\theta}S + \varepsilon^{SE}E + \rho^{S}\theta + \Delta D_{NL} \quad (2)$$

$$\sigma = \tau^{E}S + \rho^{S}E + r^{ES}\theta + \Delta\sigma_{NL}, \quad (3)$$

where the nonlinear contribution, with all the constants defined in the Appendix I, are described in (4)-(6)

$$\Delta T_{NL} = \frac{1}{2}\left(c_2^{E\theta}S^2 - \varphi_3E^2 - \varphi_4\theta^2\right) + \varphi_5SE + \varphi_6S\theta - \varphi_7E\theta... \quad (4)$$
$$+\frac{1}{6}\left(c_3^{E\theta}S^3 - e_{3,E}^{\theta}E^3 - \chi_5\theta^3\right) - \chi_6SE\theta...$$
$$+\frac{1}{2}\left(\chi_7SE^2 + \chi_8S\theta^2 - \chi_9S^2E - \chi_{10}S^2\theta - \chi_{11}E\theta^2 - \chi_{12}E^2\theta\right)$$

$$\Delta D_{NL} = \frac{1}{2}\left(\varepsilon_2^{S\theta}E^2 - \varphi_5S^2 + \varphi_1\theta^2\right) + \varphi_3SE + \varphi_7S\theta + \varphi_2E\theta... \quad (5)$$
$$+\frac{1}{6}\left(\varepsilon_3^{S\theta}E^3 + \chi_9S^3 + \chi_1\theta^3\right) + \chi_{12}SE\theta...$$
$$+\frac{1}{2}\left(\chi_4SE^2 + \chi_{11}S\theta^2 - \chi_7S^2E + \chi_6S^2\theta + \chi_2E\theta^2 + \chi_3E^2\theta\right)$$

$$\Delta\sigma_{NL} = \frac{1}{2}\left(r_2^{ES}\theta^2 + \varphi_2E^2 - \varphi_6S^2\right) + \varphi_7SE + \varphi_4S\theta + \varphi_1E\theta... \quad (6)$$
$$+\frac{1}{6}\left(r_3^{ES}\theta^3 + \chi_3E^3 + \chi_{10}S^3\right) + \chi_{11}SE\theta...$$
$$+\frac{1}{2}\left(\chi_{12}SE^2 + \chi_5S\theta^2 + \chi_6S^2E - \chi_8S^2\theta + \chi_1E\theta^2 + \chi_2E^2\theta\right)$$

What follows is the simplification of the constitutive relations for the specific types of materials used in commercial SMR type resonators, which usually comprise Aluminum Nitride for the piezoelectric layer, metals for the electrodes and non-piezoelectric dielectrics for passivation, temperature compensation and Bragg mirror implementation. In the following sections the thermal expansion coefficient, $c^{E\theta}$, will be used instead of the thermal pressure, τ^E, through the $\tau^E = -c^{E\theta}\alpha^E$ relation, because it is a more commonly used material property.

A. Thermal considerations

Although we have described the entropy with (3) and (6) for completeness, we will not use those equations because we assume that the electrocaloric effect, the piezocaloric effect, the heat of polarization, and heat of deformation are negligible in the materials under consideration [13]. We will deal instead with the heat equation for the thermal domain, which takes into account the temperature rise and heat propagation through a medium [14]. The heat equation can be written as:

$$\frac{\partial\theta}{\partial t} = \frac{k}{c_p\rho}\left(\frac{\partial^2\theta}{\partial z^2}\right), \quad (7)$$

where *k*, c_p and ρ are thermal conductivity, specific heat and density respectively.

The change of in-plane dimensions in SMR resonators is dominated by the substrate and this imposes a lateral-clamped condition that especially impacts how the device expands with temperature. For this reason we will consider the change in area negligible [15], and the model will only account for dimensional changes in the vertical direction by use of the Poisson's ration.

B. Constitutive relations for Aluminum Nitride

For the specific case of Aluminum Nitride (AlN) several simplifications can be made by use of well-known properties of this material and comparisons between nonlinear measurements and simulations.

1) Assumptions related to the AlN properties

We assume that the electrocaloric and pyroelectric effects are negligible [16], what means there is no direct energy exchange, other than dissipation, between the electric and thermal domains. This assumption translates into $\rho^S = 0$.

The AlN properties around room temperature change linearly with temperature [17], so we consider that the second and third-order temperature-dependent coefficients in (4)-(6) are zero, that is $\varphi_1 = \varphi_4 = \chi_1 = \chi_2 = \chi_5 = \chi_8 = \chi_{11} = 0$.

The expansion with temperature has to be taken into account. The BAW resonator is made of thin layers, deposited on a thick Silicon substrate, that expand laterally in

temperature according to the substrate expansion coefficient. Therefore, the thermal expansion coefficient of a layer is replaced by the unit-less Poisson's ratio v_P of that layer times the thermal expansion coefficient of the silicon substrate $\alpha^E \rightarrow v_P \alpha_{Si}^E$ [18].

2) Assumptions done after comparison of simulations and measurements

Previous work has shown that the slow dynamics of temperature translate into a low-pass filter behavior of the generated 3IMD versus the envelope frequency in a classical two-tone experiment [9], and that temperature changes cannot cause third harmonic generation at the operating frequencies of the BAW devices. For this reason, and because the thermally-generated 3IMD can be modeled with first-order temperature dependence [19], we consider negligible the third-order mixed terms that are related to the thermal domain: $\chi_3 = \chi_6 = \chi_{10} = \chi_{12} = 0$.

3) Simplified constitutive equations

With the assumptions explained above, the stress *T* and charge *D* relations for the Aluminum Nitride layer are:

$$T = c^{E\theta} S - e^{\theta} E + \Delta T \tag{8}$$

$$D = e^{\theta} S + \varepsilon^{S\theta} E + \Delta D, \tag{9}$$

with

$$\Delta T = c^{E\theta} v_P \alpha_{Si}^E \theta + c_2^{E\theta} \frac{S^2}{2} + c_3^{E\theta} \frac{S^3}{6} - \varphi_3 \frac{E^2}{2} + \varphi_5 SE + \varphi_6 S\theta - \varphi_7 E\theta \tag{10}$$

$$\Delta D = \varepsilon_2^{S\theta} \frac{E^2}{2} + \varepsilon_3^{S\theta} \frac{E^3}{6} - \varphi_5 \frac{S^2}{2} + \varphi_2 E\theta + \varphi_3 SE + \varphi_7 S\theta \tag{11}$$

Note that the thermal expansion effect, although being a linear effect, has been included in the ΔT source. This makes easier the implementation of a circuit model as it will be shown in Section III.

Equations (8)-(11) can also be interpreted as the result of having a set of nonlinear parameters that define the nonlinear electro-thermo-mechanical constitutive equations for the aluminum nitride:

$$c_{NL} = c^{E\theta} \cdot \left(1 + \frac{c_2^{E\theta}}{2c^{E\theta}} S + \frac{c_3^{E\theta}}{6c^{E\theta}} S^2 + \frac{\varphi_5}{2c^{E\theta}} E + \frac{\varphi_6}{c^{E\theta}} \theta\right) \tag{12}$$

$$e_{NL} = e^{\theta} \cdot \left(1 - \frac{\varphi_5}{2e^{\theta}} S + \frac{\varphi_3}{2e^{\theta}} E + \frac{\varphi_7}{e^{\theta}} \theta\right) \tag{13}$$

$$\varepsilon_{NL} = \varepsilon^{S\theta} \cdot \left(1 + \frac{\varepsilon_2^{S\theta}}{2\varepsilon^{S\theta}} E + \frac{\varepsilon_3^{S\theta}}{6\varepsilon^{S\theta}} E^2 + \frac{\varphi_3}{2\varepsilon^{S\theta}} S + \frac{\varphi_2}{\varepsilon^{S\theta}} \theta\right), \tag{14}$$

which offer a more intuitive description of the role of each parameter. Note that the thermal expansion term is not included in the previous equations and should be kept in the linear constitutive equations.

C. Constitutive relations for non-piezoelectric dielectrics and metals

Non-piezoelectric dielectrics and metals are used in several parts of the resonator and for different purposes, especially in SMR technology. However, for a classic BAW resonator configuration, most of the electromagnetic energy is confined in the piezoelectric layer between the electrodes. This fact makes the modeling of the electric domain unnecessary for the other layers, which only need a thermo-mechanical description.

Nevertheless, electric losses in the metal electrodes must be considered to properly model the linear response of the BAW resonator and the Joule effect contribution to the temperature rise. In our model, a simple electromagnetic description of the electrodes as lumped resistors is accurate enough to properly account for the conducting losses.

On the other hand, the fact that polarization in metals is negligible and the dielectric layers, other than the piezoelectric, are not under electric field makes piezoelectricity, pyroelectricity and electrocaloric effects not present in these layers. We only consider linear effects in these materials, with the exception of temperature dependent properties, because of the lower level of the acoustic and electric fields outside the piezoelectric layer, and this hypothesis will be confirmed with the good agreement of simulations and measurements. With these considerations, we get the same electro-thermal constitutive relations for metals and dielectrics:

$$T = c^{E\theta} S + \Delta T \tag{15}$$

with

$$\Delta T = c^{E\theta} v_P \alpha_{Si}^E \theta + \varphi_6 S\theta \tag{16}$$

III. Circuit Model

The circuit model of the materials stack consists of a cascade of layers with their specific material properties, and in turn, each layer consists of a cascade of circuit cells. Each cell represents a thin section of material to reproduce the distributed nature of the acoustic propagation and thermal diffusion.

The constitutive relations described in the previous section, Newton's second law and heat equation, are implemented at each thin section interrelating electric, acoustic and thermal domains. Reference [20] details the steps to derive the Mason model from the electro-acoustic equations whereas [9] describes the basis of the thermal model.

A. Materials stack

Fig. 5 illustrates the typical structure of a SMR type resonator. It is usually composed of a piezoelectric layer between two metal electrodes, which are all deposited on a Bragg mirror made of a succession of high and low acoustic impedance layers. The main acoustic mode is longitudinal along the vertical *z* axis, and it is induced by the polarization of the piezoelectric layer. Moreover, as it will be discussed in Section III.B, the heat can also be considered to propagate mainly along the vertical direction until it reaches the substrate, and then, the heat diffusion is semispherical. Fig. 2 illustrates a section of the circuit implementation.

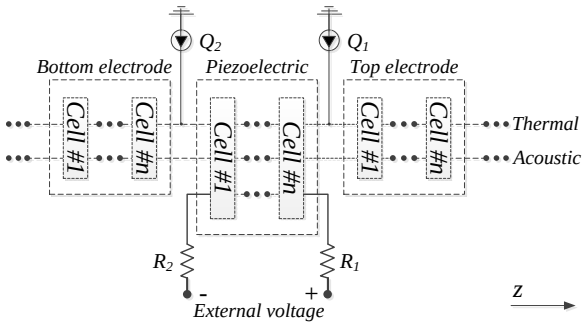

Fig. 2. Block-diagram that illustrates the circuit implementation of three layers of the BAW resonator. Each layer is constructed as a cascade of electro-thermo-mechanical cells. The electric losses are implemented as lumped resistors and their dissipated heat is coupled to the thermal domain.

Note that the piezoelectric layer implements the electric, acoustic and thermal domains in a distributed way, whereas all the other layers only model the acoustic and heat propagation. The electric domain of the electrodes is represented by the lumped resistors R_1 and R_2. The current sources Q_1 and Q_2 couple the dissipated heat on R_1 and R_2, respectively, to the thermal domain.

1) Aluminum Nitride layer

The electro-acoustic model of the piezoelectric layer is implemented in a distributed configuration based in the Mason model [12], as done in [10] and [5][11]. Here, we have included the thermal domain to provide a complete picture of the physics in a BAW resonator.

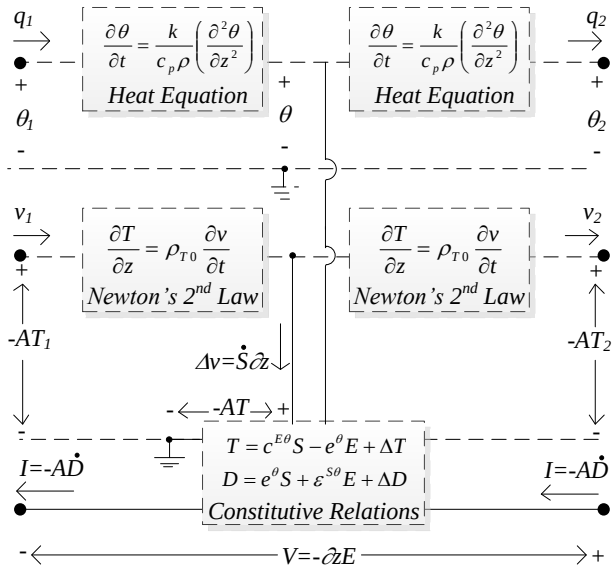

Fig. 3. Block-diagram of a piezoelectric cell implementation with the governing equations for the electric, acoustic and thermal domains.

Fig. 3 illustrates the block-diagram. The governing electro-acoustic equations are described by use of an equivalent circuit with voltage and current being equivalent to force F and particle velocity v respectively. Re-arranging (1) and (2) in the stress T and electric-field E form provides a clear circuit model implementation where

$$T = c^{D\theta} S - \frac{e^{\theta}}{\varepsilon^{S\theta}} D + T_C \tag{17}$$

$$E = \frac{D - e^{\theta} S}{\varepsilon^{S\theta}} - V_C \tag{18}$$

with

$$T_C = \Delta T + \frac{e^{\theta}}{\varepsilon^{S\theta}} \Delta D \tag{19}$$

$$V_C = \frac{\Delta D}{\varepsilon^{S\theta}} \tag{20}$$

and

$$c^{D\theta} = c^{E\theta} + \frac{\left(e^{\theta}\right)^2}{\varepsilon^{S\theta}} \tag{21}$$

as the stiffened elasticity. The acoustic domain results in an acoustic transmission line that obeys the telegrapher equations, with the following distributed parameters for a section of length Δz:

$$C_{\Delta z} = \frac{\Delta z}{A c^{D\theta}} \tag{22}$$

$$L_{\Delta z} = \Delta z \rho A \tag{23}$$

We group the nonlinear sources in T_C and V_C, as done in [5][11], to differentiate between the linear and nonlinear parts of the circuit and provide an easier implementation.

On the other hand, the thermal domain is governed by the heat equation, which also has its electrical analogy. A distributed series resistance and shunt capacitance are the analogs of thermal resistivity and heat capacity respectively [19]. The thermal resistance and capacitance for a section of length Δz are related to the material thermal properties as

$$R_{\theta,\Delta z} = \frac{\Delta z}{Ak} \tag{24}$$

$$C_{\theta,\Delta z} = A c_p \Delta z \tag{25}$$

where A is the area, k is the thermal conductivity and c_p is the heat capacity. This allows identifying the analogs of voltage and current, in the thermal domain, as temperature θ and heat rate q respectively. Fig. 4 shows the circuit implementation of a Δz section of Aluminum Nitride cell, in which the dashed box contains the electro-mechanical constitutive relations that are specific of the piezoelectric.

It is necessary to include losses in the model if we want to accurately capture the resonator's behavior and account for self-heating effects. The fact that dielectric losses in Aluminum Nitride are minor when compared to other sources of loss in BAW resonators [21] makes us consider them negligible. Therefore, only the acoustic damping, by use of a complex elasticity in which the imaginary part is linked to the material viscosity [22], is introduced in the Aluminum Nitride model:

$$c^{D\theta} \rightarrow c^{D\theta} + j\omega\eta^{D\theta}, \tag{26}$$

where $\eta^{D\theta}$ is the acoustic damping coefficient, being $\eta^{D\theta} = v_L \tau$ [23]. In the previous definition, v_L is the acoustic propagation velocity in the longitudinal direction and τ is the viscous relaxation time. The acoustic losses translate into a conductance as follows:

$$G_{\Delta z} = \frac{\Delta z}{A\eta^{D\theta}}. \tag{27}$$

Therefore, the dissipation is implemented as a heat source in the thermal domain, making the introduction of different types of dissipation more flexible:

$$Q_{\Delta z} = \frac{v^2}{G_{\Delta z}}. \tag{28}$$

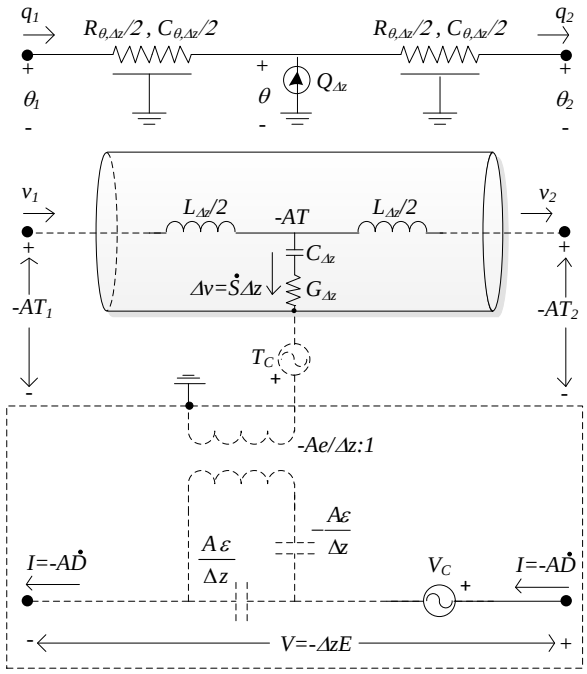

Fig. 4. Circuit model implementation of a Δz long section of piezoelectric.

2) *Non-piezoelectric dielectrics and metals*

As discussed in the previous section, materials other than piezoelectric used in BAW resonators keep the same governing equations for the thermal and acoustic domains than the piezoelectric layer, but the electric field inside of them is negligible. Therefore, non-piezoelectric dielectrics and metals keep the same circuit implementation of Fig. 4 but without the dashed box that contains the electro-acoustic coupling of piezoelectricity. Instead, the T_C source, which is now $T_C = \Delta T$ because ΔD=0, is connected to ground.

B. *Thermal boundaries*

Section IV presents the results of measurements on different samples that have been performed to validate the model. Therefore, the considerations and assumptions on the thermal boundaries to be included in the model have to be in accordance with the specific measurement setup.

To achieve a temperature-controlled environment, a cryogenic probe station has been used, and this allows for an accurate stable reference temperature at the bottom of the resonator. Moreover, the resonator is in complete thermal contact with the copper chuck by use of high thermal conductivity silver paint. The bottom thermal boundary is easily implemented, in the circuit model, by use of a voltage source with the reference temperature value.

The atmosphere of the cryogenic chamber of the probe station is in vacuum, although measurements without vacuum have also been performed, at room temperature, to check that the air acoustic impedance and thermal convection are negligible. Nevertheless, if radiation and convection effects want to be taken into account, although negligible at reasonable power levels, we can use [14]

$$R_C = \frac{1}{Ah_c} \tag{29}$$

$$R_r = \frac{1}{Ah_r} \tag{30}$$

where h_c and h_r are the convection and radiation heat transfer coefficients respectively, and h_r is defined as:

$$h_r = \varepsilon\sigma\left(T_s + T_A\right)\left(T_s^{\,2} + T_A^{\,2}\right), \tag{31}$$

with σ, ε, T_s and T_A being the Stefan-Boltzmann constant, the emissivity and temperature of the top layer and the ambient temperature respectively. Equations (29) and (30) are implemented as two parallel electrical resistances connected to the top of the thermal domain model at one end and a voltage source with ambient temperature at the other end.

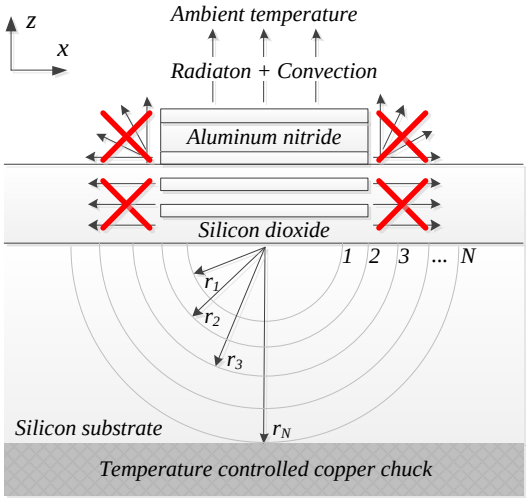

Fig. 5. Cross-section of a SMR type resonator. The figure also illustrates the thermal considerations for the modeling.

Thermal conduction is the main heat propagation mechanism in the devices under study [8]. The resistance to heat flow, as shown in (24), is inversely proportional to the surface area. Therefore, the very high aspect ratio of the Bragg mirror segment, that is the ratio of the in-plane area to the vertical area that surrounds the Bragg mirror, translates into negligible lateral heat flow.

On the other hand, the Silicon substrate is very thick and the previous assumption cannot be made, so semispherical heat diffusion is considered. Figure 5, which summarizes all these assumptions, illustrates several semispherical shells with numbers 1 to N, with the N cell being at reference temperature. Each shell represents a thermal transmission line, of the same form of that in Fig. 4, given by:

$$R_{Si,\Delta z} = \frac{d_{Si}/N}{k2\pi r_i^{\,2}} \tag{32}$$

$$C_{Si,\Delta z} = 2\pi r_i^{\,2}\rho c_p d_{Si}/N, \tag{33}$$

where d_{Si} is the thickness of the Silicon substrate and r_i is the shell radius. The area of the first shell is the resonator area, so that r_1 is obtained from $A=2\pi r_1$, and the other radius are calculated as follows:

$$r_{i+1} = r_i + \frac{d_{Si}}{N}. \quad (34)$$

It has been checked with simulations that less than 20 shells is enough to achieve convergence with accurate results.

IV. Measurements and Simulations

This section presents different types of measurements on BAW resonators along with the simulations of the circuit model that have been done to validate it. The linear performance is evaluated under different temperatures and electric field biasing conditions, which reproduces different situations on the electro-thermo-mechanical diagram of Fig. 1 and allows obtaining field-derivative material properties. Moreover, intermodulation and harmonic measurements are carried out to serve as a second independent way to validate the model.

A. The devices

We perform measurements on two one-port state-of-the-art commercial BAW resonators, having different materials stack composition that corresponds to a series and a parallel resonator, in a Ground-Signal configuration. The different layers structure serve as a way to check that the nonlinearities are correctly defined as geometry-independent material properties. Although the details of the resonators structure cannot be disclosed, the devices are made of Aluminum (Al), Tungsten (W), Aluminum Nitride (AlN), Silicon Dioxide (SiO_2), Silicon (Si) and Silicon Nitride (Si_3N_4). For sake of clarity, in the following subsections we only show the results of the parallel resonator.

B. Temperature measurements and simulations

We perform scattering parameters measurements at different temperatures, by use of a cryogenic probe station as explained in Section III.B, with the purpose of identifying the dominant material temperature derivatives. To do that, we first setup the linear circuit model using commercial software [23] with the electro-acoustic material properties provided by the manufacturer and fine-tune them to perfectly agree with measurements at 293 K. It is important to note that a correct linear modeling not only predicts the main mode resonance but also the spurious longitudinal resonances. As long as the spurious resonances are linked to specific energy distributions in the materials stack, we use the viscosity value of each material to accurately predict the magnitude and phase of them.

Once the linear model at 293 K is properly implemented, the next step consists on adjusting the circuit model response to fit the measurements at different temperatures and obtain the material temperature derivatives. We perform scattering parameters measurements at 220 K and 320 K and use literature values for the material temperature derivatives to obtain a first approximation.

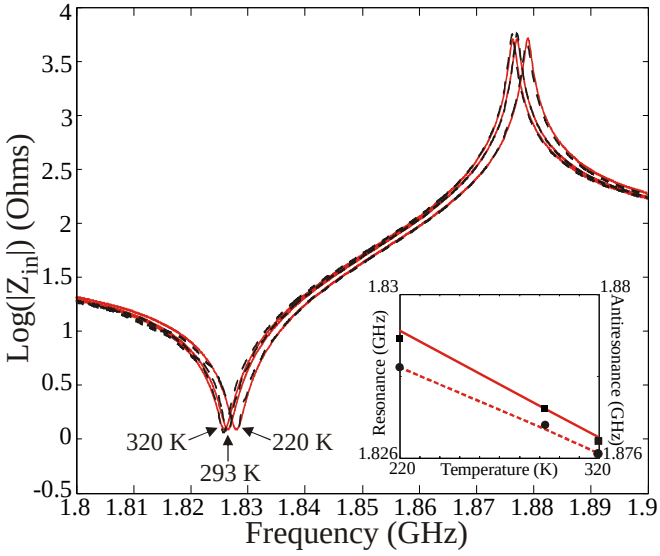

Fig. 6. Measurements and simulations of the magnitude of the impedance for temperatures 220 K, 293 K and 320 K. The inset shows the linear dependence of the resonance and antiresonance frequencies on temperature. In the main plot, the solid lines are simulations whereas the dashed lines are measurements. In the inset, circles and squares represent the measurements at resonance and antiresonance respectively, whereas the dashed line and the solid line represent the simulations at resonance and antiresonance respectively.

TABLE I
Materials Temperature Derivatives

Material	$\varphi_6/c^{E\theta}$ (10^{-6}/K)	$\varphi_2/\varepsilon^{S\theta}$ (10^{-6}/K)	φ_7/e^{θ} (10^{-6}/K)
Al	-300	-	-
AlN	-48	150	10
Si_3N_4	-24.4	-	-
Si	-75	-	-
SiO_2	239	-	-
W	-91	-	-

We use material properties from [6] for all materials, with the exception of the Si_3N_4 value [25] and the Al and AlN values, which obtained through a fine-tuning. Fig. 6 shows the results of measurements and simulations, and Table I summarizes the temperature derivatives we use.

C. Second-order nonlinearities

BAW resonators generate a high level second harmonic and their resonant frequencies linearly change with an applied electric field. Both effects are manifestations of second-order nonlinearity and no consensus exists on its origin yet [11][26]. Up to date, there is no article predicting both effects with a unique model. Therefore, we perform scattering parameters measurements, under different bias voltages, and also second harmonic measurements to validate, by two independent ways, the presented model in Section II.

In the harmonic experiments, the frequency is swept in a 200 MHz range around the mechanical resonance frequency. References [27][28] illustrate the usefulness of sweeping the central frequency in harmonic or IMD experiments because the frequency dependence gives information about the origins of the nonlinearity. This procedure is more deeply developed in [11] to illustrate how different frequency dependences of

the second harmonic and 3IMD can be correlated with different constants of a set of constitutive equations. More specifically, this procedure shows that φ_3 and $\varepsilon_2^{S\theta}$ must be negligible, because it would produce a second harmonic with a frequency dependence that is not consistent with the measurements.

Reference [11] also suggests that the second harmonic is exclusively due to φ_5 which implies, as shown in Table III of the Appendix I, a piezoelectric constant e that depends on the stress. The authors of [11] reached that conclusion after checking that the second-order nonlinearities of c^E that depend on the stress, that is $c_2^{E\theta}$, must be negligible because, although the frequency dependence of the second harmonic is the same as the frequency dependence caused by φ_5, the third-order intermodulation distortion would be overestimated. This is true if no other causes of 3IMD, that could compensate the 3IMD, are considered. However, we show in this section how the hypothesis $c_2^{E\theta} = 0$ is consistent with two different experiments; second harmonic measurements and scattering parameters with an applied DC voltage. As far as we know, this is the first time that these two different manifestations of nonlinearity are explained by use of the same nonlinear parameter.

1) Frequency shift with DC bias

A T-Bias, connected to a voltage source, is introduced in the linear measurement setup to isolate the network analyzer from the DC voltage. Additionally, an OSL calibration is performed for each applied voltage to de-embed the BAW resonator impedance. The results, with an applied voltage ranging from -40 V to +40 V, are summarized in Fig. 7.

By use of simulations of the circuit model, we identify φ_5 in (10) as the dominant term responsible for the frequency shift with electric field. This term in (10), as shown in Appendix I, can be either seen as a strain-dependent piezoelectric constant or an electric field dependent elasticity: $\varphi_5 = -c_{2,E}^{\theta} = -e_{2,S}^{\theta}$. For this experiment, it is easier to understand φ_5 as an electric field dependent elasticity because it directly depends on the applied field. It is found that a value of φ_5=-25.5 N/(V·m), agrees with the measurements, which corresponds to a relative change in $c^{E\theta}$ of $\varphi_5/2c^{E\theta}$=-3.5·10^{-11} m/V.

As shown in the left inset of Fig. 7, the electric field not only changes the frequency, through changing the real part of the elasticity, but also the acoustic losses, through changing the imaginary part of the elasticity. To take this effect into account we introduce the imaginary part of the elasticity of (26), defined in the frequency domain, into (12) and obtain the following definition for the nonlinear viscosity:

$$\eta^{D\theta} \rightarrow \eta^{D\theta} \cdot \left(1 + K_\eta \frac{\varphi_5}{2c^{E\theta}} E\right) \tag{35}$$

where K_η is a unitless factor, valued K_η=65, that multiplies the nonlinear term φ_5 to adjust the impact of the electric field on the acoustic losses.

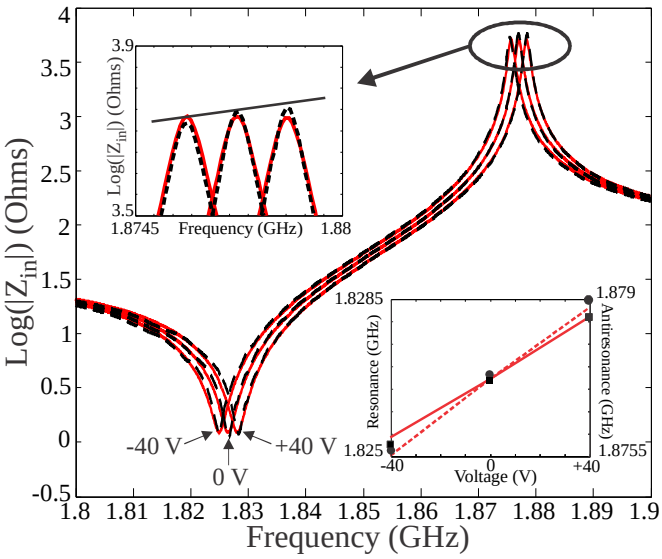

Fig. 7. Measurements and simulations of the magnitude of the impedance for an applied voltage ranging from -40 V to +40 V. The right inset shows the linear dependence of the resonance and antiresonance frequencies on voltage. The left inset shows a zoomed plot of the antiresonance. In the main plot and left inset, the solid lines are simulations whereas the dashed lines are measurements. In the right inset, circles and squares represent the measurements at resonance and antiresonance respectively, whereas the dashed line and the solid line represent the simulations at resonance and antiresonance respectively.

Fig. 8 shows a detailed plot of measurements and simulations at the resonance by taking into account the electric field dependent acoustic losses through and added contribution to equation (10):

$$\Delta T_\eta = j\omega\eta^D K_\eta \frac{\varphi_5}{2c^{E\theta}} SE. \tag{36}$$

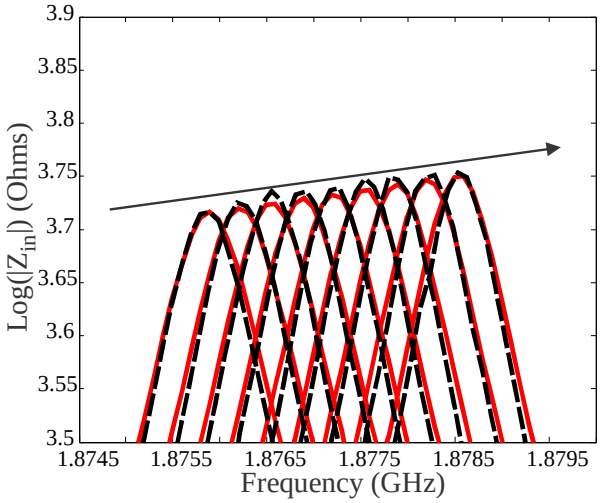

Fig. 8. Measurements and simulations of the magnitude of the impedance for an applied voltage ranging from -40 V to +40 V in 10 V steps at the antiresonance. The impact of the electric field on the acoustic losses translates into an increasing impedance level, at antiresonance, for increasing voltages. The model given by equation (35) is used in these simulations. The solid lines are simulations whereas the dashed lines are measurements.

2) Second harmonic

We perform second harmonic measurements to validate the model by a second independent way. The measurement setup consists on a two-tone configuration, like that in [28], with a balanced output power of 20 dBm for each tone and a tone

spacing of 1 KHz. The frequency of the tones is swept from below the resonance frequency to above the antiresonance frequency while keeping the tone spacing constant. The measurement system itself is characterized by use of four-ports scattering parameters measurements, so that the output of the device can be normalized with respect to its input and the effects introduced by the measurement system can be totally de-embedded. The details on the measurement setup and the normalization procedure can be found in [28].

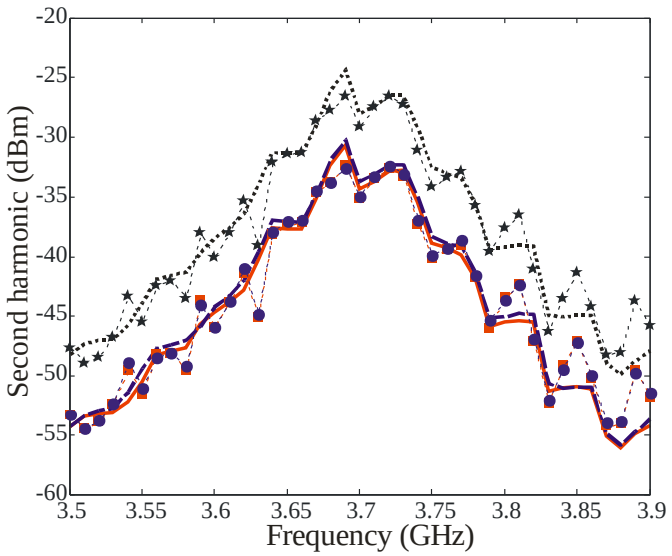

Fig. 9. Measurements and simulations of the second harmonic and second-order intermodulation response and for an input power of +20 dBm. Dashed lines with stars, rectangles and circles represent measurements of f_1+f_2, $2f_1$ and $2f_2$ respectively. Dotted line, solid line and dashed line represent simulations of f_1+f_2, $2f_1$ and $2f_2$ respectively.

Fig. 9 shows the de-embedded second harmonic output for a 20 dBm input power at each tone along with the simulations by use of the circuit model. The frequency dependence of the second harmonic clearly points to a strain squared S^2 contribution as the responsible term. The simulations confirm that the φ_5 term in equation (11) is the dominant term for second harmonic generation. Moreover, the same value φ_5=-25.5 N/(V·m) that predicts the frequency shift with electric field can accurately predict the second harmonic, which corresponds to a relative change of e^{θ} of $\varphi_5/2e^{\theta}$=-8.5. Therefore, the model has been checked to be consistent with two independent manifestations of the second-order nonlinearity and unveil the dominant terms for each specific experiment.

D. Third-order nonlinearities

Third-order nonlinearity gives rise to a variety of effects like third harmonic and third-order intermodulation distortion generation. Moreover, different nonlinear mechanisms contribute to the 3IMD generation, including self-heating and intrinsic nonlinearity. To face the complex characterization of third-order nonlinearity, and because the tested devices do not show a measurable third harmonic, we focus on different types of measurements of the 3IMD to unveil the existent contributions. The same measurement setup and normalization process, used for the second harmonic characterization, is used for these measurements.

1) Self-heating contribution

Subsection IV.B characterizes the performance of the BAW resonator in temperature and reveals the materials' temperature derivatives. Apart from producing a frequency shift with temperature, the dependence of materials properties on temperature also produces a parametric frequency mixing of the fundamental signal and the dynamic variations of temperature due to self-heating. This parametric mixing, whose details can be found in [19], gives rise to 3IMD. Therefore, the modeling of the 3IMD contribution due to self-heating is an independent way to check that the temperature-dependent modeling is correct.

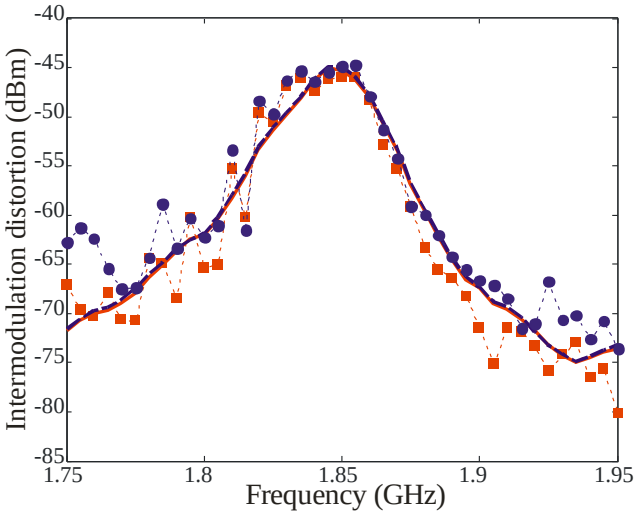

Fig. 10. Measurements and simulations of the low-frequency third-order intermodulation distortion response for a tone spacing of $\Delta f=f_2-f_1$=1 KHz. For this tone spacing, the 3IMD is dominated by self-heating effects. Dashed lines with rectangles and circles represent measurements of $2f_1-f_2$ and $2f_2-f_1$ respectively. Solid line and dashed line represent simulations of $2f_1-f_2$ and $2f_2-f_1$ respectively.

In a two-tone measurement the envelope of the signal $\Delta f/2=(f_2-f_1)/2$ is the main responsible for the temperature oscillations because the dissipation process, related to the square of the signal, creates a heat frequency component at twice that frequency. As explained in [19], the 3IMD level of the self-heating contribution versus envelope frequency has a low-pass filter nature due to the slow dynamics of the temperature. Therefore, two types of measurements have to be carried out in order to accurately characterize the dynamic thermal behavior. The first measurement is at constant tone spacing while sweeping the central tones frequency and allows validating the frequency dependence of the dissipation sources. The second measurement involves sweeping the tone spacing while keeping the central tones frequency constant and allows unveiling the thermal impedance of the device.

We setup the complete circuit model presented in Section III, including the thermal domain, with the material thermal

properties provided by the manufacturer and couple the dissipation in their corresponding position of the thermal domain. Fig. 10 shows measurements and simulations of the 3IMD for a tone spacing of 1 KHz. It can be observed that the resulting 3IMD is the result of dissipation in the electric and acoustic domains, both having different frequency dependences.

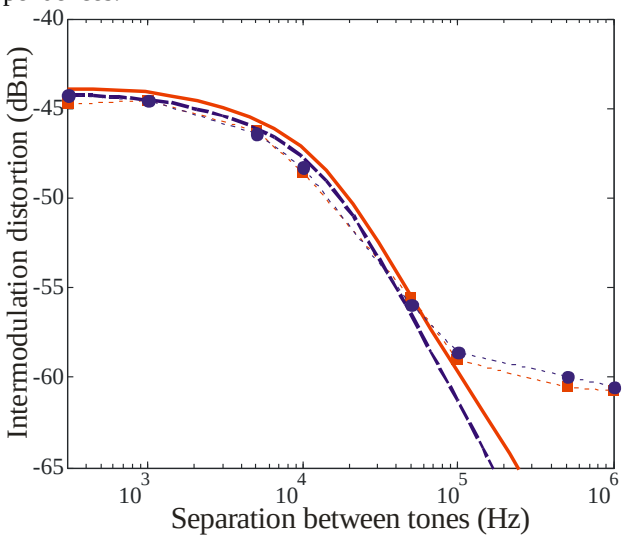

Fig. 11. Measurements and simulations of the low-frequency third-order intermodulation distortion response for a tone spacing ranging from 300 Hz to 1 MHz. The central frequency is kept constant at $f_0=f_1+\Delta f/2= f_2-\Delta f/2=1.845$ GHz. The simulations include the self-heating effects. Dashed lines with rectangles and circles represent measurements of $2f_1-f_2$ and $2f_2-f_1$ respectively. Solid line and dashed line represent simulations of $2f_1-f_2$ and $2f_2-f_1$ respectively.

The second measurement we perform is shown in Fig. 11 along with the simulations by use of the model. Measurements and simulations agree to the expected low-pass filter behavior, which is also a good way to observe the thermal time constant of the device, in the order of milliseconds. The disagreement for tone spacing above 100 KHz is because intrinsic third-order nonlinearity has not been introduced in the model so far, and is explained in the following subsection.

An accurate modeling and understanding of the 3IMD due to self-heating is important because it is responsible for in-band signal integrity degradation, resulting, for example, in an increased Error Vector Magnitude (EVM).

2) *Intrinsic third-order nonlinearity*

The constant 3IMD level observed above 100 KHz in Fig. 11 reveals the existence of a contribution arising from intrinsic third-order nonlinearity. Intrinsic nonlinearity, defined as the dependence of material properties on fields other than temperature, generates harmonics and intermodulation distortion levels that do not depend on the envelope frequency. Although one might think that the lower level of intrinsic nonlinearity, when compared to self-heating 3IMD, makes it a negligible effect, the reality is that it can result in important signal quality degradation in a BAW filter. The main non-desired effect of intrinsic nonlinearity is receiver desensitization, which occurs when an intermodulation product, generated by the mixing of the transmitted signal with a jammer signal, falls within the receiver band [29]. This makes the understanding and modeling of intrinsic third-order nonlinearity an important aspect of BAW technology.

Third-order nonlinearities in BAW resonators have been less explored than second-order nonlinearities. The BAW resonators used in this work show no measurable third-harmonic with the current measurement setup, therefore only the frequency dependence of the intrinsic 3IMD can be used to unveil the dominant third-order terms [9]. The candidate terms to dominate on the 3IMD level are $c_3^{E\theta}$, $\varepsilon_3^{E\theta}$, e_3^{θ}, χ_7 and χ_9.

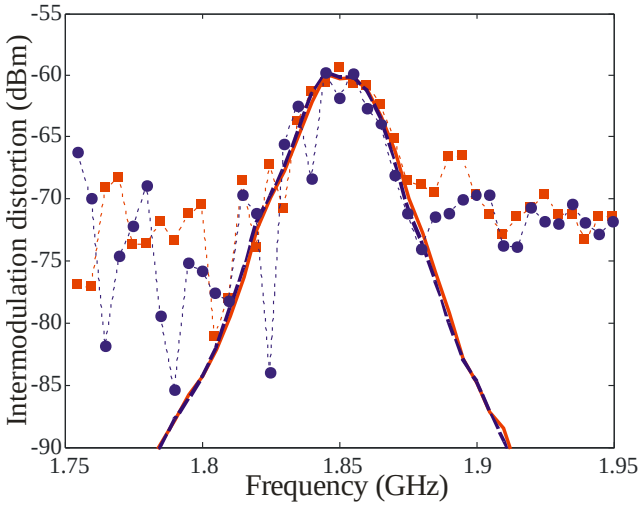

Fig. 12. Measurements and simulations of the low-frequency third-order intermodulation distortion response for a tone spacing of $\Delta f=f_2-f_1=1$ MHz. For this tone spacing, the 3IMD is dominated by intrinsic nonlinearities. Dashed lines with rectangles and circles represent measurements of $2f_1-f_2$ and $2f_2-f_1$ respectively. Solid line and dashed line represent simulations of $2f_1-f_2$ and $2f_2-f_1$ respectively.

We perform two-tone measurements with tone spacing of Δf=1 MHz, to ensure that intrinsic nonlinearity dominates above self-heating effects, and sweep the central frequency as previously done in Fig. 10. It is found by simulation that the contribution of $c_3^{E\theta}/(6c^{E\theta})$=-18.5 is needed to reproduce the frequency dependence of the measurements, as show in Fig. 11. The obtained nonlinear term is the third-order elasticity.

With the nonlinear terms obtained from the frequency dependence for Δf=1 MHz we expect the model to be complete and able to reproduce the 3IMD level stabilization observed in the measurements. Figure 13 shows the agreement between measurements and simulations when intrinsic third-order nonlinearity is introduced in the model.

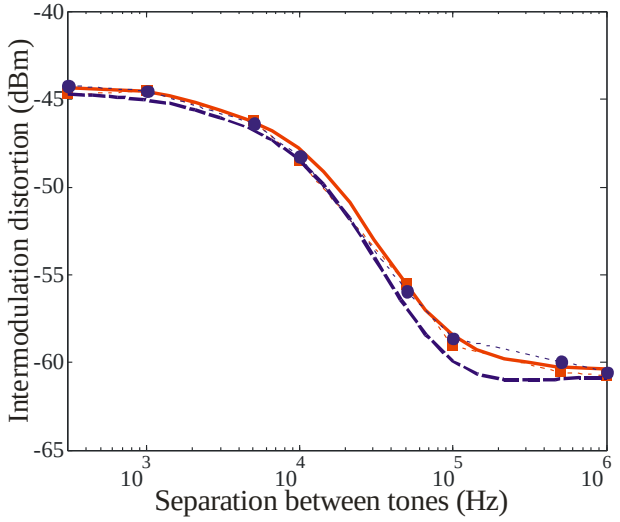

Fig. 13. Measurements and simulations of the low-frequency third-order intermodulation distortion response for a tone spacing ranging from 300 Hz to 1 MHz. The central frequency is kept constant at $f_0=f_1+\Delta f/2= f_2-\Delta f/2=1.845$ GHz. The simulations include the self-heating effects and the intrinsic third-order intermodulation distortion. Dashed lines with rectangles and circles represent measurements of $2f_1-f_2$ and $2f_2-f_1$ respectively. Solid line and dashed line represent simulations of $2f_1-f_2$ and $2f_2-f_1$ respectively.

V. Discussion and Conclusion

We have presented a unified electro-thermo-mechanical description of the constitutive relations in a BAW resonator. The study lies on the expansion of the Gibbs electrical energy function and provides useful relations that allow one to truly relate all the observables to their physical origins. To do that we translate the obtained equations into a circuit model that is used, along with measurements on BAW resonators, to characterize the linear and nonlinear terms.

The obtained model is able to predict the BAW resonator behavior on temperature, its self-heating induced nonlinearities, and the harmonics and intermodulation distortion generation, as well as the frequency shift with DC voltage. In fact, the results point that the frequency shift with DC voltage and the second harmonic generation arise from the same nonlinear term φ_5.

The mathematical derivation in Appendix I states that φ_5 can be either understood as a strain-dependent piezoelectric coefficient or an electric-field dependent elasticity, due to the Maxwell Relations for energy conservation. This can be explained from an atomistic perspective, because on the zero electric field and zero strain situations the atoms are in electrostatic-mechanical equilibrium. In other words, the position of each atom is given by the charge attraction and mechanical elasticity forces, given an isothermal situation. Any variation from the equilibrium, by an applied strain or electric field, translates into an equivalent strain-dependent piezoelectric coefficient or an electric-field dependent elasticity. This means that when a deformation occurs, the atoms gradually lose their relative distance between them, because of internal electrostatic-mechanical forces redistribution. In other words, the dipole moment depends on the deformation in the vertical direction because the relative distances between atoms change with the deformation. This translates into a strain-dependent piezoelectric constant.

The principle above also gives rise to an electric field-dependent elasticity. The elasticity is the material property that relates a stress with a deformation, so as we gradually apply an electric field we change the electrostatic forces between atoms. This fact redistributes the forces equilibrium, so that the effective elasticity changes. This explanation is reinforced by the fact that not only the frequency shift with DC voltage is consistent with the change on the real part of the elasticity, but the DC voltage also induces a change in the imaginary part of the elasticity, which is related to the acoustic loss. For this reason, we have also addressed the impact of DC voltage on acoustic losses. With all these considerations, the obtained nonlinear relations are as follows:

$$c_{NL} = c^{E\theta}\cdot\left(1+\frac{c_3^{E\theta}}{6c^{E\theta}}S^2+\frac{\varphi_5}{2c^{E\theta}}E+\frac{\varphi_6}{c^{E\theta}}\theta\right)\ldots \quad (37)$$
$$+\, j\omega\eta^D\cdot\left(1+K_\eta\frac{\varphi_5}{2c^{E\theta}}E\right)$$

$$e_{NL} = e^{\theta}\cdot\left(1-\frac{\varphi_5}{2e^{\theta}}S+\frac{\varphi_7}{e^{\theta}}\theta\right) \quad (38)$$

$$\varepsilon_{NL} = \varepsilon^{S\theta}\cdot\left(1+\frac{\varphi_2}{\varepsilon^{S\theta}}\theta\right), \quad (39)$$

A circuit model that implements a unified physical description and accounts for the thermal, acoustic and electrical domains and all their observable effects, is of crucial need to predict the linear and nonlinear behavior of BAW resonators at the design stage. Such a model can be used to accurately predict the linear figures of merit and nonlinear indicators like the Error Vector Magnitude, and to design resonators with mitigated nonlinear effects.

Appendix I

Electro-thermo-mechanical relations

In connection with Fig. 1 and by virtue of the first law of thermodynamics, one can define the differential of internal energy of an adiabatically insulated body as the sum of mechanical, electrical and thermal energy [29]:

$$dU = TdS + EdD + \theta d\sigma, \quad (40)$$

where T, S, E, D, θ and σ are stress, strain, electric field, displacement current, temperature and entropy respectively. The natural independent variables of (40) are S, D, and σ, but we are interested in using S, E and θ as the independent variables. Therefore we use the electric Gibbs free energy function $G(S,E,\theta)$, obtained through the appropriate Legendre transformation 0: $G=U-ED-\sigma\theta$, whose differential form can be obtained by use of (40):

$$dG = TdS - DdE + \sigma d\theta. \quad (41)$$

Therefore, the dependent variables T, D and σ are related to the Gibbs function as:

$$T = \left.\frac{\partial G}{\partial S}\right|_{E,\theta};\ D = -\left.\frac{\partial G}{\partial E}\right|_{S,\theta};\ \sigma = -\left.\frac{\partial G}{\partial \theta}\right|_{S,E} \quad (42)$$

$$T = G_S;\ D = -G_E;\ \sigma = -G_\theta, \quad (43)$$

where y_x represent the partial derivative of y with respect to x. The relations in (42) can be expanded into a Taylor series, around the zero fields point, as a three-variable function as follows:

$$f(S,E,\theta)=\sum_{n=0}^{\infty}\sum_{q=0}^{\infty}\sum_{p=0}^{\infty}\frac{\partial^{n+q+p}f}{\partial S^n\partial E^q\partial\theta^p}\frac{S^n}{n!}\frac{E^q}{q!}\frac{\theta^p}{p!}, \quad (44)$$

which up to the third-order can be written as:

$$\begin{aligned} f = {} & f_S S + f_E E + f_\theta \theta + f_{SS}S^2 + f_{EE}E^2 + f_{\theta\theta}\theta^2 + f_{SSS}S^3 \ldots \\ & + f_{EEE}E^3 + f_{\theta\theta\theta}\theta^3 + f_{SE}SE + f_{S\theta}S\theta + f_{E\theta}E\theta + f_{SE\theta}SE\theta \ldots \\ & + f_{SEE}SE^2 + f_{S\theta\theta}S\theta^2 + f_{ESS}ES^2 + f_{E\theta\theta}E\theta^2 + f_{\theta SS}\theta S^2 + f_{\theta EE}\theta E^2, \end{aligned} \quad (45)$$

where f is T, D, or σ. If we replace (43) in (45) the partial derivatives can be written in terms of G, what allows identifying the equivalent partial derivatives, for example, $T_E=G_{SE}=-D_S$. Table II, shows the nomenclature we will follow for the material constants.

TABLE II
MATERIAL CONSTANTS

T_S	$c^{E\theta}$	Elasticity	D_{EEE}	$\varepsilon_3^{S\theta}$	3rd-order permittivity
T_{SS}	$c_2^{E\theta}$	2nd-order elasticity	σ_θ	r^{ES}	Heat capacity
T_{SSS}	$c_3^{E\theta}$	3rd-order elasticity	$\sigma_{\theta\theta}$	r_2^{ES}	2nd-order heat capacity
D_E	$\varepsilon^{S\theta}$	Permittivity	$\sigma_{\theta\theta\theta}$	r_3^{ES}	3rd-order heat capacity
D_{EE}	$\varepsilon_2^{S\theta}$	2nd-order permittivity			
$T_E=G_{ES}=G_{SE}=-D_S$			$-e^\theta$		Piezoelectric constant
$T_\theta=G_{S\theta}=G_{\theta S}=-\sigma_S$			$-\tau^E$		Thermal pressure
$D_\theta=G_{E\theta}=G_{\theta E}=-\sigma_E$			$-\rho^S$		Electro-caloric constant

Note that the subscript denotes the order and the superscript denotes the independent variables that are kept constant. Table III shows the second-order material constants which are also written in the first column as derivatives of the material constants of Table II. The second column is the nomenclature that indicates the order and, as an example, the first row should be read as "E-dependent heat capacity is equal to θ-dependent electro-caloric coefficient", which allows to clarify the equivalent second-order interactions between physical magnitudes in Fig. 1. The third column shows the nomenclature we will use.

TABLE III
2ND ORDER MATERIAL CONSTANTS

$D_{\theta\theta}=\sigma_{E\theta}=-\rho_\theta^S=r_E^{ES}$	$r_{2,E}^S=\rho_{2,\theta}^S$	φ_1
$D_{E\theta}=\sigma_{EE}=-\rho_E^S=\varepsilon_\theta^{S\theta}$	$-\rho_{2,E}^S=\varepsilon_{2,\theta}^S$	φ_2
$T_{EE}=-D_{SE}=-e_E^\theta=-\varepsilon_S^\theta$	$-e_{2,E}^\theta=-\varepsilon_{2,S}^\theta$	φ_3
$T_{\theta\theta}=\sigma_{S\theta}=-\tau_\theta^E=-r_S^{ES}$	$-\tau_{2,\theta}^E=-r_{2,S}^E$	φ_4
$T_{SE}=-D_{SS}=c_E^{E\theta}=-e_S^\theta$	$-c_{2,E}^\theta=-e_{2,S}^\theta$	φ_5
$T_{S\theta}=-\sigma_{SS}=-\tau_S^E=c_\theta^{E\theta}$	$-\tau_{2,S}^E=c_{2,\theta}^E$	φ_6
$T_{E\theta}=-D_{S\theta}=-\sigma_{SE}=e_\theta^\theta=\tau_E^E=\rho_S^S$	$e_{2,\theta}=\tau_{2,E}=\rho_{2,S}$	φ_7
$D_{\theta\theta\theta}=\sigma_{E\theta\theta}=-\rho_\theta^S=r_E^{ES}$	$r_{2,E}^S=\rho_{2,\theta}^S$	φ_1

Table IV shows the third-order material constants, which are also related to the linear material properties of Table II.

TABLE IV
3RD ORDER MATERIAL CONSTANTS

$D_{\theta\theta\theta}=\sigma_{E\theta\theta}=\rho_{\theta\theta}^S$	$\rho_{3,\theta}^S$	χ_1
$D_{E\theta\theta}=\sigma_{EE\theta}=\varepsilon_{\theta\theta}^{S\theta}=r_{EE}^{ES}$	$\varepsilon_{3,\theta}^S=r_{3,E}^S$	χ_2
$D_{EE\theta}=\sigma_{EEE}=\rho_{EE}^S$	$\rho_{3,E}^S$	χ_3
$T_{EEE}=-D_{SEE}=-e_{EE}^\theta$	$-e_{3,E}^\theta$	$-\chi_4$
$T_{\theta\theta\theta}=\sigma_{S\theta\theta}=-\tau_{\theta\theta}^E$	$-\tau_{3,\theta}^E$	$-\chi_5$
$T_{SE\theta}=-D_{SS\theta}=-\rho_{SS}^S$	$-\rho_{3,S}$	$-\chi_6$
$T_{SEE}=-D_{SSE}=c_{EE}^{E\theta}=-\varepsilon_{SS}^{S\theta}$	$c_{3,E}^\theta=-\varepsilon_{3,S}^\theta$	$-\chi_7$
$T_{S\theta\theta}=-\sigma_{SS\theta}\Rightarrow c_{\theta\theta}^{E\theta}=-r_{SS}^{E,S}$	$c_{3,E}^\theta=-r_{3,S}^E$	χ_8
$T_{SSE}=-D_{SSS}=-e_{SS}^\theta$	$-e_{3,S}^\theta$	$-\chi_9$
$T_{SS\theta}=-\sigma_{SSS}=-\tau_{SS}^E$	$-\tau_{3,S}^E$	$-\chi_{10}$
$T_{E\theta\theta}=-D_{S\theta\theta}=-\sigma_{SE\theta}=-e_{\theta\theta}^\theta$	$-e_{3,\theta}$	$-\chi_{11}$
$T_{EE\theta}=-D_{SE\theta}=-\sigma_{SEE}=-\tau_{EE}^E$	$-\tau_{3,E}$	$-\chi_{11}$

The complete nonlinear constitutive equations up to third-order read:

$$T=c^{E\theta}S-e^\theta E-\tau^E\theta+\Delta T_{NL} \quad (46)$$

$$D=e^\theta S+\varepsilon^{SE}E+\rho^S\theta+\Delta D_{NL} \quad (47)$$

$$\sigma=\tau^E S+\rho^S E+r^{ES}\theta+\Delta\sigma_{NL} \quad (48)$$

where the nonlinear contribution is:

$$\begin{aligned} \Delta T_{NL} = {} & \frac{1}{2}\left(c_2^{E\theta}S^2-\varphi_3E^2-\varphi_4\theta^2\right)+\varphi_5SE+\varphi_6S\theta-\varphi_7E\theta\ldots \\ & +\frac{1}{6}\left(c_3^{E\theta}S^3-e_{3,E}^\theta E^3-\chi_5\theta^3\right)-\chi_6SE\theta\ldots \\ & +\frac{1}{2}\left(\chi_7SE^2+\chi_8S\theta^2-\chi_9S^2E-\chi_{10}S^2\theta-\chi_{11}E\theta^2-\chi_{12}E^2\theta\right) \end{aligned} \quad (49)$$

$$\begin{aligned} \Delta D_{NL} = {} & \frac{1}{2}\left(\varepsilon_2^{S\theta}E^2-\varphi_5S^2+\varphi_1\theta^2\right)+\varphi_3SE+\varphi_7S\theta+\varphi_2E\theta\ldots \\ & +\frac{1}{6}\left(\varepsilon_3^{S\theta}E^3+\chi_9S^3+\chi_1\theta^3\right)+\chi_{12}SE\theta\ldots \\ & +\frac{1}{2}\left(\chi_4SE^2+\chi_{11}S\theta^2-\chi_7S^2E+\chi_6S^2\theta+\chi_2E\theta^2+\chi_3E^2\theta\right) \end{aligned} \quad (50)$$

$$\begin{aligned} \Delta\sigma_{NL} = {} & \frac{1}{2}\left(r_2^{ES}\theta^2+\varphi_2E^2-\varphi_6S^2\right)+\varphi_7SE+\varphi_4S\theta+\varphi_1E\theta\ldots \\ & +\frac{1}{6}\left(r_3^{ES}\theta^3+\chi_3E^3+\chi_{10}S^3\right)+\chi_{11}SE\theta\ldots \\ & +\frac{1}{2}\left(\chi_{12}SE^2+\chi_5S\theta^2+\chi_6S^2E-\chi_8S^2\theta+\chi_1E\theta^2+\chi_2E^2\theta\right) \end{aligned} \quad (51)$$

REFERENCES

[1] R. Aigner, J. Kaitila, J. Ella, L. Elbrecht, W. Nessler, M. Handtmann, T. R. Herzog, S. Marksteiner, "Bulk-acoustic-wave filters: performance optimization and volume manufacturing", *2003 IEEE MTT-S International Microwave Symposium Digest*, vol. 3, pp. 2001- 2004, 8-13 June 2003

[2] A. Reinhardt, G. Parat, E. Defay, M. Aid, F. Domingue, "Acoustic technologies for advanced RF architectures", *2010 8th IEEE International NEWCAS Conference*, vol., no., pp.161-164, 20-23 June 2010

[3] R. Aigner, "SAW and BAW technologies for RF filter applications: A review of the relative strengths and weaknesses", *2008 IEEE International Ultrasonics Symposium*, vol., no., pp.582-589, 2-5 Nov. 2008

[4] L. Mourot, P. Bar, G. Parat, P. Ancey, S. Bila, J. F. Carpentier, "Stopband filters built in the BAW technology [Application Notes]", *IEEE Microwave Magazine*, vol. 9, no. 5, pp. 104-116, Oct. 2008

[5] D. S. Shim, D. A. Feld, "A general nonlinear mason model of arbitrary nonlinearities in a piezoelectric film". *2010 IEEE International Ultrasonics Symposium* (early access).

[6] B. Ivira, P. Benech, R. Fillit, F. Ndagijimana, P. Ancey, G. Parat, "Modeling for temperature compensation and temperature characterizations of BAW resonators at GHz frequencies", *IEEE Transactions on Ultrasonics, Ferroelectrics and Frequency Control*, vol. 55, no. 2, pp. 421-430, February 2008

[7] D. Petit, N. Abele, A. Volatier, A. Lefevre, P. Ancey, J. F. Carpentier, "Temperature Compensated Bulk Acoustic Wave Resonator and its Predictive 1D Acoustic Tool for RF Filtering", *2007 IEEE International Ultrasonics Symposium*, vol., no., pp.1243-1246, 28-31 Oct. 2007

[8] B. Ivira, R. Y. Fillit, F. Ndagijimana, P. Benech, G. Parat, P. Ancey, "Self-heating study of bulk acoustic wave resonators under high RF power", *IEEE Transactions on Ultrasonics, Ferroelectrics and Frequency Control*, vol. 55, no. 1, pp. 139-147, January 2008

[9] E. Rocas, C. Collado, J. C. Booth, E. Iborra, R. Aigner, "Unified model for Bulk Acoustic Wave resonators' nonlinear effects", *2009 IEEE International Ultrasonics Symposium*, vol., no., pp.880-884, 20-23 Sept. 2009

[10] Y. Cho, J. Wakita, "Nonlinear equivalent circuits of acoustic devices", *1993 IEEE International Ultrasonics Symposium*, vol., no., pp.867-872 vol.2, 31 Oct-3 Nov 1993

[11] D. A. Feld, D. S. Shim, "Determination of the nonlinear physical constants in a piezoelectric AlN film". *2010 IEEE International Ultrasonics Symposium* (early access).

[12] W. P. Mason, "Electronical transducers and wave filters", Van Nostrand, New York, c1948.

[13] R. E. Newnham, Properties of materials: anisotropy, symmetry, structure, Oxfors university press, 2004.

[14] F. P. Incropera, D. P. DeWitt, T. L. Berqman A. S. Lavine, "Fundamentals of Heat And Mass Transfer", John Wiley & Sons Inc, 2002

[15] N. B. Hassine, D. Mercier, P. Renaux, D. Bloch, G. Parat, B. Ivira, P. Waltz, C. Chappaz, R. Fillit, S. Basrour, "Self heating under RF power in BAW SMR and its predictive 1D thermal model", *2009 IEEE International Frequency Control Symposium Joint with the 22nd European Frequency and Time forum*, vol., no., pp. 237-240, 20-24, April 2009.

[16] M. A. Dubois and P. Muralt, "Properties of aluminum nitride thin films for piezoelectric transducers and microwave filter applications", *Applied Physics Letters*, 74, p. 3023, 1999.

[17] J. D. Larson III, Y. Oshrnyansky, "Measurement of effective kt^2, Q, R_p, R_s vs. Temperature for Mo/AlN FBAR resonators", *2002 IEEE Ultrasonics Symposium*, vol. 1, no., pp. 939- 943 vol.1, 8-11 Oct. 2002

[18] C. Kittel, Introduction to solid state physics, 7th Edition, John Wiley & Sons, New York, Chichester, 1996.

[19] E. Rocas, C. Collado, N. D. Orloff, J. Mateu, A. Padilla, J. M. O'Callaghan, J. C. Booth, "Passive Intermodulation Due to Self-Heating in Printed Transmission Lines", *IEEE Transactions on Microwave Theory and Techniques*, vol. 59, no. 2, pp. 311-322, Feb. 2011

[20] G. S. Kino, Acoustic waves, Prentice-Hall, Englewood Cliffs, 1987.

[21] R. Thalhammer, R. Aigner, "Energy loss mechanicms in SMR-type BAW devices", *2005 IEEE MTT-S International Microwave Symposium Digest*, vol., no., pp. 4 12-17 June 2005

[22] B. A. Auld, Acoustic Fields and Waves in Solids (Krieger, Malabar, Florida), Vol. I, 1990

[23] P. Muralt, J. Antifakos, M. Cantoni, R. Lanz, F. Martin, "Is there a better material for thin film BAW applications than A1N?", *2005 IEEE Ultrasonics Symposium*, vol. 1, no., pp. 315- 320, 18-21 Sept. 2005

[24] Advanced Design System (ADS)

[25] B. Smirnov, Yu. Burenkov, B. Kardashev, D. Singh, K. Goretta, A. Arellano-López, "Elasticity and inelasticity of silicon nitride/boron nitride fibrous monoliths", *Physics of the Solid State*, Volume 43, Number 11, November 2001, pp. 2094-2098(5)

[26] J. D. Larson III, S. Mishin, S. Bader, "Characterization of Reversed c-axis AlN Thin Films", *2010 IEEE International Ultrasonics Symposium* (early access).

[27] C. Collado, E. Rocas, J. Mateu, A. Padilla, J. M. O'Callaghan, "Nonlinear Distributed Model for Bulk Acoustic Wave Resonators", *IEEE Transactions on Microwave Theory and Techniques*, vol. 57, no. 12, pp. 3019-3029, Dec. 2009

[28] C. Collado, E. Rocas, A. Padilla, J. Mateu, J. M. O'Callaghan, N. D. Orloff, J. C. Booth, E. Iborra, R. Aigner, "First-Order Elastic Nonlinearities of Bulk Acoustic Wave Resonators", *IEEE Transactions on Microwave Theory and Techniques*, vol.PP, no.99, pp.1, 2010 (early access).

[29] M. Ueda, M. Iwaki, T. Nishihara, Y. Satoh, K. Hashimoto, "Investigation on nonlinear distortion of acoustic devices for radio-frequency applications and its supression", *2009 IEEE International Ultrasonics Symposium*, vol., no., pp. 876-879, 20-23 Sept. 2009.

[30] H. B. Callen, Thermodynamics, John Wiley & Sons, Inc. 1960.

[31] R. Gausmann, Nichtlineares dynamisches Verhalten von piezoelektrischen Stabaktoren bei schwachem elektrischen Feld, Cuvillier Verlag, Gottingen 2005.

CONCLUSION

Large-signal modeling is a topic of increasing importance in the microwave industry. In this work, different approaches to account for the linear and nonlinear response of a variety of passive microwave devices have been presented. The methodology has included measurements with advanced characterization techniques, as well as modeling both with a phenomenological and a physical perspective.

In chapter I, nonlinear transmission lines are analyzed, with an emphasis on High Temperature Superconductors, and models are derived to account for the nonlinear behavior. Such models can be used as building blocks for devices that make use of transmission lines, like filters or couplers, to predict their performance under large-signal conditions. Moreover, circuit modeling allows testing the designs with real complex signals, like WCDMA, and obtaining performance indicators that are of crucial importance to fulfill the requirements of today's communications industry regulations. As an application example, the use of High Temperature Superconductor transmission lines as power limiters in a multiplexer filter bank is considered, and its nonlinear model allows for its behavior prediction. Additionally, the analytical expressions of impedance mismatched nonlinear transmission lines are provided.

In chapter II lumped elements models and distributed models, both from a phenomenological perspective, are presented for Bulk Acoustic Wave resonators. The phenomenological models represent a fast way to take into account the nonlinear response of BAW resonators, and their correct scaling with area allows using them to

predict the filter's response. Moreover, chapter II presents advanced measurement configurations and techniques to unveil the response of the devices under test without taking into account the effects introduced by the measurement setup, which allows for an accurate characterization of the device.

Chapter III sheds light on the impact of temperature rise in passive microwave devices performance. More specifically, transmission lines made of regular metals and dielectrics are considered, as well as transmission lines with thin-film ferroelectrics and Bulk Acoustic Wave devices. Physical electro-thermo-mechanical models are obtained, which can be used to predict the performance of the devices at different temperatures and assess the impact of self-heating on passive intermodulation distortion. As a result, electromagnetic and electro-acoustic devices have been properly characterized and their nonlinear material properties identified. The presented circuit models can be used to optimize the linear and nonlinear response, which is of extreme importance in proposing designs with reduced nonlinearity or even total cancellation. Additionally, the presented circuit models allow one to use them in integration into more complex systems and obtain performance indicators. Two of these works, Appendix A and B, are a submitted article which is pending for acceptation to be published and an article to be submitted, respectively.

IMPACT FACTORS OF THE PUBLICATIONS

According to the Journal Citation Reports® (JCR) database of Thomson Scientific and the SciVerse Scopus® SJR index of Elsevier B. V., the impact factors, on March 2011, are as follows:

Journal/Proceedings	**JCR***	**SJR***
IEEE Transactions on Applied Superconductivity	**1.310**	**0.075**
IEEE Transactions on Microwave Theory and Techniques	**2.076**	**0.217**
Proceedings of the IEEE MTT-S International Microwave Symposium	**-**	**0.071**
Proceedings of the IEEE UFFC-S International Ultrasonics Symposium	**-**	**0.036**

*The JCR and SJR indexes have different scales, according to their calculation method.

VITA

Eduard Rocas received the Telecommunication Engineering degree from the Universitat Politècnica de Catalunya (UPC) in 2005, where his final project was associated with the creation of the Intelligent Communications and Avionics for Robust Unmanned Aerial Systems (ICARUS) research group. From September 2005 to July 2006, he was involved in the simulation and modeling of advanced SONARs at the Computer Vision and Robotics Group (VICOROB - University of Girona) as a FPU Grant Holder. Since November 2006 until June 2011 he stayed with UPC as a PhD Student (FPI Grant Holder) focusing his research on new materials and structures for novel RF/MW devices. Since January 2009 until June 2011 he stayed as a Guest Researcher at the National Institute of Standards and Technology (NIST), Boulder, CO.

Eduard Rocas may be reached at Universitat Politècnica de Catalunya (UPC). His email is eduard.rocas@tsc.upc.edu.